TRANSPORT OF HEAT AND MOMENTUM IN NON-EQUILIBRIUM WALL-BOUNDED FLOWS

BY

ALIREZA EBADI

B.Sc. Mechanical Engineering, Sharif University of Technology, Iran, 2010

DISSERTATION

Submitted to the University of New Hampshire
in Partial Fulfillment of
the Requirements for the Degree of

Doctor of Philosophy

in

Mechanical Engineering

December 2016

This dissertation has been examined and approved in partial fulfillment of the requirements for the degree of Doctor of Philosophy in Mechanical Engineering by:

Dissertation Director, Christopher M. White,
Associate Professor of Mechanical Engineering

Gregory P. Chini,
Associate Professor of Mechanical Engineering

Yves Dubief,
Associate Professor of Mechanical Engineering

Diane Foster,
Professor of Mechanical and Ocean Engineering

Joseph Klewicki,
Professor of Mechanical Engineering

on October 24, 2016.

Original approval signatures are on file with the University of New Hampshire Graduate School.

*To mom and dad, **Gorji Hashemi** and **Ali Ebadi**, for a lifelong self-sacrifice and unconditional support.*

ACKNOWLEDGMENTS

I would like to thank my advisor, Professor Christopher M. White, for his intelligent guidance and boundless support over the past six years. This work would not have been possible without his support and encouragement. Thank you *Chris* for being a friend, a mentor and an advisor who taught me to be my first critic. I am grateful for all the help and many invaluable contributions from my committee members: Professors Gregory Chini, Yves Dubief, Joseph Klewicki and Diane Foster. *Diane*, I am also grateful for your continuous support as a friend.

I would like to thank my friends, fellow graduate students, the Fluid Book Club and specifically my labmates: Michael Allard, Drummond Biles and Nicholas DeMarchi. *Mike* and *Drummond*, I am grateful for all that I have learned from you over the past few years. I am also grateful for the help and support from the Mechanical Engineering Department faculty and staff, specifically Tracey Harvey, Sheldon Parent and James Abare.

I am utterly grateful for all the support, encouragement and love from my late dad, mom and my brothers, *Akbar* and *Arash*. I would not be able to finish this work without their infinite support, and my gratitude to them is beyond words. *Agha*, I learned to strive for excellence from you. Your memories are forever with me, and I will always carry your love in my heart. Finally, I would like to extend my deepest gratitude to Yassamin for her patience, encouragement and boundless love. *Yassamin*, thank you for making this ride joyful, and keeping my life in order.

TABLE OF CONTENTS

Page

CHAPTER

APPENDICES

LIST OF TABLES

LIST OF FIGURES

ABSTRACT

Transport of Heat and Momentum In Non-Equilibrium Wall-Bounded Flows

by

Alireza Ebadi

University of New Hampshire, December, 2016

Transport of momentum and heat in non-equilibrium wall-bounded flows is studied analytically and experimentally to better understand the underlying physics, transition dynamics, and appropriate flow scaling in non-equilibrium flows. Non-equilibrium flows, in which the mean flow time scales are comparable to turbulent flow time scales, do not exhibit universal behaviors and cannot be characterized only in terms of local parameters. Pressure gradients, fast transients and complex geometries are among the sources that can perturb a flow from an equilibrium state to a non-equilibrium state. Since all or some of these perturbation sources are present in many engineering application relevant flow systems and geophysical flows, understanding and predicting the non-equilibrium flow dynamics is essential to reliably analyze and control such flows.

Reynolds-averaged Navier-Stokes (RANS) simulations are extensively used to model and predict fluid transport across a wide range of disciplines. The shortcoming is that most turbulence models used in RANS simulations use almost exclusively wall-models based on equilibrium boundary layer behaviors, despite the fact that many basic assumptions required of equilibrium boundary layers are not satisfied in the majority of the flow systems in which RANS simulations are used. In particular, pressure gradients, dynamic walls, roughness, and large-scale flow obstacles produce boundary layers that are strongly non-equilibrium in nature. Often the prediction of RANS simulations in complex engineering systems (with perturbations that induce non-equilibrium flow behaviors) fail spectacularly primarily owing to the fact that the turbulence models do not incorporate the correct physics to accurately capture the transport behaviors in non-equilibrium boundary layers. These failures result in over-engineered and hence, less efficient designs. This lack of efficiency manifests in higher economic and environmental costs. The broad objective of this dissertation

work is to develop analytical and experimental tools needed to better understand the underlying transport physics in non-equilibrium boundary layers.

The key scaling parameter in wall-bounded flows is the wall flux of momentum and heat. It follows that an accurate determination of the wall fluxes is essential to study the dynamics of non-equilibrium wall-bounded flows. As part of this dissertation research, an integral method to evaluate wall heat flux suitable for experimental data is developed. The method is exact and does not require any streamwise gradient measurements. The integral method is validated using simulation and experimental data. Complications owing to experimental limitations and measurement error in determining wall heat flux from the method are presented, and mitigating strategies are described. In addition to the ability to evaluate the wall heat flux, the method provides a means to connect transport properties at the wall to the mean flow dynamics.

The integral method is further developed to formulate a novel and robust validation technique of Reynolds-averaged Navier-Stokes (RANS) turbulence models. Validation of the turbulence models employed in RANS simulations is a critical part of model development and application. The integral based validation technique is used to evaluate the performance of two low-Reynolds-number and two high-Reynolds number RANS turbulence models of reciprocating channel flow, and results are compared to the so-called standard validation technique. While the standard validation technique indicates that the low-Reynolds-number models predict the wall heat flux well, the integral validation technique shows that the models do not accurately capture the correct physics of thermal transport in reciprocating channel flow. Moreover, it shows that the correct prediction of the wall heat flux by the models is owed to the serendipitous cancellation of model errors.

One of the identified failures of the RANS simulations of reciprocating channel flow is the inability to accurately predict the flow dynamics during the laminar-turbulence transition. The development of improved RANS turbulence models, therefore requires an improved understanding of the underlying laminar-turbulent transition mechanisms. As part of this dissertation work, the balance of the leading order terms in the phase-averaged mean momentum equation are used to study the transition mechanism in a reciprocating channel flow. It is concluded that the emergence of an internal layer in the late acceleration phase of the cycle triggers the flow to transition from a self-sustaining transitional regime to an intermittently turbulent regime. In the absence of this internal layer, the flow remains transitional throughout the cycle.

Lastly, since experimental studies of heat transfer in non-equilibrium wall-bounded flows are very limited, a unique experimental facility was developed to study non-equilibrium boundary layers with heat transfer. The facility consists of boundary layer wind tunnel that nominally measures $303mm \times 135mm$ cross-section and $2.7m$ in length. A freestream heater and a thermal wall-plate are used to maintain the desired outer and inner thermal boundary conditions, respectively. A rotor-stator assembly is fabricated to generate a periodic pressure gradient used to produce pulsatile boundary layer flow. The facility is first validated for equilibrium flow conditions, and then used to study the transport of momentum in a pulsatile boundary layer (PBL). The results show that although the PBL flow at each phase departs from equilibrium, the time-average profiles, except for the streamwise turbulent intensity $\overline{u'^2}$, appears similar to steady-state, zero-pressure-gradient boundary layer flow. Using $\overline{u'^2}$ as a metric for departure of the time mean flow from equilibrium, a critical frequency range $0.014 < \omega_c^+ < 0.020$ was identified, where $\omega^+ = \frac{\omega}{u_\tau^2/\nu}$, ω is the angular frequency of the pressure gradient modulation, u_τ is the friction velocity and ν is the fluid viscosity. For $\omega^+ > \omega_c^+$, $\overline{u'^2}$ does not exhibit significant difference from ZPG boundary layer flow. For $\omega^+ < \omega_c^+$, however, $\overline{u'^2}$ has a higher value compared to ZPG boundary layer flow where magnitude of the differences is inversely proportional to flow frequency. The wall shear stress modulation is investigated to study the perturbation field in PBL. The perturbation wall shear stress of the two lower frequency cases is in phase with the freestream and the amplitude of modulation matches the Stokes' boundary layer solution. For the highest frequency case, however, the perturbation wall shear stress leads the freestream and the amplitude of modulation is slightly larger than the Stokes' boundary layer solution. It is, therefore, concluded that the perturbation flow of the highest frequency case is non-equilibrium and eddy-viscosity model (EVM) simulation models fail to predict the perturbation field accurately.

CHAPTER 1

INTRODUCTION

1.1 Motivation

The transport of mass, momentum, and heat in turbulent boundary layers play critical role in the performance, efficiency, and life-cycle of many engineered systems, and control or contribute to the dynamics of many geophysical flows (Borman and Nishiwaki, 1987; Ristorcelli and Lumley, 1992). The need to reliably analyze, predict, and control boundary layer transport is therefore critically important across a broad spectrum of applications and scientific disciplines. In these pursuits, computational fluid dynamics (CFD) simulations are widely employed. The ideal approach is to employ direct numerical simulation (DNS) to numerically solve the governing equations, yielding the full temporal and spatial evolution of a given flow field at all relevant time and length scales. The limitation, however, is that DNS of full-scale engineering systems (e.g., a jet engine) or geophysical flows (e.g., atmospheric transport) is not possible even with the current processing power of supercomputers.

The only rational approach to circumvent the limitations of DNS is to model (simulate with some empirical assumptions) the system to reduce the complexity. The traditional CFD approach employs a Reynolds-Averaged Navier-Stokes (RANS) formulation to describe the evolution of the mean fields. Here a mean/fluctuation decomposition is used to decompose the governing equations into the so-called RANS equations. This procedure leads to the well-known closure problem: the averaged equations for the mean fields contain unknown correlations of the fluctuation fields. To close the system of equations, *ad hoc* or phenomenological closure models of the unknown fluctuating field correlations are invoked. Furthermore, in turbulent boundary layer simulations most CFD codes utilize wall functions, which assume the form for the solution of the velocity and temperature fields in the near-wall region to reduce the number of computational grid points near a wall. It follows that the potential for CFD simulations to accurately predict boundary layer transport clearly depends on the specifics of the closure model and wall functions used.

In general, the development of turbulent closure models and wall functions are directed, refined, and validated by experimental data. One limitation of this approach is the relatively small number of experimental datasets acquired in complex flows typical of engineered systems. Consequently, turbulence closure models and wall functions are generally based on data from canonical flows, such as steady two-dimensional developing boundary layers, channel flow, or pipe flow. Such flows are considered to be in statistical equilibrium, in that the time scales over which the mean field vary are large compared to local turbulent time scales. In turn, the turbulent field rapidly adjusts to mean field variations, and the flow exhibits universal behaviors when scaled by local parameters (Townsend, 1976; Davidson, 2004).

One very important universal behavior is the logarithmic dependence of the mean velocity profile in the so-called logarithmic region

$$U^+ = \frac{1}{\kappa}\log(y^+) + C_1, \tag{1.1}$$

where the superscript $^+$ denotes normalization by the friction velocity $u_\tau = \sqrt{\tau_w/\rho}$ and kinematic viscosity ν, where τ_w is the shear stress at the wall and ρ the fluid density; $1/\kappa$ (typically κ is called the von Kármán coefficient) is the slope; y^+ is the wall-normal coordinate; and C_1 is the intercept at $y^+ = 1$. Equation 1.1 is referred to as the law of the wall with constants (at sufficiently high Reynolds number) $\kappa \approx 0.4$ and $C_1 \approx 5$, varying for a given canonical flow type (Nagib and Chauhan, 2008). For the distribution of temperature in the boundary layer, using similar dimensional scaling arguments used to derive Eq. 1.1 yields the law of the wall for temperature

$$\Theta^+ = \frac{(\Theta_w - \Theta)}{q''_w/(\rho c_p u_\tau)} = \frac{1}{\kappa_\Theta}\log(y^+) + C_2(Pr), \tag{1.2}$$

where Θ_w is wall temperature, q''_w is the wall heat flux, c_p is specific heat, $1/\kappa_\Theta$ is the slope, and C_2, the intercept at $y^+ = 1$, which is a function of the Prandtl number, $Pr = \nu/\alpha$ where α is thermal diffusivity. In general, $\kappa_\Theta \approx 0.48$ is taken as a universal constant. Since $\kappa_\Theta \approx \kappa$, the formulation is consistent with Reynolds' analogy between heat transfer and momentum transfer, with the effect of the Pr captured by C_2.

In many engineering flows, however, the time scales over which the mean field vary are small compared to local turbulent time scales, and the flow field cannot be characterized solely in terms of local parameters (Townsend, 1976). Such rapid changes in the mean field typically result from pressure gradients, wall curvature, strong three-dimensionality, wall roughness, or dynamic walls. For simple non-equilibrium boundary layers, in which an equilibrium boundary layer flow experiences a single sudden perturbation (e.g., flow over an obstacle/cavity or flow subjected to a pressure gradient), there has been extensive, and continuing, research to understand the redistribution of the velocity field when equilibrium is disturbed (Antonia and Luxton, 1971; Bradshaw and Wong, 1972; Bandyopadhyay and Ahmed, 1993; Castro and Epik, 1998). In general, these studies show that: (a) in a small local region of a strong perturbation the log-layer is obliterated (i.e., the law of the wall given by Eq. 1.1 does not hold), (b) downstream of the perturbation, in the so-called recovery region, an internal stress equilibrium layer grows and the boundary layer recovers towards equilibrium. Conceptually, the effect of (b) relative to Eq. 1.1 is a spatially developing slope and intercept that asymptote to their universal values at the edge of the recovery region, where the functional form of the spatial dependence depends on the perturbation.

While the effects of non-equilibrium boundary layers on the velocity field have been extensively studied, heat transfer in non-equilibrium boundary layers has received far less attention. Nevertheless, despite the somewhat limited data, it is a well-accepted fact that the law of the wall for temperature is more affected by mean field variations than the velocity field (Blackwell *et al.*, 1972; Kader and Yaglom, 1991; Bradshaw and Huang, 1995; Kong *et al.*, 2001; Houra and Nagano, 2006; Wang *et al.*, 2008). For example, in non-equilibrium boundary layer flow subjected to a pressure gradient, the constants in Eq. 1.2 vary significantly with pressure gradient while the constants in Eq. 1.1 vary little. This difference in sensitivity is unexpected given that Eqs. 1.1-1.2 were derived from analogous dimensional scaling arguments, and has brought into question the validity of the law of the wall (Bradshaw and Huang, 1995; Wei *et al.*, 2005b). Moreover, the high sensitivity of the temperature-field to pressure gradient flows is remarkable since the pressure gradient does not appear in the transport equation for temperature. The consensus, although not entirely well-understood, is that while the law of the wall for velocity is fairly resilient, the law of the wall for temperature is very strongly affected by upstream disturbances. The implication is that the scaling used to derive the law of the wall for velocity and, in particular, temperature fails to describe the behaviors of the mean dynamics in flows with large gradients in the mean flow direction, or with small Peclet number, $Pe = Pr\delta^+$, where δ^+ is the inner-normalized boundary layer height (Wei *et al.*, 2005b). Consequently, to capture non-linear effects on mean field dynamics, the present state of the research is to introduce adjustments to the law of the wall (Volino and Simon, 1997), devise new scaling laws (Wei *et al.*, 2005b; Wang *et al.*, 2008; Araya and Castillo, 2012), or use single-point closure models (i.e., eddy viscosity or mixing length models) informed by experimental data (Mellor and Yamada, 1982; Kantha and Clayson, 1994).

Extrapolating the results discussed above to strong non-equilibrium flows, in which mean field perturbations vary rapidly in magnitude and in space and time (i.e., in-cylinder engine flows during a typical drive cycle), a logical conclusion is that with respect to the law of the wall given by Eqs. 1.1-1.2 that either (a) they will not hold or (b) there will be will be strong spatio-temporal variations of the slope and intercept. Moreover, the high sensitivity of the temperature field to mean field perturbations is strongly suggestive that CFD simulations utilizing wall functions based on equilibrium boundary layer behaviors will not accurately capture heat transfer in strong non-equilibrium flows. Consequently, in most engineering systems with complex geometries and unsteady flow forcing mechanisms RANS simulations fail spectacularly. These failures result in over-engineered and hence, less efficient designs. This lack of efficiency is manifested in higher economic and environmental costs. One obstacle for formulating new engineering heat transfer models that better captures the physics of non-equilibrium flows (i.e., flows with complex dynamics) is the lack of robust experimental data needed to both formulate and validate models.

In the present work, the objective is to use complementary direct numerical simulation (DNS) and numerical simulation models, and physical experiments to investigate both thermal and momentum transport in non-equilibrium wall-bounded flows. The broad objective is to advance the fundamental knowledge of transport in non-equilibrium boundary layers and improve turbulence models that account for non-equilibrium flow behaviors. The project work involves:

- developing novel integral method to evaluate wall heat flux,
- introducing new evaluation technique of RANS turbulent models,
- proposing the mechanism of transition to turbulence in oscillating wall-bounded flows,
- developing experimental infrastructure to study non-equilibrium thermal boundary layers, and
- performing the experimental investigation of momentum transport in pulsatile boundary layer flow.

1.2 Turbulent Wall-Bounded Flows

Equilibrium Wall-Bounded Flows and Wall Functions:

The so-called “no-slip" boundary condition states that the relative velocity between a fluid and a bounding wall is zero. For a non-stationary fluid, the no-slip boundary condition imposes a shear stress on the wall with an equal and opposite shear stress on the fluid layer attached to the wall. The effects of the wall shear stress penetrate into the flow by both molecular and turbulent diffusion, thus reducing the fluid momentum over a finite layer of fluid adjacent to the wall. The layer of fluid that experiences this momentum drop is called the boundary layer. Conversely, the fluid layer outside of the boundary layer does not feel the effects of the wall shear stress and is termed the freestream flow.

Owing to the momentum loss caused by the presence of the wall, the velocity field within the boundary layer exhibits spatial velocity gradients. These gradients are associated with the presence of vorticity (i.e., fluid rotation) defined as follows:

$$\vec{\Omega} = \vec{\nabla} \times \vec{u} \tag{1.3}$$

where $\vec{\Omega}$ is vorticity, $\vec{\nabla}$ is the gradient vector and $\vec{u}$ is the velocity vector. Therefore, the boundary layer can be defined as fluid layer in the vicinity of the wall that contains vorticity. Conversely, the freestream can be defined as the region of the flow away from the wall that is absent vorticity (i.e., irrotational).

A canonical steady-state equilibrium boundary layer is two-dimensional and, as described earlier, exhibits universal behaviors when scaled by local parameters; most notable of these universal behaviors is that the distribution of velocity and temperature follow Eqs. 1.1 and 1.2, respectively, in the so-called logarithmic region of the flow. Importantly, similar universal behaviors are observed in the near-wall layer of other turbulent wall-bounded flows such as channel flow and pipe flow. These universal scaling behaviors are employed in high-Reynolds number RANS modeling of wall-bounded flows by the use of wall functions. The purpose of the wall functions is to circumvent the excessive grid requirements to resolve the boundary layer (owing to the large spatial gradients found in the boundary layer) by assuming *apriori* behaviors of the mean fluid dynamics in the near-wall layer. Specifically, with the use of wall functions, the first grid point can be located at a relatively large distance from the wall (i.e., within the so-called logarithmic layer) where the velocity is assumed to follow Eq. 1.1. The implication is that a relatively coarse grid can be used to resolve the mean boundary layer dynamics since the flow in the near-wall layer (where the gradients are largest) is assumed. The gain in computational efficiency with the use of wall-functions can be several orders of magnitude (Wilcox *et al.*, 1998), and is a key element in the simulation of high-Reynolds number wall-bounded flows.

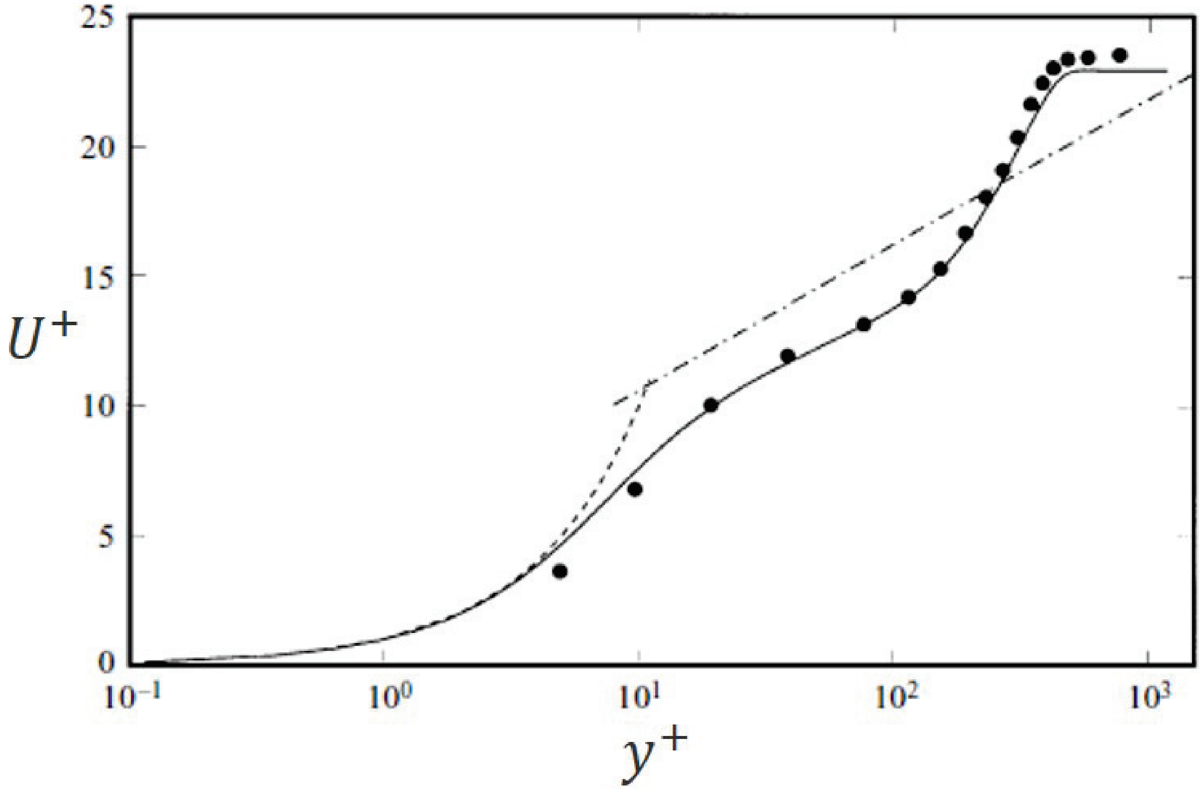

Figure 1.1: Mean velocity profile in the recovery region of flow behind a backward facing step. Data acquired at $x/h = 19$, where x is the streamwise distance behind the step and h is the step height (the recovery region starts at $x/h \simeq 7$). Dashed line represents $U^+ = y^+$ and dotted-dashed line represents $U^+ = \frac{1}{0.41}log(y^+) + 5.0$. Solid line is the DNS performed by Le *et al.* (1997), and circles represent experimental measurements of Jovic and Driver (1994, 1995).

Non-Equilibrium Wall-Bounded Flows

It is important to differentiate between the terminology “equilibrium layer" defined by Townsend (1961) and “equilibrium boundary layer” used in this dissertation. Townsend defined the equilibrium layer as a region within the boundary layer where the turbulent dissipation and production rates are locally in balance. The term equilibrium boundary layer, as used in this dissertation, has a fundamentally different meaning, and is best defined by flows that satisfy a set of given conditions. De Graaff and Eaton (2000) defined an equilibrium boundary layer as a flow where the shear stress distribution is balanced by the wall shear stress. Clauser (1956) defined an equilibrium boundary layer as a flow in which the driving force (i.e., the pressure gradient) and the resisting

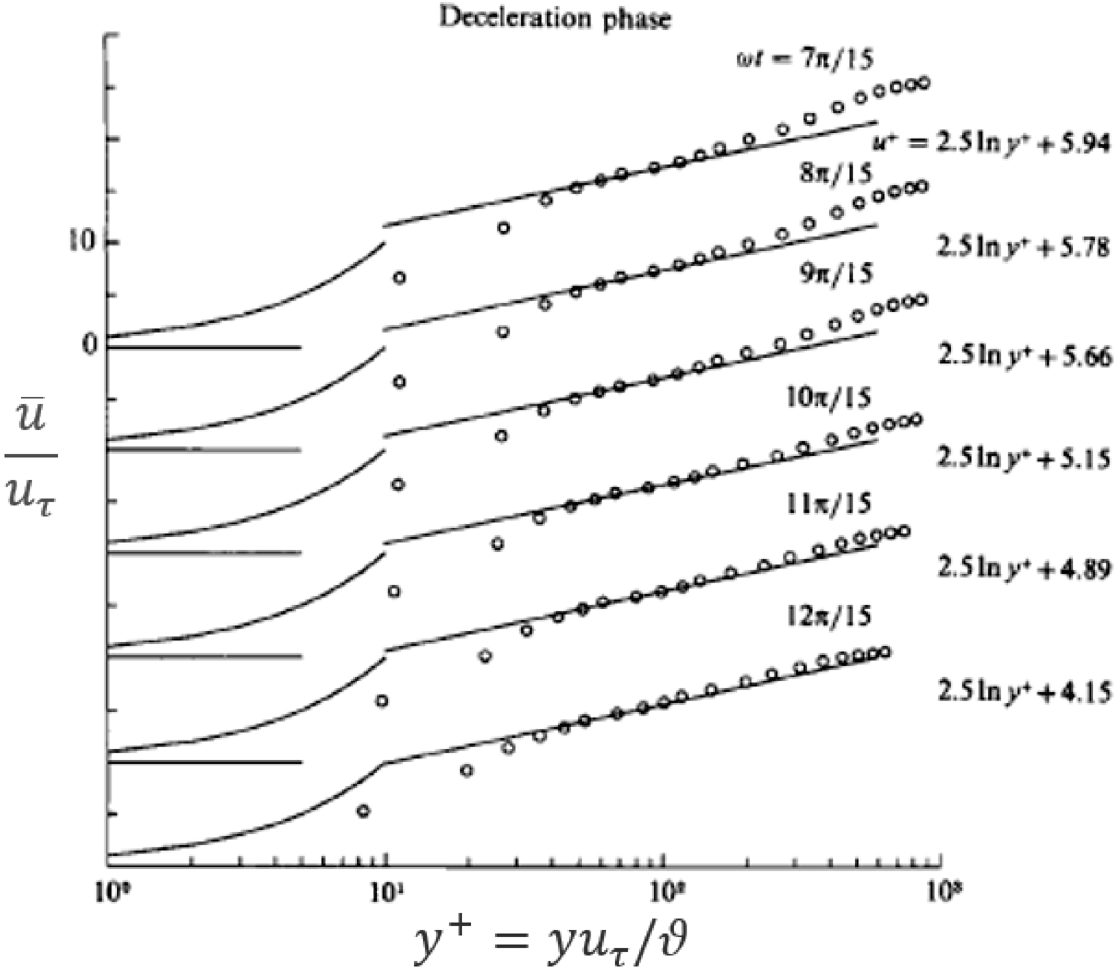

Figure 1.2: Ensemble-averaged velocity profiles for turbulent oscillatory flow in a circular pipe. Circles represent experimental data of Akhavan *et al.* (1991a) in decelerating phase of the flow and solid log-linear lines are logarithmic fits to data.

force (i.e., the wall shear stress) are in balance. The Clauser equilibrium condition is satisfied when $\beta = \delta^*(dp/dx)/\tau_w$ is constant, where δ^* is the displacement thickness, τ_w is the wall shear stress and dp/dx is the streamwise pressure gradient. Zero pressure gradient boundary layer (ZPGBL) and fully-developed channel/pipe flows are the most common equilibrium wall-bounded flows. It follows that non-equilibrium boundary layer flows are flows that do not satisfy the set of conditions defined by DeGraaff and Eaton or by Clauser.

Non-equilibrium boundary layer flows arise when the time scales associated with mean field variations are comparable to turbulent time scales such that the the turbulent field does not have sufficient time to adjust to changes in the mean field. Consequently, the flow field cannot be characterized by local parameters and the flow behaviors of the near-wall layer are not universal. Pressure gradient, obstacles in the boundary, wall curvature, and fast transients in the flow forcing, are typical perturbations that lead to non-equilibrium boundary layer behaviors. Two common examples of non-equilibrium wall-bounded flows (i.e., variable β) are adverse pressure gradient boundary layer (APGBL) flow and periodic wall-bounded flow. In the former τ_w is varying; in the latter there is a phase difference between dp/dx and τ_w even though both parameters oscillate with the same frequency. For a given non-equilibrium wall-bounded flow, some or all of the universal behaviors observed in the near-wall layer of equilibrium wall-bounded flows are absent (Aubertine and Eaton, 2005). For example, Samuel and Joubert (1974) studied a boundary layer flow in an increasingly adverse pressure gradient and concluded all universal models for collapsing the data fail other than the law of the wall. Antonia and Luxton (1971) investigated the response of a turbulent boundary layer to a smooth-to-rough change in surface condition and concluded while the outer layer remains fairly unchanged, the internal layer dynamics such as mixing length and turbulent production are altered significantly. While departure of the mean velocity profile from the universal log law had been established in the separation region of APGBL flow (Dengel and Fernholz, 1990; Bradshaw and Huang, 1995; Bradshaw, 1996), experimental measurements of Jovic and Driver revealed the velocity profile in the recovery region of a flow behind a backward-facing step falls below the universal log-law (Jovic and Driver, 1994, 1995). Downward shift of the mean velocity profile from the universal log-law in the recovery region of a flow behind a backward facing step was later confirmed by DNS of Le *et al.* (1997). It is now established that in mild to strong APG wall-bounded flows the mean velocity profile is shifted downward from the log law, the wake region is amplified, and hence the extent of the logarithmic region is shrunk (Aubertine and Eaton, 2005; Monty *et al.*, 2011). Akhavan *et al.* (1991a) empirically predicted and experimentally showed the y-intercept of Eq. 1.1 is strongly modified in a periodic wall-bounded flow. Figures 1.1 and 1.2 show departure of mean velocity profile in non-equilibrium wall-bounded flows. Other investigations of non-equilibrium wall-bounded flows such as flow over curved channel (Shima *et al.*, 2000), flow behind vehicles (Menter and Kuntz, 2004), to name a few, confirm that the slope and y-intercept of Eq. 1.1 are strongly modified in the mild to strong APG flows. It follows that RANS simulations of non-equilibrium boundary layers that employ wall-functions based on equilibrium boundary layer behaviors will fail spectacularly.

Despite its importance in engineering, industrial, and geophysical flows, there are few experimental studies of heat transport mechanisms in non-equilibrium boundary layers. The overwhelming majority of studies of non-equilibrium wall-bounded flows with heat transfer are focused on the comparison of the heat transfer in those flows with their equilibrium counterparts (Moretti and Kays, 1965; Aharwal *et al.*, 2008; Bharadwaj *et al.*, 2009; Pehlivan, 2013). The lack of experimental studies is not surprising given that controlling thermal boundary conditions is non-trivial, and the simultaneous measurement of temperature and velocity fluctuations in turbulent boundary layers with forced convection is very difficult. In addition, direct measurement of the wall-heat flux, which is the primary scaling variable to study thermal boundary layers, is challenging. Experimental measurements of Perry *et al.* (1966), Tsou *et al.* (1967), Blackwell *et al.* (1972) and Orlando *et al.* (1974) are among the first attempts of simultaneous measurement of temperature and velocity fluctuations in non-equilibrium wall-bounded flows. Afanasyev *et al.* (1993) studied the heat transfer characteristics on surfaces shaped by spherical cavities and more recently, Houra and Nagano (2006, 2008) provided reliable experimental data in non-equilibrium adverse pressure gradient boundary layers. A review of the experimental investigation of heat transfer in non-equilibrium boundary layers, specifically in separated flows, can be found in Togun *et al.* (2011). Nevertheless, the experimental measurements of Perry *et al.* (1966) and Blackwell *et al.* (1972) are still used for validation purposes (Araya and Castillo, 2012), which is an indicator of the scarcity of experimental data.

The limited studies, however, show that the distribution of temperature is more sensitive to pressure gradients compared to the velocity field. As stated earlier, this is remarkable since the pressure gradient does not appear in the transport equation for temperature. This sensitivity of the temperature field is illustrated in Fig. 1.3 that shows that the slope and y-intercept of Eq. 1.2 is

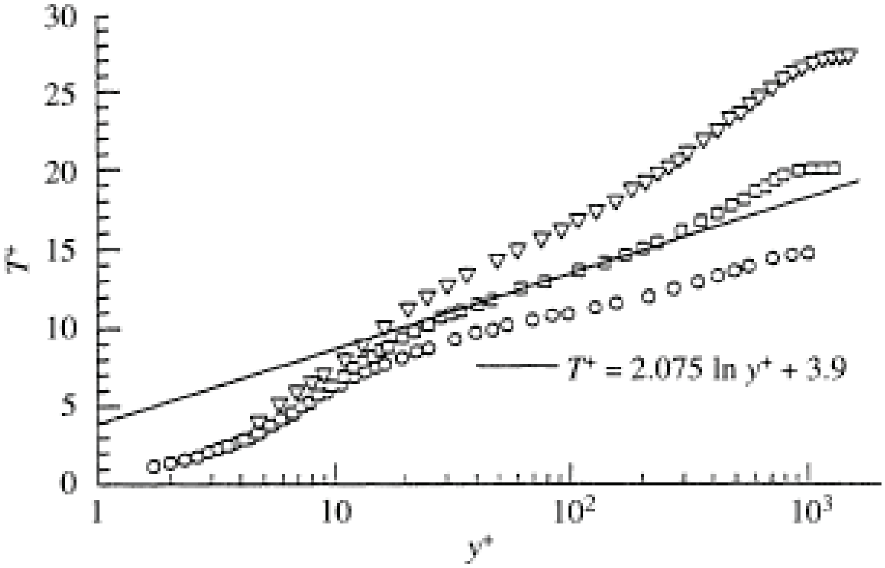

Figure 1.3: Mean temperature profile in wall units. Solid line represent Eq. 1.2, open triangles, squares and circles represent FPG, ZPG and APG flow, respectively. Figure adopted from Bradshaw and Huang (1995)

significantly altered under favorable and adverse pressure gradient. In fact, the law of wall breaks down in the flows where the law of wall for velocity is still valid (Bradshaw and Huang, 1995). Since the law of wall for temperature (Eq. 1.2 is derived with the same scaling argument as the law of wall for velocity (Eq. 1.1), their range of validity is expected to be roughly the same. Experimental observations contradictory of these expectations raise the question that Bradshaw and Huang (1995) stated: *Is the tenacity of the law of wall for velocity just good luck, and if so when does our luck run out?*

It follows that reliable data and robust methodologies are required to address the validity of wall functions and to evaluate the performance of turbulence models in non-equilibrium flows. The contributing work of this dissertation to provide reliable data and introduce robust analytical methodologies to better study and understand non-equilibrium wall-bounded flows are summarized next.

1.3 Organization of the Dissertation

The work of this dissertation can be divided into two primary approaches: analytical and experimental. A brief description of these separate but complementary efforts is provided below, followed by an outline of the dissertation Chapters.

The analytical work involves the development of a mathematically exact, integral method to evaluate wall heat flux in turbulent wall-bounded flows. The method is amenable to experimental studies and provides a mean to connect transport properties at the wall to the bulk flow dynamics. The latter is important for heat transfer model development in non-equilibrium boundary layers. An extension of this integral method is used to formulate a robust validation technique for RANS simulations. This validation technique has the advantage of providing a direct connection between wall fluxes and mean flow dynamics. Lastly, the mean flow dynamics of reciprocating channel flow is studied to better understand the mechanism of transition to turbulence in periodic flow.

On the experimental front, we have developed the UNH Non-Equilibrium and Thermal (NEAT) boundary layer wind tunnel. The facility has been purposefully designed to investigate non-equilibrium thermal boundary layers. The flow configuration studied is boundary layer flow over a heated surface. A freestream heater and feedback system are used to set and maintain the freestream temperature. A thermal wall-plate and feedback controllers are used to set and maintain the thermal boundary condition at the lower wall. A rotor-stator assembly upstream of the test section produces a freestream velocity that varies sinusoidally in amplitude at a set frequency. Experiments will be conducted in the NEAT tunnel to evaluate the transport of momentum and heat in pulsatile channel flow.

The dissertation is organized into the following chapters:

- **Chapter 2: Flow, Simulation and Facility**

  Non-equilibrium periodic wall-bounded flows are reviewed in the first part of this chapter. Next, the DNS of reciprocating channel flow performed by our collaborators at the University of Vermont are described. Lastly, the design, built, and validation results for the Non-Equilibrium and Thermal (NEAT) boundary layer wind tunnel are presented.

- **Chapter 3: An Exact Integral Method to Evaluate Wall Heat Flux In Spatially Developing Two-Dimensional Wall-Bounded Flows**

  In this chapter, the integral method to evaluate wall heat flux in turbulent wall-bounded flows is presented and validated.

- **Chapter 4: Integral Validation Technique of RANS Turbulence Models**

  The formulation for the RANS validation technique based on the integral method developed in Chapter 3 is described. To assess the value of the technique, it is used to evaluate the performance of two low- and two high Reynolds-number turbulence models against DNS of reciprocating channel flow with heat transfer.

- **Chapter 5: Transition to Turbulence in Reciprocating Channel Flow**

  The contributing terms in the RANS equations are studied to better understand the mechanism of transition to turbulence in periodic wall-bounded flows.

- **Chapter 6: Experimental Details and Validation of Flow Facility**

  The experimental details are explained and the NEAT facility is validated for equilibrium flow conditions, i.e., zero pressure gradient boundary layer (ZPGBL).

- **Chapter 7: Pulsatile Boundary Layer Flow**

  The momentum transport in pulsatile boundary layer (PBL) is experimentally studied and results are compared to ZPGBL.

- **Chapter 8: Conclusions and Future Work**

  The significant results of the current study are summarized and suggestions for future work are provided.

CHAPTER 2

FLOW, SIMULATION AND FACILITY

This dissertation is focused on the study of wall-bounded periodic flows with and without heat transfer. This particular flow type was chosen since it is an unsteady, non-equilibrium flow that is simple enough for direct numerical simulation (DNS), but complex enough to test the performance of RANS turbulence models in a complex flow relevant to engineering applications such as internal combustion engines, heat exchangers, industrial mixers, or pumping systems. In this chapter, wall-bounded periodic flows are first described and their governing equations are presented. Next, the numerical methods used in both the DNS and RANS simulations of reciprocating channel flow are introduced. Lastly, the non-equilibrium and thermal (NEAT) boundary layer wind tunnel facility purposefully built to study pulsatile boundary layer flows with and without heat transfer is described in detail.

2.1 Governing Equations of Fluid Dynamics

The governing equations of fluid dynamics for an incompressible, Newtonian, fluid are first provided in their most general form. The fundamental equation set, given in indicial notation, consists of the continuity equation:

$$\frac{\partial u_i}{\partial x_i} = 0, \tag{2.1}$$

where u_i and x_i are the velocity and spatial vector components;

the Navier-Stokes equation:

$$\rho\left(\frac{\partial u_i}{\partial t}+u_j\frac{\partial u_i}{\partial x_j}\right)=-\frac{\partial p}{\partial x_i}+\mu\frac{\partial^2 u_i}{\partial x_j^2}, \tag{2.2}$$

where ρ is density, p is pressure, and μ is the absolute viscosity;

and the thermal transport equation:

$$\rho c_p\left(\frac{\partial \theta}{\partial t}+u_i\frac{\partial \theta}{\partial x_i}\right)=\lambda\frac{\partial^2\theta}{\partial x_i^2}+\phi_v+\dot{q}, \tag{2.3}$$

where c_p is the specific heat, θ is temperature, λ is the thermal conductivity of the fluid, $\dot{q}$ is the heat generation and ϕ_v is the heat dissipation due to viscous forces, with the latter being negligible in many engineering applications. Note that for the flows studied in this dissertation both $\dot{q}$ and ϕ_v are negligible. In addition to the governing equations, appropriate initial/boundary conditions are needed to solve the system of equations.

Nondimensionalization of the governing equations is valuable to identify similarity parameters and to elucidate the dominant terms with respect to prescribed initial/boundary conditions. Defining characteristic length, velocity, time and temperature scales as L, U, T and Θ, respectively, the nondimensional variables, identified by an overhead tilde are $\tilde{u}_i=\frac{u_i}{U}$, $\tilde{p}=\frac{p}{\rho U^2}$, $\tilde{x}_i=\frac{x_i}{L}$, $\tilde{t}=\frac{t}{T}$, $\tilde{\theta}=\frac{\theta}{\Theta}$. It follows that the nondimensionalized continuity, Navier-Stokes, and thermal transport equations take the forms:

$$\frac{\partial \tilde{u}_i}{\partial \tilde{x}_i}=0, \tag{2.4}$$

$$\left(\frac{L}{UT}\right)\frac{\partial \tilde{u}_i}{\partial \tilde{t}}+\tilde{u}_j\frac{\partial \tilde{u}_i}{\partial \tilde{x}_j}=-\frac{\partial \tilde{p}}{\partial \tilde{x}_i}+\frac{1}{Re}\frac{\partial^2 \tilde{u}_i}{\partial \tilde{x}_j^2}, \tag{2.5}$$

and

$$\left(\frac{L}{UT}\right)\frac{\partial \tilde{\theta}}{\partial \tilde{t}}+\tilde{u}_i\frac{\partial \tilde{\theta}}{\partial \tilde{x}_i}=\frac{1}{RePr}\frac{\partial^2 \tilde{\theta}}{\partial \tilde{x}_i^2}, \tag{2.6}$$

respectively. The similarity parameters are $Re=\frac{UL}{\nu}$ where $\nu=\mu/\rho$, $Pr=\nu/\alpha$ where $\alpha=\lambda/\rho c_p$, and $\frac{L}{UT}$. The latter is typically removed by defining $T=L/U$. In the next section, we will reformulate the governing equations specific to periodic flows.

2.2 Periodic Wall-Bounded Flows

Unsteady flows are generally separated into two categories: periodic or non-periodic. Periodic flows occur across a wide-range of geophysical (Collins, 1963; Walterscheid, 1981), biological (Nerem *et al.*, 1972; Craciunescu and Clegg, 2001) and engineering (Dec and Keller, 1989; Mackley and Stonestreet, 1995) systems. Owing to their importance in these systems, there has been extensive-and continuing-research studying periodic flows that spans almost a century (Richardson and Tyler, 1929; Vardy and Brown, 2007; O'donoghue *et al.*, 2011). Periodic flows can be further classified as reciprocating or pulsatile. The cycle-averaged flow rate in reciprocating flow is zero, while it is non-zero and unidirectional in pulsatile flow. In reciprocating flow, the mean flow over a half-period first accelerates to maximum velocity, next decelerates to zero velocity, then reverses direction. In pulsatile flow, the mean flow over a half-period first accelerates to maximum velocity then decelerates to the mean velocity. During the next half-period, the flow first decelerates to minimum velocity then accelerates to the mean velocity. For both flows, the cycle is repeated indefinitely (Di Liberto and Ciofalo, 2009).

2.2.1 Governing Equations in Periodic Flows

Defining the characteristic time scale, T, of a periodic flow as $1/\omega$, where ω is the characteristic angular frequency of the flow, Eqs. 2.5 and 2.6 become:

$$\left(\frac{L\omega}{U}\right)\frac{\partial \tilde{u_i}}{\partial \tilde{t}} + \tilde{u_j}\frac{\partial \tilde{u_i}}{\partial \tilde{x_j}} = -\frac{\partial \tilde{p}}{\partial \tilde{x_i}} + \frac{1}{Re}\frac{\partial^2 \tilde{u_i}}{\partial \tilde{x}_j^2}, \tag{2.7}$$

and

$$\left(\frac{L\omega}{U}\right)\frac{\partial \tilde{\theta}}{\partial \tilde{t}} + \tilde{u_i}\frac{\partial \tilde{\theta}}{\partial \tilde{x_i}} = \frac{1}{RePr}\frac{\partial^2 \tilde{\theta}}{\partial \tilde{x}_i^2}, \tag{2.8}$$

respectively. The continuity equation (Eq. 2.4) is unchanged. Next, by introducing the Womersley number $W = L\sqrt{\omega/\nu}$, the nondimensional Navier-Stokes and thermal transport equations in a periodic flow can be written as:

$$\left(\frac{W^2}{Re}\right)\frac{\partial \tilde{u_i}}{\partial \tilde{t}} + \tilde{u_j}\frac{\partial \tilde{u_i}}{\partial \tilde{x_j}} = -\frac{\partial \tilde{p}}{\partial \tilde{x_i}} + \frac{1}{Re}\frac{\partial^2 \tilde{u_i}}{\partial \tilde{x}_j^2}, \tag{2.9}$$

and

$$\left(\frac{W^2}{Re}\right)\frac{\partial \tilde{\theta}}{\partial \tilde{t}} + \tilde{u_i}\frac{\partial \tilde{\theta}}{\partial \tilde{x_i}} = \frac{1}{RePr}\frac{\partial^2 \tilde{\theta}}{\partial \tilde{x}_i^2}. \tag{2.10}$$

It follows that the momentum transport in periodic flows are characterized by two parameters, Re and W, and heat transfer is characterized by three parameters, Re, W, and Pr. Note that the square of the Womersley number, W^2, characterizes the ratio of the diffusion time scale L^2/ν to the oscillation time scale ω^{-1}.

2.2.2 Stokes Boundary Layer Solution

Laminar flow near a plane wall driven by a cosinusoidal (or sinusoidal) pressure gradient is known as Stokes' boundary layer flow. Its solution is reviewed here since it serves as a baseline comparison to study transition to turbulence in periodic flows and elucidates many features of periodic wall-bounded flows.

For a unidirectional, low Re, flow with $\vec{u} = u(y,t)\hat{\imath}$, where y is the wall-normal direction and $\hat{\imath}$ is the unit vector parallel to the wall (i.e., in the flow direction, denoted as the x-direction), the NS-equation in the x-direction reduces to:

$$\frac{\partial u}{\partial t} = \nu\frac{\partial^2 u}{\partial y^2} - \frac{1}{\rho}\frac{\partial p}{\partial x}, \tag{2.11}$$

where

$$\frac{1}{\rho}\frac{\partial p}{\partial x} = \overline{P_x} + P_0 cos(\omega t), \tag{2.12}$$

is the driving force, where $\overline{P_x}$ is the steady-state pressure gradient and P_0 is the amplitude of the cosinusoidal pressure gradient. By decomposing the velocity into a steady-state and an oscillating component:

$$u = u_{ss} + u_{osc}, \tag{2.13}$$

and inserting the decomposed velocity into Eq. 2.11, where u_{ss} is the steady-state velocity due to $\overline{P_x}$ and u_{osc} is the oscillatory velocity due to $P_0 cos(\omega t)$, the governing equation becomes

$$\left(\cancelto{0}{\frac{\partial u_{ss}}{\partial t}} - \nu\frac{\partial^2 u_{ss}}{\partial y^2} + \overline{P_x}\right) + \left(\frac{\partial u_{osc}}{\partial t} - \nu\frac{\partial^2 u_{osc}}{\partial y^2} + P_0 cos(\omega t)\right) = 0, \tag{2.14}$$

where the steady-state and time-dependent terms are grouped and segregated. The steady-state equation is

$$\nu\frac{\partial^2 u_{ss}}{\partial y^2} = \overline{P_x}, \tag{2.15}$$

with solution

$$u_{ss} = \frac{\overline{P_x} y^2}{2\nu} + Ay + B, \tag{2.16}$$

where A and B are constants determined by boundary conditions and will vary between boundary layer, fully-developed channel, and pipe flow.

The time-dependent equation is

$$\frac{\partial u_{osc}}{\partial t} = \nu\frac{\partial^2 u_{osc}}{\partial y^2} - P_0 cos(\omega t). \tag{2.17}$$

A Fourier representation of the trigonometric terms (i.e., $cos(\omega t) = \mathcal{R}\{e^{i\omega t}\}$, with $i^2 = -1$ and $\mathcal{R}\{\bullet\}$ denoting the real part of the quantity between the brackets) in the time-dependent equation is used to reduce the complexity of the equations. The solution, achieved by separation of variables, then follows as

$$u_{osc} = \mathcal{R}\{F(y)e^{i\omega t}\}, \tag{2.18}$$

where $F(y)$ is the time-independent part of the solution. Plugging Eq. 2.18 into Eq. 2.17, the time-dependent equation will be

$$i\omega F\cancel{e^{i\omega t}} = \nu\frac{\partial^2 F}{\partial y^2}\cancel{e^{i\omega t}} - P_0\cancel{e^{i\omega t}}, \tag{2.19}$$

with the boundary conditions:

$F(y) = 0$ for $y = 0$, and

$\frac{dF(y)}{dy} = 0$ for $y \rightarrow +\infty$,

which are invariant for boundary layer, fully-developed channel, and pipe flows.

The general solution of Eq. 2.19 for F is

$$F = Csinh\left(\sqrt{\frac{i\omega}{\nu}}y\right) + Dcosh\left(\sqrt{\frac{i\omega}{\nu}}y\right) - \frac{iP_0}{\omega}, \tag{2.20}$$

where C and D can be determined by the boundary conditions. Applying the boundary conditions, the solution reduces to

$$F = i\frac{P_0}{\omega}\left(1 - e^{-\sqrt{\frac{i\omega}{\nu}}y}\right). \tag{2.21}$$

Plugging Eq. 2.21 into Eq. 2.18 and incorporating $\sqrt{i} = \frac{i+1}{\sqrt{2}}$, the oscillating velocity will be:

$$u_{osc} = \mathcal{R}\left\{Fe^{i\omega t}\right\} = \mathcal{R}\left\{i\frac{P_0}{\omega}\left(1 - e^{y/l_s}\right)e^{i\omega t}\right\} = \frac{P_0}{\omega}\left(sin(\omega t) - e^{-y/l_s}sin(\omega t - y/l_s)\right), \tag{2.22}$$

where $l_s = \sqrt{\frac{2\nu}{\omega}}$ is the wavenumber in the y direction and is called the Stokes' layer thickness. Since l_s is a characteristic length scale in oscillating flows, a Reynolds number based on the Stokes'

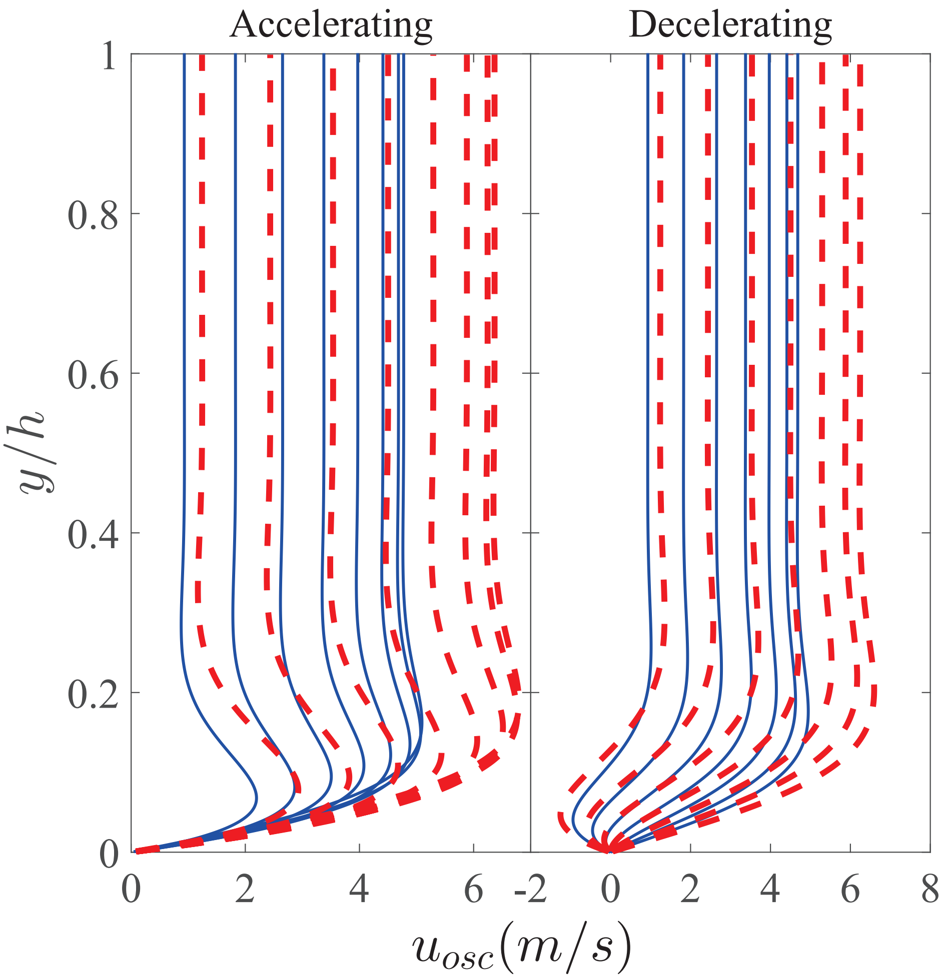

Figure 2.1: Oscillatory velocity profiles of a periodic laminar flow for $\omega = 2\pi/30$ (blue solid lines) and $\omega = 2\pi/40$ (red dashed lines). For the accelerating portion of the cycle, the angular phase of the profiles, $\phi = \omega t$, from left to right is $\frac{1\pi}{16}$ to $\frac{8\pi}{16}$. For the decelerating portion of the cycle, the angular phase of the profiles from right to left is $\frac{9\pi}{16}$ to $\frac{15\pi}{16}$.

layer thickness is defined as $Re_s = U_m l_s/\nu$. The characteristic velocity, U_m, is usually chosen to be the maximum amplitude of the cross-sectional average velocity defined

$$U_m = max\left(\frac{\int_0^{y_t} udy}{y_t}\right), \tag{2.23}$$

where y_t is the limit of integration and can be chosen as channel half-height, pipe diameter or boundary layer thickness. Note that the ratio of the peak Reynolds number to the Womersley number is proportional to the Stokes' Reynolds number, i.e., $Re_p/W = \sqrt{2}Re_s$, where $Re_p =$

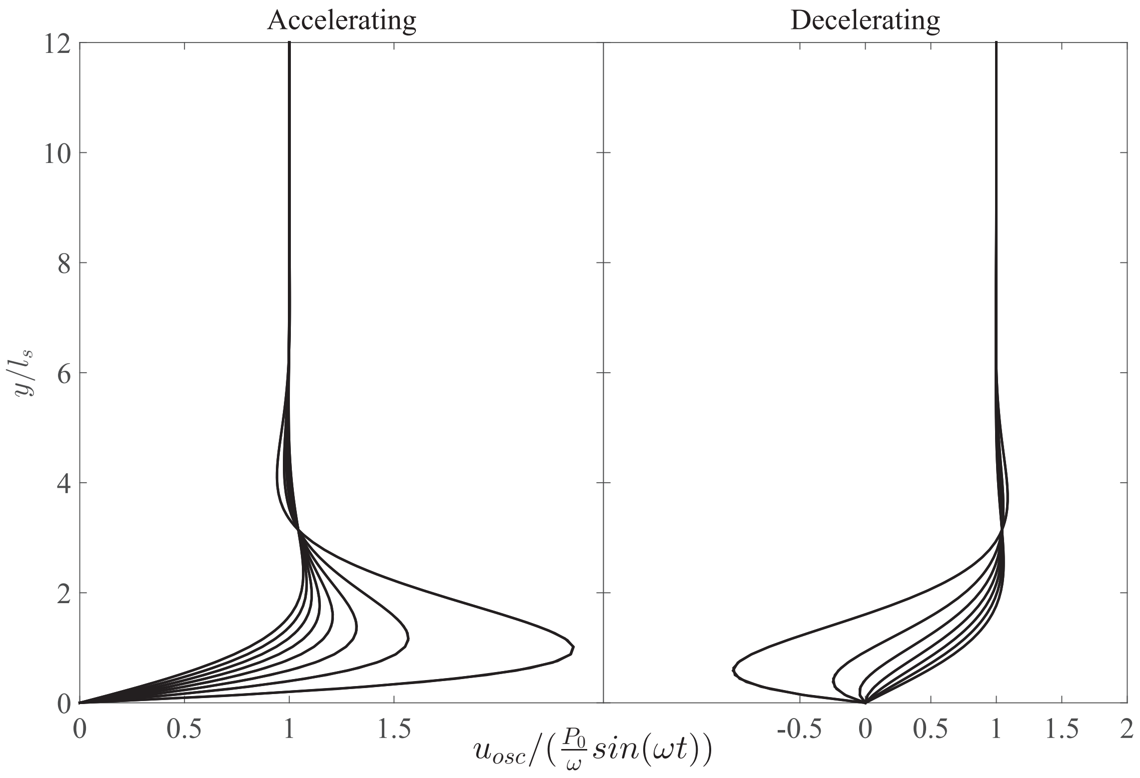

Figure 2.2: Normalized oscillatory velocity profiles of a periodic laminar flow. For the accelerating portion of the cycle, the angular phase of the profiles from left to right is $\frac{1\pi}{16}$ to $\frac{8\pi}{16}$. For the decelerating portion of the cycle, the angular phase of the profiles from right to left is $\frac{9\pi}{16}$ to $\frac{15\pi}{16}$. The profiles are invariant of the flow period.

$2U_m h/\nu$. Effectively, the Stokes' Reynolds number incorporates both scaling parameters in Eq. 2.9. Figure 2.1 shows the time-dependent velocity profiles of a reciprocating channel flow with channel half-height $h = 1$ and $P_0 = 1$ for $\omega = 2\pi/30$ and $\omega = 2\pi/40$. The parameters are chosen since they are the same parameters used in the numerical simulation incorporated in the dissertation. The effect of an increase in Re_s results in the increase of the bulk flow velocity and the Stokes' layer thickness (Fig. 2.1). Choosing the characteristic length and velocity scales as $L = l_s$ and $U = \frac{P_0}{\omega}sin(\omega t)$ and plotting $\frac{y}{L}$ versus $\frac{u_{osc}}{U}$ reveals the self-similarity of the flow (Fig. 2.2).

The wall shear stress of the oscillatory unidirectional flow is calculated as

$$\tau_w = \mu\frac{du_{osc}}{dy}|_{y=0} = \frac{\mu P_0}{\omega l_s}\left(sin(\omega t) + cos(\omega t)\right) = \frac{\sqrt{2}\mu P_0}{\omega l_s}sin(\omega t + \frac{\pi}{4}). \tag{2.24}$$

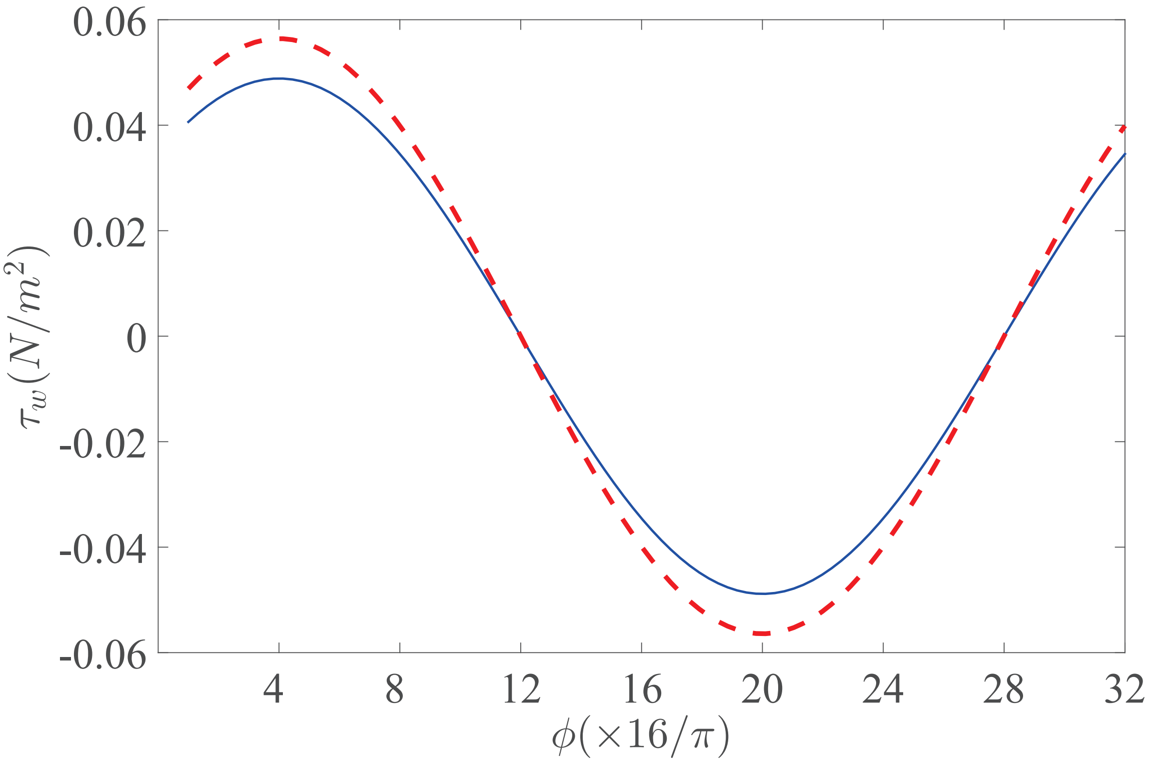

Figure 2.3: Wall shear stress profiles of a periodic laminar flow for $\omega = 2\pi/30$ (blue solid lines) and $\omega = 2\pi/40$ (red dashed lines).

The wall shear stress profiles for $\omega = 2\pi/30$ and $\omega = 2\pi/40$ are shown in Fig. 2.3.

2.3 Reciprocating Flow Regimes and Dynamics

The above analysis constitutes the solution to a laminar periodic flow driven by a harmonic pressure gradient. With increasing Re_s (i.e., a decreasing W and/or an increasing Re_p), a reciprocating flow (i.e., a zero-mean flow) will transition from a laminar flow to a turbulent flow. Owing to the periodicity of the flow, the mechanism of transition and the stages of transition are different compared to their steady-state counterparts (Scotti and Piomelli, 2001). For example, owing to the unsteady pressure gradient, the flow may exhibit both laminar and transitional flow behaviors over portions of the cycle. Due to these complexities, reciprocating flows are often categorized into five flow regimes based on the Stokes' Reynolds number Re_s (Ozdemir *et al.*, 2014)[1] :

- ***(I) Laminar–*** The flow is unidirectional and the Stokes' solution is valid at all phases. The laminar regime is mostly reported for $Re_s < 280$ (Akhavan *et al.*, 1991a).
- ***(II) Disturbed laminar–*** Small amplitude fluctuations are observed in the velocity profile during the accelerating phases of the cycle, but the fluctuations do not have sufficient energy to modify the mean velocity profile from the Stokes' solution. The reported Reynolds number range for the disturbed laminar regime is $280 < Re_s < 500$ (Ozdemir *et al.*, 2014).
- ***(III) Self-sustaining transition*** The mean velocity profiles depart from Stokes' solution at all phases of the cycle. However, fully developed turbulence is not observed in any of the phases. The reported Reynolds number range for the self-sustaining transitional regime is $500 < Re_s < 750$ (Ozdemir *et al.*, 2014).
- ***(IV) Intermittently turbulent*** The mean velocity profiles exhibit behaviors similar to fully-developed turbulent flow during the early decelerating phases of the cycle. The intermittently turbulent regime is reported for $750 < Re_s < 3460$ (Jensen *et al.*, 1989).
- ***(V) Fully-developed turbulent*** The flow stays fully turbulent for the entire oscillation period. The critical Reynolds number reported for the fully-developed turbulence in a periodic flow is $Re_s = 3460$ (Jensen *et al.*, 1989).

Owing to practical constraints, flow regime ***V*** is rarely observed. The focus of this dissertation is on flow regimes ***III*** and ***IV***. In addition to understanding the fundamental flow dynamics in these flow regimes, the mechanisms of transition between the two flow regimes will be investigated.

---

[1] Pulsatile flow regimes are discussed in details in Chapter 7.

2.4 Numerical Simulation of Reciprocating Channel Flow

DNS and RANS simulations of reciprocating channel flow are used: a) to study the transition dynamics from regime *III* to flow regime *IV*, b) to evaluate four RANS turbulence models using the integral validation technique developed as part of this study and c) as a baseline to compare and validate experimental measurements. The descriptions of the numerical simulations and the turbulent models are provided below.

The simulations[2] employ a cartesian domain defined by the orthonormal vector base $(\mathbf{e}_x, \mathbf{e}_y, \mathbf{e}_z) = (\mathbf{e}_1, \mathbf{e}_2, \mathbf{e}_3)$ where boldface denotes a vector, and x, y and z are the streamwise, wall-normal, and spanwise directions, respectively. The components of the velocity vector $u_i = \mathbf{u}$ are u, v, and w in the x, y and z directions, respectively. The flow is incompressible,

$$\frac{\partial u_i}{\partial x_i} = 0\,, \tag{2.25}$$

and driven by a cosinusoidal pressure gradient of amplitude $P_{x,0}$ at a prescribed frequency ω, given by the last term on the right hand side of the following momentum transport equation:

$$\frac{\partial u_i}{\partial t} + u_j \frac{\partial u_i}{\partial x_j} = -\frac{1}{\rho}\frac{dp}{dx_i} + \nu \frac{\partial^2 u_i}{\partial x_j^2} + \frac{1}{\rho} P_{x,0} \cos(\omega t) \delta_{i1}, \tag{2.26}$$

where ρ is the fluid density, p is pressure, and δ_{ij} is the Kronecker delta. The computational domain is periodic in the streamwise (x) and spanwise (z) directions. The wall boundary conditions are no-slip and no-through. The design of the forcing term yields a net-zero flow rate over a full period.

Temperature is incorporated in the simulation as a passive scalar with a transport equation:

$$\frac{\partial \theta}{\partial t} + u_i \frac{\partial \theta}{\partial x_i} = \frac{\nu}{Pr} \frac{\partial^2 \theta}{\partial x_i^2}, \tag{2.27}$$

---

[2] Numerical simulations and turbulent models described in this section are performed by Dr. Yves Dubief's group at The University of Vermont (primarily by Ian Pond) as a collaborative work with the current research.

where θ is temperature and $Pr \equiv \nu/(\lambda/\rho Cp)$ is the Prandtl number, where λ is the fluid thermal conductivity and Cp is the fluid specific heat. In all simulations $Pr = 0.7$. The temperature transport mechanism in the flow is driven by isothermal boundary conditions at the walls. The bottom wall is set to a non-dimensional temperature of 1 and the top wall to 0.

The studies of Di Liberto and Ciofalo (2011) and Ozdemir *et al.* (2014) were used to identify two periods: $T = 30\frac{h}{Um}$ and $T = 40\frac{h}{U_m}$, with Womersley numbers of 20.47 and 17.72, respectively, where h is the channel half-height and U_m is the amplitude of the centerline velocity modulation. The former period is within the self-sustaining transitional regime (III), whereas the latter is well within the intermittently turbulent regime (IV) and exhibits fully turbulent behaviors over a portion of the cycle. The statistics presented are phase-averaged over 10 periods for the DNS. For the RANS simulations, statistical convergence is achieved after 15 periods. A period is divided into 32 phases: $1\pi/16 \leq \phi \leq 32\pi/16$, where ϕ denotes the phase angle. Wall-normal distributions of velocity and temperature statistics are collected at each phase.

2.4.1 Direct Numerical Simulation (DNS)

DNS were carried out in a domain of dimensions $L_x = 10h$, $L_y = 2h$ and $L_z = 5h$ in the streamwise, wall-normal and spanwise directions, respectively. These dimensions are identical to the computational domain used in Di Liberto and Ciofalo (2011), although the present resolution is higher with most simulations using 128^3 cells. Statistics collected at a higher resolution of 256^3 did not show appreciable deviation from the lower resolution simulations.

The DNS code is a well-validated finite difference code (Dubief *et al.*, 2005) using non-dissipative second-order schemes for spatial derivatives on a staggered grid. The fractional step method enforces incompressibility. The time advancement is 3^{rd}-order Runge-Kutta for the advection terms in all directions and the diffusive terms in the streamwise and spanwise directions. To relax the viscous stability constraint, the wall-normal diffusive term is advanced with a 2^{nd}-order Crank-Nicolson scheme. All simulations are performed with a dynamic time step which satisfies the Courant-Friedrichs-Lewy condition, $\Delta t u_i/\Delta x_i \leq 0.9$, and a viscous stability condition, $\nu\Delta t/\min(\Delta x, \Delta z) < 0.2$. Both conditions are satisfied well below their maximum values for the numerical methods used here.

2.4.2 Reynolds Average Navier-Stokes (RANS)

The RANS simulations were carried out with OpenFOAM version 2.3.0 using the PISO incompressible transient flow solver in a 2D computational domain with streamwise periodic boundary condition. The present study compares two types of turbulence models: low-Reynolds-number and high-Reynolds-number models. The low-Reynolds-number models require the first grid point to be within a viscous unit, i.e. at $y^+ \leq 1$, where the superscript + denotes normalization by friction velocity $u_\tau = \sqrt{\tau_w/\rho}$ and kinematic viscosity ν, where τ_w is the shear stress at the wall. Computational grids were created to satisfy this condition for the maximum phase-averaged wall shear stress. A grid refinement study determined that the solution is grid independent for $N_y = 256$ for both periods. For high-Reynolds number models, the viscous sublayer and buffer layer are modeled assuming logarithmic behavior of the mean velocity distribution for $y^+ \gtrsim 30$. The first grid point is therefore located at $y^+ = 30$ based on the maximum of the wall shear stress. A grid refinement study resulted in $N_y = 40$ and $N_y = 60$ for periods $T = 30\frac{h}{U_m}$ and $40\frac{h}{U_m}$, respectively.

In all RANS simulations, Eqs. (2.25-2.27) are phase-averaged and each variable is decomposed into its phase-average and its fluctuations: $a_i = A_i + a_i'$, where a denotes a generic variable, a capitalized variable denotes its phase average, and a prime denotes its fluctuations. The resulting governing equations correspond to:

$$\frac{\partial U_i}{\partial x_j} = 0, \tag{2.28}$$

$$\frac{\partial U_i}{\partial t} + U_j\frac{\partial U_i}{\partial x_j} = -\frac{1}{\rho}\left(\frac{\partial P}{\partial x_i} + \mu\frac{\partial^2 U_i}{\partial x_j^2} - \frac{\partial(\rho\overline{u_i'u_j'})}{\partial x_j}\right), \tag{2.29}$$

$$\frac{\partial \Theta}{\partial t} + U_i\frac{\partial \Theta}{\partial x_i} = \frac{\nu}{Pr}\frac{\partial^2\Theta}{\partial x_i^2} - \frac{\partial\left(\overline{u_i'\theta'}\right)}{\partial x_i}, \tag{2.30}$$

where μ is the dynamic viscosity and an overbar denotes a correlation of fluctuating fields. Equations (2.29) and (2.30) include two new terms which result from the averaging process, the turbulent or Reynolds stress $(-\rho\overline{u_i'u_j'})$ and the turbulent heat flux $(-\overline{u_i'\theta'})$, both require models for closure.

2.4.3 Low-Reynolds-number turbulence models

The low-Reynolds-number models are the focal point, as they produce the best prediction of wall shear stress and wall heat flux. The specific models are the widely used Launder-Sharma (LS) k-ε (Launder and Sharma, 1974) model and the v^2-f model (Durbin, 1995; Iaccarino and Durbin, 2000). Both models use the transport of average turbulent kinetic energy (k) and the rate of dissipation of the average turbulent kinetic energy (ε). The transport equations for both low-Reynolds-number models are presented below. Similar to base EVM presentation, the subscripted $C's$ denote a model constant and the subscripted $\sigma's$ denote a turbulent Prandtl number, where the subscript serves as an identifier that typically contains an associated variable. The LS model has the following transport equations and turbulent viscosity (ν_T):

$$\frac{\partial k}{\partial t}+U_j\frac{\partial k}{\partial x_j}=\frac{\partial}{\partial x_j}\left[\left(\nu+\frac{\nu_T}{\sigma_k}\right)\frac{\partial k}{\partial x_j}\right]+\nu_T\left(\frac{\partial U_i}{\partial x_j}+\frac{\partial U_j}{\partial x_i}\right)\frac{\partial U_i}{\partial x_j}-\left(\widetilde{\varepsilon}+D\right), \tag{2.31}$$

$$\frac{\partial \widetilde{\varepsilon}}{\partial t}+U_j\frac{\partial \widetilde{\varepsilon}}{\partial x_j}=\frac{\partial}{\partial x_j}\left(\frac{\nu_T}{\sigma_\varepsilon}\frac{\partial \widetilde{\varepsilon}}{\partial x_j}\right)+C_{\varepsilon 1}\frac{\widetilde{\varepsilon}}{k}\nu_T\left(\frac{\partial U_i}{\partial x_j}+\frac{\partial U_j}{\partial x_i}\right)\frac{\partial U_i}{\partial x_j}-C_{\varepsilon 2}f_2\frac{\widetilde{\varepsilon}^2}{k}+E, \tag{2.32}$$

$$\nu_T=C_\mu f_\mu\frac{k^2}{\widetilde{\varepsilon}}, \tag{2.33}$$

$$\varepsilon=\widetilde{\varepsilon}+D, \qquad D=2\nu\left(\frac{\partial\sqrt{k}}{\partial y}\right)^2\approx 2\nu\left(\nabla\sqrt{k}\right)^2, \tag{2.34}$$

$$f_\mu = \exp\left(\frac{-3.4}{(1+Re_T/50)^2}\right), \qquad f_2 = 1 - 0.3\exp(-Re_T^2), \tag{2.35}$$

$$E = 2\nu\nu_T\left(\frac{\partial^2 U}{\partial y^2}\right)^2, \qquad Re_T = \frac{k^2}{\nu\widetilde{\varepsilon}}. \tag{2.36}$$

The v^2-f model uses the standard (k) and (ε) equations of a high-Reynolds-number model as well as an equation for the transport of the wall normal fluctuating velocity and an elliptic relaxation function (f):

$$\frac{\partial k}{\partial t} + U_j\frac{\partial k}{\partial x_j} = \frac{\partial}{\partial x_j}\left[\left(\nu + \frac{\nu_T}{\sigma_k}\right)\frac{\partial k}{\partial x_j}\right] + \nu_T\left(\frac{\partial U_i}{\partial x_j} + \frac{\partial U_j}{\partial x_i}\right)\frac{\partial U_i}{\partial x_j} - \varepsilon, \tag{2.37}$$

$$\frac{\partial \varepsilon}{\partial t} + U_j\frac{\partial \varepsilon}{\partial x_j} = \frac{\partial}{\partial x_j}\left(\frac{\nu_T}{\sigma_\varepsilon}\frac{\partial \varepsilon}{\partial x_j}\right) + C_{\varepsilon 1}\frac{\varepsilon}{k}\nu_T\left(\frac{\partial U_i}{\partial x_j} + \frac{\partial U_j}{\partial x_i}\right)\frac{\partial U_i}{\partial x_j} - C_{\varepsilon 2}\frac{\varepsilon^2}{k}, \tag{2.38}$$

$$\frac{\partial \overline{v'^2}}{\partial t} + U_j\frac{\partial \overline{v'^2}}{\partial x_j} = kf - \frac{\overline{v'^2}}{k}\varepsilon + \frac{\partial}{\partial x_j}\left[\left(\nu + \frac{\nu_T}{\sigma_{\overline{v'^2}}}\right)\frac{\partial \overline{v'^2}}{\partial x_j}\right], \tag{2.39}$$

$$L^2\nabla^2 f - f = \frac{C_1 - 1}{\Lambda}\left(\frac{\overline{v'^2}}{k} - \frac{2}{3}\right) - C_2\frac{P_k}{\varepsilon}, \tag{2.40}$$

$$\nu_T = C_\mu \overline{v'^2}\Lambda \tag{2.41}$$

$$L = C_L \max\left[\frac{k^{3/2}}{\varepsilon}, C_\eta\left(\frac{\nu^3}{\varepsilon}\right)^{1/4}\right], \qquad \Lambda = \max\left[\frac{k}{\varepsilon}, C_T\left(\frac{\nu}{\varepsilon}\right)^{1/2}\right]. \tag{2.42}$$

As seen in Eqs. (2.32) and (2.33), the LS model requires the use of damping functions listed in equation (2.35). These functions are necessary to accurately damp the turbulent quantities as they approach the wall, otherwise unrealistic values would be predicted. Conversely, the v^2-f model does not require the use of damping functions. This is an important characteristic of the model. In its formulation, the use of the fluctuating wall normal velocity $\overline{v'}^2$ provides the correct scaling for the damping of turbulence near the wall, hence the use of damping functions is removed. It also accounts for anisotropic effects with the inclusion of the elliptic relaxation function f. For a more in depth description of the v^2-f model see Durbin (1995); Laurence *et al.* (2005).

2.4.4 High-Reynolds Number models

High-Reynolds-number models solve the same set of equations as low-Reynolds-number models but employ wall-functions to reduce the computational grid size. The unresolved region near the wall ($y^+ \lesssim 30-50$) is reconstructed under the assumption that the resolved mean velocity distribution ($y^+ \gtrsim 30-50$) follows a logarithmic behavior ($U_1^+ = \kappa^{-1}\ln y^+ + B$), where κ and B are known constants, and the Reynolds shear stress balances the wall shear stress ($-\overline{u'v'} = u_\tau^2$). In this logarithmic region, the production of turbulence $\mathcal{P}$ and the dissipation rate of turbulent kinetic turbulence ε balance each other. For the location of the first node away from the wall y_p, the dissipation rate of turbulent kinetic energy can be estimated as

$$\varepsilon_p = \mathcal{P}_p = -\overline{u_1'u_2'}\frac{\partial U_1}{\partial y} = \frac{u_\tau^3}{\kappa y_p} = \frac{C_\mu^{3/4}k_p^{1/2}}{\kappa y_p} \tag{2.43}$$

where the subscript p denotes quantities computed at y_p. The boundary condition for the dissipation rate of turbulent kinetic energy is ε_p. A Neumann boundary conditions is used for the kinetic energy at the wall, the pressure and velocity boundary conditions remain the same as for low-Reynolds-number models.

2.4.5 Turbulent Heat Flux Closure

In the present simulations, the turbulent heat flux $(-\overline{u_i'\theta})$ is closed using the simple eddy diffusivity approach much like that of the eddy viscosity approach for the turbulent stress:

$$-\overline{u_i'\theta'} = \frac{\nu_T}{Pr_T}\frac{\partial \Theta}{\partial x_i}. \tag{2.44}$$

A main component of this closure is the application of Reynolds analogy, which assumes that the turbulent momentum flux is proportional to the turbulent heat flux. The Reynolds analogy is incorporated in the RANS simulations by the use of a turbulent Prandtl number $(Pr_T = \nu_T/\alpha_T)$, where α_T is the turbulent thermal diffusivity. For the RANS simulations of reciprocating channel flow with heat transfer Pr_T = 0.9, which is a common assumption in many engineering applications.

2.5 Facility

The non-equilibrium and thermal (NEAT) boundary layer facility was purposefully designed to study non-equilibrium thermal boundary layers.[3] The NEAT facility, shown in Fig. 2.4, is an open-circuit suction-type boundary layer wind tunnel. The test-section of the tunnel nominally measures 303mm × 135mm cross-section and 2.7m in length and is made of plexiglass to allow full optical access. The inlet section to the tunnel consists of a resistive heater bank, a seeding manifold, a turbulent management section (containing 4 screens of decreasing mesh size and honeycomb) and a 4:1 contraction. A frequency controller is used to control and maintain constant flow speed in the test-section. The freestream velocity can vary between 1 and 12m/s. A proportional integral derivative (PID) controller is used to maintain constant inlet air temperature. A feed-back controlled thermal wall plate sits on the floor of the tunnel and is used to control the lower wall-temperature. Downstream of the test-section is a rotor-stator assembly used to produce a sinusoidal pressure gradient. The components of the facility are described in detail below.

---

[3] The facility is developed by a collaborative work of the author, Michael Allard, and Drummond Biles. Contribution of each person will be indicated throughout this dissertation.

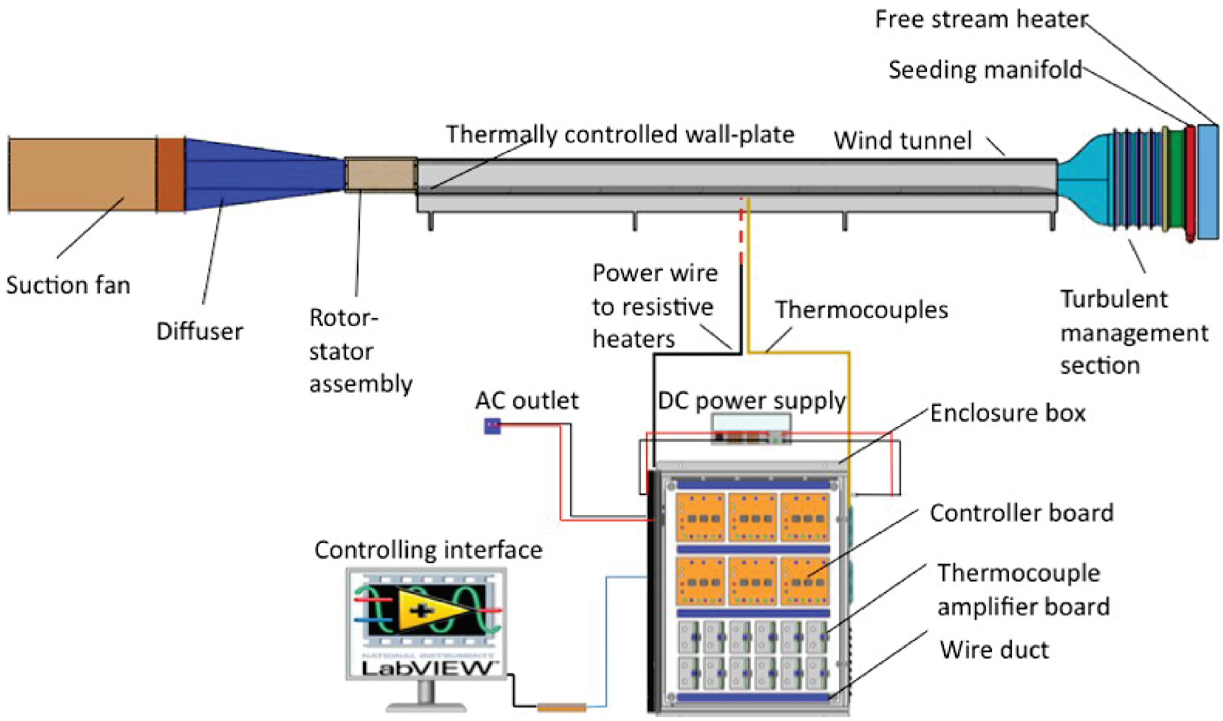

Figure 2.4: The UNH NEAT boundary layer facility. Flow direction is from right to left.

2.5.1 Test-Section

The test-section is constructed from plexiglass to provide optical access for laser-based or imaging measurements. The development length of the test-section is 2.7m. The inlet cross-section area is 303mm × 124mm, with the larger edge in the spanwise direction. The upper wall of the test section is inclined at $0.23°$ to closely maintain a ZPG boundary layer flow. The outlet cross-section area is is 303mm × 135mm. The inlet cross-section area with the thermal-wall plate inserted into the test-section reduces to 303mm × 95mm. The suction fan, controlled by a variable frequency drive (VFD), can produce a Reynolds number based on the length of the tunnel up to 2×10^6. Three glass window inserts 254mm × 102mm are located on the top-wall of the test-section for introduction of laser light and for infrared imaging. The optical quality of the glass inserts are better than the plexiglass walls.

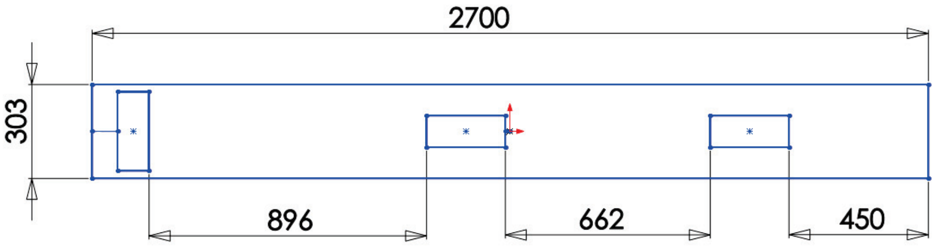

Figure 2.5: The arrangement of the windows on the top wall of the NEAT test section. Units are in mm and flow direction is from right to left.

2.5.2 freestream Heater

The air entering the tunnel first passes over nine-sheathed resistive heaters with heating density of 0.0403 W/mm^2 that provide the maximum power of $12kW$. The heaters, manufactured by OMEGA Engineering, are powered by 3-phase 208 VAC, and feedback controlled using a silicon controlled rectifier paired with a PID controller. A J-type thermocouple located in the freestream $1m$ downstream of the test-section inlet is used for feedback for the PID controller. With this arrangement, the freestream temperature in the test-section can be controlled to within $\pm 0.1°C$ at a 95% confidence interval.

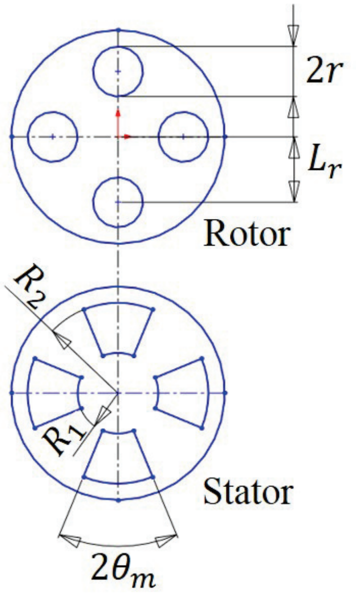

Figure 2.6: Rotor-stator assembly design adopted from Al-Asmi and Castro (1993); θ_m is chosen such that $r = L_r sin(\theta_m)$, $R_1 = L_r - r$ and $R_2 = L_r + r$.

2.5.3 Rotor-Stator Assembly

A rotor-stator assembly located downstream the test-section is used to produce a pulsatile boundary layer flow. The rotor-stator assembly design, shown in Fig. 2.6, is adapted from the work of Al-Asmi and Castro (1993). A Labview controlled DC stepper motor drives the rotor at a set angular frequency, ω_{rotor}. There are four holes and four matching slots on the rotor and stator, respectively. The angular frequency of the pulsatile flow is, therefore, $\omega_{flow} = 4\omega_{rotor}$. The design also incorporates adjustable bleed slots in the stator to regulate the incoming flow. Two rotor-stator assemblies are fabricated: one that can be installed between the test-section and the diffuser and one that can be installed between the diffuser and the suction fan. The former is called RSTD[4]

---

[4] RSTD is designed and fabricated by D. Biles.

and the latter is called RSDF[5]. Both RSTD and RSDF were used in the experimental studies of pulsatile boundary layer flow. The dimensions of each design is summarized in Table 2.1:

Table 2.1: Dimensions of the fabricated rotor-stator assemblies.

	RSTD	RSDF
$r(mm)$	12.700	35.179
θ_m	$\pi/8$	$\pi/8$
$L_r(mm)$	38.100	91.821
$R_1(mm)$	25.400	56.642
$R_2(mm)$	50.800	127.000

2.5.4 Thermal Wall Plate

The thermal wall-plate[6] (shown in Fig. 2.7) is a sectioned wall design where each section is independently heated and controlled. The design is modeled after the work of Blackwell *et al.* (1972). Each section consists of an aluminum 6061 plate, resistive heaters (affixed to the bottom of the aluminum plate), and a calcium silicate holder used for thermal isolation of the aluminum plate. (The thermal conductivity of calcium silicate is four-orders of magnitude less than aluminum 6061.) Embedded thermocouples in each aluminum plate are used to monitor wall temperature and for feedback control of wall heating. The streamwise (flow direction) length of each section increases with downstream position such that the convective heat transfer from plate-to-plate does not vary by more than 15%. The section components sit in a Delrin (acetal) frame, chosen for its low thermal conductivity and machinability.

The leading edge of the frame is a super-ellipse designed to prevent flow separation (Narasimha and Prasad, 1994). Wall-normal velocity profiles acquired slightly downstream of the leading edge agree, within experimental uncertainty, with the Blasius profile-verifying that the flow does not separate at the leading edge. To investigate turbulent boundary layers, a $3mm$ rod extending the

---

[5] RSDF is designed and fabricated by the author.

[6] The thermal wall-plate is designed and built by D. Biles.

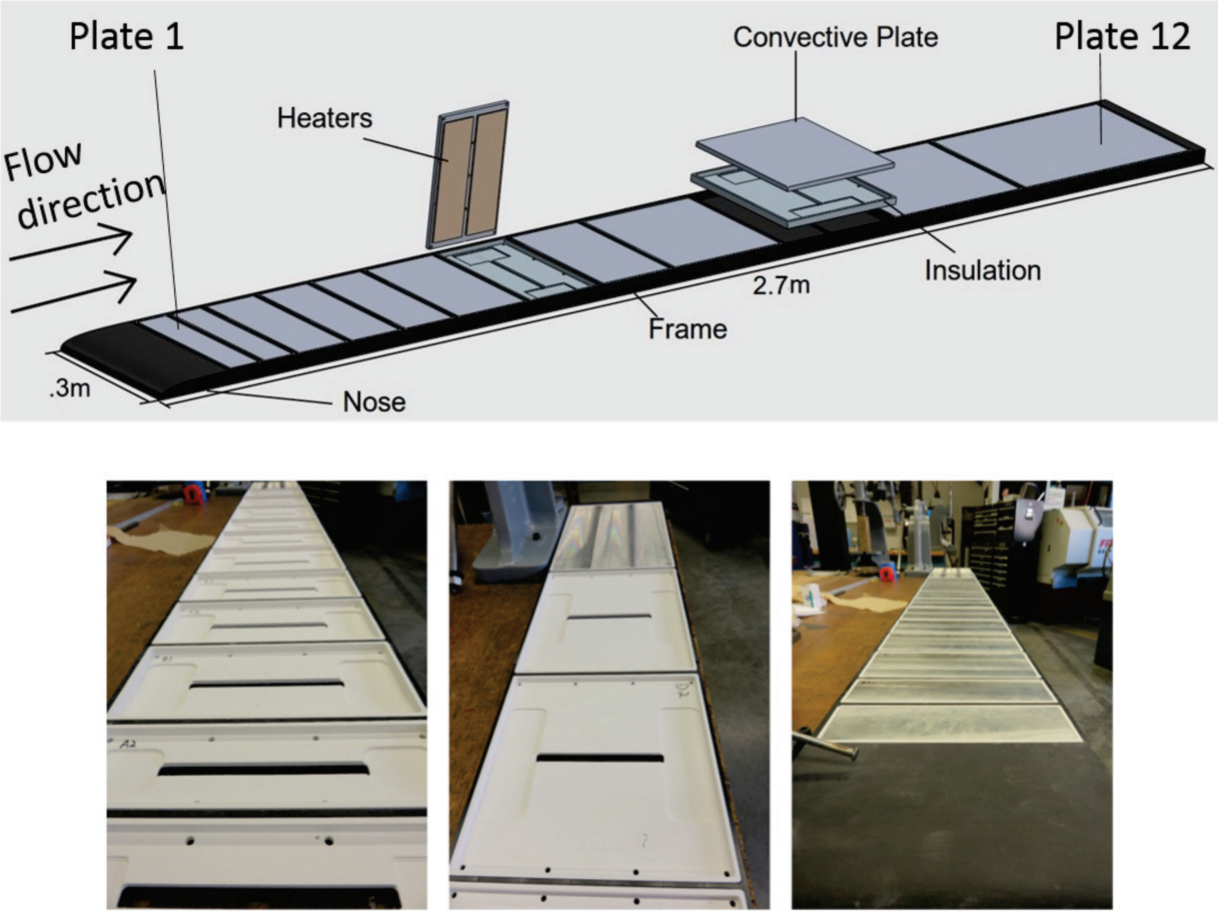

Figure 2.7: Top: computer-aided design of the thermal wall plate; bottom: photographs of the manufacturing process of the plate.

spanwise extent of the test-section is placed at the rear of the leading-edge nose, just upstream of the first convective plate. The rod induces transition to the turbulence and fixes (on average) the starting location of a developing turbulent boundary layer. The convective plate design and its feedback controller are described in detail below.

- ***Convective plates*** The sectioned wall-plate consists of twelve $9.5mm$ thick aluminum 6061 plates. The length of the plates are summarized in Table 2.2. Each plate is heated by a pair of Kapton Polyimide-Film flexible resistive heaters with heating density of $0.0155\frac{W}{mm^2}$ affixed to the bottom of the aluminum plate. Each plate is maintained at constant temperature using a feedback controller (one controller per plate). Three spanwise aligned J-type thermocou-

Table 2.2: The length of the convective plates. Plate 1 is at the upstream and plate 12 is at the downstream of the wind tunnel.

Plate number	Length (in)
1, 2	2.9528
3, 4, 5	4.9213
6, 7, 8	6.8898
9, 10	10.8268
11	12.8346
12	16.9291

ples are embedded in each plate to monitor wall temperature and for feedback control of wall heating. The thermocouples are embedded $2.5mm$ below the plate to better estimate the surface temperature and to minimize heat loss due to conduction. As a measure of temperature uniformity across the plates, the Biot number[7], Bi, is calculated as follows:

$$Bi = \frac{h_\infty L_{AL}}{k_{Al}} \tag{2.45}$$

where h_∞ is the convection heat transfer coefficient of the flow, L_{Al} is thickness of the plates and k_{Al} is the thermal conductivity of the plates. $Bi \ll 1$ indicates a uniform temperature distribution, which is ideal in the current case. For all the flow configurations in this study, i.e., $U_\infty < 10\frac{m}{s}$, $Bi < 0.0014$, which satisfies the required condition of a $Bi \ll 1$.

The time constants of the convective plates τ_{Al} are also calculated as follows:

$$\tau_{Al} = L_{Al}\rho_{Al}c_{p,Al}/h_\infty \tag{2.46}$$

where ρ_{Al} and $c_{p,Al}$ are the density and the specific heat coefficient of the plate. The upstream plates have the smallest time constants since the convective heat transfer coefficient is the largest at these locations. For all the flow configurations investigated in this study $\tau_{Al} > 600s$. The advantage of a large time constant for the plates is that the thermal wall-boundary

---

[7] Biot number provides a measure of the temperature drop in the solid relative to the temperature difference between the surface and the fluid (Incropera and DeWitt, 1985).

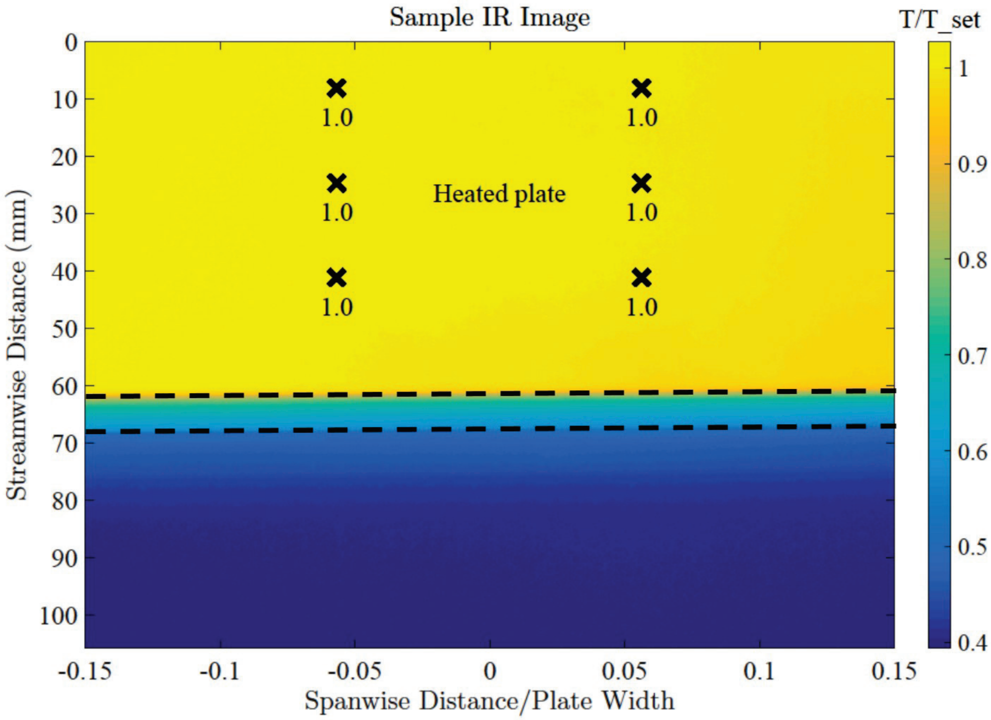

Figure 2.8: Temperature distribution across two convective plates, one heated (top) and one unheated (bottom) acquired by a FLIR SC645 infrared camera. The horizontal dashed lines mark the edges of the two plates.

conditions can be considered fixed even in pulsatile flow. Conversely, the disadvantage of a large time constant is that it takes a long time the for the wall-plate to reach its steady-state temperature. To overcome this disadvantage, the suggested procedure is to turn on the heaters on with no air flow until the plates reach their steady-state temperature; whereafter the suction fan is turned on.

2.5.5 Feedback Controller

The temperature of each convective plate in the sectioned thermal wall-plate is monitored and maintained by its own feedback controller[8]. Labview is used to define and implement the controller settings. Each controller consists of a $10A$ silicon controlled rectifier (SCR) and an NPN

---

[8] The feedback controller is designed and built by the author.

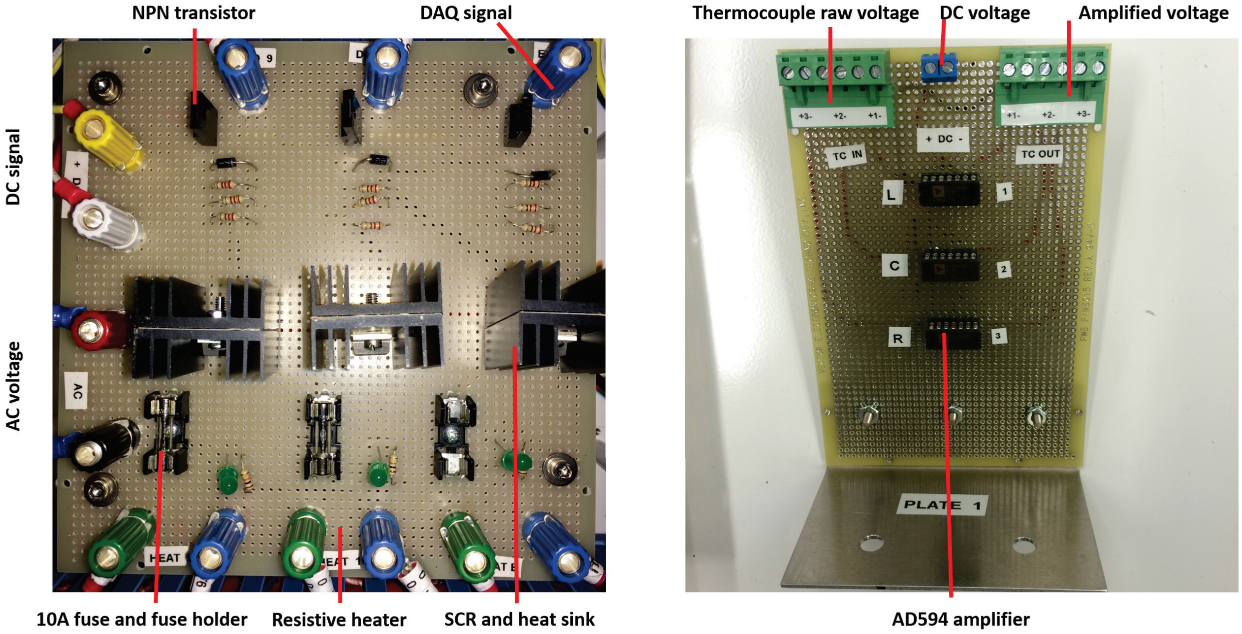

Figure 2.9: Left: photograph of a controller board. Right: photograph of the thermocouple amplifier board.

transistor. The average temperature of the three embedded thermocouples in each convective plate serves as the feedback parameter to direct the SCR to block/pass the 110 VAC that powers the resistive heaters (effectively the SCR serves as a quick switch to turn the heaters on/off). The feedback controller time constant is limited by the AC voltage frequency, sampling rate of the data acquisition device, and the run-time of the controlling program. The latter one has the slowest frequency, which for the current program is $\sim 10Hz$. Therefore, the feedback controller time constant is limited to $\tau_c = 100ms$, which is orders of magnitude smaller than the convective plate time constant. Consequently, the controller can monitor and adjust the heat-input to the convective plate much faster than the plate can lose (gain) heat to (from) the flow. With this setup, the controller can maintain the plate temperature to within $\pm 0.5°C$. The temperature tolerance of the convective plates is determined with the three embedded thermocouples. In addition, a FLIR SC645 infrared camera is used to provide two-dimensional distribution of the temperature across the heated plate. Figure 2.8 shows the spatial uniformity of the heated plate. Importantly, the design allows for the application of a wide-range of thermal boundary conditions: e.g., isothermal,

Figure 2.10: Top: the assembly process of the electronics in the enclosure box. Bottom: the final preview of the enclosure box before wiring the heaters and thermocouples.

streamwise temperature gradient, discrete temperature steps, among others. More details on the controllers, thermocouple amplifiers, wiring diagram, and enclosure to house the electronics are provided in Appendix A.

CHAPTER 3

AN EXACT INTEGRAL METHOD TO EVALUATE WALL HEAT FLUX IN SPATIALLY DEVELOPING TWO-DIMENSIONAL WALL-BOUNDED FLOWS

The wall heat flux, defined as the local power per unit area transferred between a fluid and a bounding wall, provides a primary scaling variable to study and characterize thermal boundary layer flows (Grossmann and Lohse, 2000; Wei *et al.*, 2005b; Wang *et al.*, 2008). It is an indicator of near-wall dynamics and hence a very stringent measure for verifying turbulence heat transfer models (Hosni *et al.*, 1991; Han and Reitz, 1997; Roy and Blottner, 2006; Rakopoulos *et al.*, 2010). The wall heat flux is used in industry as a diagnostic to test and evaluate system performance and to assess problems. With respect to this dissertation work, an accurate measurement of the local heat flux is a primary measurement needed to study heat transfer in non-equilibrium thermal boundary layers.

Due to its immense value in thermal transport physics and engineering, there has been considerable interest in determining and evaluating different methodologies to measure wall heat flux (Childs *et al.*, 1999; Taler and Taler, 2012). The most commonly used methods are based on temperature difference measurements across a substrate (i.e., an extra-wall or the bounding wall itself) to deduce heat flux using analytical, numerical, or inverse heat conduction methods (Taler, 1996; Reichelt *et al.*, 2002; Li and Yan, 2003; Hendricks and Ghandhi, 2012); analog methods that measure (or estimate) mass or momentum transfer and infer the wall heat flux using flow analogies (Neal, 1975; Goldstein and Cho, 1995), and direct measurement of the near-wall temperature gradient. Among the various techniques to measure wall heat flux, a few may be classified as “direct”, in the sense that they do not rely on any *a priori* assumptions regarding the behavior of the flow or temperature fields, and do not require calibration. Nevertheless, determining the wall heat flux, even from direct methods, has its challenges. For example, the accuracy of an experimentally determined mean temperature gradient near the wall is limited by the spatial resolution of the measurement system, where this limitation is exacerbated with increasing Reynolds number. Moreover, measuring fluid temperature near the wall is experimentally difficult owing to interfering inputs from the wall itself. For immersion probes, the near-wall interfering inputs generally include aerodynamic, electrical, and thermal disturbances induced by interactions between the probe and the wall. For optical measurement techniques, near-wall interference generally includes reflections of laser light, low tracer density, and limited or obscured optical access. Consequently, for most temperature measurements, the data points closest to the wall have the largest measurement error and can often be erroneous.

In this chapter, an integral method that provides a direct measurement of the wall heat flux is presented. The method is an extension of the works of Mehdi and White (2011) and Mehdi *et al.* (2014) to evaluate the skin friction coefficient in turbulent wall-bounded flows. Following Fukagata *et al.* (2002), Mehdi and White (2011) thrice integrated the momentum equation, replaced streamwise gradient terms by mathematically equivalent wall-normal gradient terms, and derived a mathematically exact integral equation for evaluating the wall stress suitable for experimental data. Here, we apply the same approach to the thermal transport equation and derive a mathematically exact integral equation for evaluating the wall heat flux. The primary advantages of the present approach are that (a) the wall heat flux can be determined exactly using only wall-normal profiles of mean temperature and turbulent heat flux at a single streamwise position, (b) being an integral method (as opposed to a differential method), the present approach is less sensitive to measurement noise (and erroneous data), in particular in the near-wall region of the flow, and (c) the method provides a means to connect transport properties at the wall to the mean flow dynamics and quantify their contributions on the wall heat flux. To evaluate and demonstrate the usefulness of this method, it is applied to existing datasets for both forced and natural convection boundary layer flow for which independent estimates of the wall heat flux were known. Complications owing to experimental limitations and measurement error in determining wall heat flux from the proposed method are presented, and mitigating strategies are proposed and evaluated.

3.1 Mathematical formulation

For a two-dimensional, wall-bounded incompressible turbulent flow, in which viscous heating is negligible, the Reynolds-averaged thermal transport equation in the streamwise (x-coordinate) direction reduces to

$$\frac{\partial \Theta}{\partial t} + G_x - \frac{\partial}{\partial y}\left(\alpha \frac{\partial \Theta}{\partial y} - \overline{v'\theta'}\right) = 0, \tag{3.1}$$

where

$$G_x = U\frac{\partial \Theta}{\partial x} + V\frac{\partial \Theta}{\partial y} - \frac{\partial}{\partial x}\left(\alpha \frac{\partial \Theta}{\partial x} - \overline{u'\theta'}\right), \tag{3.2}$$

where x, y are the streamwise and wall-normal directions, U, u', V, v' are the mean and fluctuating velocities in the x and y directions respectively, Θ, θ' are the mean and fluctuating temperatures, α is the thermal diffusivity, and an overline denotes a correlation. Integrating Eq. 3.1 in the y direction from the wall to an arbitrary height y_t, the following expression is obtained:

$$\int_0^{y_t} \frac{\partial \Theta}{\partial t}\, dy + \int_0^{y_t} G_x\, dy - \alpha \frac{\partial \Theta}{\partial y} + \overline{v'\theta'} + \cancelto{-\frac{q''_w}{\rho c_p}}{\alpha \frac{\partial \Theta}{\partial y}\Big|_{y=0}} - \cancelto{0}{\overline{v'\theta'}\Big|_{y=0}} = 0, \tag{3.3}$$

where q''_w is the wall heat flux and c_p is the fluid specific heat. Integrating Eq. 3.3 again in the y direction from the wall to an arbitrary height y_t, and incorporating integration by parts results in the following expression:

$$y_t \int_0^{y_t} \frac{\partial \Theta}{\partial t} dy - \int_0^{y_t} y \frac{\partial \Theta}{\partial t} dy + y_t \int_0^{y_t} G_x dy - \int_0^{y_t} y G_x dy - \alpha(\Theta - \cancelto{\Theta_w}{\Theta_{y=0}}) - \frac{q''_w}{\rho c_p} y_t + \int_0^{y_t} \overline{v'\theta'} dy = 0, \tag{3.4}$$

where Θ_w is the wall temperature. Finally, integrating Eq. 3.4 in the y direction from the wall to the arbitrary height y_t, and isolating the wall heat flux q_w'' yields in the following relation:

$$q_w'' = \frac{2\lambda}{y_t^2}\int_0^{y_t}(\Theta_w - \Theta)dy + \frac{2\rho c_p}{y_t^2}\int_0^{y_t}(y_t - y)\overline{v'\theta'}dy + \frac{\rho c_p}{y_t^2}\int_0^{y_t}(y_t - y)^2\left(G_x + \frac{\partial \Theta}{\partial t}\right)dy, \quad (3.5)$$

where λ is the fluid conductivity. G_x contains derivatives in the streamwise directions, and quantifying these gradients is experimentally challenging since (a) it requires measurements in multiple streamwise locations, and (b) due to the slow streamwise development of the flow, the streamwise gradients are small and hard to resolve with sufficient accuracy. Therefore, the usefulness of Eq. 3.5 is limited when applied to experimental data. However, referring to Eq. 3.1, $G_x = \frac{\partial}{\partial y}\left(\alpha\frac{\partial \Theta}{\partial y} - \overline{v'\theta'}\right) - \frac{\partial \Theta}{\partial t}$, such that G_x in Eq. 3.5 can be replaced with its mathematical equivalent, resulting in the following expression:

$$q_w'' = \frac{2\lambda}{y_t^2}\int_0^{y_t}(\Theta_w - \Theta)dy + \frac{2\rho c_p}{y_t^2}\int_0^{y_t}(y_t - y)\overline{v'\theta'}dy + \frac{\rho c_p}{y_t^2}\int_0^{y_t}(y_t - y)^2\frac{\partial}{\partial y}\left(\alpha\frac{\partial \Theta}{\partial y} - \overline{v'\theta'}\right)dy \quad (3.6)$$

It follows that determining the wall heat flux using Eq. 3.6 requires only measurements of wall-normal profiles of mean temperature and turbulent heat flux at one streamwise location up to an arbitrary height y_t.

For a turbulent boundary layer flow, normalization of Eq. 3.6 by the boundary layer thickness δ, freestream velocity U_∞, and temperature difference $(\Theta_w - \Theta_\infty)$, where Θ_∞ is the freestream temperature, results in an expression for the Stanton number, $St = \frac{q_w''}{\rho c_p U_\infty(\Theta_w - \Theta_\infty)}$

$$St = \underbrace{\frac{2}{\eta_t^2 Pe}\int_0^{\eta_t}\tilde{\Theta}d\eta}_{\text{I}} - \underbrace{\frac{2}{\eta_t^2}\int_0^{\eta_t}(\eta_t - \eta)\overline{\tilde{v}'\tilde{\theta}'}d\eta}_{\text{II}} - \underbrace{\frac{1}{\eta_t^2}\int_0^{\eta_t}(\eta_t - \eta)^2\frac{\partial}{\partial \eta}\left(\frac{1}{Pe}\frac{\partial \tilde{\Theta}}{\partial \eta} - \overline{\tilde{v}'\tilde{\theta}'}\right)d\eta}_{\text{III}}, \quad (3.7)$$

where $\eta = y/\delta$, $Pe = \frac{U_\infty \delta}{\alpha}$ is the Peclet number, $\tilde{\Theta} = \frac{\theta - \Theta_w}{\Theta_\infty - \Theta_w}$ is the normalized temperature that is decomposed into a mean temperature $\tilde{\Theta}$ and fluctuating temperature $\tilde{\theta}'$, and $\tilde{v'} = v'/U_\infty$. Eq. 3.7 consists of three contributing terms to St: I is the contribution from the mean temperature profile, II is the contribution from the turbulent heat flux, and III is the contribution from the gradient of the total (i.e., molecular plus turbulent) heat flux, or equivalently the substituted terms. The $(y_t - y)$ or $(y_t - y)^2$ weightings place more emphasis on the near wall values and, consequently, as $y_t \to \delta$, term I decreases while terms II and III increase. Consequently, in addition to the ability to evaluate the wall heat flux, this decomposition provides a means to connect transport properties at the wall to the mean flow dynamics.

3.2 Validation

The mathematical exactness of the expression for the wall heat flux (Eq. 3.6) or Stanton number (Eq. 3.7) does not necessarily mean that it will prove useful in evaluating wall heat flux from experimental data. The purpose of this section is to conduct a systematic validation of the approach to: (1) evaluate possible effects that may limit the practical application of the present method, and (2) describe strategies to minimize these limiting effects. This systematic validation is conducted by using direct numerical simulation (DNS) datasets to simulate and evaluate typical experimental limitations and uncertainties on the computed wall heat flux.

3.2.1 DNS datasets

The method is first evaluated using DNS datasets from Wu and Moin (2010) and Araya and Castillo (2012). The purpose here is to evaluate the method using well-resolved data in the absence of experimental measurement noise. These results also provide a baseline comparison to evaluate limiting effects not observed in these datasets. The Stanton number determined from the DNS datasets by evaluating Eq. 3.7 with the integration limit $\eta_t = 1$ is given in Table 3.1 column 7. The excellent agreement (effectively zero difference) in the evaluated value of St (column 7) compared

Table 3.1: Tabulated results comparing reported Stanton number (column 3) to that determined from Eq. 3.7 (column 7). Re_θ in column 1 is the Reynolds number based on momentum thickness. APG and ZPG denote adverse pressure gradient and zero pressure gradient, respectively. The first two rows are calculated using Araya and Castillo's, and the rest using Wu and Moin's DNS datasets.

Study	Pe	St $(\times 10^3)$	I $(\times 10^4)$	II $(\times 10^3)$	III $(\times 10^4)$	$St_{\mathrm{I+II+III}}$ $(\times 10^3)$
(APG)	2925	3.4228	5.2130 (15%)	2.6044 (76%)	2.9926 (9%)	3.4250
(ZPG)	14269	2.0459	1.1322 (6%)	1.5991 (78%)	3.3369 (16%)	2.0460
(ZPG)	6966	2.0846	2.4702 (12%)	1.2270 (59%)	6.1054 (29%)	2.0846
	8691	2.2114	1.9672 (9%)	1.3315 (60%)	6.8322 (31%)	2.2114
	9384	2.1742	1.8131 (8%)	1.3438 (62%)	6.4910 (30%)	2.1742
	10917	2.0694	1.5486 (7%)	1.3391 (65%)	5.7541 (28%)	2.0694
	12516	1.9855	1.3439 (7%)	1.3391 (67%)	5.1907 (26%)	1.9855
	13639	1.9539	1.2337 (6%)	1.3286 (68%)	5.0195 (26%)	1.9539
	15402	1.8886	1.0887 (6%)	1.2982 (69%)	4.8158 (25%)	1.8886
	16163	1.8605	1.0365 (6%)	1.2741 (68%)	4.8280 (26%)	1.8605

to the published value (column 3) lends credence to the method. The Table also shows the value of the individual terms given in Eq. 3.7 and their percent contribution to St. The second term is the largest, followed by the third term, where as the first term is small and decreases with increasing Pe.

The contributions to St from the three terms in Eq. 3.7 as a function of wall-normal position for the dataset of Wu and Moin (2010) at $Pe = 16163$ are shown in Fig. 3.1. The superscript + on the upper horizontal axis denotes inner normalization: $y^+ = \rho u_\tau y/\mu$, where $u_\tau = \sqrt{\tau_w/\rho}$ and τ_w is the wall shear stress. Illustrated in the figure is that the individual term contributions to St depend on the upper limit of integration. This dependency results from the combined effects of the integral and the wall-normal distance weighting of the terms. Term I, which is a function

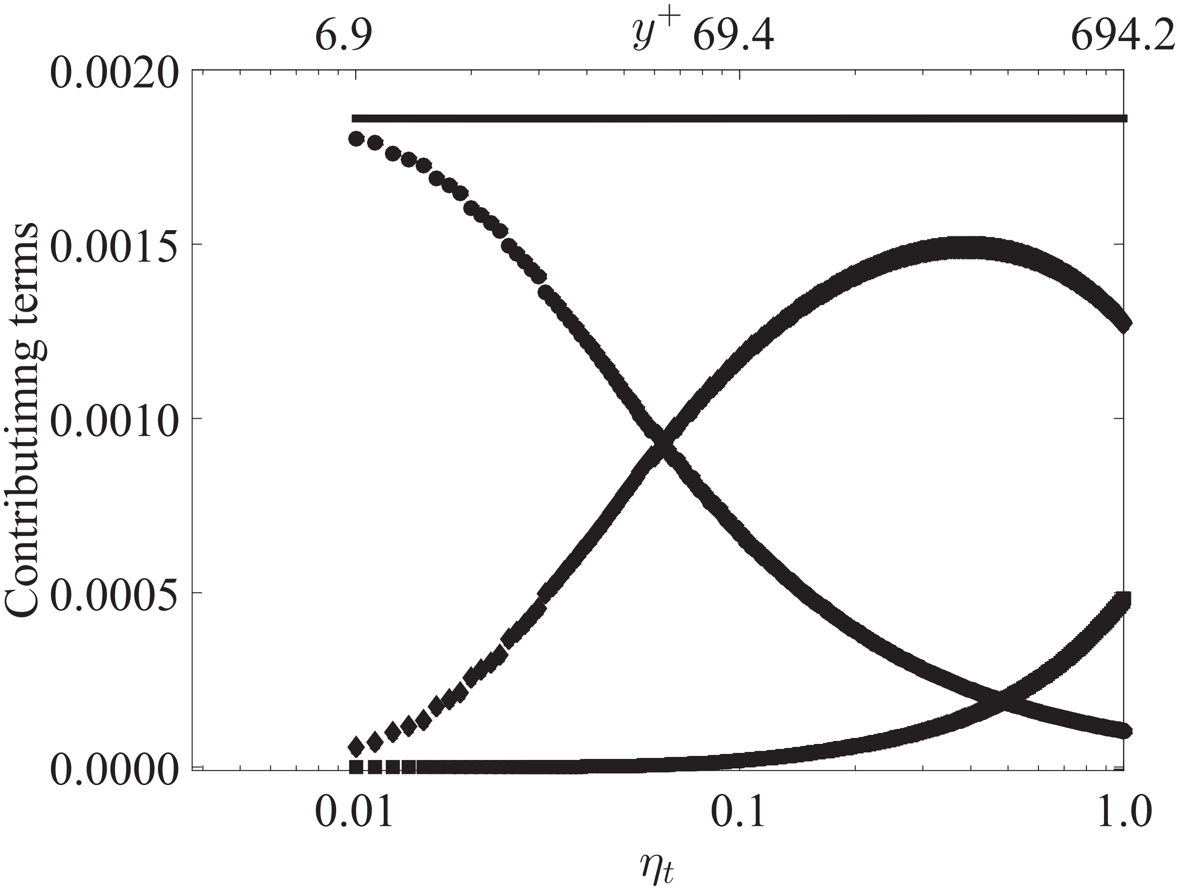

Figure 3.1: Contribution of term I (circles), II (diamonds) and III (squares) in the right hand side of Eq. 3.7 plotted as a function of wall-normal position. The sum of the three terms (i.e., St) is represented by the solid black line. The data is from Wu and Moin (2010) at $Pe = 16163$.

of the mean temperature, completely dominates in the conductive sublayer, $y^+ \lesssim 5$. The integral continues to grow with increasing wall distance but the overall term decays due to being divided by the square of the wall distance. From $5 \lesssim y^+ \lesssim 100$, term I and term II balance each other (i.e., they decrease/increase in the same proportion summing to St). Term III remains small well into the outer layer ($\eta \approx 0.1$) but eventually overtakes term I. In principle, the dependency of the contributing terms on y_t can be exploited to isolate or neglect terms depending on the measurement domain. The exact behaviors of the three terms, however, depend on the Pe. For example, with increasing Pe, term I becomes negligible over an increasing fraction of the boundary layer owing to its Pe^{-1} dependence. Table 3.1 suggests that with increasing Pe, term I decreases are balanced

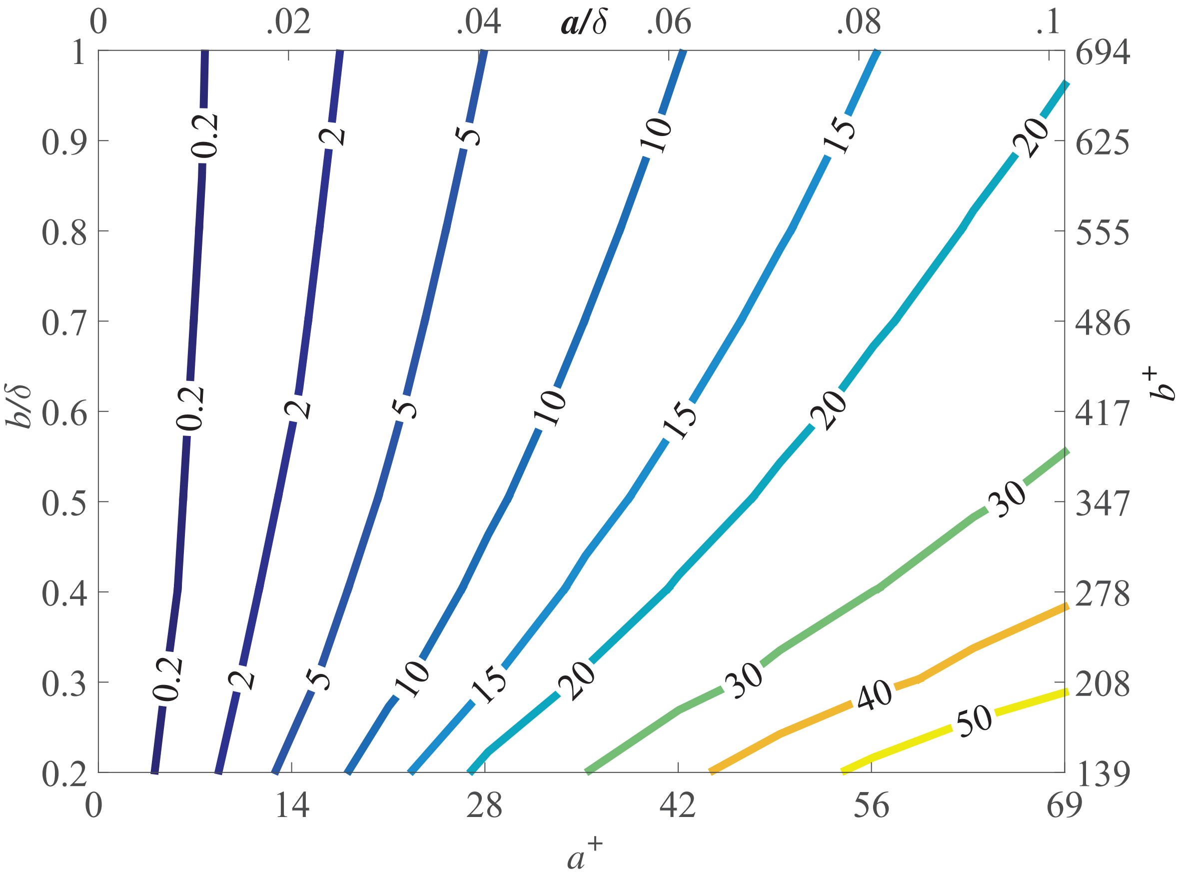

Figure 3.2: The percentage difference in St computed from Eq. 3.7 by integrating over realistic experimental domains. Same source of DNS data as in Fig. 3.1

by term II increases.

3.2.2 Effects of the limits of integration and wall-position

For wall-bounded flows, the wall-normal extent of the flow domain is $a \lesssim y \lesssim b$, where a and b are the wall-normal location of the inner and outer boundary conditions, respectively. Typically, $a = 0$ and $b = \infty$ or δ, where δ is a characteristic length scale of the outer region of the flow. In general, the experimental measurement domain does not extend across the entire flow domain. Most critical is that the data point closest to the wall will be a finite distance from the wall (typically several y^+ units from the wall). The aim here is to evaluate the relative error in the computed St

when evaluating Eq. 3.7 to an arbitrary upper limit (i.e., $y_{upperlimit} < b$) or from an arbitrary lower limit (i.e., $y_{lowerlimit} > a$). Figure 3.2 shows the percentage error in St (relative to its published value) when integrating Eq. 3.7 with varying lower and upper limits of integration for the same DNS data as in Fig. 3.1. These results, typical of all datasets investigated in Table 3.1, show that Eq. 3.7 is more sensitive to variation in the lower limit of integration compared to variation in the upper limit of integration. The practical consequence of these sensitivity differences is that when the lower limit of integration is sufficiently close to the wall (i.e., $a^+ < 10$) there is diminishing return in reducing the percentage error by increasing the upper limit of integration. Contrarily, when the lower limit of integration is far from the wall (i.e., $a/\delta > .05$), the upper limit of integration should be as large as possible to reduce the percentage error in the computed St. In general, relative to an experiment, Fig. 3.2 can be used *a priori* to select the measurement domain or *posteriori* to estimate minimum uncertainty bounds of the computed St for a given measurement domain. The importance of acquiring high-quality near-wall data is clearly illustrated in Fig. 3.2. This is not unexpected given that the wall heat-flux is a manifestation of the near-wall flow dynamics.

Determining the true position of the wall, and its implication on flow characterization is, however, nontrivial in boundary layer experiments (Örlü *et al.*, 2010). This is especially true at high Peclet (Reynolds) numbers. To simulate the effects of incorrect zero position, the wall-normal locations for the DNS data of Wu and Moin at $Pe = 16163$ are shifted by $\Delta y^+ \leq \pm 10$, and St is computed from the shifted profiles using Eq. 3.7. Figure 3.3 shows the percentage difference in the computed St corresponding to these shifts compared with the unshifted profiles. The small percentage errors illustrate the robustness of the method to uncertainty in determining the true position of the wall. Contrarily, direct measurement of the wall heat flux by measuring the mean temperature gradient at the wall is highly sensitive to wall location uncertainties.

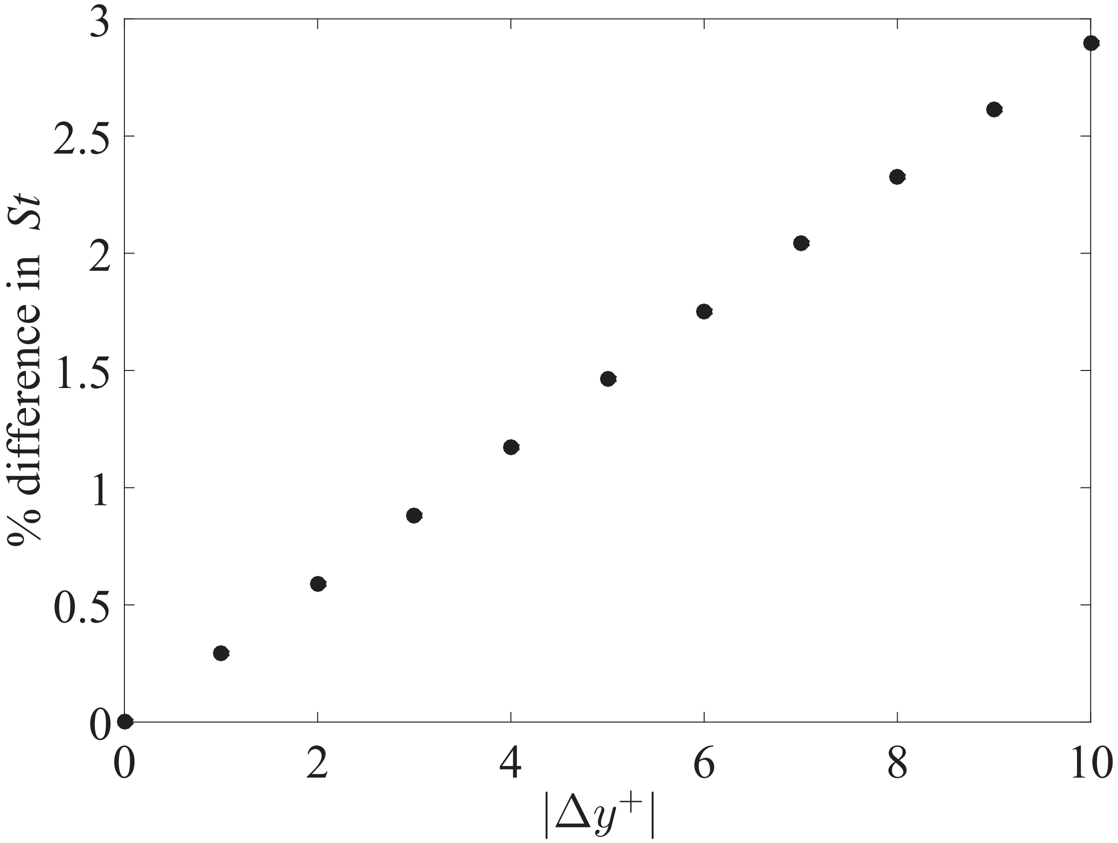

Figure 3.3: The percentage difference in St computed from Eq. 3.7 for profiles shifted by $|\Delta y^+|$ compared to unshifted profiles. Same source of DNS data as in Fig. 3.1

3.2.3 Investigation of sparse and noisy data

Experimental datasets are typically sparse and noisy compared to DNS datasets. Data sparsity results from both limited spatial resolution and finite experimental run-times. Measurement noise results from interfering inputs that are compounded by the presence of a wall, yielding low signal-to-noise ratio in the near-wall vicinity of the flow. Consequently, in most boundary layer experiments, the data points closest to the wall have the largest measurement error and can often be erroneous. When the signal-to-noise ratio is sufficiently high (i.e., absence of erroneous data), measurement noise is dominated by statistical errors owing to finite size datasets. In a turbulent boundary layer, the statistical measurement errors can be estimated by

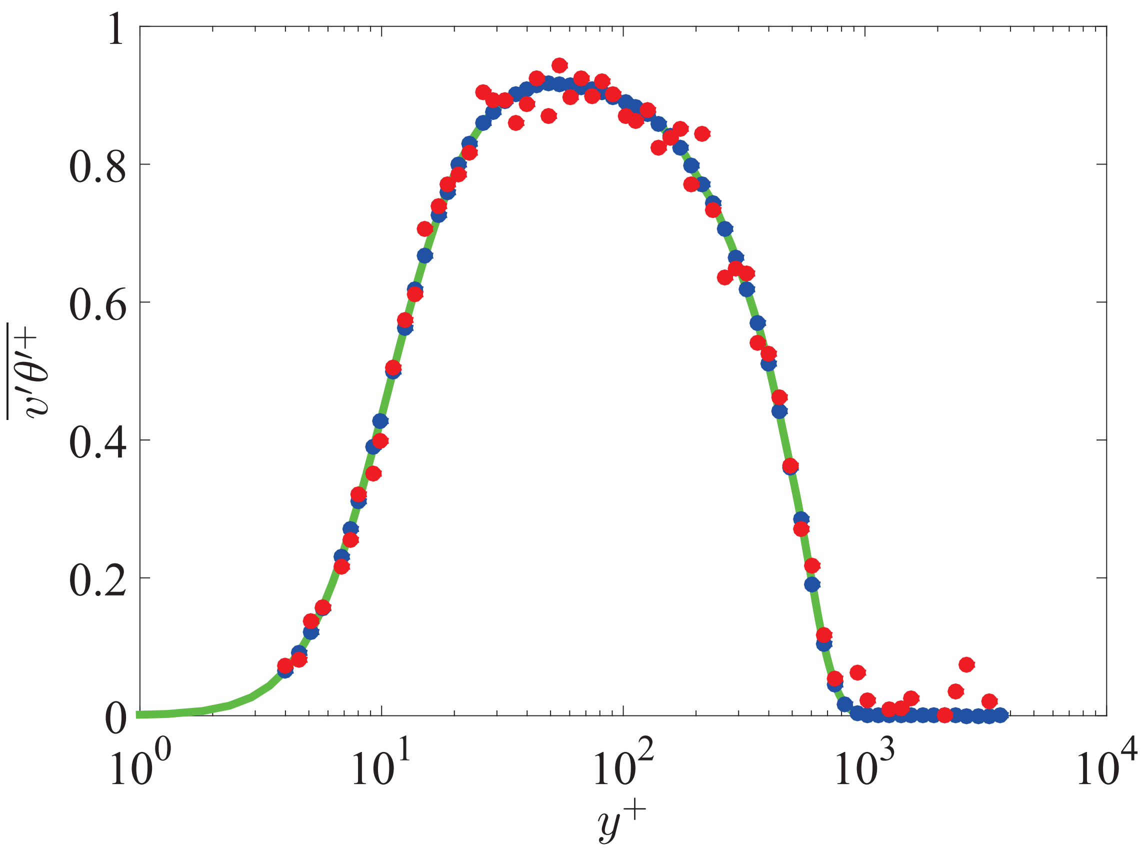

Figure 3.4: Turbulent heat flux profiles from Wu and Moin at $Pe = 16163$ for the (solid line) unaltered dataset Wu and Moin, (open circles) with data points removed, and (closed circles) with data points removed and noise added. The noise added has a mean of zero and a standard deviation of 2.8% corresponding to N = 5000 in Eq. 3.8. Note that although the DNS profile represents discrete data, a continuous line is used for clarity.

$$\frac{\epsilon_\Theta}{\Theta} \sim \frac{\theta'/\Theta}{\sqrt{N}} \sim \frac{0.05}{\sqrt{N}}; \frac{\epsilon_{\overline{v'\theta'}}}{\overline{v'\theta'}} \sim \frac{v'\theta'_{rms}/\overline{v'\theta'}}{\sqrt{N}} \sim \frac{2}{\sqrt{N}} \tag{3.8}$$

where ϵ is the fluctuation in the estimates, and N is the number of data points. The $rms/mean$ values used in Eq. 3.8 are typical values measured in the log-layer (Kawamura *et al.*, 1998; Wu and Moin, 2010; Lee *et al.*, 2013).

A sparse and noisy test dataset is constructed from the DNS dataset of Wu and Moin (2010) at $Pe = 16163$ by systematically removing data points closest to the wall, reducing the number of data points, and adding random statistical noise to the mean temperature and turbulent heat flux profiles. To approximate data that would be obtained in an actual experiment, all data points below

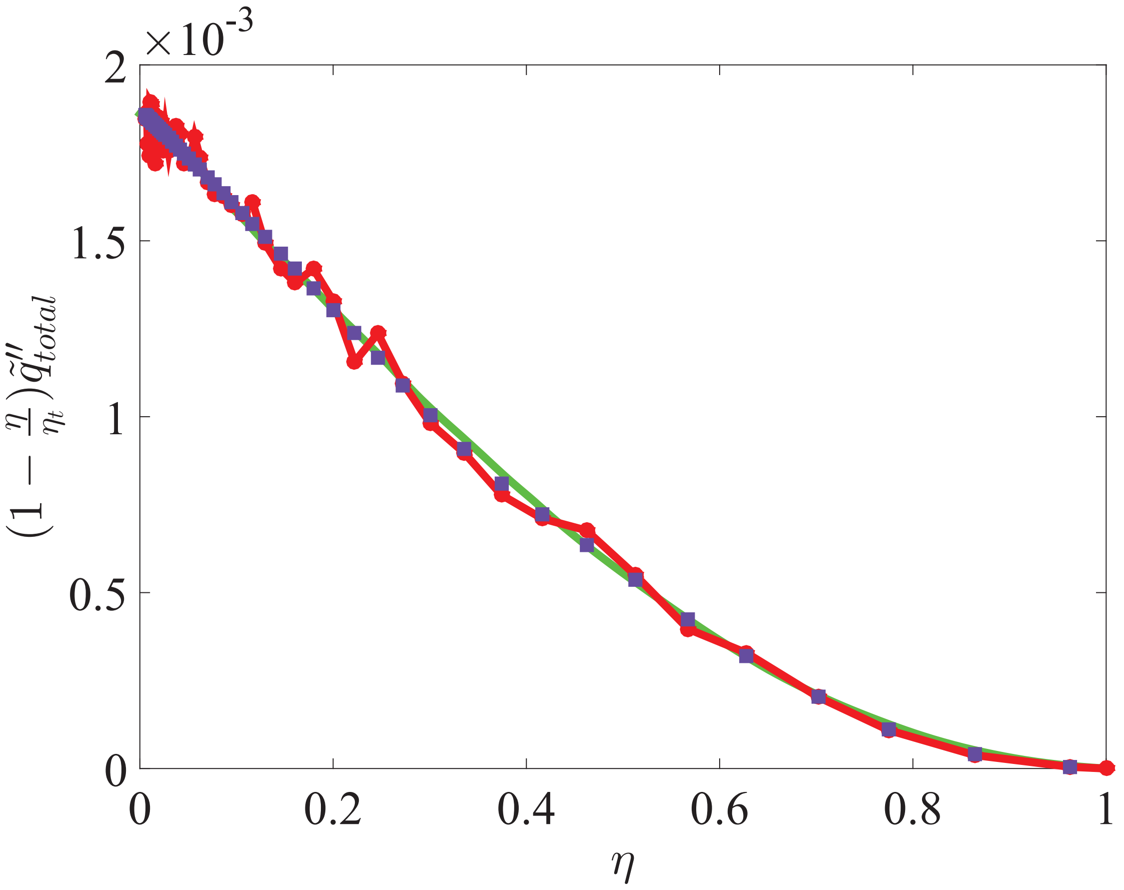

Figure 3.5: Weighted total heat flux profiles from Wu and Moin at $Pe = 16163$: solid line is the unaltered DNS, closed circles are the sparse and noisy DNS, and open squares are the Whittaker smoothed sparse and noisy DNS. The noise added corresponds to N = 5000 in Eq. 3.8.

$y^+ \approx 3.5$ and above $y/\delta \approx 1$ are discarded. The 401 y-locations in the DNS dataset are reduced to 50 logarithmically spaced locations. Gaussian noise is introduced to the reduced DNS dataset as a first approximation of experimental noise. The noise added to the mean temperature profile has a mean of zero and standard deviations of 0.14, 0.1 and 0.07%, whereas the noise added to the turbulent heat flux profile has a mean of zero and standard deviations of 2.8, 2.0 and 1.4%. These noise levels correspond to $N = $ 5000, 10000 and 20000, respectively, in Eq. 3.8. A representative simulated sparse and noisy turbulent heat flux profile with standard deviation of 2.8% is shown in Fig. 3.4. Shown for reference are the full and sparse DNS profiles without added noise.

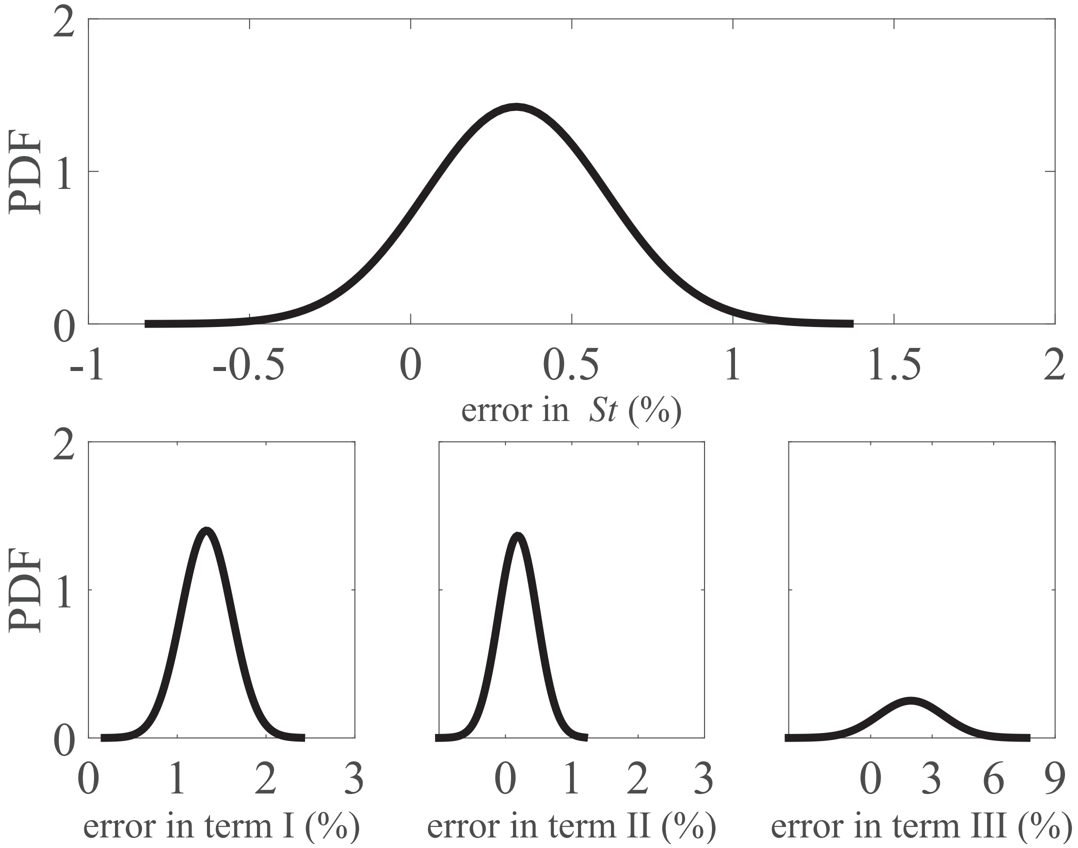

Figure 3.6: PDF of error in St calculated for sparse and noisy datasets using Eq. 3.7. The added noise has a mean of zero and standard deviations of (solid line) 1.4% and 0.07%, (dashed-dotted line) 2.0% and 0.10%, and (dashed line) 2.8% and 0.14% for the turbulent heat flux and mean temperature, respectively. Each PDF is constructed from 5000 data points.

The evaluation of term III in Eq. 3.7 requires computing the derivative of the total heat flux in the wall-normal direction. Since the simulated experimental profiles are noisy (as observed in Fig. 3.4), smoothing of the data is required to accurately compute the derivative. Following the work of Mehdi and White (2011), a Whittaker smoother is utilized to evaluate the derivative of the total heat flux from the noisy data. The Whittaker smoother is a discrete penalized least squares method based on the balance of two factors: smoothness and conformity to the actual data (i.e., the ability to follow scatter in the data). The result is a new discrete data set, which is a smoothed version of the original noisy data set. The algorithm of the smoother and its MATLAB implementation can be found in Eilers (2003).

The Whittaker smoother algorithm is used on $\tilde{q}''_{totla}\left(1-\eta/\eta_t\right)$ profiles where

$$\tilde{q}''_{total} \equiv \tilde{q}''_{molecular} + \tilde{q}''_{turbulent} = \frac{1}{Pe}\frac{\partial\tilde{\Theta}}{\partial\eta} + \left(-\overline{\tilde{v}'\tilde{\theta}'}\right). \tag{3.9}$$

Dividing the smoothed profile by $(1-\eta/\eta_t)$ yields $\tilde{q}''_{total}$ suitable for numerical differentiation, where the accent $\sim$ denotes a normalized variable (see Eq. 3.7). The benefit of using the $(1-\eta/\eta_t)$ weighting is that boundary layer physics (in the absence of a local heat source/ sink) dictates that the weighted profile need be monotonically decreasing (i.e., maximum heat flux at the wall), thus providing a means to identify erroneous near-wall data (see Mehdi and White (2011)). Figure 3.5 shows the weighted total heat flux profiles for the unaltered DNS data, the sparse and noisy data, and the Whittaker smoothed sparse and noisy data. The ability of the Whittaker smoother to effectively smooth out the noise while closely reproducing the unaltered DNS profile is evident.

The process of adding random noise to the sparse DNS data is repeated 5,000 times, and for each noisy signal the Stanton number is computed using Eq. 3.7 integrated to $\eta_t \approx 1$. Figure 3.6 shows the probability densities of the percent difference in St, and for each individual term in Eq. 3.7, for the 5,000 noisy signals. Given the discussion above and the need to use the Whittaker smoother, it is not unexpected that term III has the highest percentage error. The 95$\%$ confidence interval for the percentage errors in St for the most noisy case (i.e., N = 5000) is $\pm 2.81\%$. These results are typical of all the datasets in Table 3.1 when following the same procedure of removing data points and adding noise.

3.3 Validation using experimental data

Natural convection boundary layer datasets from Tsuji and Nagano (1988a,b) are used to validate the integral method using typical experimental data. In these experiments, hot-wire anemometry and cold-wire thermometry were used to measure the velocity and temperature field simultaneously over a heated copper plate held at constant temperature. The wall heat flux was determined by

Table 3.2: Tabulated results comparing reported value of q_w (column 2) to that determined from Eq. 3.6 (column 6). The percentage in the last column is the difference in the evaluated value of q_w compared to the reported value. The units of column 2-6 are $\mathrm{kW/m^2}$. Bracketed percent values give individual contribution from the terms on the right-hand-side in Eq. 3.6 labeled I' ; II' and III' from left to right, respectively. Data taken from Tsuji and Nagano (1988a,b).

$Gr_x(\times 10^{-10})$	$q''_{w,exp.}(\times 10)$	I' $(\times 10^2)$	II' $(\times 10^2)$	III' $(\times 10^2)$	$q''_{w,\mathrm{I}'+\mathrm{II}'+\mathrm{III}'}(\times 10)$	$\%$ Diff.
1.553	2.175	1.966 (10%)	12.826 (64%)	5.227 (26%)	2.002	7.94
3.624	2.144	1.479 (7%)	12.244 (61%)	6.275 (32%)	2.000	6.72
8.441	2.148	1.194 (6%)	12.133 (61%)	6.486 (33%)	1.981	7.78
8.986	2.288	1.363 (6%)	12.940 (60%)	7.263 (34%)	2.156	5.76
17.970	2.189	0.967 (5%)	11.838 (60%)	6.853 (35%)	1.966	10.21

computing the temperature gradient at the wall by extrapolating the temperature profile measured in the linear sublayer to the wall.

The wall heat flux for the datasets of Tsuji and Nagano (1988a,b) are computed using Eq. 3.6, employing Richardson's extrapolation for numerical differentiation and the Whittaker smoother to estimate q''_{total} suitable for differentiation. The results computed for several Grashof numbers ($Gr_x \equiv \frac{g\beta(\Theta_w-\Theta_\infty)x^3}{\nu^2}$, where g is gravity, β is the coefficient of volume expansion, x is the distance from the leading edge of the plate, and ν is the kinematic viscosity) are tabulated in Table 3.2. The percentage in the last column is the difference in the evaluated value of q''_w compared to the reported value. The magnitude of the $\%$ differences between the reported values of the heat flux and those computed using Eq. 3.6 are larger than the $\%$ differences observed for the noisy DNS datasets (see Fig. 3.6, for example). This may be a consequence of larger uncertainty in the reported value of q''_w, larger statistical measurement noise, data sparsity, or the compound effects from these and other limiting effects not included in the analysis of the DNS datasets. The table also shows the value of the individual terms in Eq. 3.6 (labeled I' , II' , and III' to represent the first, second, and third terms on the RHS of the equation) and their percent contribution to the wall heat flux. The percent

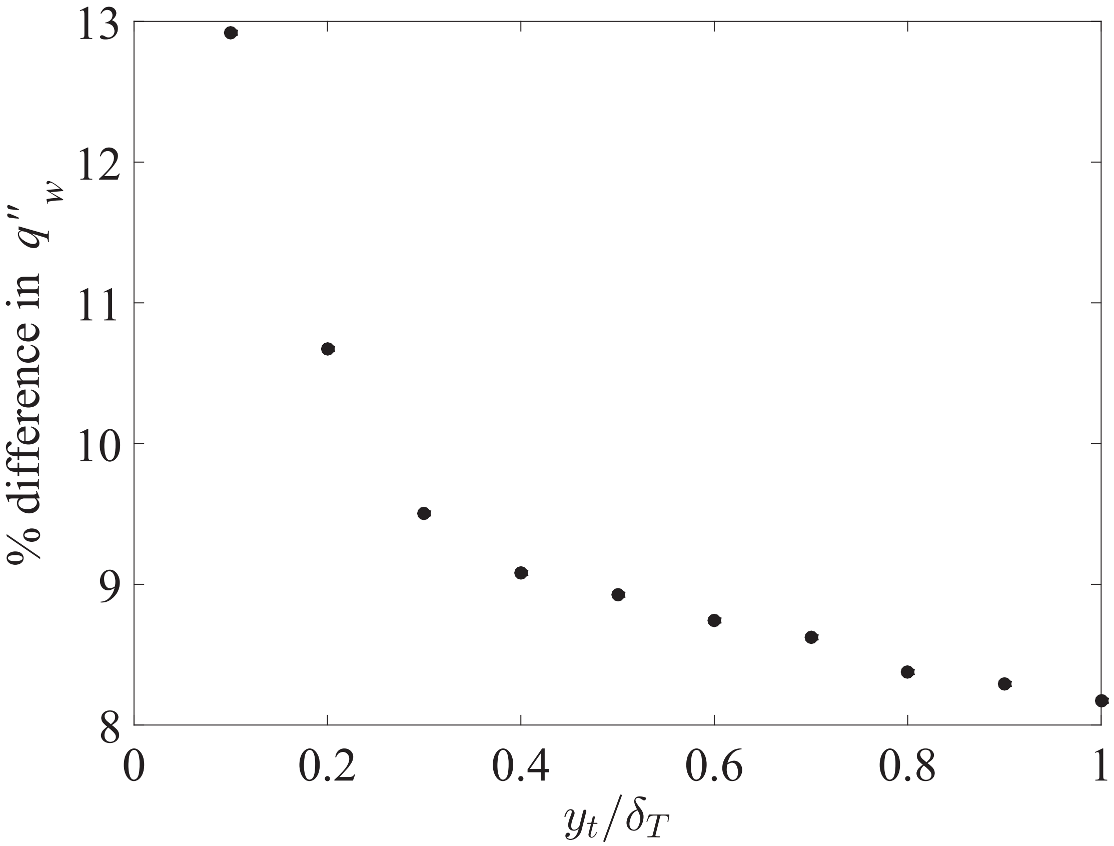

Figure 3.7: The $\%$ difference in q''_w for the experimental data of [33] for $Gr_x = 1.553 \times 10^{10}$

contributions from the three terms is similar in magnitude to the forced convection boundary layer data tabulated in 3.1.

The $\%$ difference in the computed value of q''_w using Eq. 3.6 with variable upper limits of integration compared to the reported value for $Gr_x = 1.553 \times 10^{10}$ is shown in Fig. 3.7. Observed in the figure is that the $\%$ difference decreases with increasing outer limit of integration y_t/δ_T , where δ_T is the thermal boundary layer thickness. The decrease is initially rapid until $y_t/\delta_T \approx 0.3$ after which the $\%$ difference decreases more gradually. In brief, the good agreement in the computed and reported value of q''_w demonstrates the robustness of the method applied to experimental data. In addition, Fig. 3.7 indicates that the method is fairly accurate even for limited experimental domains.

3.4 Summary

An integral method to evaluate the wall-heat flux in turbulent wall-bounded flow based on the triple integration of the Reynolds-averaged energy equation was presented. Using data from the literature, the method is shown to be fairly robust based on good agreement of the evaluated wall heat flux when compared to direct calculation of the temperature gradient at the wall using both DNS and experimental data. Complications owing to experimental limitations and measurement error in determining wall heat flux from the proposed method were presented and mitigating strategies were described. The need for this technique may be argued on grounds that it provides a direct estimate of the wall heat flux, and is useful when: (1) profiles at multiple streamwise locations are not available or feasible, (2) a flow has an ill-defined outer boundary conditions, or (3) when the measurement grid does not extend over the whole boundary layer thickness. Being an integral method, it is less sensitive to measurement noise than a differential method, in particular in the near-wall region of the flow. Furthermore, determination of wall heat flux from the present method provides a means to connect transport properties at the wall to the mean flow mechanism throughout the flow.

CHAPTER 4

INTEGRAL VALIDATION TECHNIQUE OF RANS TURBULENCE MODELS

Reynolds-averaged Navier-Stokes (RANS) numerical simulations are used extensively to address engineering fluid transport problems across a broad range of disciplines and industries (Menter, 1994; Catalano and Amato, 2003; Roy and Blottner, 2006; Stamou and Katsiris, 2006; Zhai *et al.*, 2007). The widespread application of RANS simulations is primarily due to both ease of use and low computational cost, making RANS simulations ideal for system design and optimization, or investigative studies when experimental measurements are not feasible, among other practical utilizations. One shortcoming of RANS simulations is that the most often used linear eddy viscosity models (EVM) are largely incapable of accurately simulating complex flows (Spalart, 2000; Hunt *et al.*, 2001; Menter and Kuntz, 2004; Hanjalic, 2005; Menter and Egorov, 2010). Owing to these deficiencies, the base EVM (k-ε and k-ω) have been reformulated to seek improved performance (Jones and Launder, 1972; Launder and Sharma, 1974; Wilcox, 1988; Kato, 1993; Menter, 1994; Durbin, 1996; Kalitzin *et al.*). The purportedly improved variants (some being nonlinear) of the base EVM are typically validated following what is termed here as the “standard validation technique" where the user compares averaged variable profiles (e.g., mean velocity or Reynolds shear stress) or averaged wall fluxes (e.g., wall shear stress or wall heat flux) against baseline standards. Model performance is assessed based on the “agreement" between model computed metrics and baseline standard metrics (Oberkampf and Trucano, 2002; Bardina *et al.*, 1997; Babuska and Oden, 2004; Zhang *et al.*, 2007; Gorji *et al.*, 2014).

The standard validation technique is generally sufficient for model validation in simple canonical flows, like steady boundary layers or free shear flows, since much is known about these flows and there is a wealth of data for baseline comparison (Patel *et al.*, 1985; Bardina *et al.*, 1997;

Sarkar and So, 1997; Menter and Kuntz, 2004). In complex flows, commonly found in real-world applications, the standard validation technique is often deficient since typically little is known about the underlying flow physics to justify model validation based on a qualitative comparison of a few select metrics. In the present chapter, an integral validation technique is formulated that is well-suited to validate and verify RANS turbulence models in complex flows. The metrics for the integral validation technique are attained by thrice integrating the RANS momentum and scalar temperature transport equations to derive expressions for the wall shear stress and wall heat flux, respectively, in terms of integrated mean flow variables. The strength of the technique is that a direct connection is provided between mean flow dynamics and wall fluxes that is embedded in the validation metrics. Consequently, the integral validation technique provides an improved means, compared to the standard validation technique, to better evaluate if a RANS turbulence model accurately captures the underlying flow dynamics.

Model validation and verification using the integral technique is demonstrated for reciprocating channel flow. This particular flow type was chosen since it is an unsteady, non-equilibrium flow that is simple enough for direct numerical simulation (DNS) but complex enough to test the performance of RANS turbulence models in a complex flow relevant to engineering applications such as internal combustion engines, heat exchangers, industrial mixers, or pumping systems. Two low-Reynolds-number and two high-Reynolds-number RANS turbulence models are validated against DNS first using the standard validation technique and second using the integral validation technique. The designation low-Reynolds-number model means that no wall-functions are employed and the near-wall region is solved directly, and high-Reynolds-number model means that wall-functions are employed. The specific low-Reynolds-number RANS turbulence models are the widely used Launder-Sharma (LS) k-ε (Launder and Sharma, 1974) model and the v^2-f model (Durbin, 1995; Iaccarino and Durbin, 2000). The two high-Reynolds-number RANS turbulence models are k-ε and k-ω For the standard validation technique, phase-averaged wall fluxes and wall-normal profiles of mean and fluctuating variables and their correlations are compared to the DNS results. Similarly, for the integral validation technique, the phase-averaged contributing terms to the wall shear stress and the wall heat flux are compared to the DNS results. Lastly, the two validation techniques are compared, and the benefits of the integral technique are described.

A full description of reciprocating channel flow, the DNS, and the RANS turbulence models has been described in Chapter 2. Note that in the RANS simulations, the turbulent heat flux $(-\overline{u_i'\theta})$ is closed using Reynolds' analogy and a simple eddy diffusivity approach, such that

$$-\overline{u_i'\theta'} = \frac{\nu_T}{Pr_T}\frac{\partial \Theta}{\partial x_i}.$$

where the turbulent Prandtl number, $Pr_T = \nu_T/\alpha_T$ = 0.9.

4.1 Standard Validation Technique

Phase-averaged wall-normal profiles and wall fluxes computed from the RANS simulations are first compared to the DNS profiles following the standard validation technique. For ease of interpretation, and when appropriate, data is presented only for a half-cycle (owing to anti-symmetry) and separated between the accelerating phases and decelerating phases of the cycle. The phase-averaged streamwise velocity difference profiles between the RANS turbulence models and the DNS ($U_{RANS} - U_{DNS}$) normalized by static friction velocity ($u_{\tau 0} \equiv \sqrt{\tau_0/\rho}$ where $\tau_0 = h|dP/dx|$ is the static shear stress) for Re_s = 648 (T = $30\frac{h}{Um}$) and Re_s = 1019 (T = $40\frac{h}{Um}$) are shown in Figs. 4.1 and 4.2, respectively, where h is the channel half-height and U_m is the amplitude of the centerline velocity modulation. In general, and not unexpected, is that the performance of the RANS turbulence models vary with phase and Re_s. The largest differences are observed from $5\pi/16 \leq \phi \leq 12\pi/16$ when the cross-sectional averaged flow is transitioning from an accelerating flow to a decelerating flow. Integrated across all phases and wall-normal positions, the high-Reynolds-number models generally show the largest differences while the low-Reynolds-number models shows the smallest differences. The two high-Reynolds-number models are generally well-correlated with each other, while the low-Reynolds-number models differ between each other in the near-wall region at several phases in the cycle, and in particular during the decelerating phases for $Re_s = 1019$.

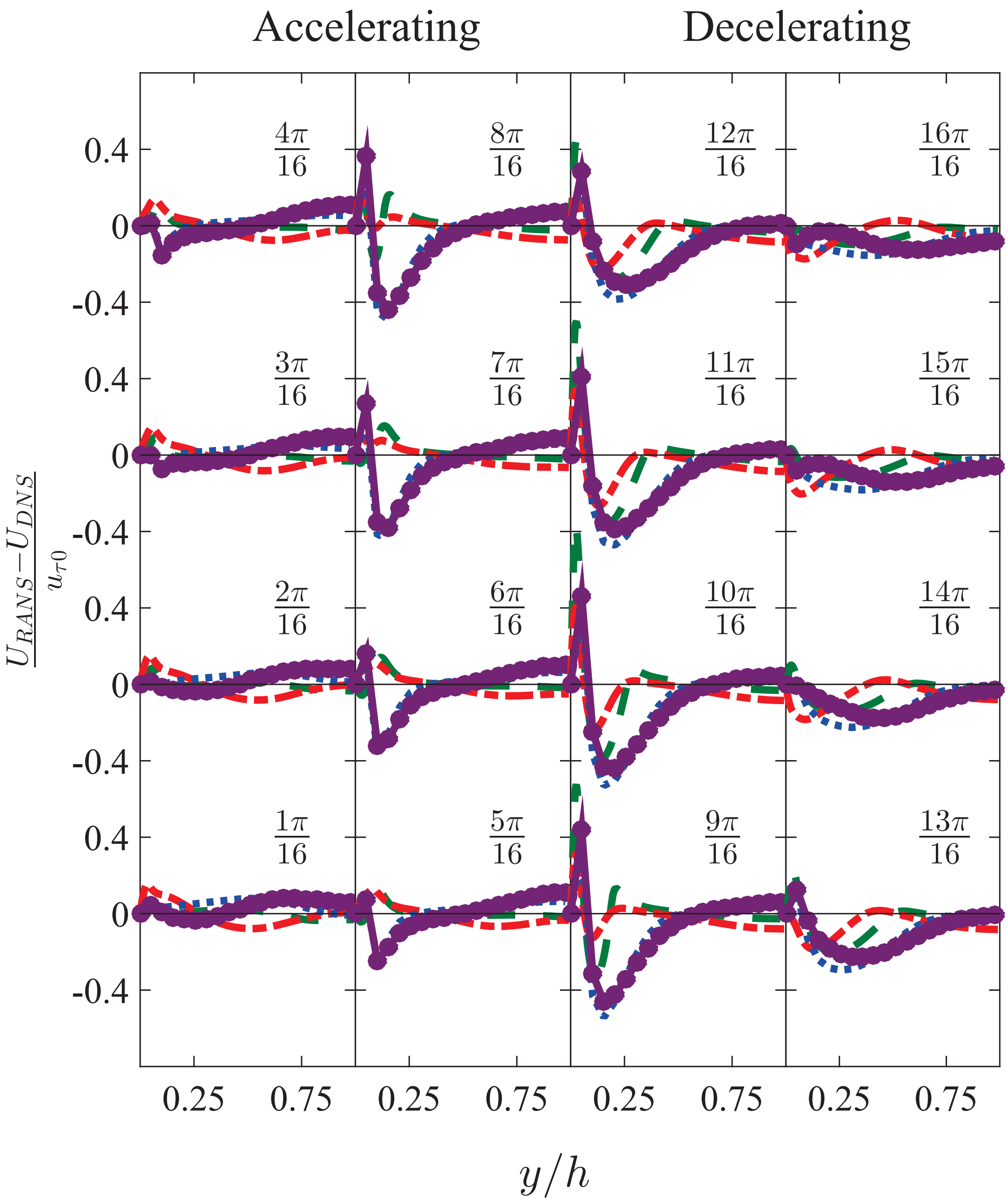

Figure 4.1: Wall-normal (y-direction) profiles of the phase-averaged streamwise velocity difference between the RANS turbulence models and the DNS normalized by static friction velocity for $Re_s = 648$ for accelerating phases (panel 1 and 3) and decelerating phases (panel 2 and 4). Phase increases from bottom-to-top in a panel and the corresponding phase is written above the curves. The line styles correspond to: -·-·- v^2-f, - - - LS, ······ k-ϵ, —●— k-ω.

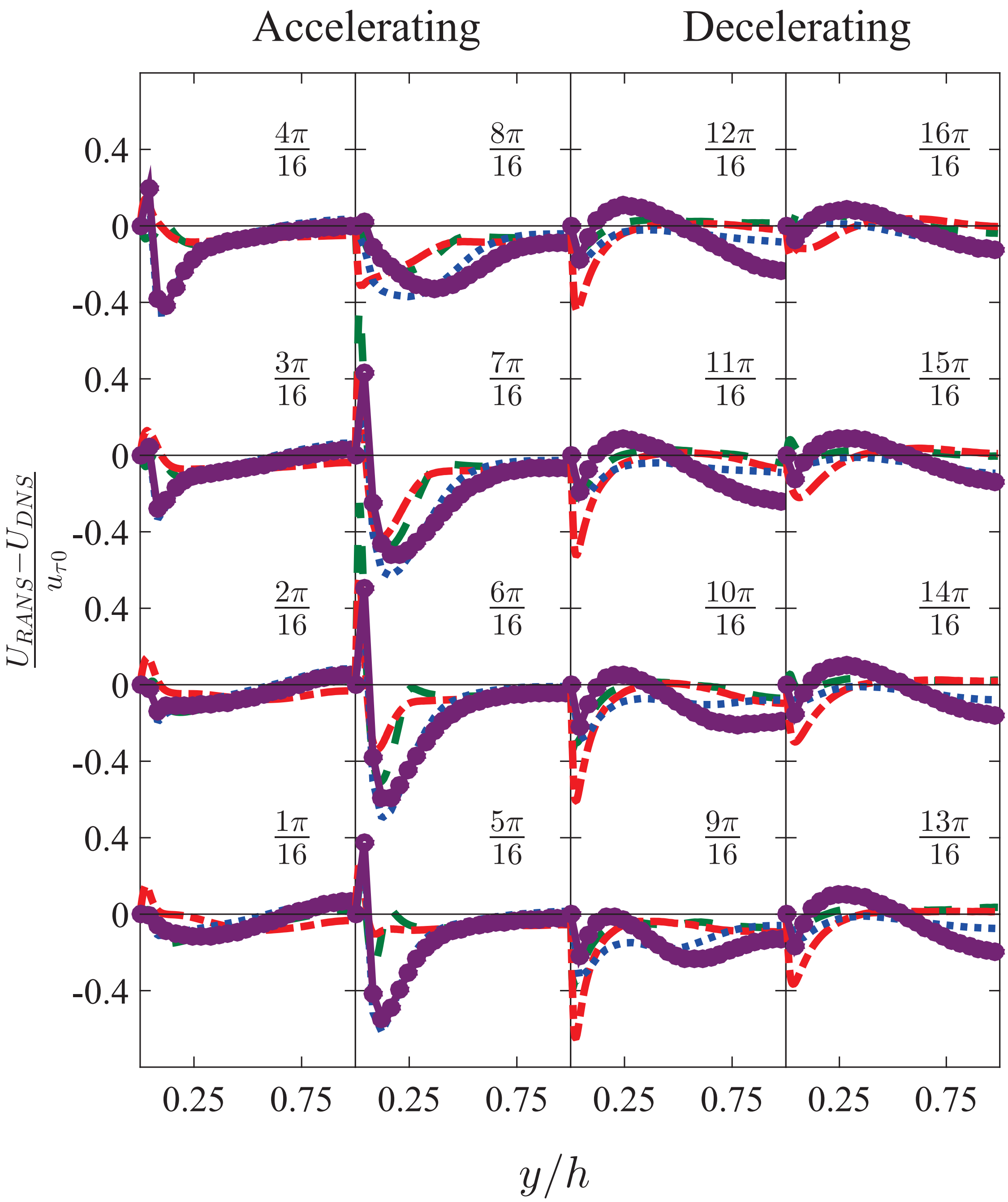

Figure 4.2: Wall-normal profiles of the phase-averaged streamwise velocity difference between the RANS turbulence models and the DNS normalized by static friction velocity for $Re_s = 1019$ Panel layout and line styles are the same as in Fig. 4.1.

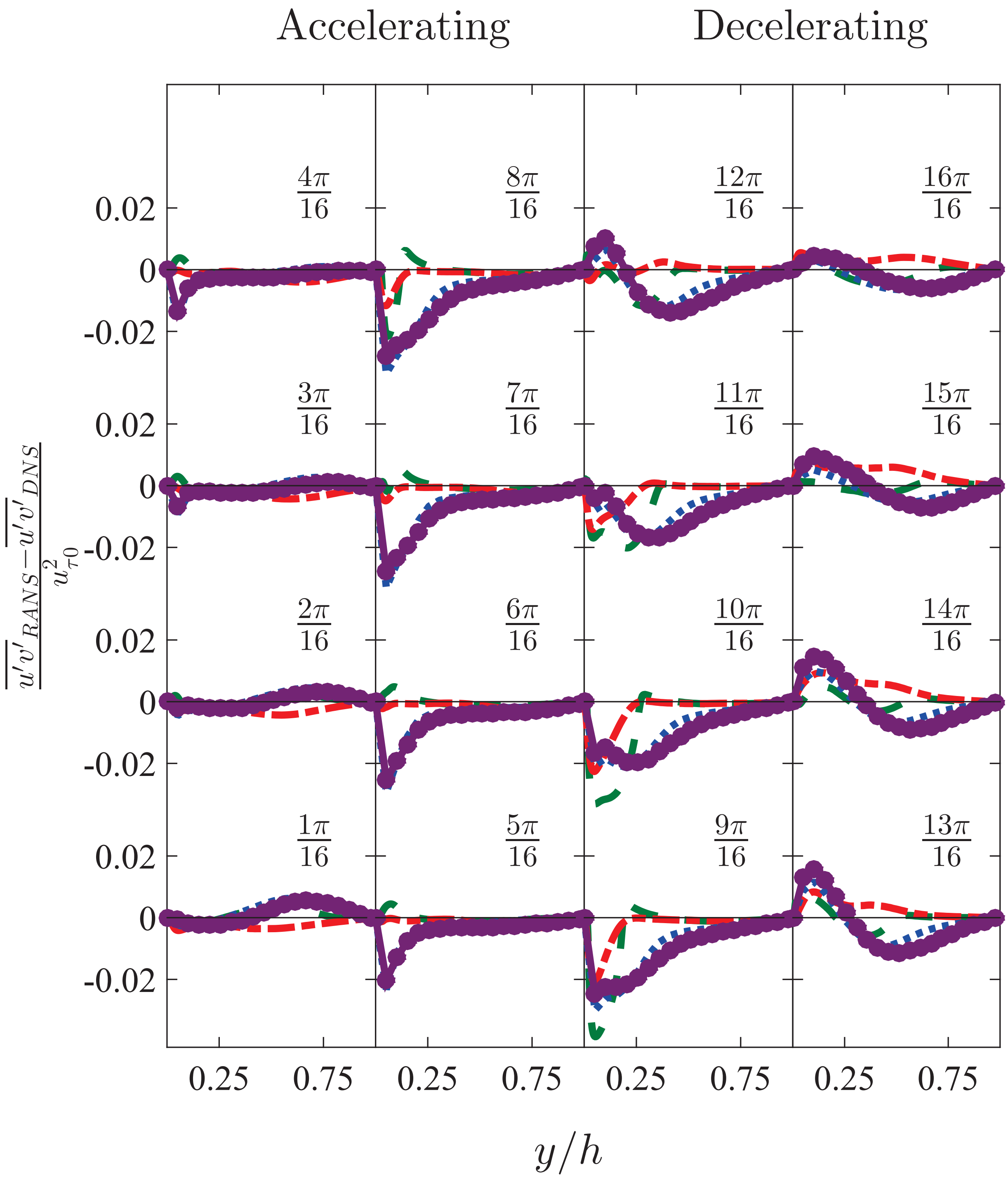

Figure 4.3: Reynolds shear stress difference profiles between the RANS turbulence models and the DNS normalized by $u_{\tau 0}^2$ for $Re_s = 648$. Panel layout and line styles are the same as in Fig. 4.1.

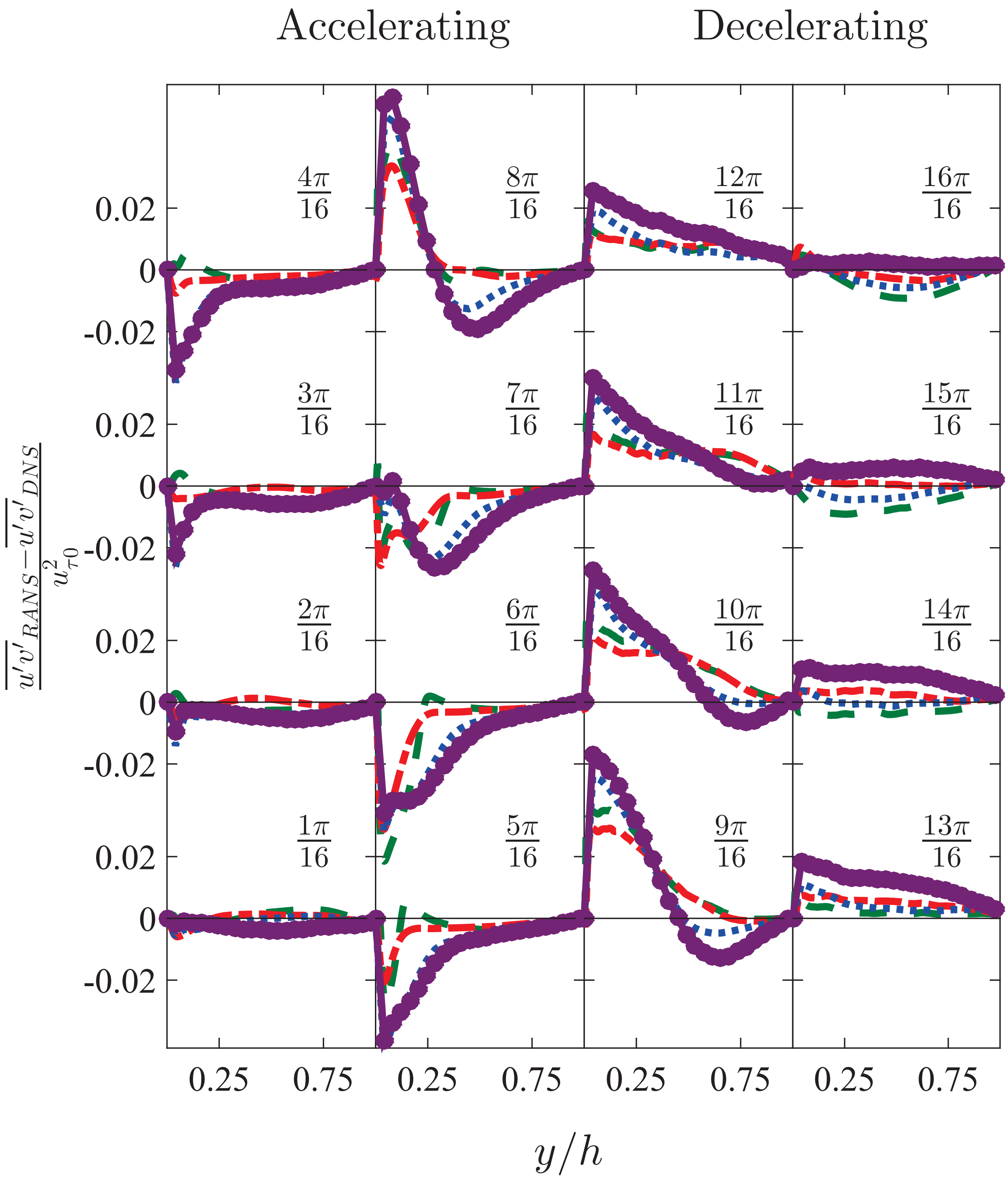

Figure 4.4: Reynolds shear stress difference profiles between the RANS turbulence models and the DNS normalized by $u_{\tau 0}^2$ for $Re_s = 1019$. Panel layout and line styles are the same as in Fig. 4.1.

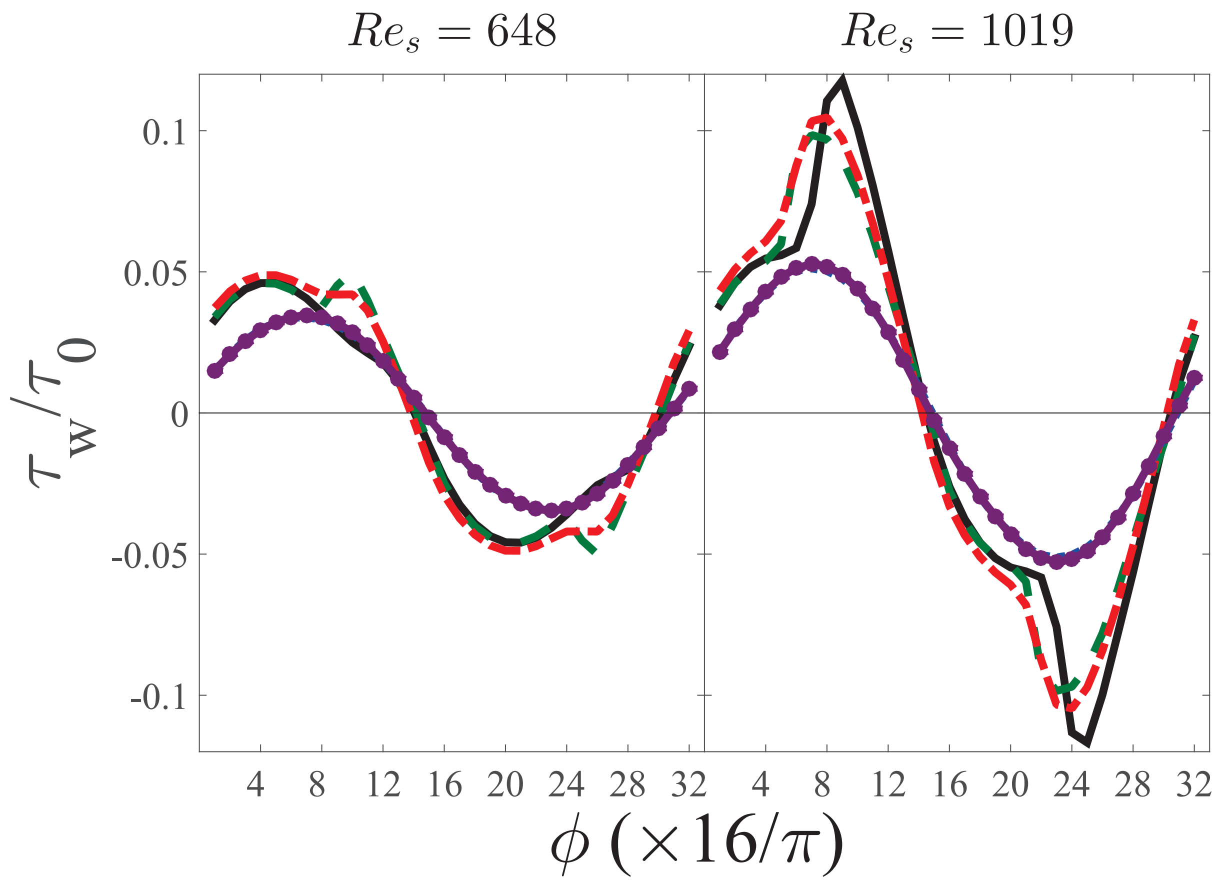

Figure 4.5: Phase-averaged normalized wall shear stress plotted as function of ϕ for $Re_s = 648$ (left panel) and $Re_s = 1019$ (right panel). The black solid line denotes the DNS. The line styles for the RANS turbulence models are the same as in Fig. 4.1.

The phase-averaged Reynolds stress difference profiles ($\overline{u'v'}_{RANS} - \overline{u'v'}_{DNS}$) normalized by $u^2_{\tau 0}$ for $Re_s = 648$ and $Re_s = 1019$ are shown in Figs. 4.3 and 4.4, respectively. For both Re_s, the largest differences between the DNS and the RANS turbulence models occur in the near-wall region from $5\pi/16 \leq \phi \leq 12\pi/16$. In addition, the differences for $Re_s = 1019$ are greater than for $Re_s = 648$. In general, the two high-Reynolds-number models are very well-correlated with each other for all phases and wall-normal positions and the two low-Reynolds-number models are better correlated with each other compared to their correlation for mean velocity.

The normalized wall shear stress, τ_w/τ_0, computed from the DNS and RANS simulations are plotted in Fig. 4.5 as a function of ϕ for $Re_s = 648$ (left panel) and $Re_s = 1019$ (right panel). Here

τ_w is computed from the velocity gradient at the wall using a finite difference method. Apparent (and not unexpected) is that the low-Reynolds-number models show much better agreement with the DNS compared to the high-Reynolds-number models. In particular, for $Re_s = 1019$, the high-Reynolds-number models do not capture the rapid rise in τ_w from $5\pi/16 \leq \phi \leq 12\pi/16$ when the cross-sectional averaged flow is transitioning from an accelerating flow to a decelerating flow. While the low-Reynolds-number models capture this rapid rise in τ_w, the peak magnitude is lower and the rise occurs at a phase-lead compared to the DNS. Since it is during these phases that the flow transitions to a turbulent flow, these results suggest that the high-Reynolds-number models do not capture the transition to turbulence, whereas the transition to turbulence for the low-Reynolds-number models occur at an early phase compared to the DNS.

The analog plots to those shown in Figs. 4.1–4.5 with respect to the thermal field are shown in Figs. 4.6–4.10. The phase-averaged mean temperature difference profiles between the RANS turbulence models and the DNS ($\Theta_{RANS} - \Theta_{DNS}$) normalized by the difference between the centerline and wall mean temperature ($\Theta_{cl} - \Theta_w$) for $Re_s = 648$ and $Re_s = 1019$ are shown in Figs. 4.6 and 4.7, respectively. Surprisingly, the low-Reynolds-number models show larger differences for $Re_s = 648$ compared to the high-Reynolds-number RANS turbulence models. At $Re_s = 1019$, however, the low-Reynolds-number models show smaller differences. The phase-averaged turbulent heat flux difference profiles ($\overline{v'\theta'}_{RANS} - \overline{v'\theta'}_{DNS}$) normalized by $u_{\tau 0}(\Theta_{cl} - \Theta_w)$ for $Re_s = 648$ and $Re_s = 1019$ are shown in Figs. 4.8 and 4.9, respectively. For $Re_s = 648$, the low-Reynolds-number models show the smallest differences. For $Re_s = 1019$, all four RANS turbulence models show the largest differences in the near-wall region from $5\pi/16 \leq \phi \leq 12\pi/16$, similar to the Reynolds shear stress differences. Again, indicating that the RANS turbulence models do not accurately capture the transition to turbulence.

The phase-averaged wall heat flux, nondimensionalized in the form of a Nusselt (Nu) number:

$$Nu = \frac{q''_w}{\lambda(\Theta_{cl} - \Theta_w)/h}, \tag{4.1}$$

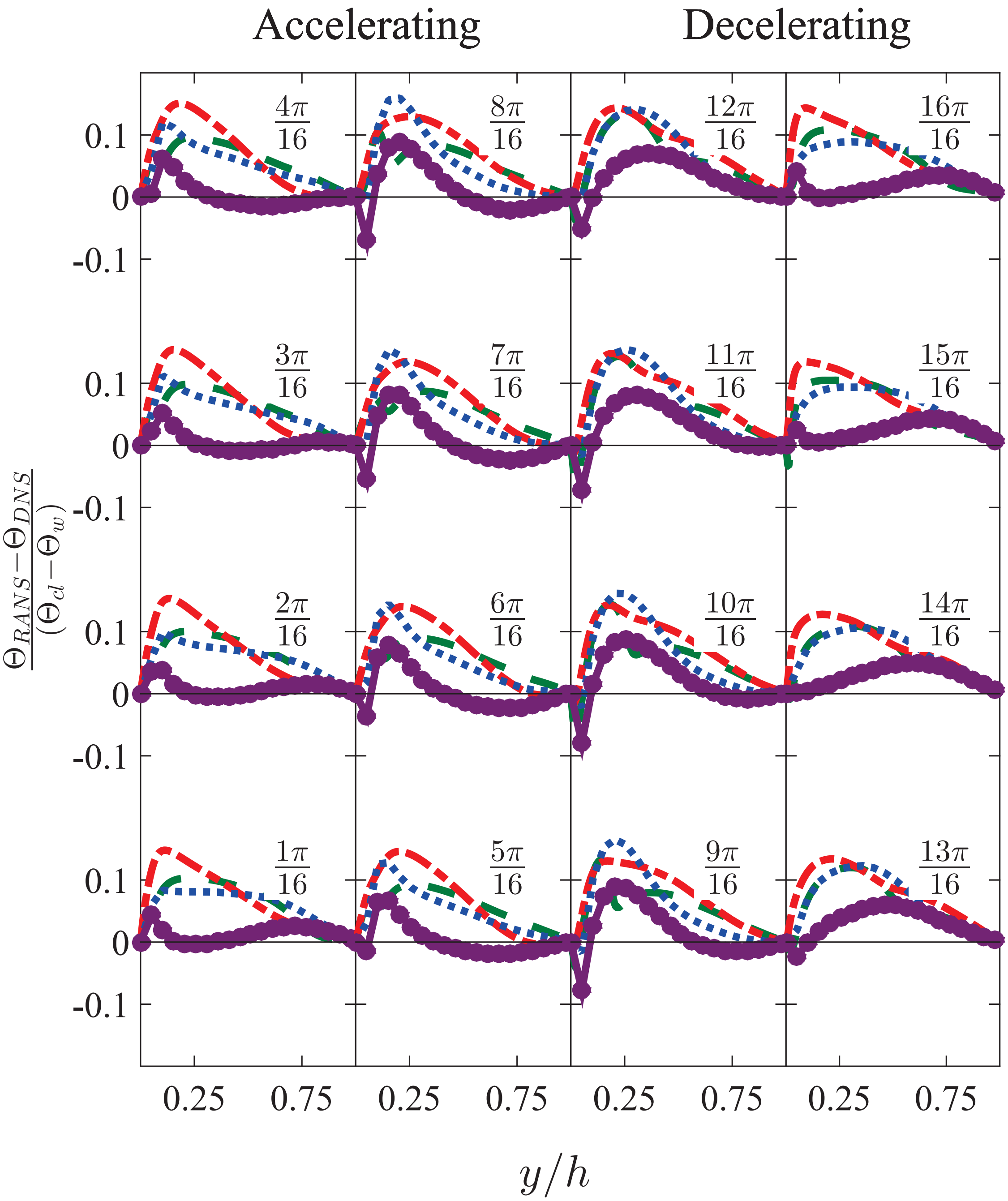

Figure 4.6: Wall-normal profiles of the phase-averaged temperature difference between the RANS turbulence models and the DNS normalized by the difference between the phase-averaged centerline temperature and wall temperature for $Re_s = 648$. Panel layout and line styles are the same as in Fig. 4.1.

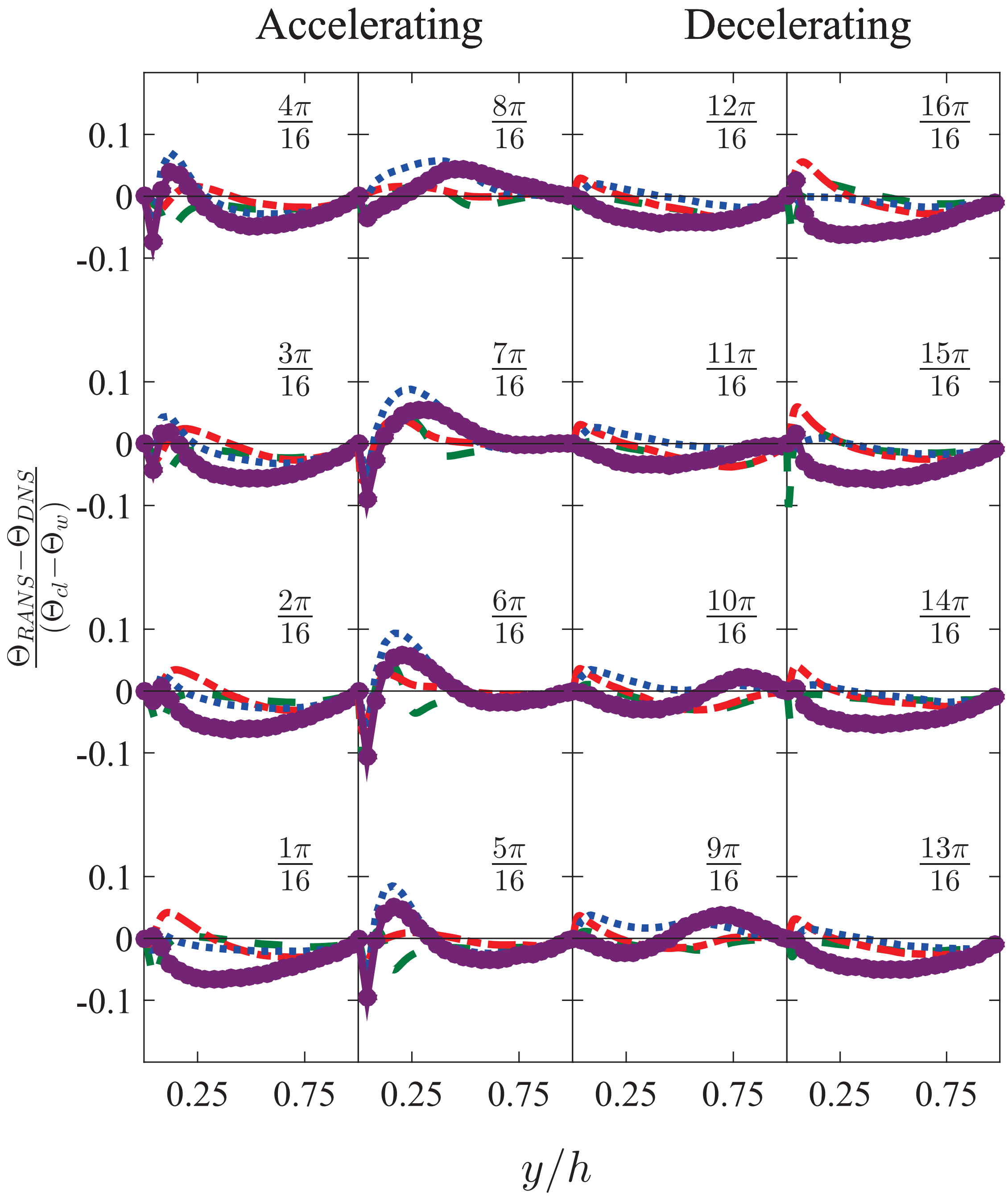

Figure 4.7: Wall-normal profiles of the phase-averaged temperature difference between the RANS turbulence models and the DNS normalized by the difference between the phase-averaged centerline temperature and wall temperature for $Re_s = 1019$. Panel layout and line styles are the same as in Fig. 4.1.

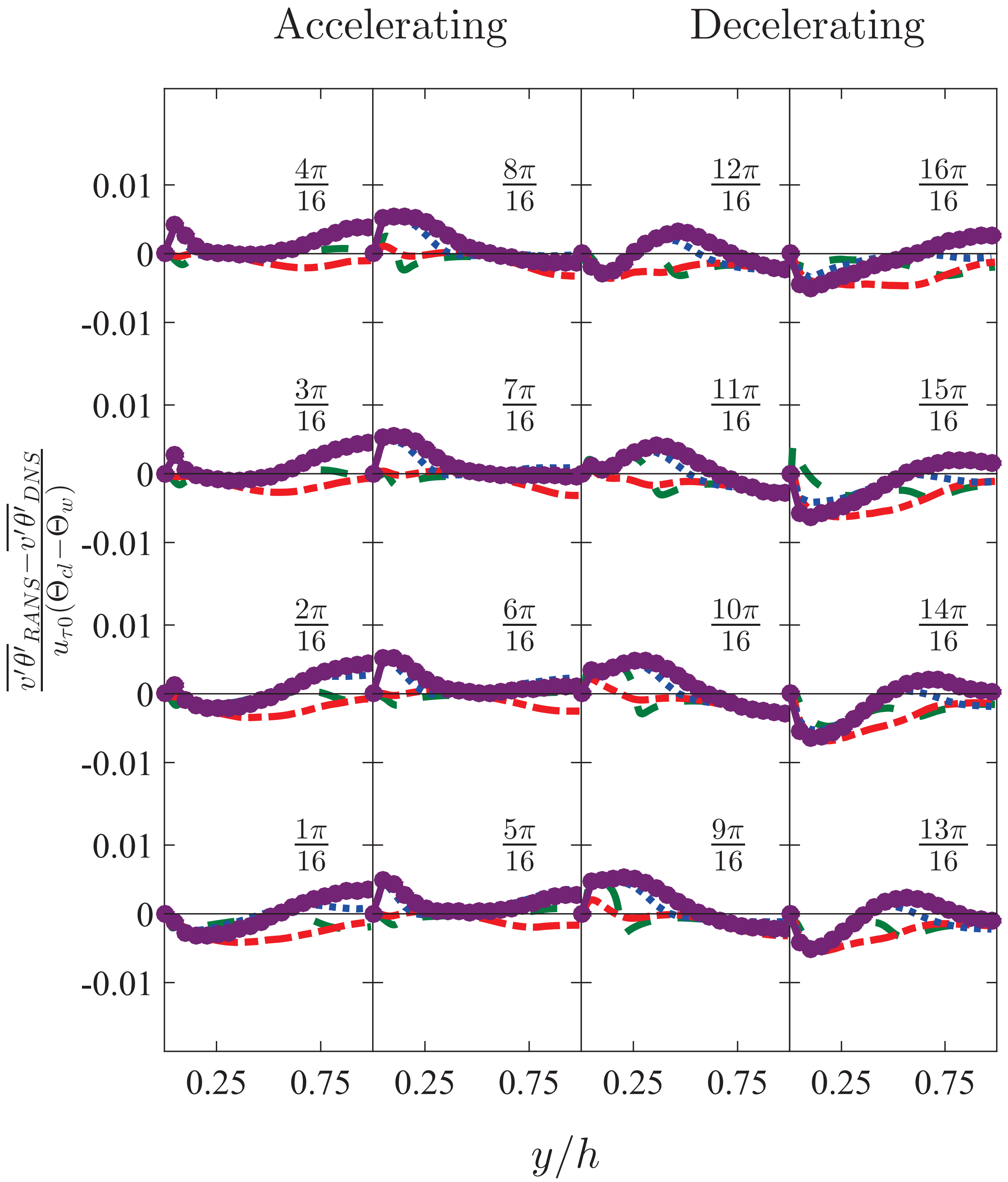

Figure 4.8: Turbulent heat flux difference profiles between the RANS turbulence models and the DNS normalized by $u_{\tau 0}(\Theta_{cl} - \Theta_w)$ for $Re_s = 648$. Panel layout and line styles are the same as in Fig. 4.1.

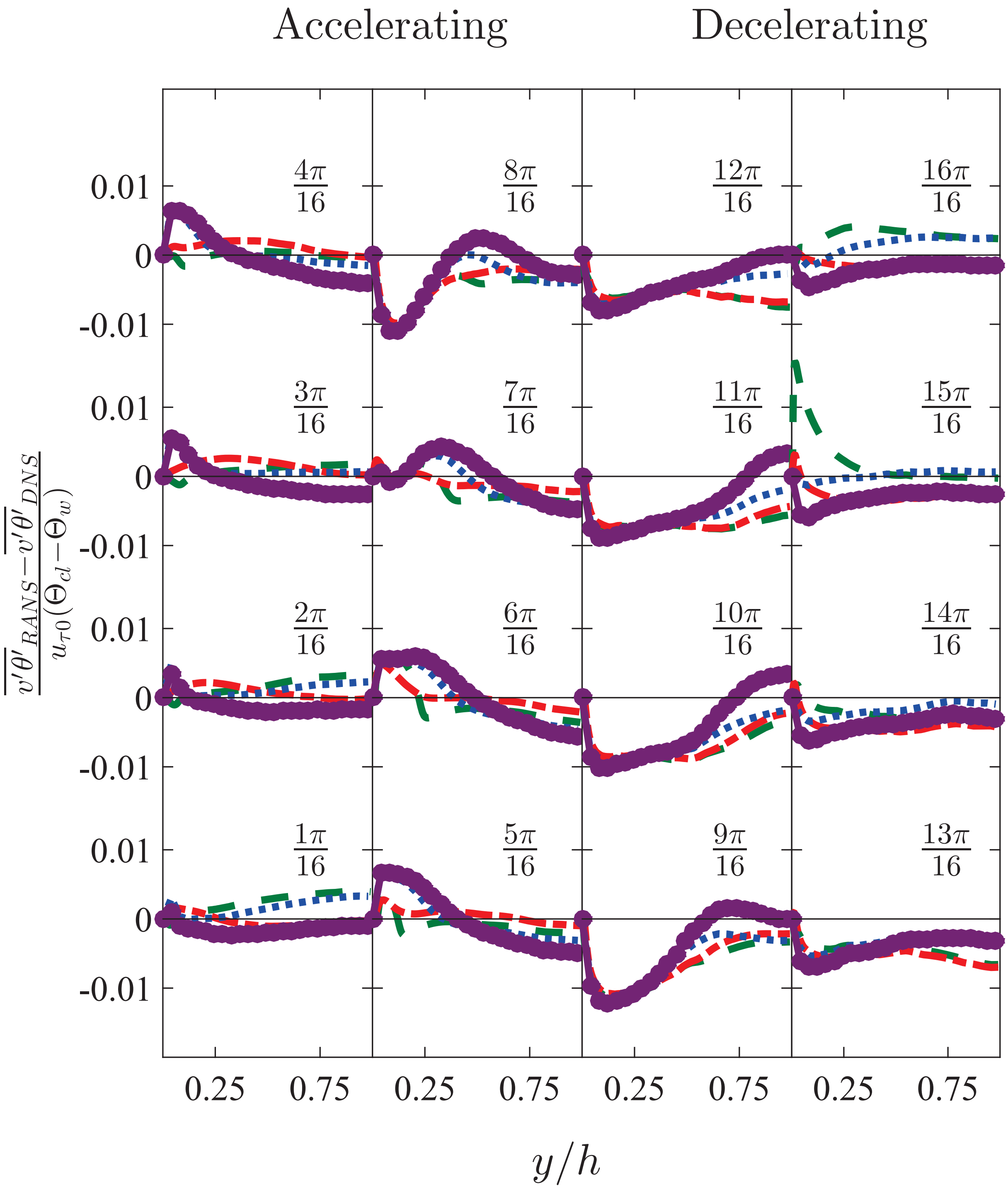

Figure 4.9: Turbulent heat flux difference profiles between the RANS turbulence models and the DNS normalized by $u_{\tau 0}(\Theta_{cl} - \Theta_w)$ for $Re_s = 1019$. Panel layout and line styles are the same as in Fig. 4.1.

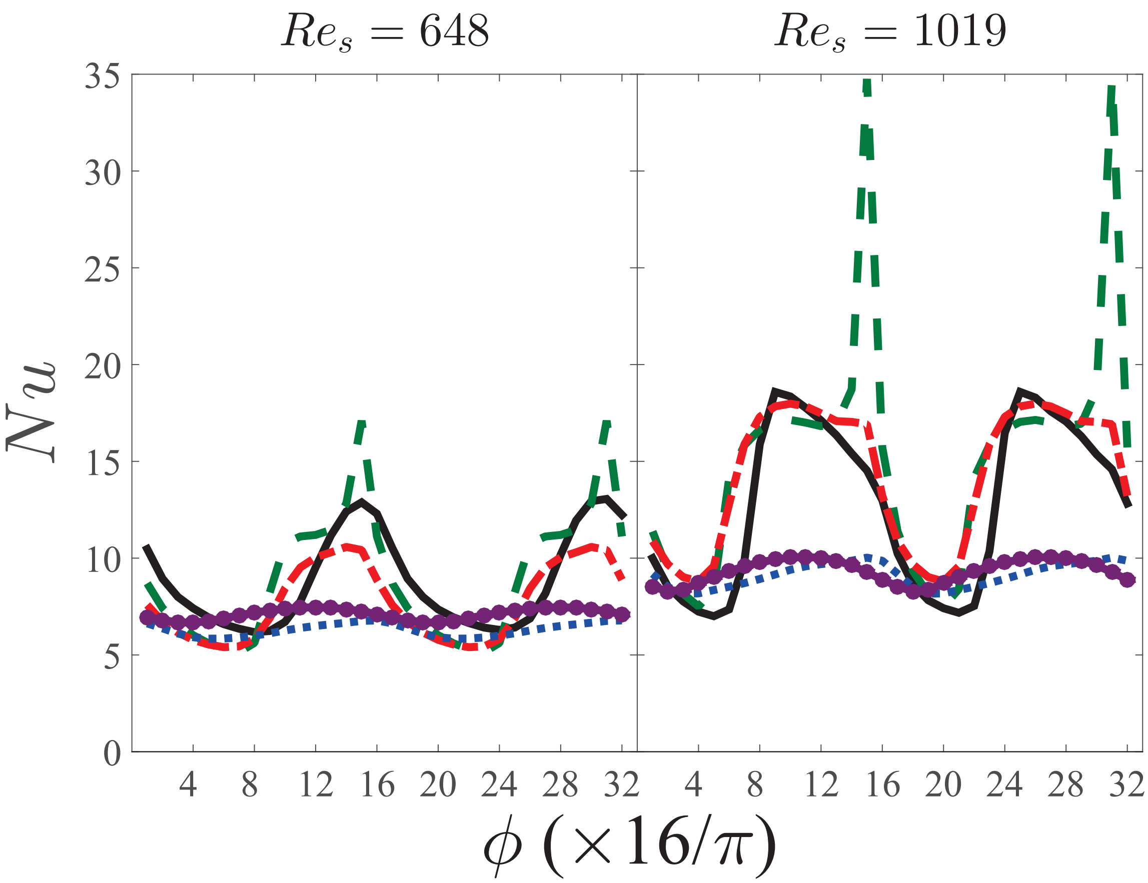

Figure 4.10: Phase-averaged normalized heat flux (i.e., Nu) plotted as function of ϕ for $Re_s = 648$ (left panel) and $Re_s = 1019$ (right panel). The black solid line denotes the DNS. The line styles for the RANS turbulence models are the same as in Fig. 4.1.

where λ is the thermal conductivity of the fluid, plotted as a function of ϕ computed from the DNS and RANS simulations at $Re_s = 648$ (left panel) and $Re_s = 1019$ (right panel) are shown in Fig. 4.10. In general, the low-Reynolds-number models do a much better job of reproducing the DNS period and magnitude of Nu compared to the high-Reynolds-number models. At Re_s=1019, both models show an overshoot spike near the end of the decelerating portion of the cycle, although the spike for the LS model is much larger than that for the v^2-f model. Lastly, similar to τ_w both low-Reynolds-number models phase lead the DNS during the later phases of the accelerating portion of the cycle.

Table 4.1: Tabulated values of $\Delta\widehat{\tau_w}$ and $\Delta\widehat{Nu}$ given by Eq. 4.2 and Eq. 4.3, respectively, for the four RANS turbulence models.

	$\Delta\widehat{\tau_w} \times 100$		$\Delta\widehat{Nu} \times 100$	
Model	$Re_s = 648$	$Re_s = 1019$	$Re_s = 648$	$Re_s = 1019$
LS	16.7	18.7	19.1	23.3
v^2-f	20.3	20.0	17.8	12.9
k-ϵ	28.9	43.4	28.0	33.0
k-ω	28.9	42.6	23.7	33.4

The wall flux predictive capabilities of the RANS turbulence models are quantified by integrating the magnitude difference between the phase-averaged wall flux values computed from the DNS and the RANS simulations over a full-cycle normalized by the cycle-averaged magnitude of the wall-flux:

$$\Delta\widehat{\tau_w} = \frac{1}{2\pi\langle|\tau_w|\rangle}\int_0^{2\pi} |\tau_{w_{RANS}} - \tau_{w_{DNS}}|\, d\phi, \tag{4.2}$$

$$\Delta\widehat{Nu} = \frac{1}{2\pi\langle Nu\rangle}\int_0^{2\pi} |Nu_{RANS} - Nu_{DNS}|\, d\phi, \tag{4.3}$$

where $|\cdot|$ denotes an absolute magnitude and $\langle\cdot\rangle$ denotes a cycle-average. The values of $\Delta\widehat{\tau_w}$ and $\Delta\widehat{Nu}$ for the four RANS turbulence models at both Re_s are tabulated in Table 4.1. The tabulated results are generally consistent with a qualitative evaluation of Figs. 4.5 and 4.10. Specifically, the $\Delta\widehat{\tau_w}$ and $\Delta\widehat{Nu}$ metric shows that the low-Reynolds-number models better predict the wall fluxes compared to the high-Reynolds-number models. The metric also shows that the v^2-f model performs the best at $Re_s = 1019$. The apparent poor performance of the LS model in predicting Nu, however, is primarily owed to the large spike at $\phi \approx 15\pi/16$. It follows that the general conclusion from this standard validation technique is that the low-Reynolds-number models do a reasonable job of modeling the flow physics of reciprocating channel flow with heat transfer at both Re_s. Additionally, it is concluded that the high-Reynolds-number models do not accurately capture the flow physics of reciprocating channel flow with heat transfer (in particular at $Re_s = 1019$) likely owing to deficiencies in the wall functions employed.

4.2 Integral Validation Technique

The wall shear stress and wall heat flux are not local quantities, but depend on the integrated effects of the flow dynamics above the wall. Consequently, a comparison of the wall flux computed from a RANS simulation to that computed from a benchmark dataset does not provide sufficient information on how well the turbulence model predicts the flow dynamics. In particular, while such a comparison can identify model failures, it cannot identify false-positives owed to the cancellation of model errors. Moreover, such a comparison cannot be used to provide physics-based guidance on how to improve a model. The integral validation technique presented here provides a direct connection between wall fluxes and mean flow dynamics, thus providing the necessary means to evaluate if a model correctly predicts the flow physics. In turn, providing needed information critical to the improved development of turbulence models.

The integral validation technique is derived following the work of Fukagata *et al.* (2002) and the complementary works of Mehdi and White (2011); Mehdi *et al.* (2014) and Ebadi *et al.* (2015). The derivation of the wall heat flux is provided in Chapter 3 while the derivation of the wall shear stress can be found in Mehdi and White (2011) and Mehdi *et al.* (2014)[1] .

$$\tau_w = \underbrace{\frac{2\mu}{y_t^2}\int_0^{y_t} U dy}_{I} - \underbrace{\frac{2\rho}{y_t^2}\int_0^{y_t}(y_t - y)\overline{u'v'}dy}_{II} - \underbrace{\frac{\rho}{y_t^2}\int_0^{y_t}(y_t - y)^2\frac{\partial}{\partial y}\left(\nu\frac{\partial U}{\partial y} - \overline{u'v'}\right)dy,}_{III} \quad (4.4)$$

---

[1] These expressions are valid in the most general case even when the advection/convection terms in the momentum and scalar temperature transport equation are non-zero. Also note that other integral expressions for τ_w and q''_w are possible depending on alternate substitution of mathematically equivalent terms.

$$q''_w = \underbrace{\frac{2\lambda}{y_t^2}\int_0^{y_t}(\Theta_w - \Theta)dy}_{I^*} + \underbrace{\frac{2\rho c_p}{y_t^2}\int_0^{y_t}(y_t - y)\overline{v'\theta'}dy}_{II^*} + \underbrace{\frac{\rho c_p}{y_t^2}\int_0^{y_t}(y_t - y)^2\frac{\partial}{\partial y}\left(\frac{\lambda}{\rho c_p}\frac{\partial \Theta}{\partial y} - \overline{v'\theta'}\right)dy}_{III^*}, \tag{4.5}$$

where μ, ρ and c_p are the kinetic viscosity, density and specific heat, respectively; and y_t is arbitrary height in the wall normal direction. The Reynolds shear stress ($-\overline{u'v'}$) and heat flux ($\overline{v'\theta'}$) in eddy viscosity RANS models are obtained from the constitutive equations:

$$-\overline{u'v'} = \nu_T\frac{\partial U}{\partial y} \text{ and } -\overline{v'\theta'} = \frac{\nu_T}{Pr_T}\frac{\partial \Theta}{\partial y}.$$

Therefore, the equivalent integral relations for the RANS turbulence models are obtained by replacing the Reynolds fluxes in terms II, II^*, III, III^* by their RANS modeling equivalent. Equations 4.4 and 4.5 each consist of three contributing terms to the wall flux: I, I^* is the contribution from the mean velocity or temperature profile, respectively; II, II^* is the contribution from the turbulent flux; and III, III^* is the contribution from the gradient of the total (i.e., molecular plus turbulent) flux, or equivalently the substituted terms (e.g., in reciprocating channel flow, term III is effectively the sum of the unsteady velocity and pressure gradient terms and term III^* is the unsteady temperature term). The $(y_t - y)$ or $(y_t - y)^2$ weightings place more emphasis on the near-wall values and, consequently, as $y_t \to h$ (or, alternatively, boundary layer thickness δ), term I, I^* decreases while terms II, II^* and III, III^* increase. As described previously, the decomposition provides two major advantages: (a) it provides a means to connect the wall flux to the mean flow dynamics and (b) the expressions are amenable to experimental validation of turbulence models requiring only measurements of wall-normal profiles of mean variables (velocity or temperature) and turbulent flux at one streamwise location up to an arbitrary height y_t (Mehdi and White, 2011; Mehdi *et al.*, 2014; Ebadi *et al.*, 2015). Here (a) is exploited to develop a robust RANS turbulence model validation technique.

The phase-averaged contributions to τ_w/τ_0 from the three terms in Eq. 4.4 when integrated to the channel half-height (i.e., $y_t = h$) are plotted in Fig. 4.11 for $Re_s = 648$ (left panel) and $Re_s = 1019$ (right panel). First inspecting the DNS data, consistent between the two periods is that the contribution from term I is small (note the scale is one order-of-magnitude smaller than the others), representing approximately 10% or less of the total wall-shear stress at all phases. Relative to the sign of τ_w, term I follows with a slight phase-lag. This phase lag is smaller for $Re_s = 1019$ compared to $Re_s = 648$. For $Re_s = 648$, term II is of opposite sign of τ_w during the first quarter-period (i.e., accelerating phases) and the same sign during the second quarter-period (i.e., decelerating phases). For $Re_s = 1019$, the sign change occurs at $\phi \approx 6\pi/16$. Term III, however, changes sign relative to τ_w at a phase = $12\pi/16$ for both Re_s. Observe that at the phase where $\tau_w = 0$ (i.e., flow reversal at the wall), the contributing terms to the wall-shear stress are all finite but sum to zero.

In general, the low-Reynolds-number models follow the DNS better compared to the high-Reynolds-number models. The largest differences for the low-Reynolds-number models are for $Re_s = 1019$, where term I is well-predicted, term II is slightly over predicted during the accelerating phases of the cycle and under predicted during the early phases of deceleration ($9\pi/16 \leq \phi \leq 11\pi/16$), and term III is over predicted during the late phases of acceleration ($6\pi/16 \leq \phi \leq 8\pi/16$). The sum of the differences in term II and III is observed in the predicted τ_w, where the RANS turbulence models phase-lead the DNS at the late phases of acceleration. In brief, the low-Reynolds-number models perform better than the high-Reynolds-number models and show the largest differences compared to the DNS from $6\pi/16 \leq \phi \leq 11\pi/16$ when the cross-sectional averaged flow is transitioning from an accelerating flow to a decelerating flow. Similar, to the conclusions drawn from the standard validation technique, the low-Reynolds-number models do not accurately capture the transition to turbulence.

The phase-averaged contributions to Nu from the three terms in Eq. 4.5, when integrated to the channel half-height (i.e., $y_t = h$), are plotted in Fig. 4.12 for $Re_s = 648$ (left panel) and $Re_s = 1019$ (right panel). The DNS data shows that the period of each term is half the forcing

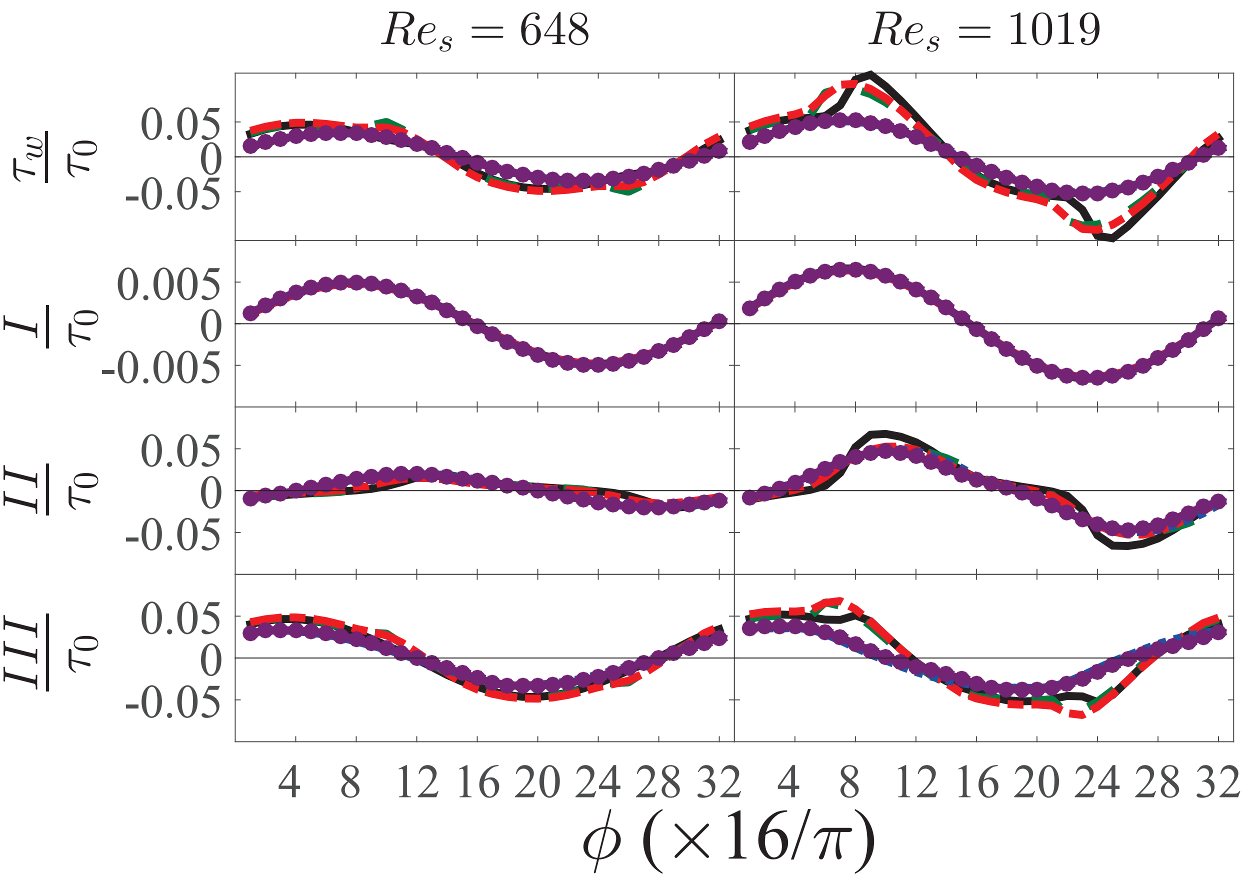

Figure 4.11: Contribution of term I (2nd row), II (third row) and III (fourth row) in the right hand side of Eq. 4.4 plotted as a function of ϕ for $Re_s = 648$ (left panel) and $Re_s = 1019$ (right panel). The top row is τ_w/τ_0 shown for reference. Note that at any ϕ the sum of I, II, III equals τ_w/τ_0. Panel layout and line styles are the same as in Fig. 4.5.

period, unlike the terms for τ_w which have a period equal to the forcing period[2]. The dominant contribution is term II^*, the contribution from term I^* is small, and term II^* and III^* are 180^0 out of phase. Compared to τ_w, the RANS turbulence models perform far worse in predicting the contributing terms to Nu. Similar to earlier observations from the mean temperature profiles, the high-Reynolds number models better predict term I^* at $Re_s = 648$, while the low-Reynolds-number models better predict term I^* at the higher Re_s. For $Re_s = 1019$, both the low- and high-Reynolds-number models underestimate term II^* but have the correct phase. Surprisingly,

---

[2] Details of a toy model developed to relate the modulation frequency of Nu and τ_w to the forcing frequency are provided in Appendix B.

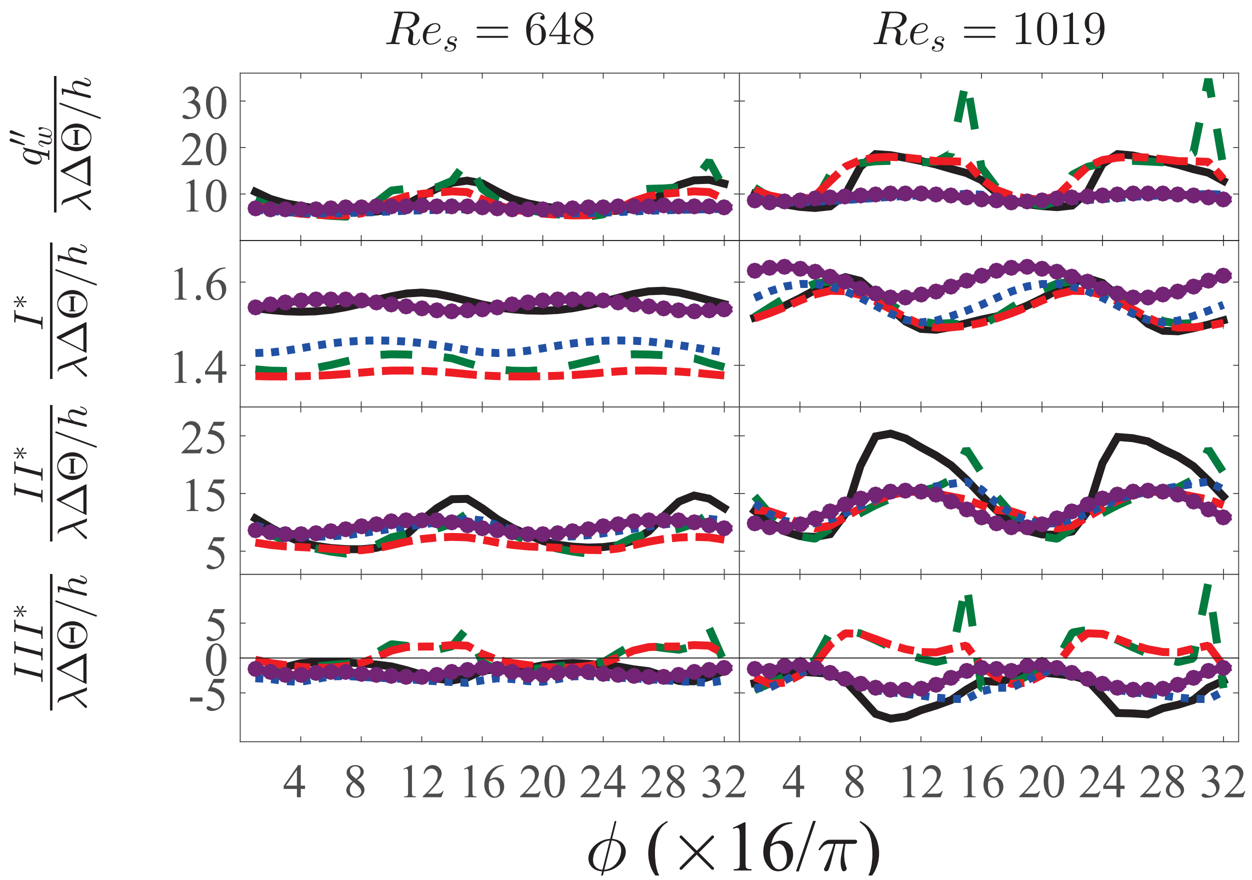

Figure 4.12: Contribution of term I^* (2nd row), II^* (third row) and III^* (fourth row) in the right hand side of Eq. 4.5 plotted as a function of ϕ for $Re_s = 648$ (left panel) and $Re_s = 1019$ (right panel). The top row is Nu shown for reference, where $\Delta\Theta = \Theta_{cl} - \Theta_w$. Note that at any ϕ the sum of I^*, II^*, III^* equals Nu. Panel layout and line styles are the same as in Fig. 4.10.

for term III^* the high-Reynolds-number models perform better than the low-Reynolds-number models. Specifically, although the high-Reynolds-number models underestimate the magnitude of term III^* they are roughly in phase with the DNS and have the correct sign. Conversely, for the low-Reynolds-number models, term III^* is 180^0 out of phase and, during the late phases of acceleration and almost all phases of deceleration ($6\pi/16 \leq \phi \leq 16\pi/16$), of opposite sign compared to the DNS. Since in reciprocating channel flow term III^* is effectively the unsteady temperature term (i.e., $\partial\Theta/\partial t$), these results suggest that the evolution of the unsteady term is not well-modeled. Importantly, for the low-Reynolds-number models, the differences in terms II^* and

III^* serendipitously cancel to yield a reasonable prediction of the wall heat flux compared to the DNS.

A similar metric as used for the standard validation technique is used here to quantify the differences between the phase-averaged RANS predicted integral terms in Eqs. 4.4 and 4.5 compared to the DNS:

$$\Delta\widehat{i} = \frac{1}{2\pi\langle|i|\,\rangle}\int_0^{2\pi} |i_{RANS} - i_{DNS}|\, d\phi, \tag{4.6}$$

where $i = \{I, I^*, II, II^*, III, III^*\}$. The values of $\Delta\widehat{I}, \Delta\widehat{I^*}$; $\Delta\widehat{II}, \Delta\widehat{II^*}$; and $\Delta\widehat{III}, \Delta\widehat{III^*}$ are tabulated in Table 4.2, 4.3, and 4.4, respectively. The tabulated results are consistent with the qualitative evaluation of Figs. 4.11 and 4.12 and their accompanying descriptions. Specifically, term I, I^* are generally well-predicted by the high-Reynolds number models at both Re_s. For the low-Reynolds-number models, term I, I^* are better predicted at $Re_s = 1019$. Note that the good prediction of term I, I^* does not necessarily mean that the U and Θ profiles are well predicted, it only means that the integral contributions to the wall-flux from U and Θ are well-predicted. For all four models, the differences in term II, II^* are significantly larger compared to the differences in term I, I^*, indicating that the turbulent models are not accurately modeling the turbulent flux terms. Surprisingly, as described above, the high-Reynolds-number models better predict term III^* compared to the low-Reynolds-number models.

In summary, while validation based on comparisons of Nu alone suggests that the low-Reynolds-number models perform reasonably well, the integral validation technique demonstrates that RANS turbulence models do not accurately capture the underlying flow physics. The technique also identifies that the unsteady term is not well-modeled from the late-stages of the acceleration portion of the cycle through the decelerating portion of the cycle. Moreover, the reasonable success in predicting the integral terms for τ_w and the failure in predicting the terms for Nu is strong evidence that at least one issue in the RANS modeling lies in the assumption that the turbulent Prandtl number is constant.

Table 4.2: Tabulated values of $\Delta\widehat{I}$ and $\Delta\widehat{I}^*$ given by Eq. 4.6 for the four RANS turbulence models.

	$\Delta\widehat{I} \times 100$		$\Delta\widehat{I}^* \times 100$	
Model	$Re_s = 648$	$Re_s = 1019$	$Re_s = 648$	$Re_s = 1019$
LS	1.6	2.5	9.2	0.8
v^2-f	2.1	2.8	11.0	0.7
k-ϵ	3.1	1.0	6.7	1.8
k-ω	2.8	1.0	1.4	4.2

Table 4.3: Tabulated values of $\Delta\widehat{II}$ and $\Delta\widehat{II}^*$ given by Eq. 4.6 for the four RANS turbulence models.

	$\Delta\widehat{II} \times 100$		$\Delta\widehat{II}^* \times 100$	
Model	$Re_s = 648$	$Re_s = 1019$	$Re_s = 648$	$Re_s = 1019$
LS	28.1	25.7	17.0	28.6
v^2-f	35.6	22.1	28.7	28.8
k-ϵ	67.6	33.5	21.9	26.1
k-ω	72.4	40.7	29.2	30.5

Table 4.4: Tabulated values of $\Delta\widehat{III}$ and $\Delta\widehat{III}^*$ given by Eq. 4.6 for the four RANS turbulence models.

	$\Delta\widehat{III} \times 100$		$\Delta\widehat{III}^* \times 100$	
Model	$Re_s = 648$	$Re_s = 1019$	$Re_s = 648$	$Re_s = 1019$
LS	11.8	12.6	125.2	122.8
v^2-f	15.8	15.7	126.3	115.3
k-ϵ	30.4	46.4	85.9	28.2
k-ω	28.6	41.8	59.2	43.3

4.3 Reynolds Analogy

The fact that the RANS turbulence models better predict the contributing integral terms to τ_w compared to q''_w suggests that the turbulent heat flux closure is not properly modeled. Specifically, since the Reynolds analogy is employed in the RANS numerical simulations, it suggests that Reynolds

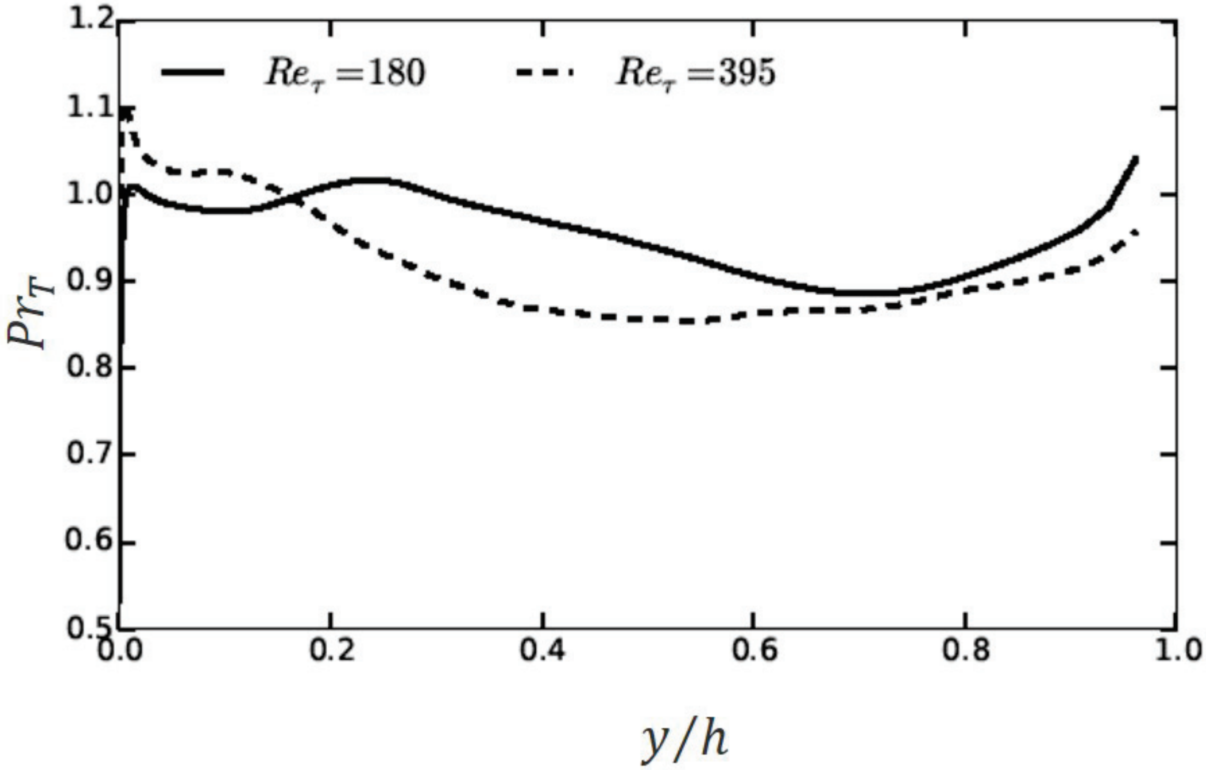

Figure 4.13: Pr_T profiles as a function of the distance from the wall in a steady channel flow, with temperature as a passive scalar. Figure courtesy of Samir Sid.

analogy may not hold in reciprocating channel flow. The potential breakdown of Reynolds analogy in reciprocating channel flow is, therefore, briefly explored here.

The Reynolds analogy relies on the assumption that there exists a turbulent Prandtl number Pr_T, which relates the momentum scales to the thermal scales. In standard modeling practice, Pr_T is assumed to be a constant across the flow domain. This assumption is relatively valid in steady equilibrium flow but is known to breakdown in non-equilibrium flow (Blackwell *et al.*, 1972; Bradshaw and Huang, 1995; Araya and Castillo, 2012). Importantly, to assess the validity of Reynolds analogy, DNS allows for the Pr_T to be computed directly:

$$Pr_T = \frac{\nu_T}{\alpha_T} = \frac{\overline{u'v'}\,(\partial\Theta/\partial y)}{\overline{v'\theta'}\,(\partial U/\partial y)}. \tag{4.7}$$

It follows that examination of Pr_T profiles allows for a direct evaluation of the validity of Reynolds analogy. For example, Fig. 4.13 shows wall-normal profiles of Pr_T in steady-state turbulent channel flow at two $Re_\tau = u_\tau h/\nu$. Evident is that Pr_T is approximately constant across the channel height, and that the degree of constancy is greater for the higher Re_τ.

Wall-normal profiles of Pr_T computed from the DNS of reciprocating channel flow for $Re_s = 648$ and $Re_s = 1019$ are shown in Figs. 4.14 and 4.15, respectively. Apparent is that Pr_T is highly variable both across the channel half-height as well as between different phases. With the exception of a few decelerating phases at $Re_s = 1019$, the Pr_T does not approximate a constant across the flow domain. In particular, the Pr_T profiles are complex and of generally similar shape for many of the phases. For both Re_s and during the accelerating phases of the cycle, Pr_T decreases with increasing y in the inner-region of the flow with a phase-dependent y-position zero crossing followed by a rapid decrease/rapid increase (with a second zero crossing). Pr_T then approaches either a constant value, decays to zero, or has some complex behavior as the channel centerline is approached. The first zero crossing is where $\overline{u'v'}$ changes sign and the rapid sign change occurs at the zero crossing of $\partial U/\partial y$. It is apparent from Figs. 4.14 and 4.15 that Reynolds analogy is a flawed assumption in reciprocating channel flow.

The underlying failure of Reynolds analogy is most likely caused by the combined effects of the flow being intermittently turbulent (i.e., transitional like at most phases) and forced by an unsteady pressure gradient. Regarding the latter effect, as described by Bradshaw and Huang (1995) and Bradshaw (1996), Reynolds analogy may breakdown in flows with imposed pressure gradients because the velocity field depends on the pressure field while the temperature field does not (explicitly) depend on the pressure field. It follows that the inability of the RANS turbulence models to accurately predict the contributing integral terms to Nu is most likely due to a combination of deficiencies in the turbulence models employed and the use of Reynolds analogy, either way new models or modification to the current models should be investigated.

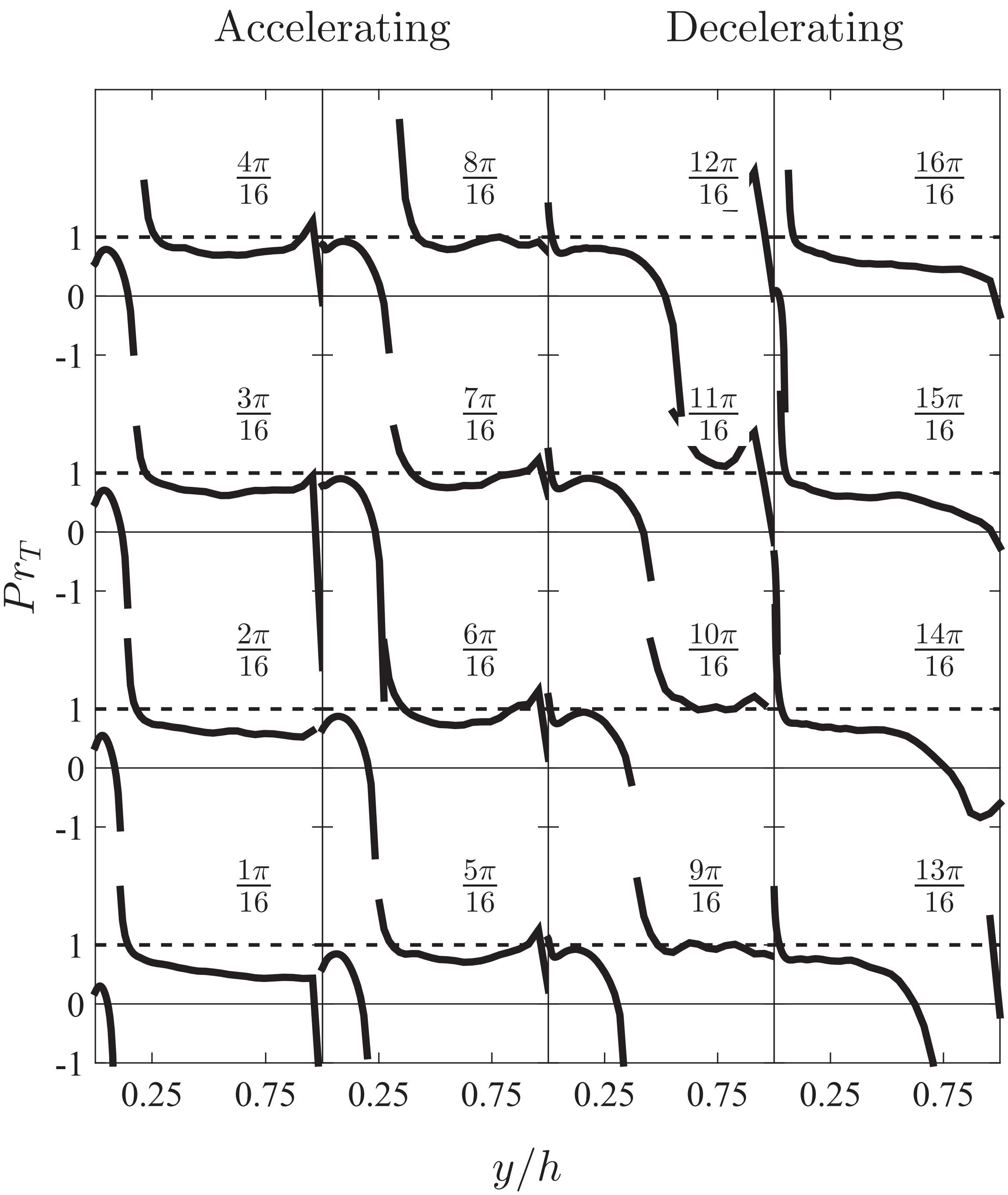

Figure 4.14: Pr_T profiles as a function of distance from the wall for $Re_s = 648$. The horizontal dashed lines correspond to Pr_T = 1. Panel layout is the same as in Fig. 4.1.

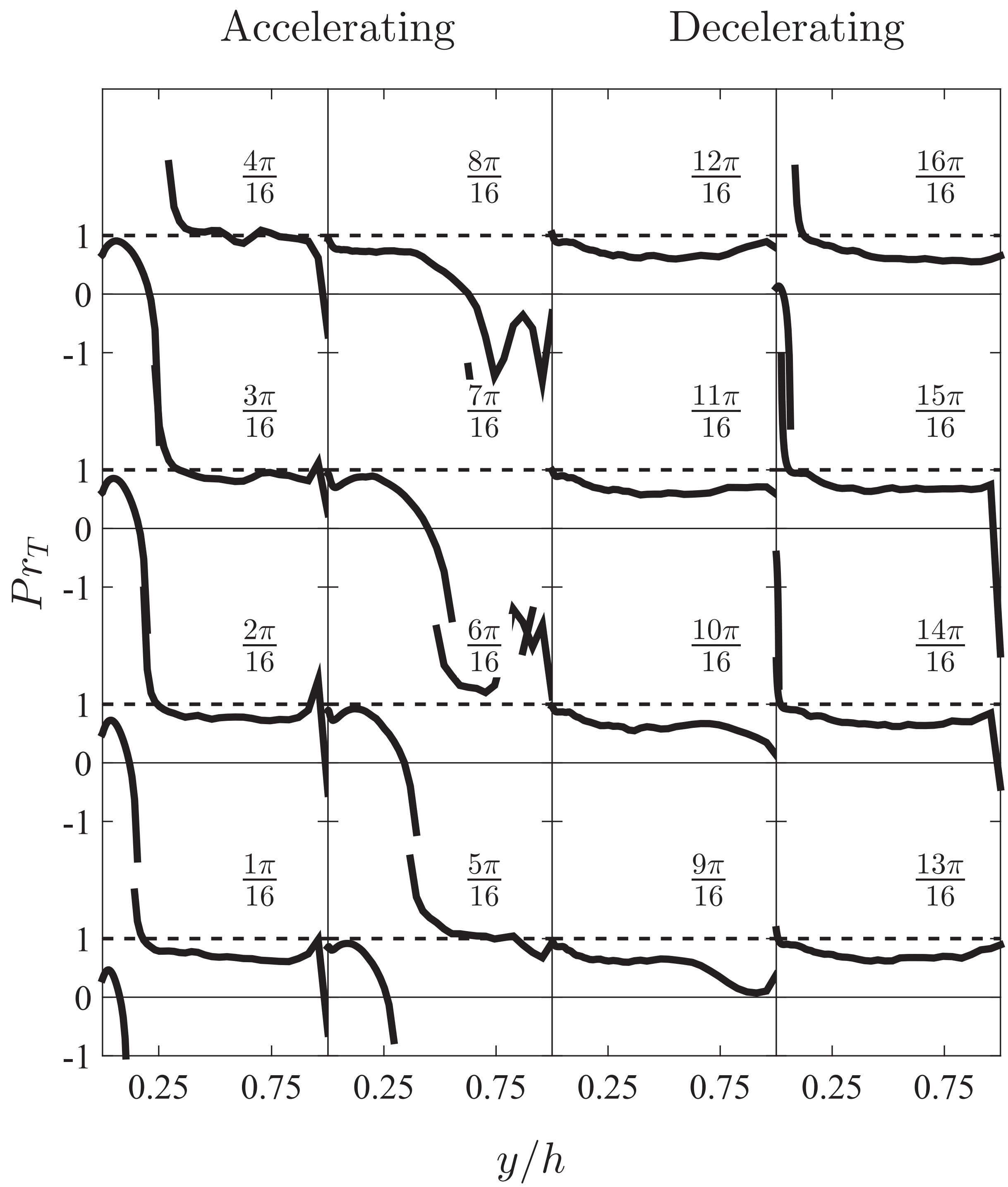

Figure 4.15: Pr_T profiles as a function of distance from the wall for $Re_s = 1019$. The horizontal dashed lines correspond to Pr_T = 1. Panel layout is the same as in Fig. 4.1.

4.4 Summary

DNS of reciprocating channel flow with heat transfer was used to evaluate the performance of two low-Reynolds-number and two high-Reynolds-number RANS turbulence models. Two validation techniques were used in the evaluation: (1) the so-called standard validation technique, where results from RANS simulations of averaged variable profiles and wall fluxes are compared to the DNS dataset, and (2) an integral validation technique, where the contributing terms to the wall shear stress and wall heat flux are compared between the RANS results and the DNS dataset. The contributing terms to the wall shear stress and wall heat flux used in the integral validation technique were obtained by thrice integrating the momentum and scalar temperature transport equation, respectively.

The standard validation technique indicated that the two low-Reynolds-number models reasonably predicted the transport of momentum and thermal energy in reciprocating channel flow. Specifically, the mean variable profiles predicted by the RANS simulations qualitatively agreed reasonably well with the DNS profiles. Moreover, using the wall flux of momentum and wall flux of heat as validation metrics, both low-Reynolds-number turbulence models predicted the wall-shear stress and wall-heat flux to within approximately 20% of the DNS results as quantified by Eqs. 4.2 and 4.3, respectively. The largest differences observed between the low-Reynolds-number models and the DNS were from $6\pi/16 \leq \phi \leq 11\pi/16$, when the flow transitions from an accelerating flow to a decelerating flow. Since it is during these phases that the flow transitions to a turbulent flow, it can be concluded that the RANS turbulence models do not accurately capture this transition. With respect to the wall fluxes, this modeling deficiency manifested itself in a phase-lead of the RANS modeled wall fluxes compared to the DNS computed wall fluxes.

The results of the integral validation technique, however, provided a very different assessment of the performance of the RANS turbulence models. The most striking result is that while the low-Reynolds-number models performed reasonably well in predicting the contributing terms to the wall shear stress, the models performed rather poorly in predicting the contributing terms to the wall heat flux. Specifically, the contributions from the turbulent heat flux (term II^*) were under predicted by as much as approximately 40% during the decelerating phases of the cycle. In addition, the contribution from the gradient of the total heat flux (term III^*, which is effectively the contribution from the unsteady temperature), was of opposite sign and 180^o out-of-phase compared to the DNS. Importantly, the differences in term II^* and III^* serendipitously canceled each other yielding a reasonable prediction of the wall heat flux compared to the DNS. Consequently, despite a reasonable agreement in predicting the wall heat flux, the low-Reynolds-number models do not accurately model the transport of thermal energy in reciprocating channel flow. This important conclusion likely would have been missed using the standard validation technique. In addition, the integral validation technique identified the root causes of the modeling failures, namely the breakdown of Reynolds analogy and deficiencies in the turbulence heat flux model. This information is critical to the improved development of turbulence models.

CHAPTER 5

TRANSITION TO TURBULENCE IN RECIPROCATING CHANNEL FLOW

Reciprocating flow is typically categorized into five flow regime types: I (laminar), II (disturbed laminar), III (self-sustaining transition), IV (intermittently turbulent), and V (fully-developed turbulent) as described in Chapter 2 (Ozdemir *et al.*, 2014; Akhavan *et al.*, 1991a). Understanding the mechanisms of transition between flow regime types is important to understand and predict the transport mechanisms in many biological and engineered flow systems. Importantly, owing to the profound differences in the transport behaviors between laminar and turbulent flow, there has been extensive work towards understanding the underlying mechanisms of transition between the laminar and turbulent flow regimes in periodic flow (Eckmann and Grotberg, 1991; Kurzweg *et al.*, 1989).

In this Chapter, the DNS of reciprocating channel flow described in Chapter 2 (and used to evaluate RANS turbulence models as described in Chapter 4) is used to study transition to turbulence in periodic flows. The simulations are performed for $Re_s = 648$ and 1019, representing type III (self-sustaining transition) and type IV (intermittently turbulent) flow regimes, respectively. The phase-averaged mean momentum balance is analyzed to determine the leading order terms as a function of phase angle. Turbulence is defined when the magnitude ordering of the leading order terms in the mean momentum equation matches with the four layer structure first introduced by Wei *et al.* (2005a) for fully-developed wall-bounded turbulent flows. Mean flow properties such as the turbulent inertia and the temporal acceleration are investigated prior to and during the onset of turbulence to understand the underlying mechanisms of transition.

5.1 Literature Review

Critical Re_s of Flow Regime Transitions

Experimental studies investigating transition to turbulence in reciprocating flows include Miller and Fejer (1964), Sergeev (1966), Akhavan *et al.* (1991a), Schmirler *et al.* (2014), Eckmann and Grotberg (1991). Similarly, numerical simulations include Spalart and Baldwin (1989), Akhavan *et al.* (1991b), Scotti and Piomelli (2001), Di Liberto and Ciofalo (2011) and Ozdemir *et al.* (2014). Collectively, these studies demonstrate that the transition between different flow regime types occur at a critical Stokes Reynolds number: $Re_s = \frac{U_m l_s}{\nu}$, where U_m is the amplitude of the cross-sectional average velocity, $l_s \equiv \sqrt{2\frac{\nu}{\omega}}$ is the Stokes layer thickness, ω is the angular frequency of the oscillation and ν is the kinematic viscosity of the fluid. Given that there are five flow regime types there will be four critical Re_s values. The four critical values of Re_s denoted here by $Re_{s,a\to b}$, where a, b denotes the flow regimes from which the flow transitions from and to, respectively. $Re_{s,a\to b}$ is determined empirically by defining arbitrary thresholds of turbulent intensity, skin friction coefficient, and the turbulent kinetic energy growth rate, among other statistical variables, (Di Liberto and Ciofalo, 2011; Hedley and Keffer, 1974). A summary of the four critical values of Re_s and a brief description of the transition are described below:

1. $Re_{s,I\to II} \approx 280$ (Akhavan *et al.*, 1991a): This transition is from a laminar flow (I) to a disturbed laminar flow (II). A disturbed laminar flow shows fluctuations in the instantaneous velocity, however, the mean velocity profile does not depart from the laminar profile. Since the onset of velocity fluctuations are very sensitive to initial and background disturbances, there is noticeable scatter in the report critical value of $Re_{s,I\to II}$ from different studies.

2. $Re_{s,II\to III} \approx 500$ (Ozdemir *et al.*, 2014): This transition is from a disturbed laminar flow (II) to a self-sustaining transitional flow (III). In a self-sustaining transitional flow, the mean velocity profiles depart from laminar flow profiles. The energy of the velocity fluctuations transfer from one phase to the next, however, the energy is insufficient to trigger transition to a turbulent flow. Flow regime III was first proposed by Spalart and Baldwin (1989) and has

been extensively studied by Ozdemir *et al.* (2014). $Re_{s,II \rightarrow III} \approx 500$ is reported by Ozdemir *et al.* (2014).

3. $Re_{s,III \rightarrow IV} \approx 750$ (Ozdemir *et al.*, 2014): This transition is from a a self-sustaining transitional flow (III) to a intermittently turbulent flow (IV). In an intermittently turbulent flow, fully-developed turbulent flow behaviors are first observed in the early decelerating phases of the cycle. Dimensional analysis performed by Akhavan *et al.* (1991a) predicts a modified logarithmic mean velocity profile for the phases that exhibit fully-developed turbulent flow behaviors.

4. $Re_{s,IV \rightarrow V} \approx 3460$ (Jensen *et al.*, 1989): This transition is from an intermittently turbulent flow (IV) to a fully-developed turbulent flow (V). In a fully-developed turbulent flow, the flow exhibits fully-developed turbulent flow behaviors over the entire cycle and a logarithmic mean velocity profile is absent for only 10% of the oscillation period around the phase corresponding to flow reversal (Jensen *et al.*, 1989).

Mechanisms of Flow Regime Transitions

Theoretical studies on the mechanisms of flow regime transitions in periodic flow are primarily based on linear instability analysis as reported by Morkovin and Obremski (1969), Von Kerczek and Davis (1974), Blennerhassett and Bassom (2002), Blennerhassett and Bassom (2006), Luo and Wu (2010). These theoretical studies can be categorized into two groups:

(a) ***Quasi-steady***: In this approach, the time variation of the base flow is neglected, and the flow is analyzed as an ensemble of frozen profiles at different phases (Morkovin and Obremski, 1969; Von Kerczek and Davis, 1974). The method is valid only when the time scale of the base flow (for example, the oscillation period) is much longer than the advection time scale of the growth (or decay) rate of the instabilities. Using a quasi-steady approach, Von Kerczek and Davis (1974) predicted $Re_{s,III \rightarrow IV}$ = 86. Compared to experimental observations (as described previously), this predicted critical Re_s is much too low, indicating that the quasi-steady formulation does not capture the correct mechanism of transition. A likely reason being that the instabilities are damped on a time-scale much shorter than the time-scale of the base flow, which would not be captured by a quasi-steady analysis.

(b) ***Time-dependent theories***: In this approach, which is an extension of the Floquet theorem, the time variation is retained (Hall, 1978; Blennerhassett and Bassom, 2006). However, the amplitude of the velocity fluctuations are assumed to be small at all phases of the cycle (Akhavan *et al.*, 1991b; Ozdemir *et al.*, 2014). Employing the time-dependent approach, Blennerhassett and Bassom (2006) predicted $Re_{s,III\rightarrow IV}$ = 1416, which is much greater than the experimentally observed critical Re_s. Again, suggesting that the time-dependent approach does not capture the correct mechanism of transition.

It can be conjectured, given the under/over predictions of $Re_{s,III\rightarrow IV}$ from the quasi-steady and time-dependent formulations, respectively, that the time-dependency cannot be neglected and the amplitude of velocity fluctuations cannot be considered small. An analysis that retains the time-dependency and considers order one (large) velocity fluctuations has, to the best of author's knowledge, not been performed. Nevertheless, these theoretical investigations coupled with numerical simulations (Akhavan *et al.*, 1991b; Ozdemir *et al.*, 2014) provide reasonable insights into the underlying transition mechanisms, as outlined below.

1. Transition from regime I to regime II: Infinitesimally small disturbances grow linearly to finite amplitude. Next, these finite-amplitude disturbances grow nonlinearly in the late accelerating and early decelerating phases of the cycle, but are damped in the late decelerating and early accelerating phases of the cycle. In this stage, even a 20% disturbance in velocity amplitude does not lead to sustained departure from the laminar velocity profile (see Eq. 2.22) (Ozdemir *et al.*, 2014).

2. Transition from regime II to regime III: Finite-amplitude disturbances grow nonlinearly and the unsteady fluctuations are sustained from one cycle to the next. This transition depends strongly on the amplitude of the initial disturbances (Ozdemir *et al.*, 2014).

3. Transition from regime III to regime IV: The unsteady finite-amplitude velocity fluctuations grow exponentially during the acceleration phase of the cycle.

4. Transition from regime IV to V: Owing to strong nonlinear disturbances in regime IV, linear instability analysis is not applicable.

While providing insightful information on the evolution of infinitesimally small flow disturbances, linear instability analysis has not been successful in predicting the onset of turbulence in reciprocating wall-bounded flows (Ozdemir *et al.*, 2014). Therefore, other approaches are necessary to better understand the dynamics of the base flow that underlies the exponential growth of the finite-amplitude velocity fluctuations and triggers transition from a self-sustaining transitional flow (III) to a intermittently turbulent flow (IV). One such interesting approach is that by Studer *et al.* (2006). Following Obremski and Fejer (1967), Studer *et al.* (2006) assumed two different transition mechanisms in a reciprocating boundary layer: transition due to instabilities and transition due to a laminar-turbulent interface. In the former, the transition mechanisms are the same as for a steady flow, such as Tollmien-Schlichting waves and bypass transition mechanisms. In the latter, turbulent fronts emerge from upstream transitions (Studer *et al.*, 2006). The metric used to determine the type and spatial position of the transition is the amplitude and skewness of the wavelet transfer function of the temporal velocity signal. One limitation of the method is, however, that although a transition is detected, the underlying mechanism of transition is presumed to be either transition due to instabilities or transition due to a laminar-turbulent interface. Furthermore, the method is local (i.e., restricted to the probe location) and requires a very long sampling length ($>$1000 periods).

In the present study, the balance of the leading order terms in the phase-averaged mean momentum equation are used to define the onset of turbulence in type IV flows. The results confirm that fully-developed turbulence first emerges at the early phases in the decelerating portion of the cycle. By comparing the leading-order terms in the momentum balance as a function of wall-normal position between regime III and regime IV flows, the underlying mechanism of the laminar to turbulent transition is the emergence of an internal layer that first develops during the late phases of the accelerating portion of the cycle. In the absence of this internal layer, the flow remains transitional over the entire cycle.

5.2 Direct Numerical Simulations

The data used in the analysis is the DNS of reciprocating channel described in previous chapters. The study of Di Liberto and Ciofalo (2011) was used to identify two Stokes Reynolds numbers: $Re_s = 648$ and 1019 (corresponding to periods $T = 30\frac{h}{U_m}$ and $T = 40\frac{h}{U_m}$ with Womersley numbers of 20.47 and 17.72, respectively, where h is the channel half-height and U_m is the amplitude of the centerline velocity modulation.). The former Re_s is at the edge of the interface between a disturbed laminar flow (type III) and an intermittently turbulent flow (type IV), whereas the latter Re_s is well within the intermittently turbulent regime (type IV) and exhibits fully turbulent behaviors over a portion of the cycle.

Since $Re_{s,III \to IV}$ is approximate (i.e., ≈ 750), classification of flow regime types simply based on Re_s is inexact. As described previously, type IV flows exhibit fully-developed turbulent behaviors during a portion of the cycle. These turbulent behaviors are most often evaluated by the absence/existence of logarithmic behavior of the mean velocity profile, and how closely the y-intercept and slope of the logarithmic velocity corresponds to those observed in equilibrium wall-bounded flows (Akhavan *et al.*, 1991a).

In equilibrium wall-bounded flow, a logarithmic (i.e., overlap) velocity profile is a dimensional necessity when the inner ($\delta_\nu = \nu/u_\tau$) and outer (h) length scales are sufficiently separated, i.e., when h^+ is sufficiently large (Smits *et al.*, 2011). In reciprocating flow, Akhavan *et al.* (1991a) introduced a third length scale, termed the unsteady length-scale $\delta_t = u_\tau/\omega$, where ω is the angular frequency of the oscillating pressure gradient. These authors argued that logarithmic behavior is a dimensional necessity whenever at least two of the three length scales are widely separated, and proposed four possible scenarios for logarithmic behavior:

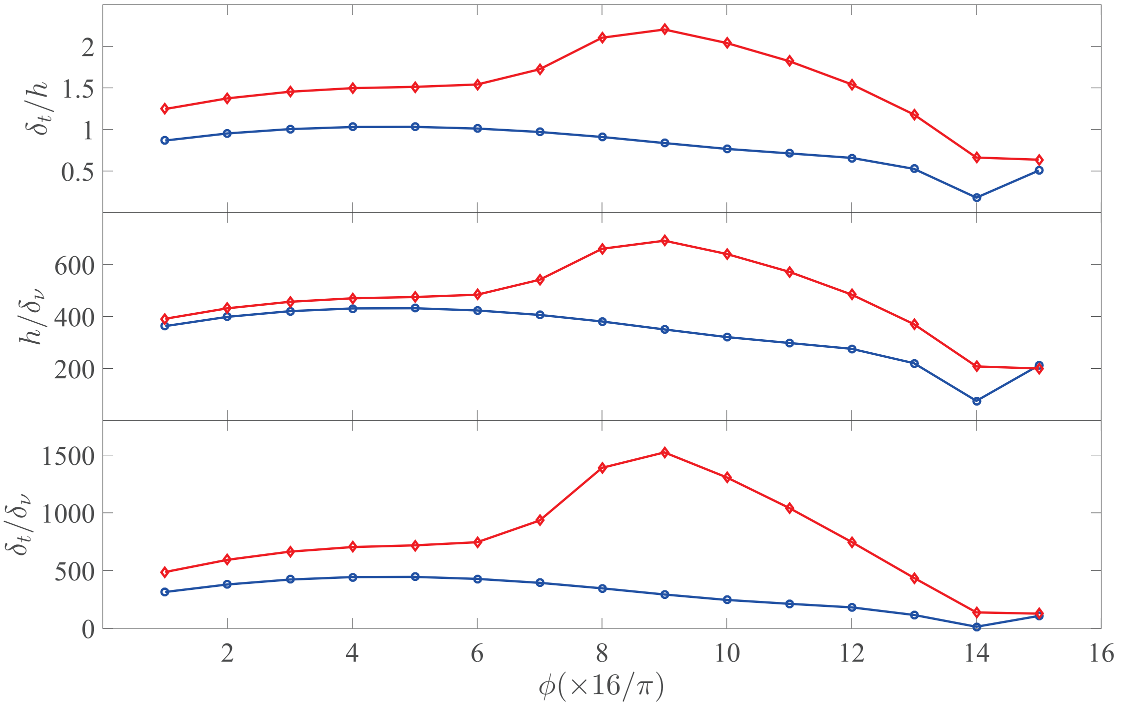

Figure 5.1: The ratio of the unsteady to the outer (top), the outer to the viscous (middle), and the unsteady to the viscous (bottom) length scales for $Re_s = 648$ (blue circles) and $Re_s = 1019$ (red diamonds) as a function of phase.

1. ***Case 1:*** $\delta_t \gg h \gg \delta_\nu$: The universal law of the law applies, $U^+ = \frac{1}{\kappa} log(y^+) + B$, where κ is the von-Karman coefficient ($\simeq 0.4$) and B ($\simeq 5$) is the y-intercept at $y^+ = 1$;
2. ***Case 2:*** $\delta_t \sim h \gg \delta_\nu$: A modified logarithmic law applies, $U^+ = \frac{1}{\kappa} log(y^+) + B_1(\frac{u_\tau}{h\omega})$, where the y-intercept $B_1 \neq B$.
3. ***Case 3:*** $h \gg \delta_t \gg \delta_\nu$: No logarithmic behavior is expected;
4. ***Case 4:*** $h \gg \delta_t \sim \delta_\nu$: A modified logarithmic law applies, i.e., $U^+ = \frac{1}{\kappa} log(y^+) + B_2(\frac{u_\tau^2}{\nu\omega})$, where the y-intercept $B_2 \neq B_1 \neq B$

The unsteady and viscous length scales in the current DNS are plotted and compared to the channel half-height in Fig. 5.1. The scale separation for $Re_s = 648$ and 1019 are similar for the most part of the cycle, and classifies the current simulation under ***Case 2***. However, different magnitude ordering of the length scales for $Re_s = 648$ and 1019 are observed at $\frac{8\pi}{16} \leq \phi \leq \frac{12\pi}{16}$. While the scale separation between δ_t and δ_ν remains two orders of magnitude throughout the cycle for $Re_s = 648$, it increases to three orders of magnitude for $Re_s = 1019$.

5.3 The Mean Momentum Equation Based Framework

The balance of the leading order terms in the mean momentum equation are explored for reciprocating channel flow using a mean momentum balance framework (Fife *et al.*, 2005). While the framework has proven valuable to better understand logarithmic scaling of the mean velocity distribution in canonical wall bounded flows, it has not been applied to non-equilibrium wall bounded flow as will be done here. A brief review of the framework of the analysis is provided here first for steady-state fully-developed channel flow and second for reciprocating channel flow. For more detailed descriptions of the framework, the reader is referred to Fife *et al.* (2005), Wei *et al.* (2005a), Klewicki *et al.* (2009), Klewicki *et al.* (2011) and Klewicki (2013).

5.3.1 Steady-State Channel Flow

For a steady-state, fully-developed, turbulent channel flow of channel half-height h the mean momentum equation is given by

$$0 = \underbrace{\frac{1}{h^+}}_{\mathrm{A}} + \underbrace{\frac{dU^+}{dy^{+2}}}_{\mathrm{B}} - \underbrace{\frac{d\overline{u'v'}^+}{dy^+}}_{\mathrm{C}}., \tag{5.1}$$

where term A is the mean pressure gradient, term B is the mean viscous force, and term C, the wall-normal gradient of the Reynolds shear stress, is the mean effect of turbulent inertia. Term C becomes non-zero shortly after the onset of the transition to turbulence. At $h^+ = 180$, the terms in Eq. 5.1 begin to nominally satisfy the four layer magnitude ordering of terms first revealed by Wei *et al.* (2005a) that is characteristic of the flow for all higher Re (Elsnab *et al.*, 2011). The

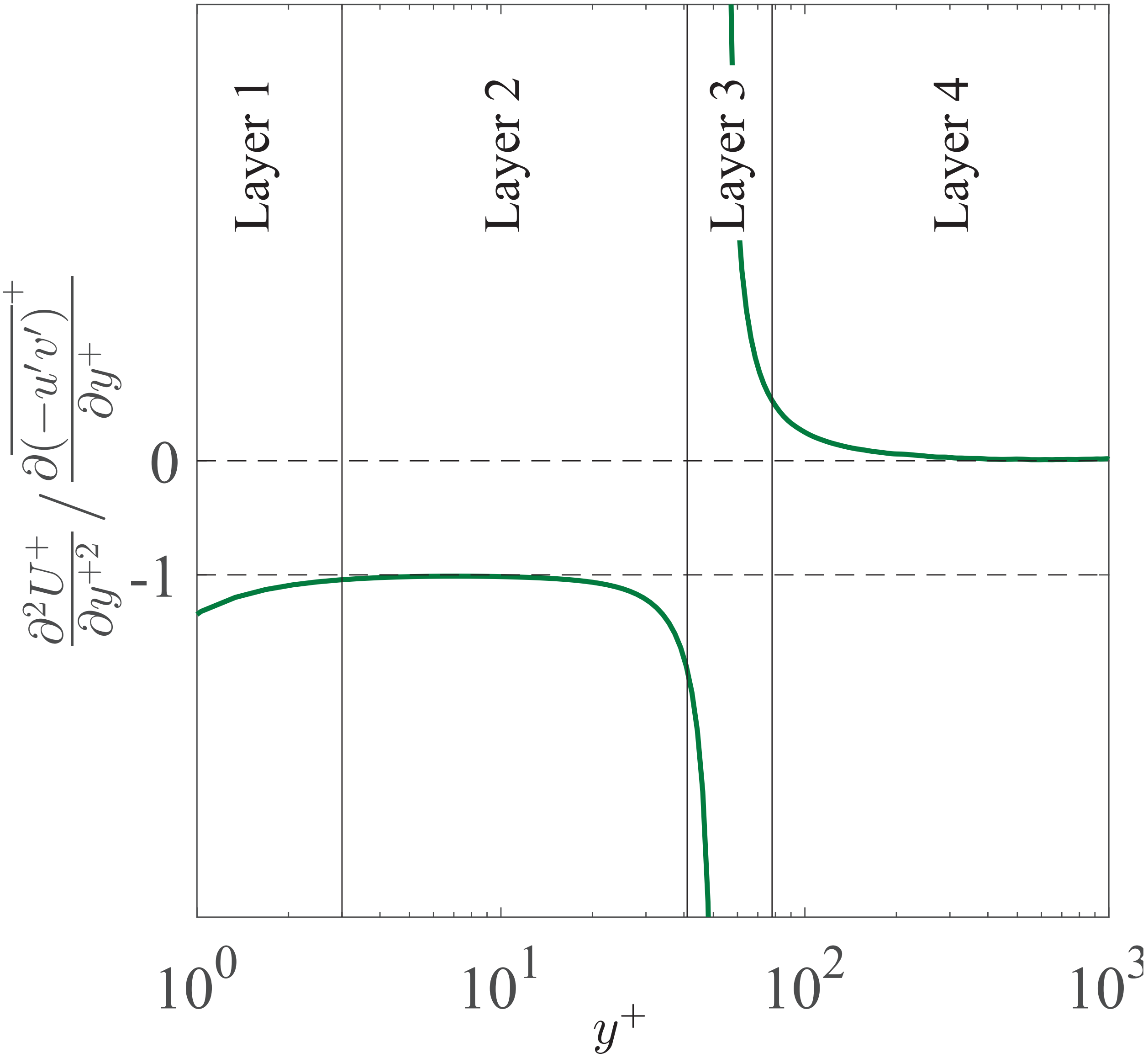

Figure 5.2: Representative profile of the ratio of the viscous force to the turbulent inertia in a steady-state fully developed channel flow. Data obtained from the Johns Hopkins turbulence data base (JHTDB) (Li *et al.*, 2008; Perlman *et al.*, 2007). The boundaries are defined using the thresholds introduced by Wei *et al.* (2005a).

four layer structure is revealed through the ratio B/C as shown in Fig. 5.2 produced from DNS channel flow data acquired from the Johns Hopkins turbulence data base (JHTDB) (Li *et al.*, 2008; Perlman *et al.*, 2007). Within three sub-regions, Eq. 5.1 is brought into balance owing to two large

Table 5.1: Magnitude ordering and scaling behaviors associated with the four layer structure of the leading order balance of mean forces in a steady turbulent channel flow of a Newtonian fluid. Note that A, B and C refer to the mean pressure gradient, mean viscous force and turbulent inertia terms that, from left to right, are given in Eq. 5.1.

Physical Layer	Magnitude Ordering	Δy Increment	ΔU Increment
1	$\lvert\mathrm{A}\rvert \simeq \lvert\mathrm{B}\rvert \gg \lvert\mathrm{C}\rvert$	$O(\nu/u_\tau)$ (≤ 3)	$O(u_\tau)$ (≤ 3)
2	$\lvert\mathrm{B}\rvert \simeq \lvert\mathrm{C}\rvert \gg \lvert\mathrm{A}\rvert$	$O(\sqrt{\nu h/u_\tau})$ $(\simeq 1.6)$	$O(U_c)$ $(\simeq 0.5)$
3	$\lvert\mathrm{A}\rvert \simeq \lvert\mathrm{B}\rvert \simeq \lvert\mathrm{C}\rvert$	$O(\sqrt{\nu h/u_\tau})$ $(\simeq 1.0)$	$O(u_\tau)$ $(\simeq 1)$
4	$\lvert\mathrm{A}\rvert \simeq \lvert\mathrm{C}\rvert \gg \lvert\mathrm{B}\rvert$	$O(h)$ $(\rightarrow 1)$	$O(U_c)$ $(\rightarrow 0.5)$

terms and one small term (layers 1, 2 and 4), while in another sub-region (layer 3) all three terms continue to contribute significantly to the balance. Thus, while all of the terms in Eq. 5.1 are of leading order over some portion of $0 \leq y^+ \leq h^+$, in three of the four layers there emerges only two dominant terms.

Table 5.1 describes the Reynolds number dependent scaling properties of the layer widths and their velocity increments (Wei *et al.*, 2005a; Klewicki *et al.*, 2011). Across layer 3 there is a *balance breaking and exchange* of mean forces. At the outer edge of layer 3 the mean viscous force loses dominant order in Eq. 5.1. Note that two of the layers scale with an intermediate length that is proportional to the geometric mean of the inner and outer length scales. Note further that the point where the turbulent inertia term crosses zero (in the middle part of layer 3) coincides with where $-\langle u'v'\rangle$ attains its maximum value. In Newtonian channel flow, this position is located at $y^+ \simeq 1.9\sqrt{h^+}$ (Afzal, 1982; Sreenivasan and Sahay, 1997; Wei *et al.*, 2005a).

5.3.2 Reciprocating Channel Flow

The Reynolds averaged x-momentum equation for a reciprocating channel flow (RCF) is

$$\underbrace{-\frac{\partial U^+}{\partial t^+} + \frac{dP^+}{dx^+}}_{\mathrm{A}*} + \underbrace{\frac{\partial^2 U^+}{\partial y^{+2}}}_{\mathrm{B}*} + \underbrace{\frac{\partial(-\overline{u'v'}^+)}{\partial y^+}}_{\mathrm{C}*} = 0, \tag{5.2}$$

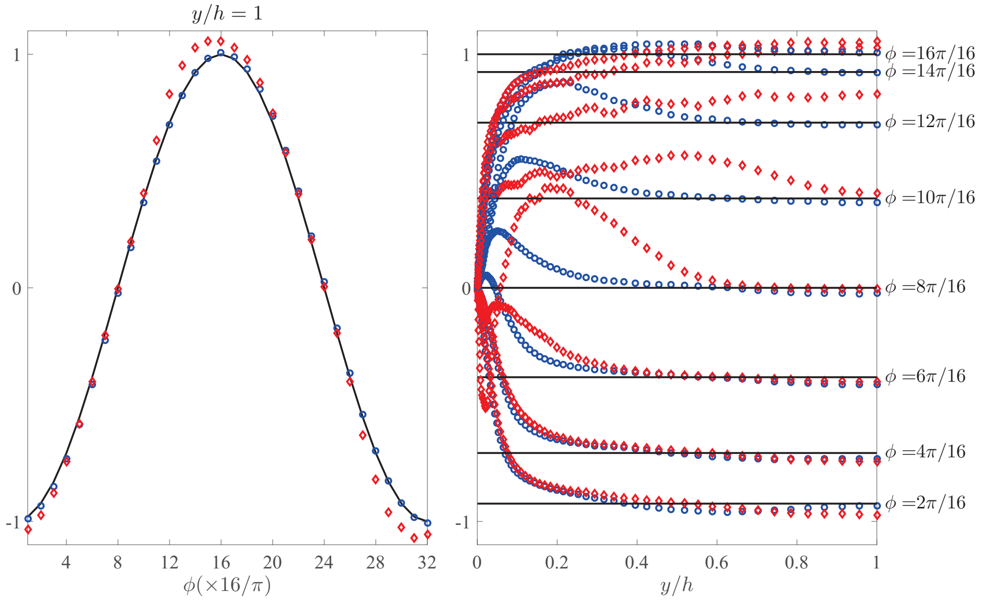

Figure 5.3: Left: The local acceleration at the channel centerline ($-\frac{\partial U}{\partial t}|_{CL}$) compared to the imposed pressure gradient ($\frac{1}{\rho}\frac{dP}{dx}$). Right: wall-normal profiles of the local acceleration and the imposed pressure gradient for select phases. Blue circles and red diamonds are, respectively, the local accelerations for $Re_s = 648$ and $Re_s = 1019$, and black solid line represent the pressure gradient.

Relative to steady-state turbulent channel flow, the structure associated with the magnitude ordering of terms in 5.2 has not previously been explored. The starting point of the analysis is to determine the relative magnitude of terms in Eq. 5.2 over $0 \leq y^+ \leq h^+$. From left-to-right, the first term is the unsteady term (called here the local acceleration), the second term is the cosinusoidal pressure gradient (known and constant across the channel half-height at any given phase), the third term is the mean viscous force, and the last term is the net mean effect of turbulent inertia.

Equation 5.2 is effectively the time-averaged statement of Newton's second law for a differential fluid element, and as such must be locally satisfied over $0 \leq y^+ \leq h^+$. For the steady-state channel flow, the ratio B/C best exposes how the balance is realized. For reciprocating channel flow, a single ratio to expose the balance is insufficient owing to the four non-zero terms in Eq. 5.2. Since the unsteady-term and the pressure gradient are in phase at the majority of the phases and in balance near the channel centerline, they are combined and labeled term A^* (Fig. 5.3). It follows that, similar to canonical wall bounded flow, the ratio $\mathrm{B}^*/\mathrm{C}^*$ can be used in reciprocating channel flow to reveal the structure associated with the magnitude ordering of terms in 5.2. A fundamental question regarding the transition from laminar to turbulent flow in reciprocating channel flow pertains as to how the magnitude ordering of terms vary with both Re_s and phase, ϕ, and when, if ever, is the four-layer structure (Figs. 5.4 $\&$ 5.7) revealed.

The ratio $\mathrm{B}^*/\mathrm{C}^*$ in Eq. 5.2 for $Re_s = 648$ as a function of wall-normal position is shown in Fig. 5.4. It is observed that a four-layer structure, similar to that described by Wei *et al.* (2005a) for canonical wall-bounded flows, does not emerge in any of the phases. The lack of fully-developed turbulent behavior for $Re_s = 648$ is further supported by the phase-averaged velocity and Reynolds shear stress profiles shown in Figs. 5.5 and 5.6, respectively, which are very different compared to the profiles in fully-developed steady-state channel flow. A four-layer structure in the profiles of $\mathrm{B}^*/\mathrm{C}^*$ for $Re_s = 1019$, similar to that observed in canonical wall bounded flow, is observed from $\frac{9\pi}{16} \leq \phi \leq \frac{11\pi}{16}$ as shown in Fig. 5.7. The difference between the four-layer structure in RCF and steady-state channel is mainly in layer 1. Unlike steady-state, in which the ratio B/C is less than -1 in layer 1, the ratio $\mathrm{B}^*/\mathrm{C}^*$ in RCF is greater than -1. The viscous force in a steady channel flow, in layer 1, is balanced by the pressure gradient. In RCF, however, it is balanced by the sum of the pressure gradient and the local acceleration. Unlike the channel centerline, the pressure gradient and the local acceleration are not in balance near the wall ($y/h \lesssim 0.2$), and combining the two terms is not justified (Fig. 5.3). Therefore, the ratio of the viscous force to the turbulent inertia in RCF is different than the steady channel flow. In spite of the slight difference in the balance of the contributing terms in layer 1, it is concluded that fully-developed turbulent flow behaviors are observed for $Re_s = 1019$ during the early phases of the decelerating portion of the cycle. This conclusion is further supported by the phase-averaged velocity and Reynolds shear stress profiles shown in Figs. 5.8 and 5.9, respectively, which show similar behaviors to the profiles in fully-developed steady-state channel flow from $\frac{9\pi}{16} \leq \phi \leq \frac{11\pi}{16}$.

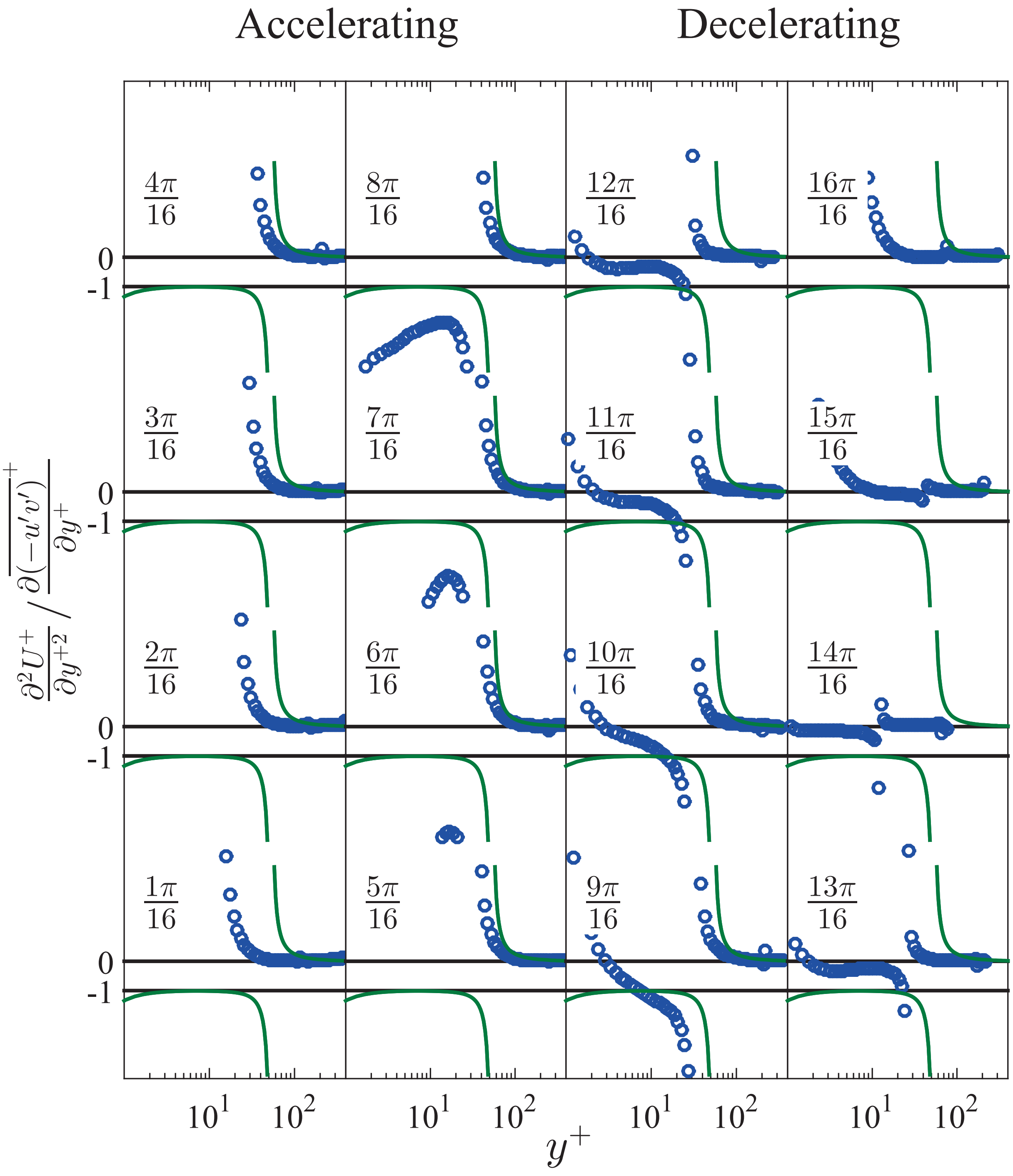

Figure 5.4: The ratio $\mathrm{B}^*/\mathrm{C}^*$ in Eq. 5.2 as a function of wall-normal position for $Re_s = 648$. Green solid lines represent steady-state channel flow obtained from the Johns Hopkins turbulence data base (JHTDB) (Li *et al.*, 2008; Perlman *et al.*, 2007). Blue circles represent the reciprocating channel flow. Horizontal black lines represent -1 and 0. The four layer structure is not observed in any of the phases.

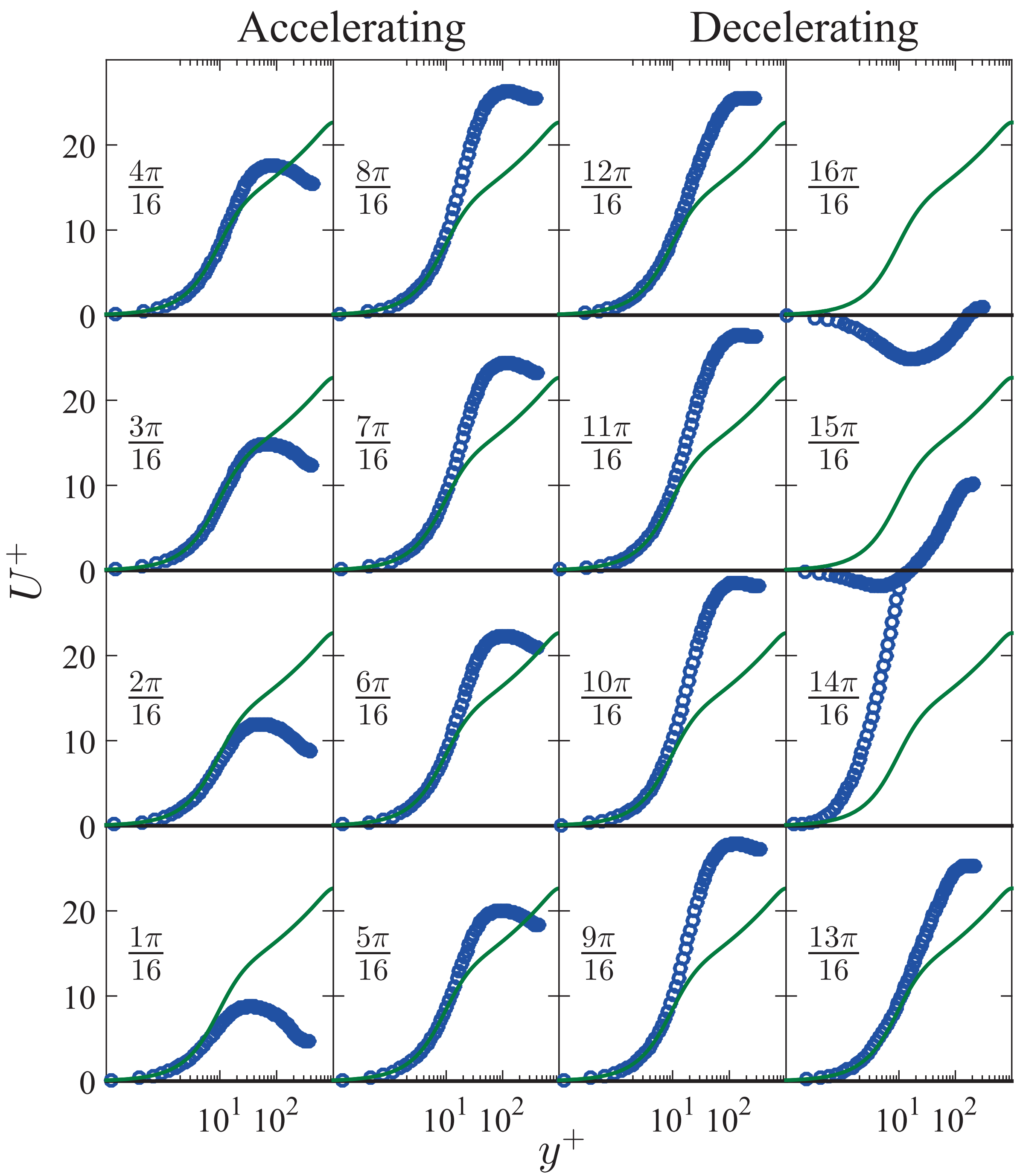

Figure 5.5: Phase-averaged profiles of velocity in wall-units for $Re_s = 648$. Color identifiers are the same as Fig. 5.4.

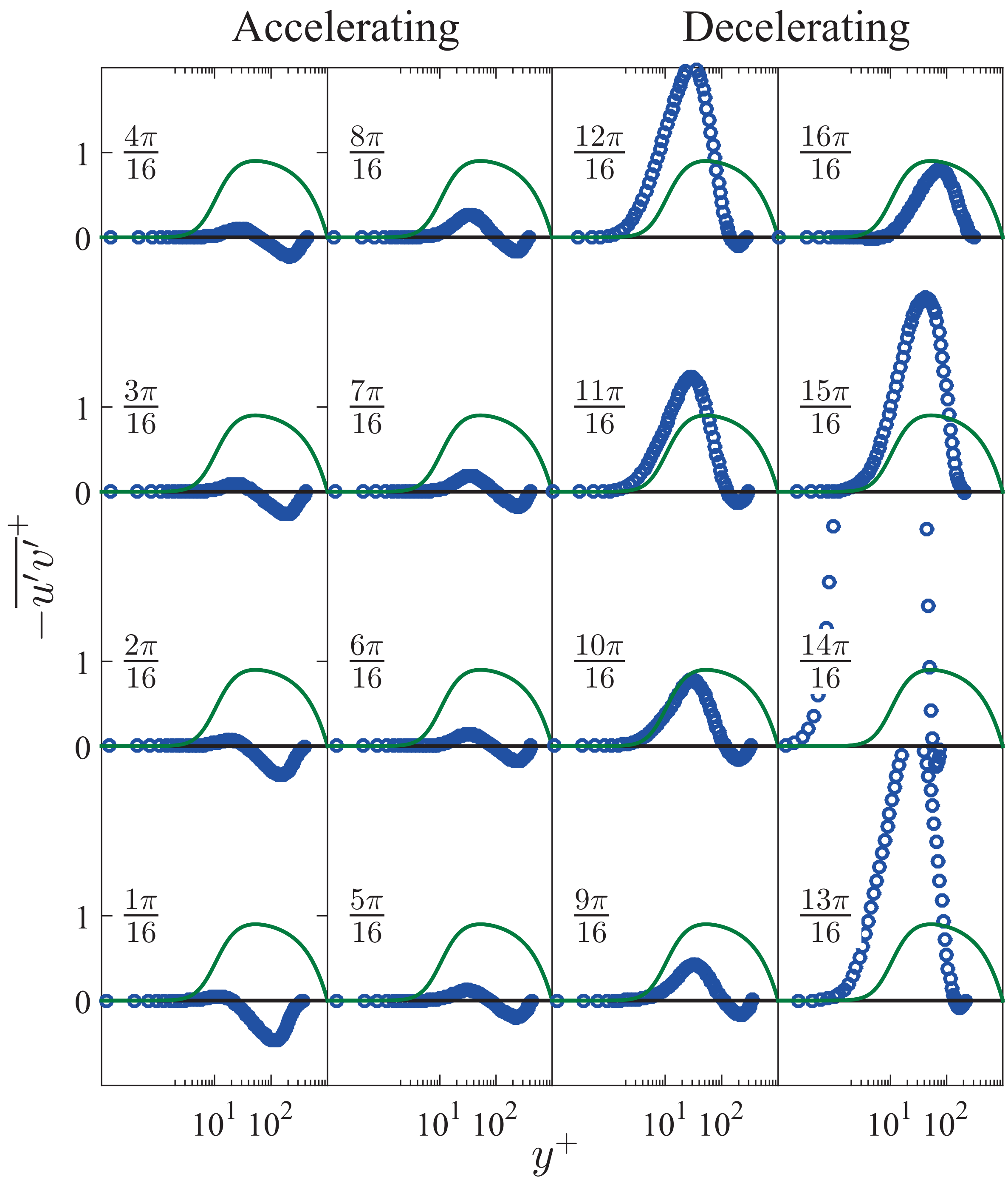

Figure 5.6: Phase-averaged profiles of Reynolds shear stress in wall-units for $Re_s = 648$. Color identifiers are the same as Fig. 5.4.

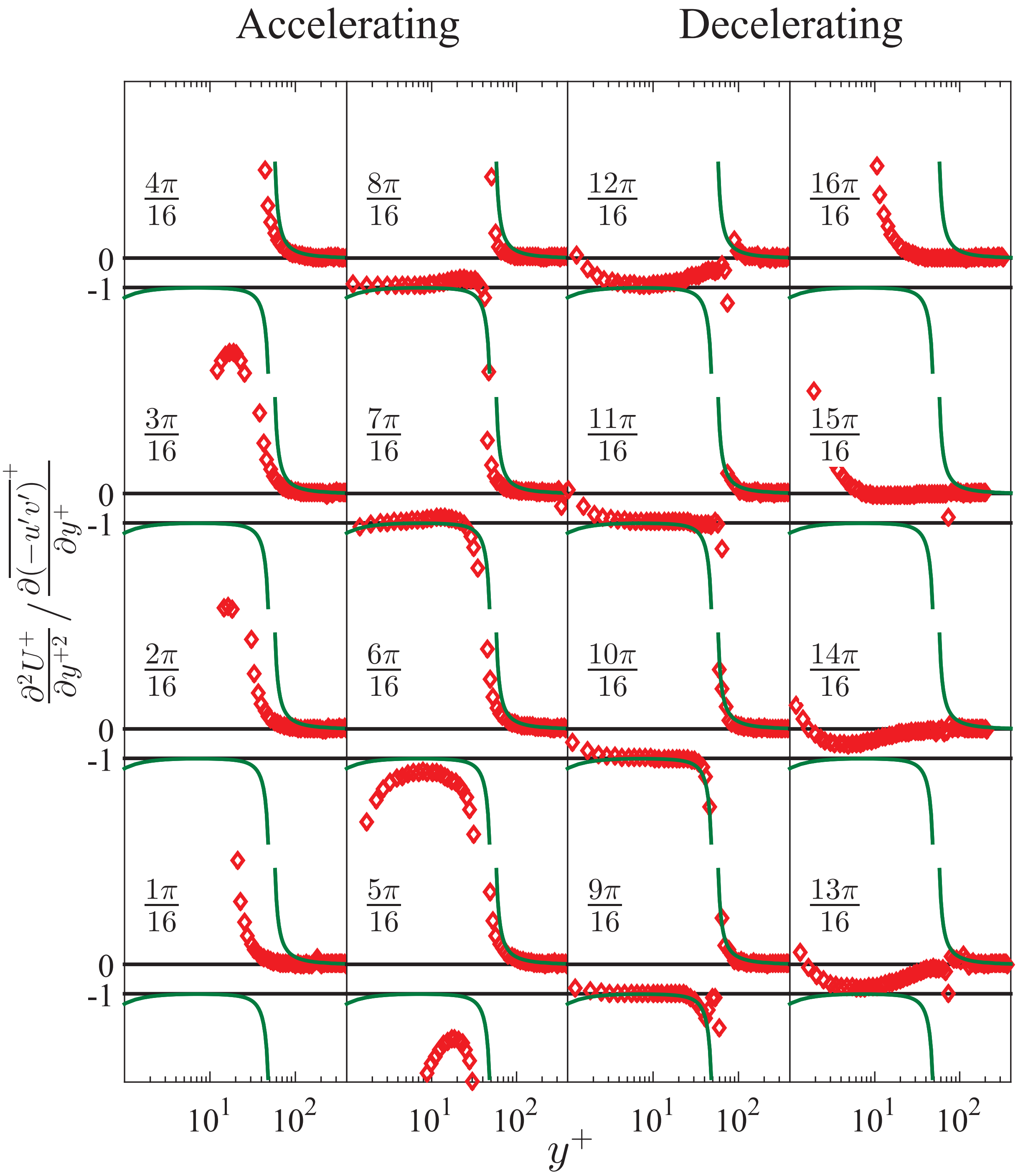

Figure 5.7: The ratio B^*/C^* in Eq. 5.2 as a function of wall-normal position for $Re_s = 1019$. Green solid lines represent steady-state channel flow obtained from the Johns Hopkins turbulence data base (JHTDB) (Li *et al.*, 2008; Perlman *et al.*, 2007). Red diamonds represent the reciprocating channel flow. Horizontal black lines represent -1 and 0. The four layer structure is emerges in phases $\phi = \frac{9\pi}{16}$, $\frac{10\pi}{16}$ and $\frac{11\pi}{16}$.

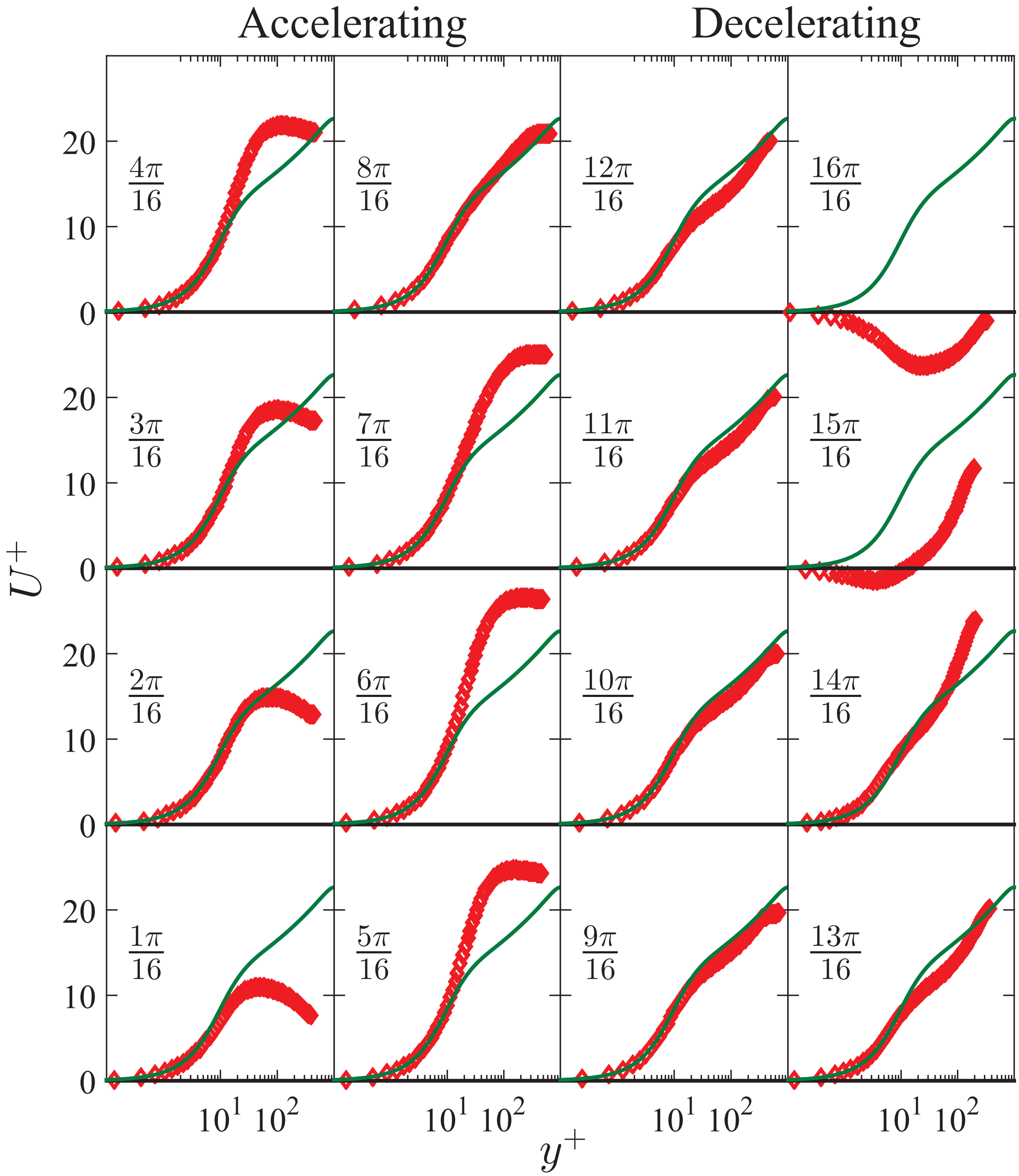

Figure 5.8: Phase-averaged profiles of velocity in wall-units for Res for $Re_s = 1019$. Color identifiers are the same as Fig.5.7.

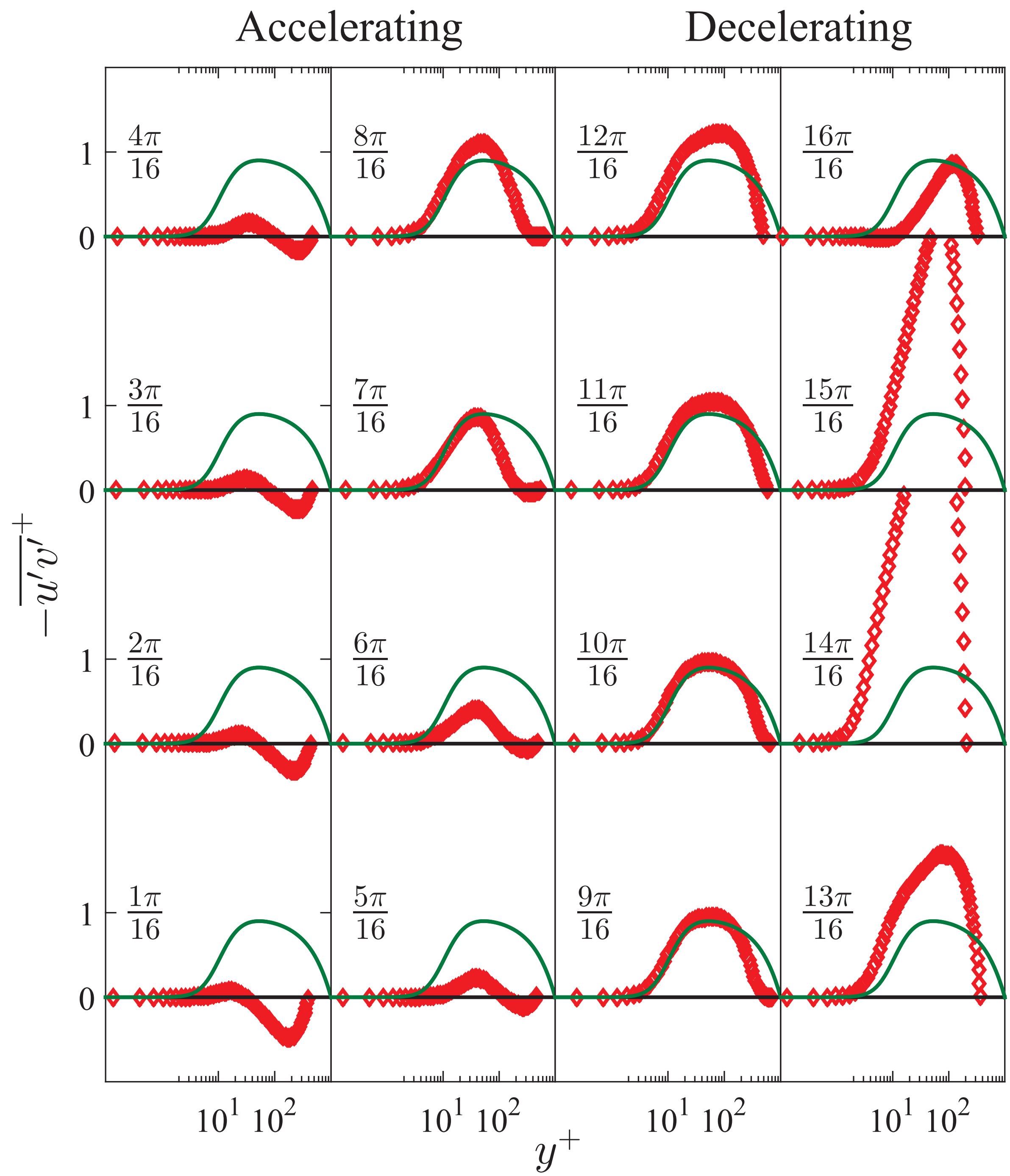

Figure 5.9: Phase-averaged profiles of Reynolds shear stress in wall-units for Res for $Re_s = 1019$. Color identifiers are the same as Fig.5.7.

5.4 Transition Mechanism

The turbulent statistics and analysis presented above clearly demonstrate that $Re_s = 648$ is a type III flow and $Re_s = 1019$ is a type IV flow. To investigate the mechanism of transition to fully-developed turbulence (from type III to IV), the contributing terms in Eq. 5.2 are examined as a function of phase angle. Particular focus is on the late stages of the accelerating portion of the cycle since this is the portion of the cycle just prior to the phases when fully-developed turbulent behaviors are observed for $Re_s = 1019$. In this analysis, the local acceleration and the turbulent inertia (terms A^* and C^* in Eq. 5.2, respectively) are of primary dynamical interest. The former because it captures the time evolution of the flow and the latter because it is a good indicator of the emerging importance of turbulent transport.

Dynamical Contribution of the Turbulent Inertia $\left(-\frac{\partial \overline{u'v'}^+}{\partial y^+}\right)$

The evolution of the turbulent inertia (Reynolds stress gradient) as a function of phase is shown in Figs. 5.10 and 5.11 for $Re_s = 648$ and $Re_s = 1019$, respectively. Note that since the the integrated momentum flux across the channel half-height owed to turbulent inertia is zero, when considered as a force, it is informative to view a positive region of turbulent inertia as a momentum source and a negative region as a momentum sink (Elsnab *et al.*, 2011). In steady-state, fully-developed channel flow (ZPG flow as well) there is a single momentum source and a single momentum sink. The momentum source, of large magnitude, is confined to a narrow region near the wall below the location of peak Reynolds shear stress. While the momentum sink, of low magnitude, extends from above the location of peak Reynolds shear stress to the channel centerline (or edge of the boundary layer in ZPG flow). See Fig. 5.12. Consequently, on average, the action of the turbulent inertia is to transport momentum from the outer layer (i.e., the sink region) to the inner layer (i.e., the source region) of the flow. This exchange of momentum between the outer and inner layer of the flow results in a more uniform distribution of momentum across the channel height compared to laminar flow.

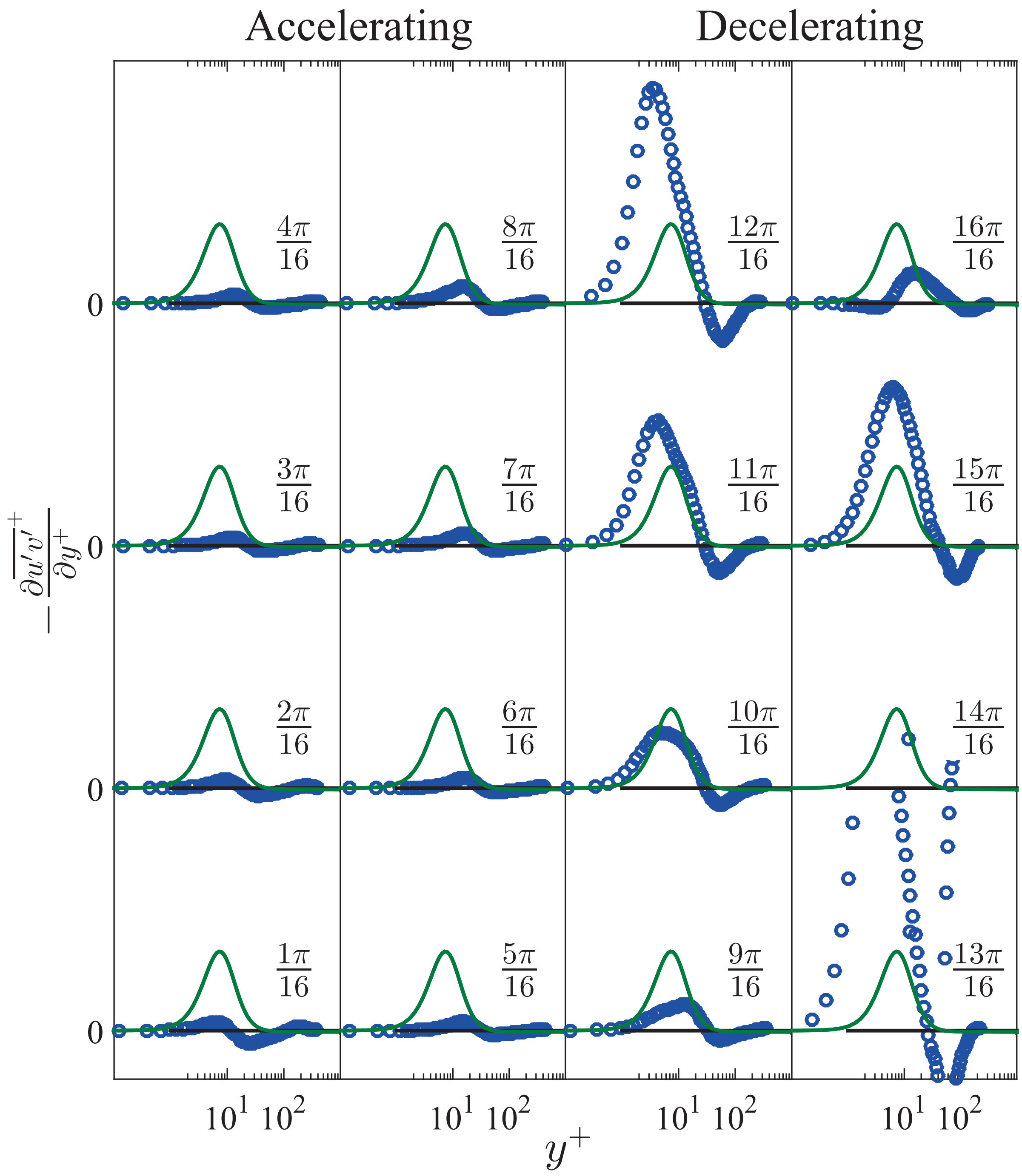

Figure 5.10: Profiles of turbulent inertia ($\frac{\partial \overline{-u'v'}}{\partial y}$) as function of phase for $Re_s = 648$. Color identifiers are the same as Fig.5.4. The turbulent inertia profiles in phases $\frac{13\pi}{16} \leq \phi \leq \frac{15\pi}{16}$ have the same general behavior, but the overshoot at $\phi = \frac{14\pi}{16}$ does not fit within the limits of the figure.

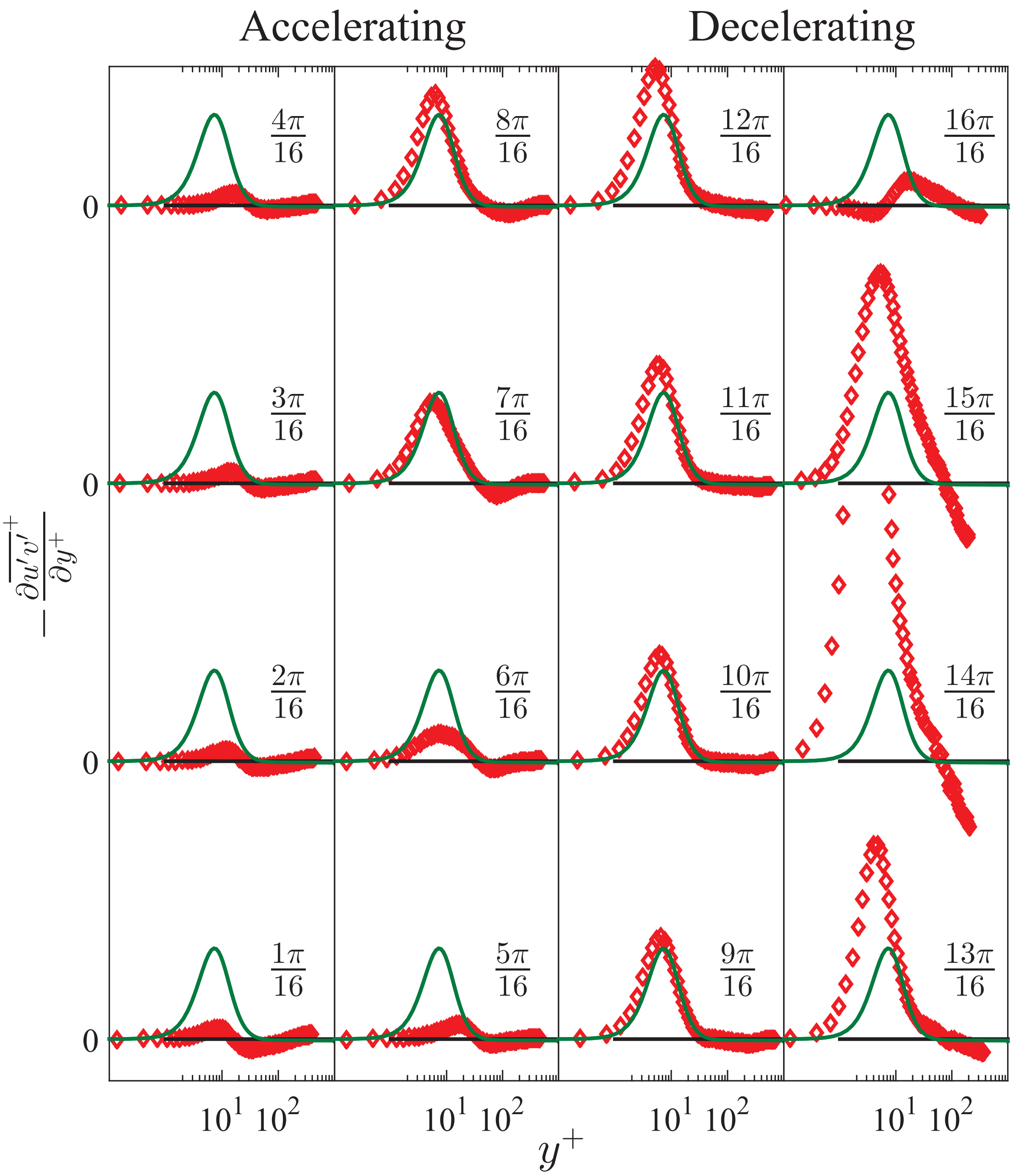

Figure 5.11: Profiles of turbulent inertia ($\frac{\partial \overline{-u'v'}}{\partial y}$) as function of phase for $Re_s = 1019$. Color identifiers are the same as Fig.5.7.

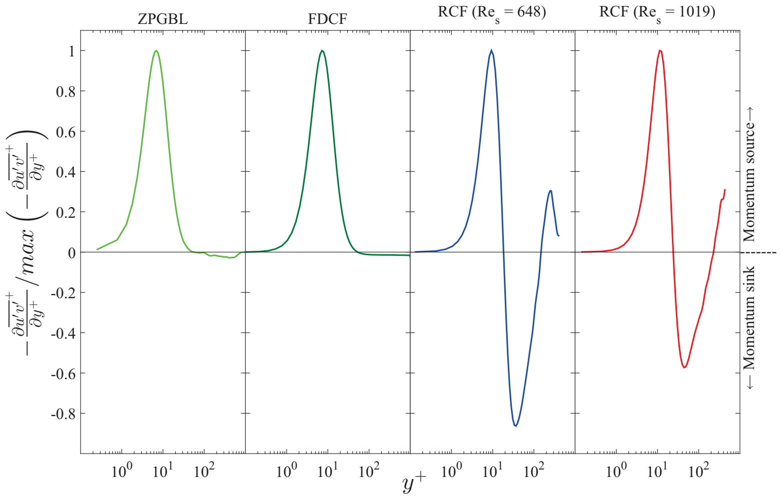

Figure 5.12: From left to right: normalized profiles of turbulent inertia for ZPG boundary layer (Wu and Moin, 2010), fully-developed channel flow (Li *et al.*, 2008; Perlman *et al.*, 2007), reciprocating channel flow ($Re_s = 648$), and reciprocating channel flow ($Re_s = 1019$). The canonical flows (ZPGBL and fully-developed CF) have one positive (momentum source) and one negative (momentum sink) region, while RCF has two positive regions, i.e., two momentum sources.

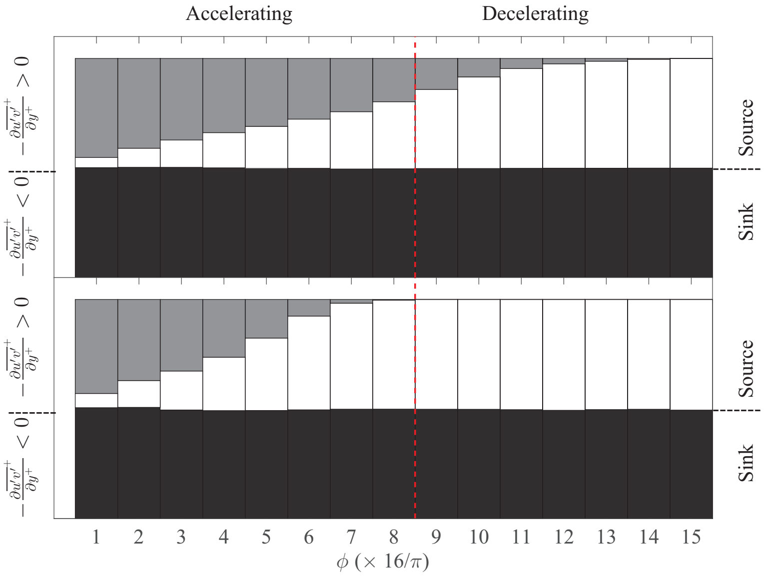

Figure 5.13: Contribution of sink-like and source-like behavior of the turbulent inertia for $Re_s = 648$ (top) and $Re_s = 1019$ (bottom). Black is the contribution of the momentum sink, white is the contribution of the "near-wall" momentum source, and gray is the contribution of the "near-centerline" momentum source. Red dashed line separates the accelerating and decelerating phases of the half-period.

The distribution of turbulent inertia in reciprocating channel flow (RCF), however, shows a second momentum source near the channel centerline (Fig. 5.12), indicating that the flow structure is different compared to its canonical counterpart. Here we term the two source regions as the “wall momentum source" and "centerline momentum source" and the sink region as the “interior momentum sink". Consequently, RCF turbulence redistributes momentum from the interior region of the flow to both the near-wall and centerline regions of the flow. The momentum redistribution mechanism can be explained by the quadrant analysis of probability density function (PDF) of the streamwise and wall-normal velocity fluctuations (u' and v', respectively). In the first quadrant $u' > 0$ and $v' > 0$; in the second quadrant $u' < 0$ and $v' > 0$; in the third quadrant $u' < 0$ and $v' < 0$; and the fourth quadrant $u' > 0$ and $v' < 0$. Events in the first quadrant correspond to the positive streamwise velocity fluctuations lifted away from the wall by the positive wall-normal velocity fluctuations; they are the so-called “outward interactions” (Bernard and Handler, 1990). Events in the second quadrant correspond to the negative streamwise velocity fluctuations lifted away from the wall by the positive wall-normal velocity fluctuations; they are the so-called “ejections” (Adrian, 2007). Events in the third quadrant correspond to the negative streamwise velocity fluctuations being moved toward the wall by the negative wall-normal velocity fluctuations; they are the so-called “inward interactions”. Events in the fourth quadrant correspond to the positive streamwise velocity fluctuations being moved toward the the wall by the negative wall-normal velocity fluctuations; they are the so-called “sweeps”. In ZPG and fully-developed channel flow, the most common events statistically are ejections and sweeps ($u'v' < 0$), which are spatially coincident with the turbulent inertia momentum source and sink, respectively. High momentum fluid in the outer layer is moved toward the wall by “sweeps” and low momentum fluid near the wall is moved away from the wall by “ejections”. In some phases of RCF, however, there are regions where $u'v' > 0$, which correspond to either first or third quadrant events (Figs. 5.6 and 5.9). These regions are spatially coincident with the portion of the interior momentum sink that is higher than local minima in the turbulent inertia profile and the centerline momentum source (Fig. 5.12). The “outward interactions” and “inward interactions” associated with the first and third quadrant events redistribute the momentum between the interior momentum sink and the centerline momentum source. While the analysis provided above is supported by the phase-averaged profiles of the Reynolds shear stress and its wall-normal gradient, the PDF profiles of u' and v' must be studied for definite conclusions. Observed in Figs. 5.10 and 5.11 is that the redistribution of momentum between the two sources varies both as a function of Re_s and ϕ. This redistribution is further quantified in Fig. 5.13, which shows the integrated magnitude of TI between the two source terms normalized by the integrated magnitude of the momentum sink.

For $Re_s = 648$, the centerline momentum source is dominant in the early phases of the accelerating portion of the cycle, decreasing monotonically with increasing phase angle. Nevertheless, it remains finite throughout most of the accelerating portion of the cycle. The centerline momentum source for $Re_s = 1019$ is also dominant in the early phases of the accelerating portion but rapidly decreases with increasing phase angle and approaches zero at approximately $\phi = \pi$, and is negligible during the decelerating portion of the cycle. In effect, the action of the TI in the decelerating portion of the cycle for $Re_s = 1019$ is similar to its canonical counterpart. Hence, one indicator of a transition from type III to type IV flows in RCF is that the contribution of the centerline momentum source is zero in the decelerating portion of the cycle. This will be termed:

Condition I: the contribution of the “near-centerline” momentum source is negligible compared to the “near-wall” momentum source.

Dynamical Contribution of The Local Acceleration $\left(-\frac{\partial U}{\partial t}\right)$

The evolution of the local acceleration as a function of phase is shown in Fig. 5.14. Profiles of local acceleration in a laminar reciprocating channel flow are included for comparison purposes. All four profiles are qualitatively similar in the first and last quarters of the half-period (left and right columns in Fig. 5.14). For $Re_s = 648$, $-\frac{\partial U}{\partial t}$ remains similar to the laminar flow solution throughout the cycle. For $Re_s = 1019$, however, the local acceleration departs considerably from the laminar flow in the late accelerating phases of the cycle, i.e., $\frac{6\pi}{16} \leq \phi \leq \frac{8\pi}{16}$. Inspection of the phases at this stage reveals the emergence of an internal layer that decelerates at a phase-lead

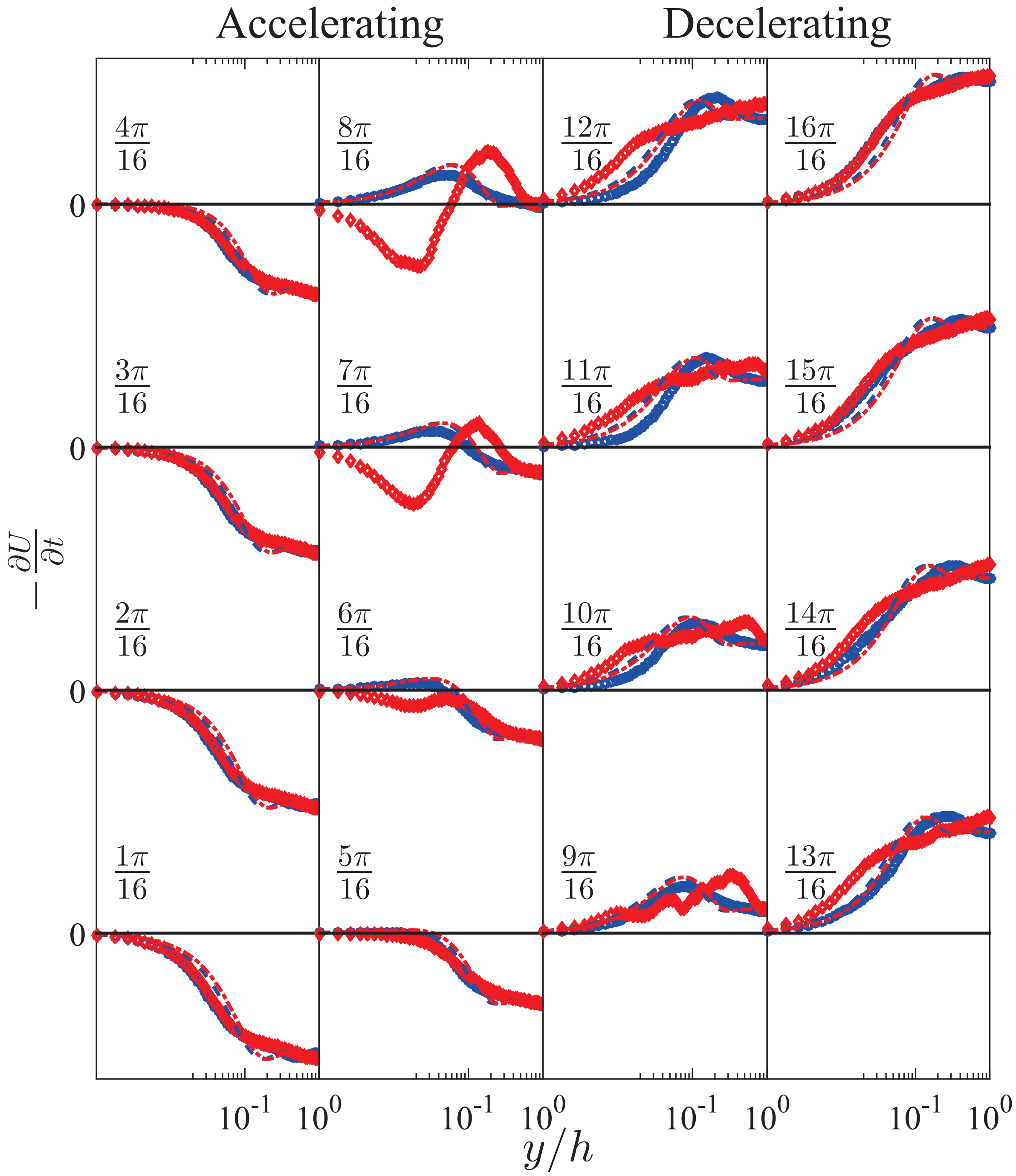

Figure 5.14: Profiles of local acceleration $\left(-\frac{\partial U}{\partial t}\right)$. Blue circles and red diamonds represent $Re_s = 648$ and $Re_s = 1019$, respectively. Blue dashed lines and red dash-dot lines correspond to the laminar flow with the same oscillation periods.

compared to the near-wall and the core regions. Importantly, this internal layer spatially coincides with the strong sink-like behavior of the turbulent inertia (TI) as observed in Fig 5.11 and occurs at the same phase when the TI rapidly increases in magnitude. For $Re_s = 648$, an internal layer does not emerge and the flow does not exhibit fully-developed turbulent like behaviors during any part of the cycle.

The role of an internal shear layer in the transition mechanism to turbulence in fully-developed channel flow has been postulated by Sandham and Kleiser (1992). In particular, an internal shear layer can be generated by a Λ-shaped vortex. The mechanism of the formation of the shear layer is vortex stretching and convection (Stuart, 1965). The high-shear layer then rolls-up into new vortices, which move towards the channel center and hence, spread the turbulence across the channel. The growth mechanism of the newly formed vortices in fully-developed channel is a shear-layer instability, with energy being extracted from the local mean into the vortex (Sandham and Kleiser, 1992). Spatial coincidence of the observed internal layer in $Re_s = 1019$ with the strong sink-like behavior of the TI suggests a similar shear-layer instability in reciprocating channel. It is conjectured that the internal layer either emerges or causes a shear layer instability that rolls-up triggering further flow instabilities that transitions the flow to a fully-developed turbulent flow in subsequent phases. Hence, a second indicator of a transition from type III to type IV flows in RCF is that the emergence of an internal layer during the late phases of the accelerating portion of the cycle. This will be termed:

Condition II: The emergence of an internal (shear) layer between the wall region and the centerline during the accelerating portion of the cycle.

5.5 Summary

The mean flow dynamics in reciprocating channel flow were studied to better understand the underlying mechanism of transition to turbulence in reciprocating channel flow. The balance of the leading order terms in the phase-averaged mean momentum equation confirms that fully-developed turbulence first emerges at the early phases in the decelerating portion of the cycle. The underlying mechanism of this transition is the emergence of an internal layer that first develops during the late phases of the accelerating portion of the cycle. In the absence of this internal layer, the flow remains transitional over the entire cycle. The internal layer is found to be spatially coincident with a strong momentum sink/source-like behavior of the turbulent inertia. It is conjectured that the internal layer emerges or causes a shear layer instability that rolls-up triggering further flow instabilities that transition the flow to a fully-developed turbulent channel in subsequent phases.

CHAPTER 6

EXPERIMENTAL DETAILS AND VALIDATION OF FLOW FACILITY

The current chapter is divided into two parts. The first part describes the experimental details, including descriptions of the particle image velocimetry (PIV) technique, the experimental procedure employed, and measurement uncertainty analysis. In the second part, validation results for zero pressure gradient (ZPG) boundary layer flow are presented and compared to the DNS data of ZPGBL flow simulated by Wu and Moin (2010).

6.1 Particle Image Velocimetry (PIV)

PIV was chosen as the primary experimental measurement diagnostic because it is one of the few non-intrusive whole-field flow measurement techniques. It is non-intrusive in a sense that no measurement probe is placed within the flow, and whole-field in a sense that it provides a two-dimensional (or three-dimensional) instantaneous measurement of the velocity field in a planar slice of the flow. The principles of PIV are simple but, in practice, data acquisition can be very challenging. A brief description of the PIV technique is provided here, the reader is referred to Adrian and Westerweel (2011) or Raffel *et al.* (2013) for detailed descriptions.

PIV is a particle-based measurement technique in which the fluid velocity is inferred from measurement of the velocity of tracer particles seeded into the flow. If the inertia of a tracer particle is small and the particle density matches the fluid density, the particle will passively follow the fluid motions. This is the ideal case, but in practice the particle will have finite inertia and a finite density difference relative to the density of the fluid. The influence of these two effects can be quantified by the particle Stokes number St_p and Froude number Fr , respectively. The former is defined as the ratio of the particle time scale $\tau_p = \frac{\rho_p d_p^2}{18\mu}$ to the flow time scale $\tau_f = (\nu/\varepsilon)^{0.5}$, and the latter is defined as the ratio of the particle settling velocity $u_p = \frac{(\rho_p - \rho) d_p^2 g}{18\mu}$ to the flow velocity $u_f = (\nu\varepsilon)^{0.25}$, where ρ_p is particle density, d_p is particle diameter, μ is the fluid dynamic viscosity, ν is the fluid kinematic viscosity, and ε is the turbulent dissipation rate per unit mass. The ideal case is when $St_p \ll 1$ and $Fr \ll 1$. In a boundary layer flow, the characteristic flow time scale and velocity scale vary as a function of wall-normal distance from the wall. Consequently, both St_p and Fr will vary as a function of wall-normal distance from the wall. Oil droplets with nominal diameter $d_p = 1\mu m$ and density $\rho_p \simeq 2.9\rho_{air}$ are used as tracer particles in the present experiments. The St_p and Fr numbers of the oil droplets are well below unity across the measurement field of view (FOV) that extends across the boundary layer thickness. The range of St_p is $3\times10^{-8} \leq St_p \leq 2\times10^{-6}$, where the lower limit corresponds to the near-wall of the lowest velocity ($2m/s$) and the upper limit corresponds to the freestream of the the highest velocity ($5m/s$). The range of Fr is $1\times10^{-6} \leq Fr \leq 7\times10^{-6}$, where the lower limit corresponds to the freestream of the highest velocity ($5m/s$) and the upper limit corresponds to the near-wall of the lowest velocity ($2m/s$).

The PIV technique uses laser light sheets formed (typically) from a pulsed laser to illuminate the tracer particles in a planar slice of the flow. The light sheets overlap in space but are separated in time, where the time separation δt is known and well-controlled. The laser light scattered by the particles is captured on two separate camera frames: the first frame captures particle images from the first of two successive laser pulses, while the second frame captures particle images from the second pulse. Cross-correlation techniques applied to the image pair provide two components of the velocity vector field in the imaged plane.

A schematic of the present experimental setup is shown in Fig. 6.1. Light is provided by a Photonics DM-series dual cavity Nd:YLF laser capable of $2 \times 30m$J per pulse. A periscope and a $90°$ turning mirror is used to direct the laser light into the tunnel test section. Sheet forming optics (cylindrical + spherical lenses) placed upstream of the turning mirror are used to form a laser sheet on the order $1mm$ thick in the streamwise/wall-normal plane (i.e., xy-plane in the chosen experimental coordinate system). The offset of the laser sheet from the tunnel centerline and

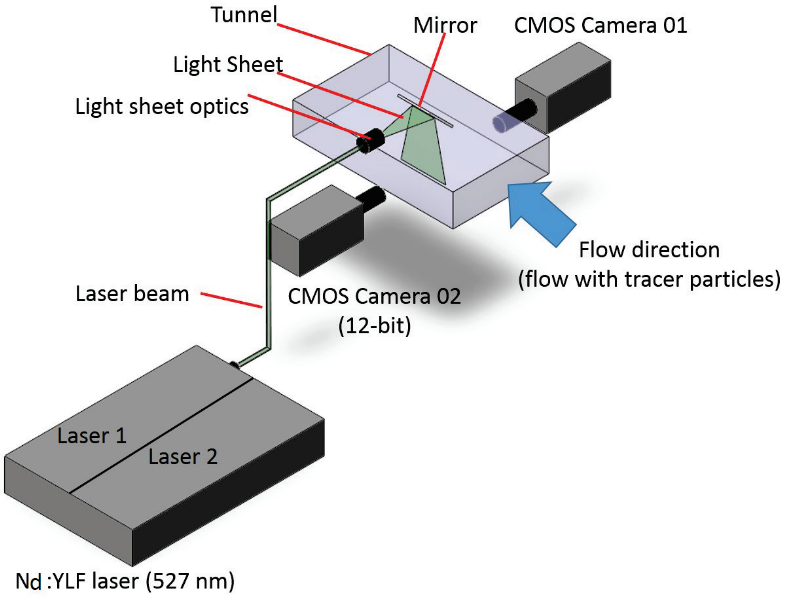

Figure 6.1: Schematic of the PIV setup.

towards camera 02 is $d = 1/15D$, where D is the tunnel width. Images of the laser light scattered off the tracer particles 90° to the incident laser sheets are acquired using two Photron FASTCAM SA4 CMOS cameras with 16GB RAM memory. The CCD array of the camera is 1024×1024 pixel^2 and provides 12-bit intensity level per pixel. Triggering and synchronization of the lasers and cameras are accomplished using the high speed controller that comes as part of the LaVision system. The PIV images are acquired and analyzed using LaVision's PIV software, DaVis 8.0.6 and DaVis 8.3.1. The magnification factor of a camera, M, is calculated as the ratio of the camera image size to the field-of-view (FOV). The magnification factor of camera 01 is $M_1 \simeq 0.38$ and the wall-normal FOV extends from $-5.0mm \lesssim\ y\ \lesssim 54mm$, where $y = 0$ denotes the location of the lower wall. The magnification factor of camera 02 is $M_2 \simeq 0.79$ and the wall-normal FOV extends from $-2.0mm \lesssim\ y\ \lesssim 26mm$. Note that the exact magnification is slightly different between experiments. A representative PIV image acquired simultaneously from camera 01 and camera 02 is shown in Fig. 6.2.

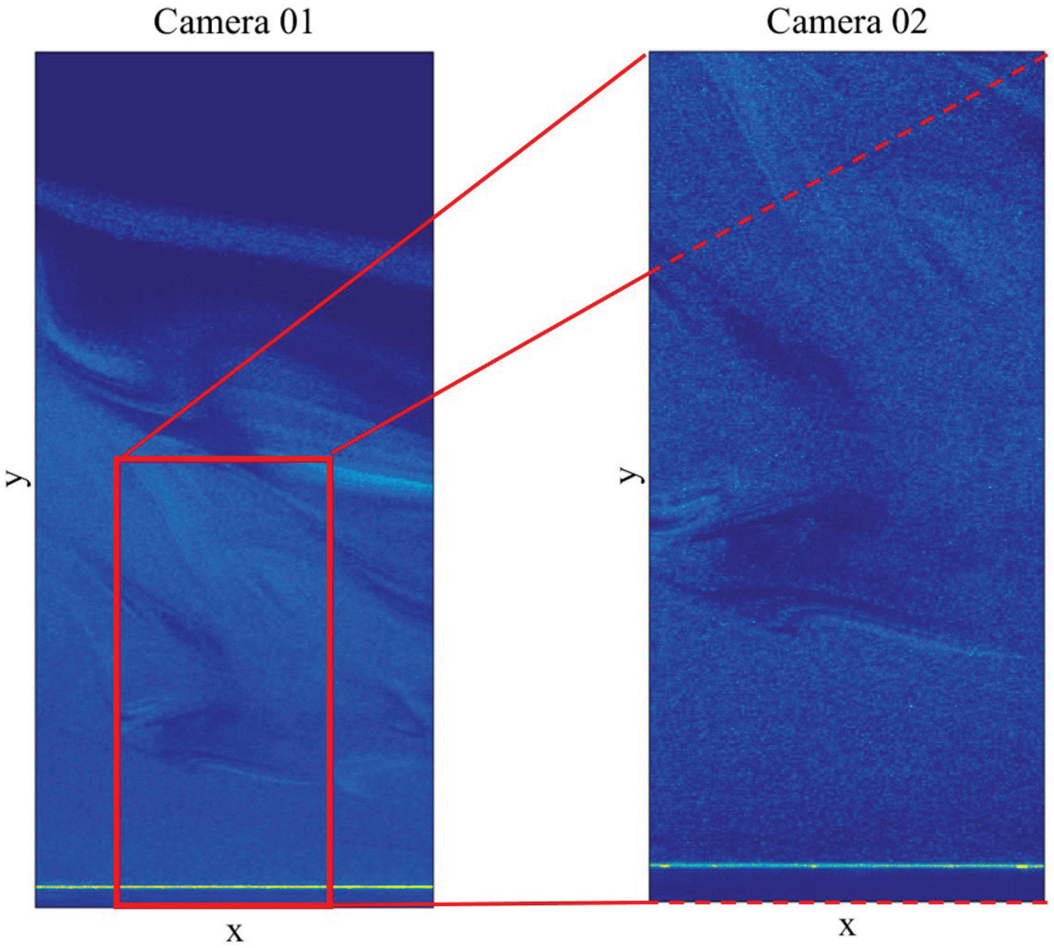

Figure 6.2: Simultaneous PIV images taken from the flow with camera 01 and camera 02. Horizontal lines in the images show the wall location. Flow direction is from right to left.

The $150ns$ pulse width of the laser is much smaller than any flow time scale, so that the particles are essentially frozen over the duration of the laser pulse. Therefore, the first image and second image contain spatial information of the particle distribution at the time of the first laser pulse, t and the second laser pulse $t + \delta t$, respectively. The velocity field is determined by dividing the particle displacement field, $\delta \mathbf{x}$, by the time separation between the two lasers, namely δt. The displacement field is calculated by dividing the image into small interrogation areas of varying size or shape, but are typically 32×32, 64×64, or 128×128 pixel^2. For a given interrogation area, the intensity field in the first image (I_1) is cross-correlated with that of the second image (I_2).

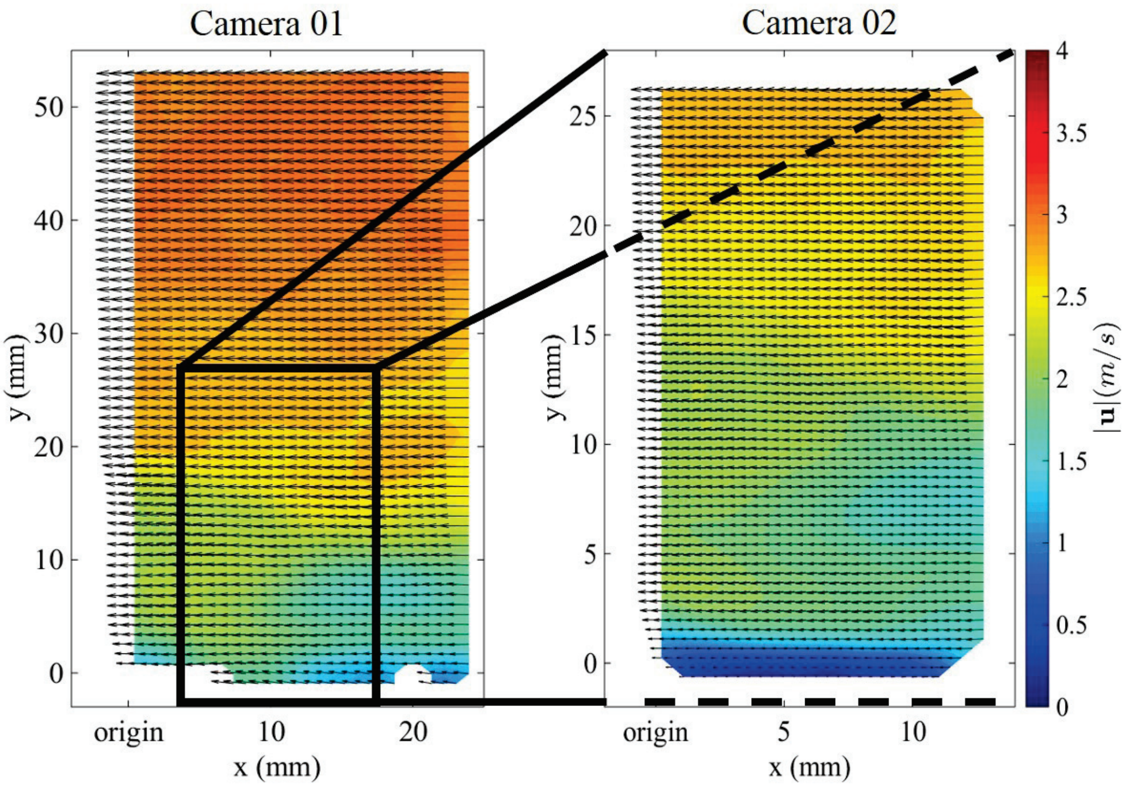

Figure 6.3: Simultaneous PIV vector fields acquired fromcamera 01 and camera 02. $y = 0$ in the vector fields show the wall location. Background color represents the magnitude of the velocity vector. Flow direction is from right to left.

The normalized cross-correlation is calculated as

$$CC(x, y) = \frac{\Sigma\Sigma I_1(i, j)I_2(i + x, j + y)}{\sigma_{I_1}\sigma_{I_2}}, \tag{6.1}$$

where $CC(x, y)$ is the normalized cross-correlation as a function of x and y, σ_{I_1} and σ_{I_2} are the standard deviation of I_1 and I_2, respectively, and i and j are the pixel indices in the x and y directions, respectively. Next, the peak value of $CC(x, y)$ is located with sub-pixel accuracy (using fitting schemes) and the average particle displacement, $\delta\mathbf{x}$, in the interrogation area is computed as a vector that originates from the center of the interrogation area to the location of the $CC(x, y)$ peak. The average particle velocity in the interrogation area is then computed as the average displacement divided by the time separation between laser pulses, i.e., $\mathbf{u}(x, y) = \delta\mathbf{x}/\delta t$.

In the majority of the experiments presented here, the PIV images are analyzed using the cross-correlation technique with multi-passing. An interrogation area of $64 \times 64\ \mathrm{pixel}^2$, with no overlap of adjacent areas, is used for the first pass and $32 \times 32\ \mathrm{pixel}^2$ with an overlap of 50%, for the second. After a vector field is calculated, it is validated using a local median filter. A vector determined to be spurious is either replaced by the vector corresponding to a secondary peak in the correlation plane or left blank. A representative PIV vector field acquired simultaneously from camera 01 and camera 02 is shown in Fig. 6.3. A step-by-step description of the experimental procedure is provided in Appendix C.

6.2 "Stitching" Profiles

Camera 01 and 02 are used for, respectively, outer and inner flow measurements. The acquired wall-normal profiles must be combined to create a uniform profile that covers the combined camera 01 and 02 wall-normal fields of view: FOV1 and FOV2, respectively. The most common "stitching" method is to average the profiles in the overlap region (Sterenborg *et al.*, 2014). Alternatively, Tang *et al.* (2008) developed a method based on obvious marks and transforming the spatial coordinate matrices of neighboring points. Shea *et al.* (2014) introduced a three-step "stitching" process: 1-calculate the ideal offset between the two images, 2-calculate the appropriate scale factor in the overlap region, and 3-merge the individual interrogation windows into a single combined window. In order to minimize the interference in the acquired data, no post-processing is performed in the overlap region. The combined wall-normal profile is attained by keeping FOV2, and including the portion of FOV1 that does not overlap FOV2. Thus, the near wall is resolved by camera 02 and near the freestream is resolved by camera 01, and there is a break point in the interface of the two fields of view that is more obvious in the pulsatile boundary layer profiles presented in the following chapter.

6.3 Uncertainty Estimates

Experimental measurements are associated with measurement errors caused by interfering inputs owed to measurement system limitations, finite sampling, or operator error. The integrated effects of the measurement errors are often quantified by a measurement uncertainty that provides a possible range of the error in the measurement. The value of the measured variable is not known exactly but rather defined by a confidence interval in which a probability is assigned to a plus or minus range about the measured value. Assuming the interfering inputs are independent, statistical analysis based on the Normal distribution is used to assign the level of confidence. The uncertainty estimation of the measured quantities and their statistical moments are explained in this section.

6.3.1 Velocity

PIV velocity vectors are evaluated as $u = \frac{x}{t}$, where x is the particle displacement and t is the time separation between laser pulses (or successive images). The uncertainty in the PIV velocity measurement is estimated using the root-sum-square method of error propagation, given as

$$\Delta u = \sqrt{\left(\frac{\partial u}{\partial x}\Delta x\right)^2 + \left(\frac{\partial u}{\partial t}\Delta t\right)^2} = \sqrt{\left(\frac{1}{t}\Delta x\right)^2 + \left(\frac{-x}{t^2}\Delta t\right)^2}, \tag{6.2}$$

where Δu, Δx and Δt are uncertainties of u, x and t, respectively. $\Delta t \simeq 10^{-9}s$, which makes the second term under the square root much smaller than the first term. Therefore, velocity uncertainty is estimated as

$$\Delta u \simeq \frac{\Delta x}{t}. \tag{6.3}$$

Using a pixel size to define the spatial resolution of the camera, $\Delta x = \pm 0.5px$, where px is the spatial resolution of a pixel in the PIV measurements. In the majority of the experiments reported in this dissertation, $px \simeq 13\mu m$. It follows that the velocity uncertainty is $\Delta u \simeq 0.09m/s$. The PIV measurements, however, employ "sub-pixel interpolation" schemes with a resolution of $\Delta x = \pm 0.1px$ (Tropea *et al.*, 2007). For this resolution, the velocity uncertainty is $\Delta u \simeq 0.018m/s$.

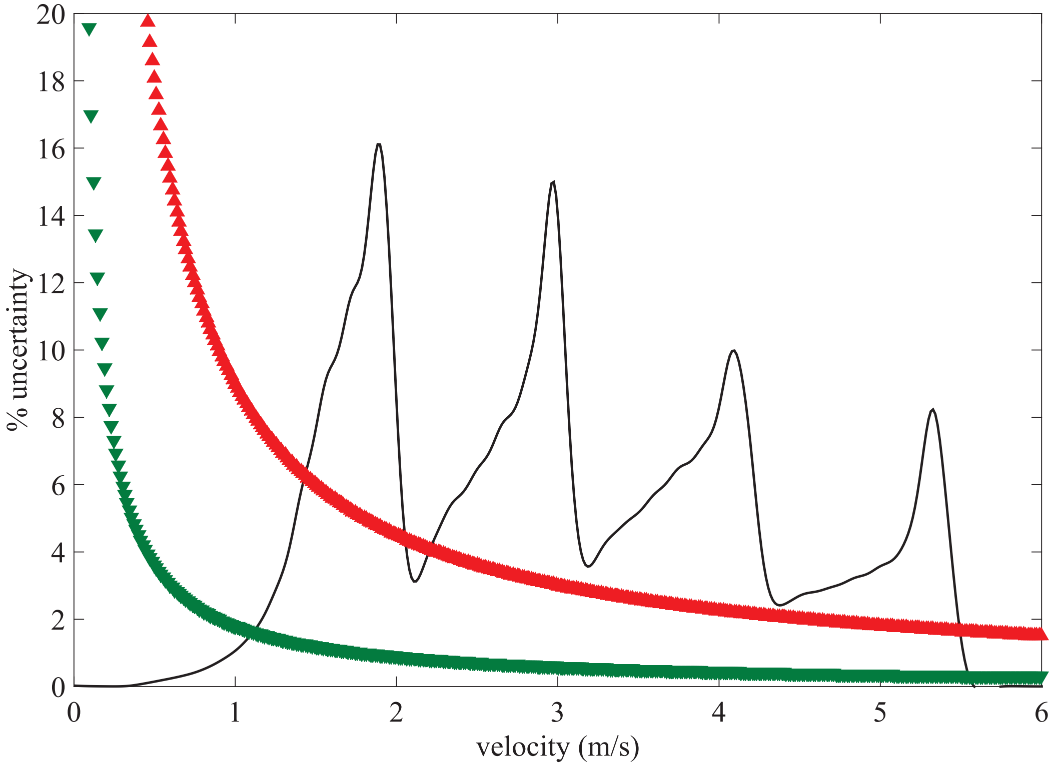

Figure 6.4: The percent uncertainty over the velocity range of the current experiment with 0.5 pixel resolution (red upward-pointing triangles) and 0.1 pixel resolution (green downward-pointing triangles). The normalized histogram of the velocity measurements in ZPG flow is plotted for reference (solid line). Different peaks correspond to different freestream velocities.

Using these two velocity uncertainties as a upper and lower bound, the percent uncertainty over the velocity range of the current experiments is shown in Fig. 6.4. The different peaks in experimental histograms of velocity correspond to different experiments using different freestream velocities (i.e., four different freestream velocities). Observe that in a boundary layer flow, the % uncertainty in the measured velocity increases exponentially near the wall where the velocity magnitudes are small and decreases as the edge of the boundary layer is approached where the velocity magnitudes are large.

6.3.2 Wall Location

The location of the wall in the PIV images is determined from images of the PIV calibration plate. Given the typical image resolution in the PIV experiments and the number of trials to locate the wall, the wall location uncertainty is estimated to be $\pm 0.1 mm$ (this corresponds to about $\pm 8 pixels$).

6.3.3 Friction Velocity

The Integral method of Mehdi *et al.* (2014) is used to estimate the wall friction velocity u_τ. Since the experimental domain of the data acquired in the current experiments is from $y^+ \simeq 17$ to $y/\delta \simeq 1$. The u_τ uncertainty for the current experimental domain is estimated to be $< 2\%$ according to Fig. 1 of Mehdi *et al.* (2014). However, since the uncertainty in the velocity measurements is slightly higher than that used to create the figure, the uncertainty in the wall shear stress is expected to be slightly above $\pm 2\%$.

6.3.4 Statistical Moments

Reynolds decomposition is used to describe the flow statistics:

$$a(y,t) = A(y) + a'(y,t), \tag{6.4}$$

where a is a generic flow parameter, A is the ensemble-averaged and a' is the fluctuations. In statistically steady flow $A \equiv \overline{a}$, where overline denoting the time-average operator. The uncertainty values in the measured statistics are determined following the procedure outlined by Sciacchitano and Wieneke (2016). The uncertainty of the average velocity, i.e U is calculated as:

$$\Delta U = \sigma_u \sqrt{\frac{1}{N_{eff}}}, \tag{6.5}$$

where ΔU is the uncertainty of U (as described above), σ_u is the standard deviation of the velocity, u, measurements, and N_{eff} is number of *independent* realizations. N_{eff} is estimated as

Table 6.1: Experimental parameter of the current ZPGBL experiments.

Symbol	$U_\infty (m/s)$	$u_\tau (m/s)$	$\nu/u_\tau (mm)$	$\delta^* (mm)$	$\theta (mm)$	H	Re_θ
●	1.94	0.0963	0.165	6.61	4.64	1.42	568
■	3.00	0.1422	0.111	5.82	4.36	1.33	814
◆	4.15	0.1835	0.087	5.77	4.39	1.31	1093
▶	5.38	0.2350	0.068	5.71	4.29	1.33	1438

$$N_{eff} \simeq \frac{T}{L/U_\infty}, \tag{6.6}$$

where T is the sampling length, L is the distance of the measurement location in the wind tunnel relative to the test-section inlet, and U_∞ is the freestream velocity. For the majority of the experiments, $\Delta U/U < 1\%$.

The uncertainty of the standard deviation, i.e., $u_{rms} \equiv \sqrt{\overline{u'^2}}$ is calculated as:

$$\Delta u_{rms} = \sigma_u \sqrt{\frac{1}{(2N_{eff} - 1)}}. \tag{6.7}$$

For the current experiments, $\Delta u_{rms}/u_{rms} < 4\%$ and $\Delta v_{rms}/v_{rms} < 4\%$. Equations 6.5 and 6.7 have an accuracy of 1% for $N_{eff} > 30$ (Ahn and Fessler, 2003), which is satisfied in the present experiments.

The uncertainty of the Reynolds shear stress $\overline{u'v'}$ is calculated as:

$$\Delta\overline{u'v'} = \sigma_u \sigma_v \sqrt{\frac{1 + \left(\frac{\overline{u'v'}}{\sigma_u \sigma_v}\right)^2}{(N_{eff} - 1)}}. \tag{6.8}$$

For the current ZPGBL flow experiments, $\Delta\overline{u'v'}/\overline{u'v'} < 14\%$ for $U_\infty \simeq 2m/s$ and 9% for $U_\infty \simeq 5m/s$, which correspond to $Re_\theta = 568$ and 1438, respectively.

6.4 Zero Pressure Gradient Boundary Layer (ZPGBL)

Boundary layer parameters and velocity profiles acquired in the NEAT facility with $dP/dx \approx 0$ are now described. This data, which will be called ZPGBL data, is acquired to validate the facility and measurement diagnostics, and to serve as a baseline comparative dataset. Data is acquired at four freestream velocities. The experimental and computed boundary layer parameters for the ZPG experiments are provided in Table 6.1 and described below:

- U_∞ is the freestream velocity.
- ν/u_τ is the wall unit.
- u_τ is the friction velocity evaluated by the integral method of Mehdi and White (2011) and Mehdi *et al.* (2014).
- $\delta^* = \int_0^1 \left(1 - \tilde{U}\right) d\tilde{y}$ is the displacement thickness, where $\tilde{U}$ is the mean streamwise velocity normalized by the freestream and $\tilde{y}$ is wall-normal dimension normalized by the boundary layer thickness.
- $\theta = \int_0^1 \tilde{U} \left(1 - \tilde{U}\right) d\tilde{y}$ is the momentum thickness.
- $H = \frac{\delta^*}{\theta}$ is the shape factor. Shape factor of a turbulent ZPGBL is $\simeq$1.3-1.4 (Schlichting *et al.*, 1979; Wu and Moin, 2010).
- $Re_\theta = \frac{U_\infty \theta}{\nu}$ is Reynolds number based on the momentum thickness.

The experimentally acquired profiles are compared to the DNS profiles of a ZPGBL flow simulated by Wu and Moin (2010). A description of the acquired profiles and how they compare to the data from Wu and Moin are described below.

- *Mean Velocity*

  The mean streamwise velocity profiles as a function of inner and outer coordinates (y^+ and y/δ, respectively) are shown in Figs. 6.5 and 6.6, respectively. The profiles show very good agreement with DNS profiles in both inner and outer coordinates.

- *Streamwise Turbulence Intensity*

  The streamwise root mean square (RMS) velocity profiles as a function of inner and outer coordinates are shown in Figs. 6.7 and 6.8, respectively. The Reynolds-number-dependence of the inner normalized profiles in the outer layer follow the same trend of the DNS data. The experimental profiles as a function of outer coordinate show very good agreement with DNS profiles within the experimental uncertainty. The underestimation of the profiles in the inner layer stems from the averaging effects of PIV. Since the PIV data is averaged within an interrogation area, the fraction of the turbulent kinetic energy that is carried by eddies smaller than the interrogation area is attenuated (De Graaff and Eaton, 2000). Multi-pass processing procedure and overlap between interrogation areas reduce the uncertainty due to averaging, but it is still not negligible. Higher turbulence level in the last few data points is likely due to low seeding density near the edge of the boundary layer.

- *Wall-Normal Turbulence Intensity*

  The wall-normal root mean square (RMS) velocity profiles as a function of inner and outer coordinates are shown in Figs. 6.9 and 6.10, respectively. The Reynolds-number-dependence of the profiles in the outer layer follow the same trend of the DNS data. Similar to the streamwise turbulence intensity, the wall-normal turbulence intensity is underestimated in the inner layer.

- *Reynolds Stress*

  The Reynolds shear stress profiles as a function of inner and outer coordinates are shown in Figs. 6.9 and 6.10, respectively. Similar to the wall-normal turbulence intensity, the Reynolds-number-dependence of the profiles in the outer layer follow the same trend of the DNS data, and profiles are underestimated in the inner layer.

In summary, the experimental ZPGBL profiles acquired in the NEAT facility with $dP/dx \approx 0$ show very good agreement with to the DNS profiles of a ZPGBL flow simulated by Wu and Moin (2010).

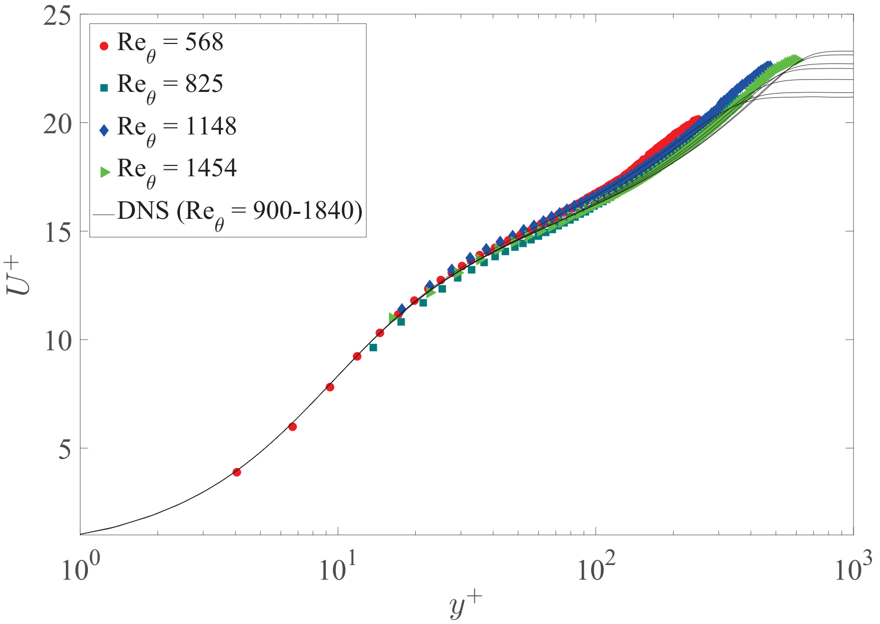

Figure 6.5: Wall-normal profiles of the mean streamwise velocity normalized by inner scales with $()^+$ denoting normalizing by u_τ and ν. DNS of a ZPGBL simulated by Wu and Moin (2010) and Moin are included for reference.

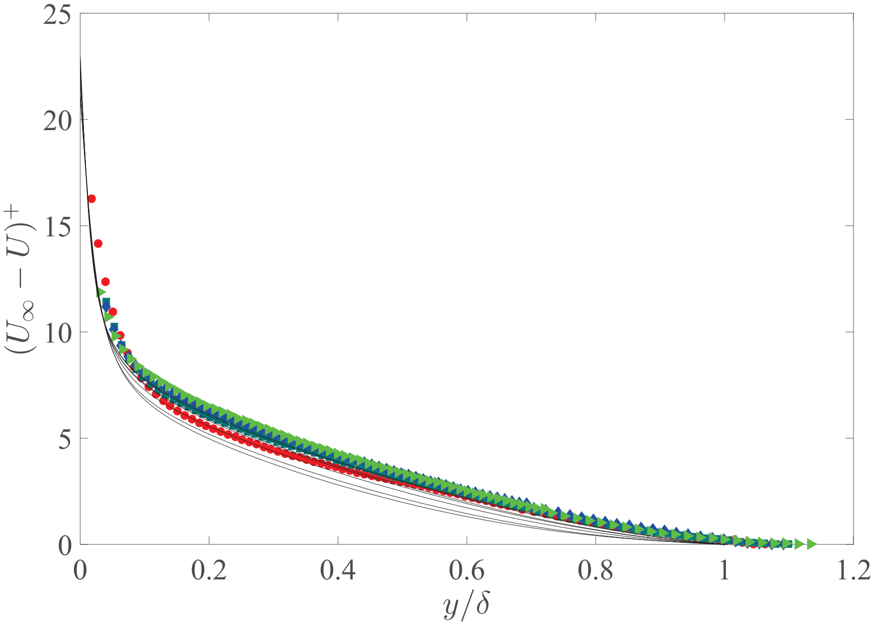

Figure 6.6: Wall-normal profiles of the mean streamwise velocity as a function of outer coordinate y/δ. Marker symbols are the same as Fig. 6.5.

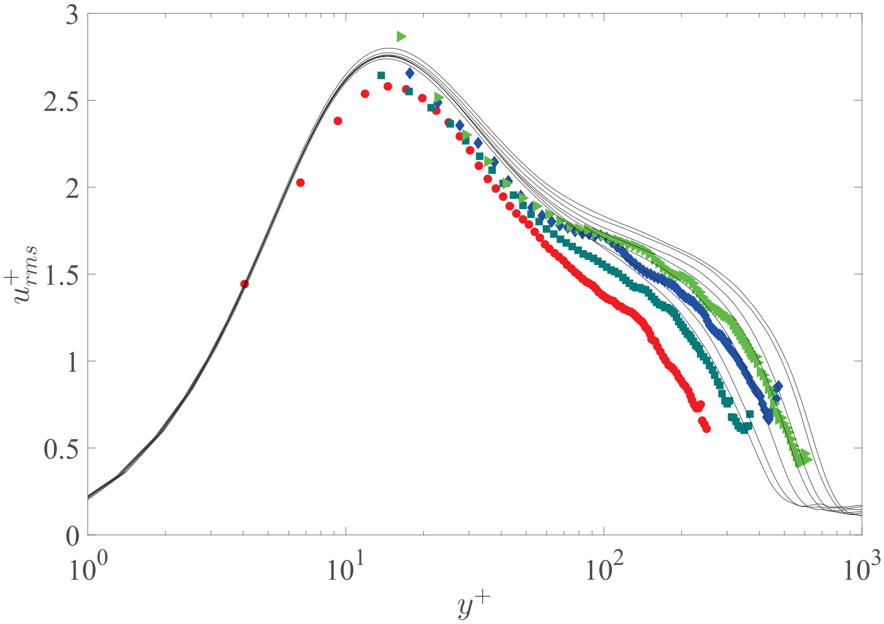

Figure 6.7: Wall-normal profiles of the streamwise RMS velocity normalized by inner scales. Marker symbols are the same as Fig. 6.5.

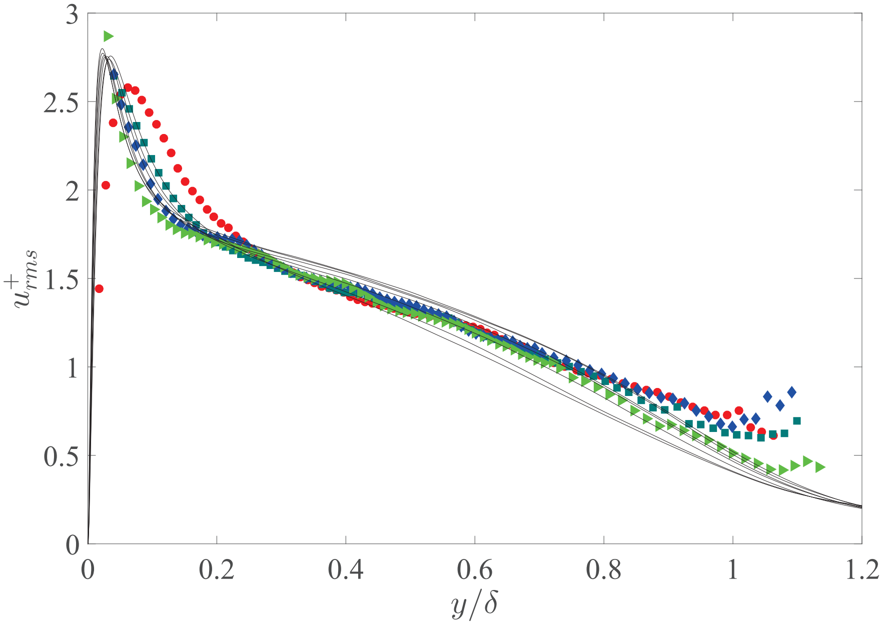

Figure 6.8: Wall-normal profiles of the streamwise RMS velocity as a function of outer coordinate y/δ. Marker symbols are the same as Fig. 6.5.

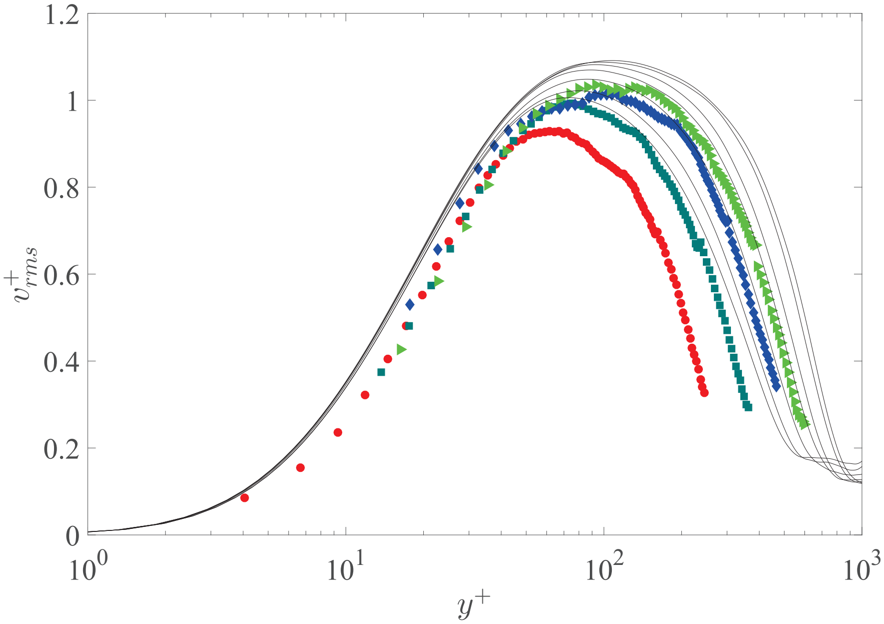

Figure 6.9: Wall-normal profiles of the wall-normal RMS velocity normalized by inner scales. Marker symbols are the same as Fig. 6.5.

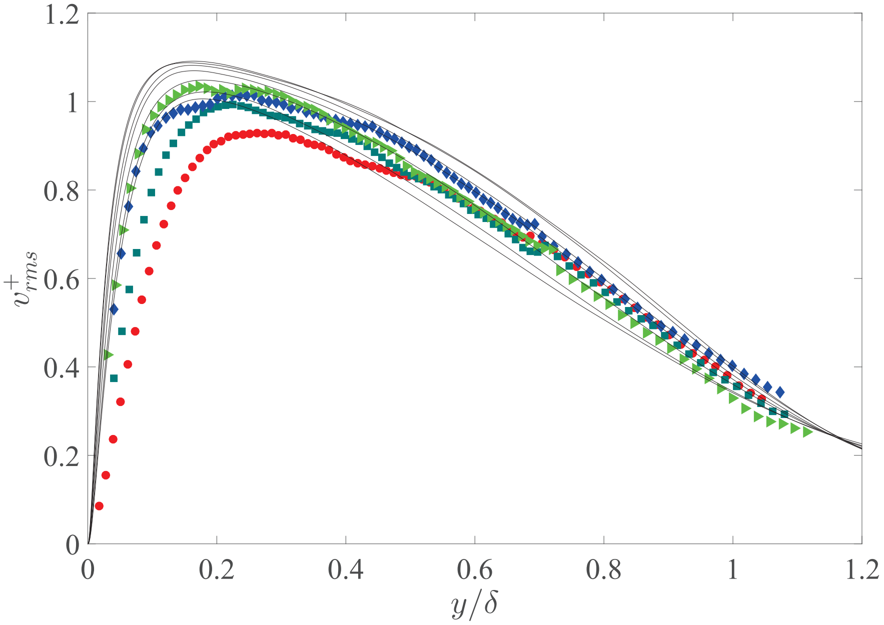

Figure 6.10: Wall-normal profiles of the wall-normal RMS velocity as a function of outer coordinate y/δ. Marker symbols are the same as Fig. 6.5.

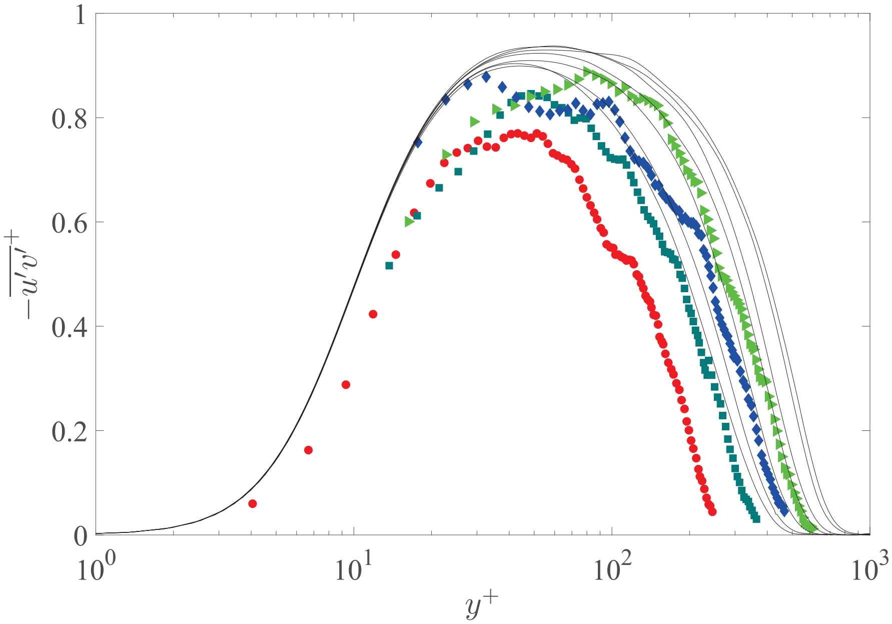

Figure 6.11: Wall-normal profiles of the Reynolds shear stress normalized by inner scales. Marker symbols are the same as Fig. 6.5.

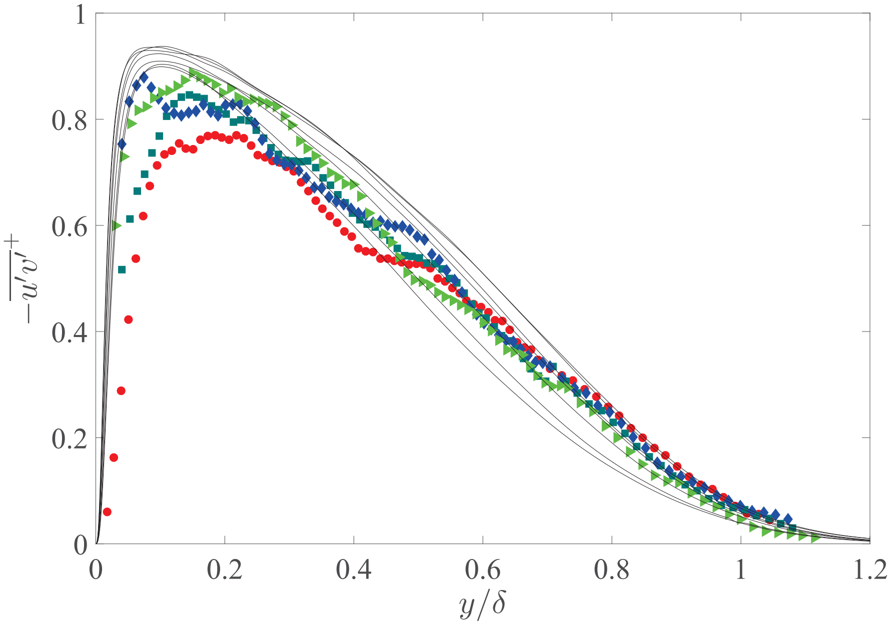

Figure 6.12: Wall-normal profiles of the Reynolds shear stress as a function of outer coordinate y/δ. Marker symbols are the same as Fig. 6.5.

CHAPTER 7

PULSATILE BOUNDARY LAYER FLOW

7.1 Literature Review

Experimental studies investigating pulsatile wall-bounded flows include Yellin (1966), Tu and Ramaprian (1983), Ramaprian and Tu (1983), Mao and Hanratty (1986), Stettler and Hussain (1986), Brereton *et al.* (1990), Einav and Sokolov (1993), Tardu and Binder (1993), Tardu *et al.* (1994), Binder *et al.* (1995) and Trip *et al.* (2012). Numerical simulations include, but not limited to Scotti and Piomelli (2001) Scotti and Piomelli (2002), Varghese and Frankel (2003), Mittal *et al.* (2003) and Weng *et al.* (2016). Using the Reynolds decomposition, the flow parameters are decomposed as follows:

$$A(y,t) = \langle A(y,t) \rangle + A'(y,t) \tag{7.1}$$

with

$$\langle A(y,t) \rangle = \frac{1}{N} \sum_{i=1}^{N} A(y, t+iT) \tag{7.2}$$

where $\langle A \rangle$ is the ensemble (phase-) average, T is the flow period, N is the number of cycles, and A' is the turbulent fluctuations component. Following Hussain and Reynolds (1970), the phase-averaged parameters in a pulsatile flow are decomposed as follows:

$$\langle A(y,t) \rangle = \overline{A}(y) + \widetilde{A}(y,t) \tag{7.3}$$

where $\overline{A}$ is time-averaged over integers of the period (cycle-), and $\widetilde{A}$ is the perturbation (oscillatory or coherent) component. Combining Eqs. 7.1 and 7.3, the flow parameters in a turbulent pulsatile flow are decomposed as follows:

$$A = \overline{A}(y) + \widetilde{A}(y,t) + A' \tag{7.4}$$

It is well-established that the time-averaged mean flow (except for a quasi-steady oscillation with large modulation amplitudes (see Tardu *et al.* (1994); Binder *et al.* (1995)) is independent of the flow frequency (Yellin, 1966; Ramaprian and Tu, 1983; Mao and Hanratty, 1986; Trip *et al.*, 2012; Weng *et al.*, 2016). Consequently, the perturbation field is the response of the flow to the imposed periodic pressure forcing. Furthermore, it also implies that the time-averaged perturbation component is zero when averaged over a period.

When the oscillation period is much larger than the turbulence relaxation time, the perturbation Reynolds stress responds immediately to the perturbation strain and redistribution of energy happens instantly. The perturbation field is therefore in equilibrium, and there is no phase difference between the oscillating strain and stress field. However, when the oscillation period is comparable to the turbulence relaxation time, the equilibrium of the perturbation field breaks down and there is a phase difference between the oscillating strain and stress field. The phase difference asymptotes to that of the Stokes' boundary layer flow, i.e., 45°, as the oscillation frequency increases (Brereton and Mankbadi, 1995; Weng *et al.*, 2016).

Most simulation models developed to predict the perturbation field in a pulsatile flow are based on extending the standard eddy viscosity model (EVM), i.e.,

$$\widetilde{r} = -C\nu_T \frac{\partial \widetilde{u}}{\partial y} \tag{7.5}$$

where $\widetilde{r} = \langle u'v' \rangle - \overline{u'v'}$ is the perturbation Reynolds shear stress with brackets denoting ensemble (or phase) averaging, the overbar denoting the time (or cycle) average, ν_T is the eddy viscosity and C is a constant, which is usually defined as $C = 2/Re$ (Weng *et al.*, 2016). The EVM models wrongly assume the Reynolds shear stress and the strain rate (LHS and RHS of Eq. 7.5) are in-phase, and hence, fail to predict the perturbation field in non-equilibrium pulsatile flows (Weng *et al.*, 2016).

Pulsatile flow frequency is often normalized by wall-units, i.e., $\omega^+ = \frac{\omega}{u_\tau^2/\nu}$, where ω^+ is the inner normalized frequency, ω is the dimensional frequency, u_τ is the friction velocity and ν is the fluid viscosity (Mao and Hanratty, 1986; Tardu and Binder, 1993; Weng *et al.*, 2016). It can be shown that $\omega^+ = \frac{2}{l_s^{+2}} = \frac{Str^2}{2}$, where $l_s \equiv \sqrt{2\nu/\omega}$ is the Stokes' layer thickness and $Str \equiv \frac{\omega}{u_\tau/l_s}$ is the Strouhal number based on l_s and u_τ. Pulsatile flow can be classified into four regimes based on the magnitude of ω^+ (Ramaprian and Tu, 1983; Brereton and Mankbadi, 1995):

- ***(i) Quasi-steady*** **($\omega^+ < 0.003$) –** The perturbation field in quasi-steady flow is negligible. Therefore, all flow properties will be the same as their steady flow counterpart at the same instantaneous Reynolds number. Consequently, there is no phase variation or amplitude overshoot of the ensemble-averaged velocity profiles in wall-normal direction (Tu and Ramaprian, 1983). Departure from quasi-steady regime is reported for $\omega^+ \gtrsim 0.003$ (Brereton and Mankbadi, 1995).

- ***(ii) Low frequency*** **($0.003 \lesssim \omega^+ \lesssim 0.006$) –** The perturbation field, which is not negligible anymore, is in equilibrium, and there is negligible phase difference between the perturbation velocity and the wall shear stress. The perturbation wall shear stress is larger than its laminar counterpart (Stokes' flow). The low frequency regime is $0.003 \lesssim \omega^+ \lesssim 0.006$ (Weng *et al.*, 2016).

- ***(iii) Intermediate (or moderate) frequency*** **($0.006 \lesssim \omega^+ \lesssim 0.02$-$0.04$) –** The perturbation field is not in equilibrium and there is phase difference ($0° < \Delta\phi < 50°$) between the straining force and the wall shear stress. The perturbation field wall shear stress is smaller than the laminar flow counterpart (Weng *et al.*, 2016). The intermediate frequency regime is often reported for $0.006 \lesssim \omega^+ \lesssim 0.02$-$0.04$ (Tardu *et al.*, 1994; Brereton and Mankbadi, 1995; Weng *et al.*, 2016).

- ***(iv) High frequency*** **($\omega^+ \gtrsim 0.02$-0.04) –** The perturbation wall shear stress amplitude and phase asymptote to the Stokes' flow values. While the flow is turbulent, the perturbation

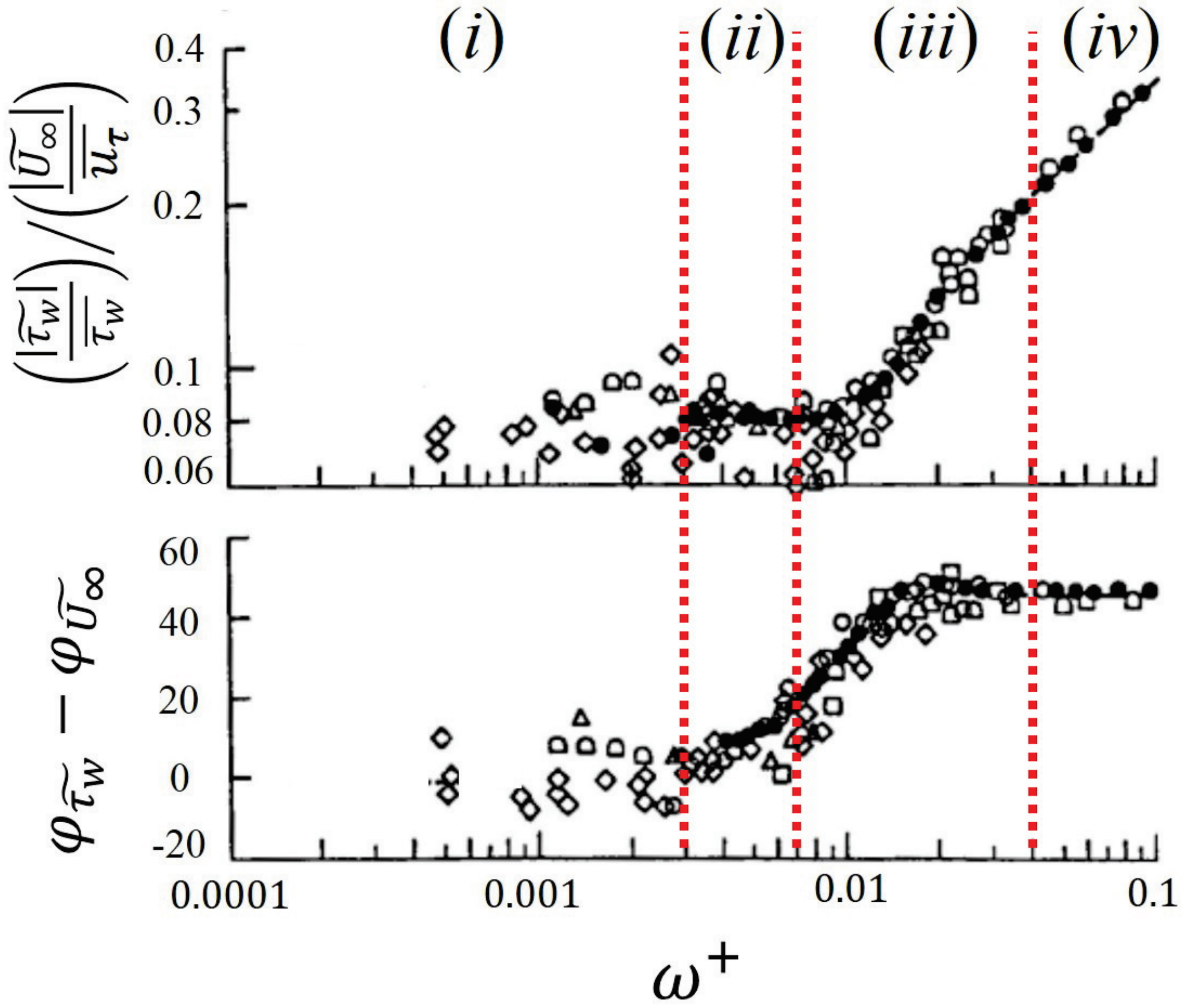

Figure 7.1: Modulation amplitude (top) and the phase lag of the perturbation wall shear stress compared to the freestream modulation (bottom) of pulsatile wall-bounded flow in different frequency regimes. The four frequency regimes are segregated by three vertical dashed lines. Marker symbols are given in Brereton and Mankbadi (1995).

field in the very high frequency regime is governed by the viscous forces (Tardu *et al.*, 1994; Brereton and Mankbadi, 1995; Scotti and Piomelli, 2001).

The four frequency regimes are shown in Fig. 7.1. The reader is referred to Brereton and Mankbadi (1995) for detailed review of pulsatile wall-bounded flows.

7.2 Experimental Details

Particle image velocimetry is used to study the transport of momentum in PBL flow. The objective of the study is to acquire velocity data in PBL flow and compare the results of the boundary layer parameters and velocity profiles to ZPGBL flow. The time-averaged mean flow is turbulent and the frequency range (1.60 - 4.95Hz) is within the *intermediate frequency* regime, such that the lowest frequency ($\omega^+ = 0.007$) is just above the *low frequency* threshold and the highest frequency ($\omega^+ = 0.020$) is at the onset of the *high frequency* threshold. Therefore, the differences in the flow behaviors across the full frequency range of the intermediate frequency regime can be evaluated.

The NEAT boundary layer wind tunnel, while being able to drive the flow with a periodic pressure gradient, does have limited capabilities. Specifically, the inherent flow blockage of the rotor-stator assembly limits the maximum flow speed in the tunnel to $\sim 3.25 m/s$. In addition, at the upper frequency limit, the amplitude of the velocity modulation is only 5%, which is amongst the lowest modulation amplitude reported for pulsatile flows (Çarpinlioğlu and Gündoğdu, 2001).

Experiments are conducted at three forcing frequencies. Boundary layer parameters measured/computed for the three forcing frequencies are reported in Table 7.1 and described below:

- f is the flow frequency, calculated using a fast Fourier transform (FFT) of the time-averaged freestream velocity signal. A typical FFT plot of the freestream velocity signal is shown in Fig. 7.2. The peak signal is used to identify the flow frequency. Note that higher harmonics were not observable in the FFT.

- $\overline{U_\infty}$ is the time-averaged freestream velocity.

Table 7.1: Experimental parameters of the current PBL experiments.

Symbol	$f(Hz)$	$\overline{U_\infty}(\frac{m}{s})$	$\overline{u_\tau}(\frac{m}{s})$	ω^+	$l_s(mm)$	l_s^+	Re	Re_s	W	$\frac{u_{osc}}{U_\infty}(\%)$
◀	1.60	3.25	0.154	0.007	1.78	17	7306	336	30.71	11
▶	3.25	3.21	0.155	0.014	1.25	12	6543	228	40.57	8
▲	4.95	3.25	0.156	0.020	1.01	10	6805	185	51.99	6

- $\overline{u_\tau}$ is the time-averaged friction velocity evaluated using the integral method of Mehdi and White (2011) and Mehdi *et al.* (2014).
- $\omega^+ \equiv \frac{\omega}{u_\tau^2/\nu}$ is the inner normalized angular frequency.
- $l_s \equiv \sqrt{2\nu/\omega}$ is the Stokes' layer thickness.
- $l_s^+ \equiv \frac{l_s}{\nu/u_\tau}$ is the inner normalized Stokes' layer thickness, which is a measure of how far the disturbances at the wall penetrate into the boundary layer.
- $Re \equiv \frac{\overline{U_\infty \delta}}{\nu}$ is the time-averaged Reynolds number, $\overline{\delta}$ is the average boundary layer thickness.
- $Re_s \equiv \frac{U_m l_s}{\nu}$ is the Stokes Reynolds number, where U_m is the amplitude of the cross-sectional average velocity.
- $W \equiv \overline{\delta}\sqrt{\omega/\nu}$ is the Womersley number.
- $\frac{u_{osc}}{U_\infty}$ is the modulation amplitude in of the freestream velocity.

The flow parameters are decomposed as follows:

$$A(y,t) = \langle A(y,t)\rangle + A'(y,t) \tag{7.6}$$

with

$$\langle A(y,t)\rangle = \overline{A}(y) + \widetilde{A}(y,t) = \frac{1}{N}\sum_{i=1}^{N} A(y, t + iT) \tag{7.7}$$

where $\langle A\rangle$ is the ensemble (phase-) average, T is the flow period and N is the number of cycles. The flow is sampled over 60 cycles with sampling interval of $\sim\frac{T}{18}$. The oscillation phases are binned into 18 bins, consequently, parameters within $\pm 10^\circ$ of the center of the bin are averaged together. The bin phases are then shifted so that the maximum phase-averaged freestream velocity is at $\phi = 90^\circ$. Using Eqs. 6.5-6.8, the statistical uncertainty of $\langle U\rangle$, $\langle u'v'\rangle$, $\langle u_{rms}\rangle$ and $\langle v_{rms}\rangle$ is estimated to be 2%, 60-100%, 10% and 10%, respectively. The pressure-gradient oscillates around the steady-state value, which is slightly favorable, and does not change sign.

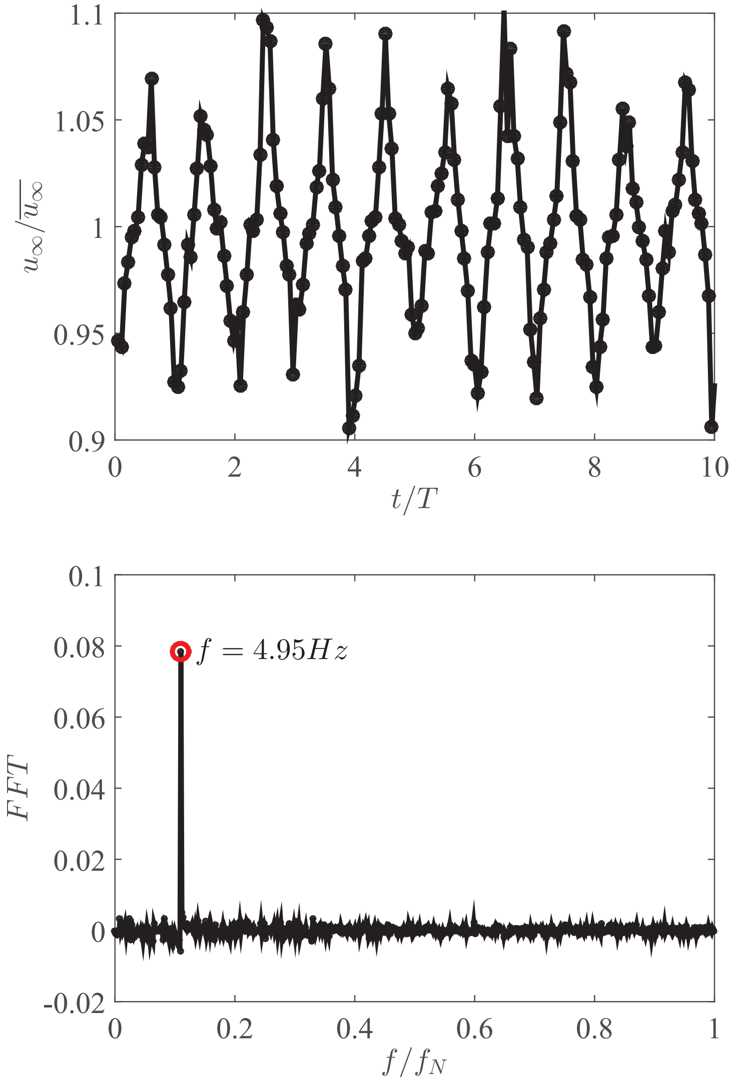

Figure 7.2: Top: Time series of the freestream velocity normalized by time-averaged plotted for ten cycles. Bottom: FFT of the freestream velocity time series. f_N is the Nyquist frequency, which is half of the sampling frequency.

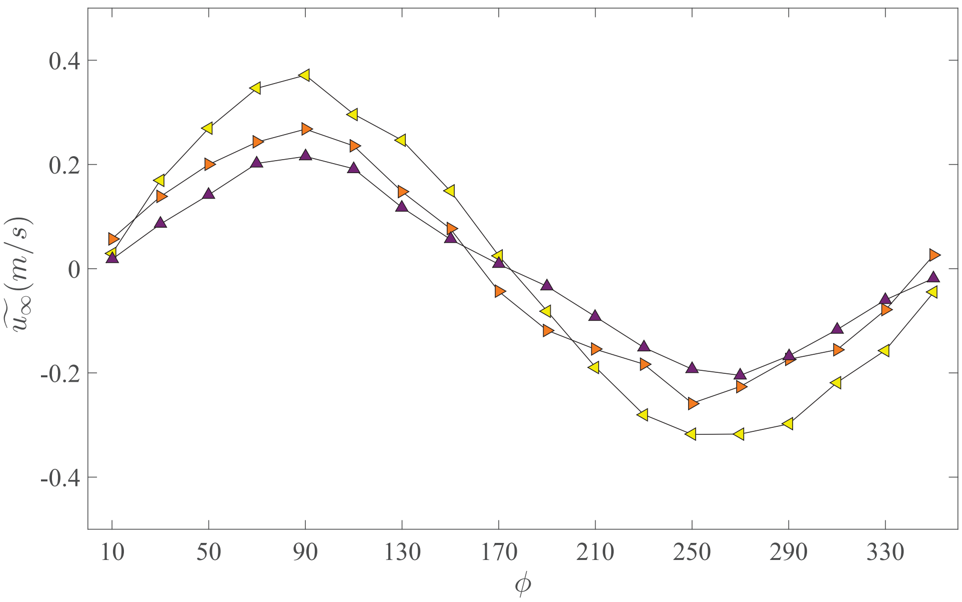

Figure 7.3: The freestream perturbation velocity modulation as a function of phase angle. Marker symbols are given in Table 7.1.

7.2.1 Results and Discussion

7.2.2 Perturbation Field

Bulk flow parameters

In PBL flow experiments, the wall-normal perturbation profiles are often compared to the Stokes' flow solution. Since the Stokes' layer ($l_s^+ \leq 17$) is not resolved in the present experiments, such comparison is not feasible. Nonetheless, the perturbation wall shear stress, which is an indicator of both the perturbation field dynamics and the response of the flow to the imposed oscillation, is discussed in detail.

- *Freestream Velocity*

  The oscillatory component of the freestream velocity in PBL as a function of phase angle is shown in Fig. 7.3. It is observed that the modulation amplitude of the freestream velocity is inversely proportional to the flow frequency, which is in agreement with previous

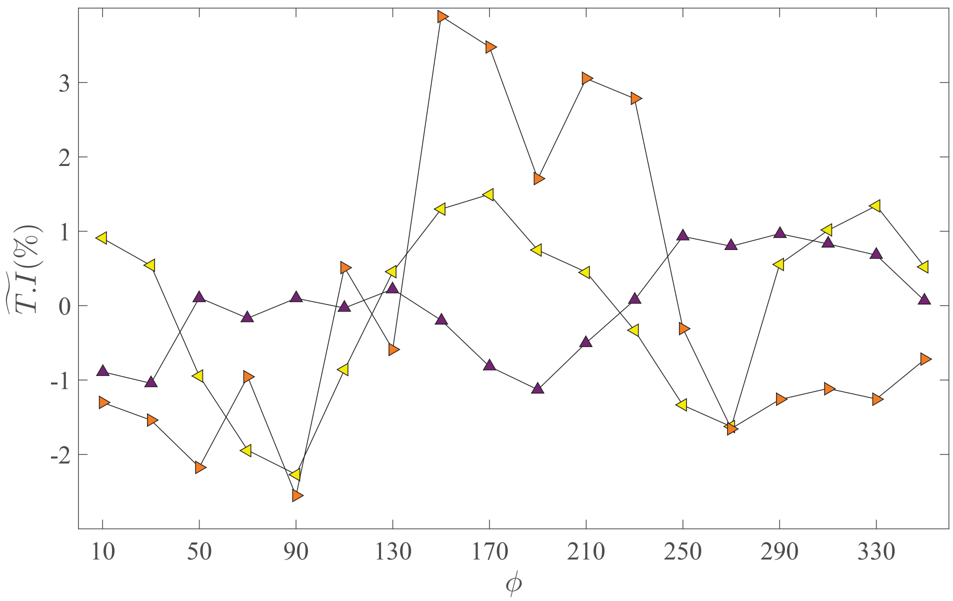

Figure 7.4: The freestream turbulent intensity modulation as a function of phase angle. Marker symbols are given in Table 7.1.

experiments (Ramaprian and Tu, 1980; Stettler and Hussain, 1986; Binder *et al.*, 1995). The freestream velocity is also in phase with the oscillation of the pressure-gradient in all cases.

- *Freestream turbulence Intensity*

The freestream turbulent intensity as a function of phase angle for the three forcing frequencies is shown in Fig. 7.4. There is a 180° phase difference between the peak freestream turbulence intensity measured at the highest forcing frequency compared to the two lower forcing frequency cases. This observed phase difference in the peak turbulent intensity between low and high-frequency forcing is in agreement with results of Ramaprian and Tu (1983).

- *Shape Factor*

The computed shape factor plotted as a function of phase angle for the three forcing frequencies is shown in Fig. 7.5. It is observed that the shape factor is anti-correlated (i.e., it is 180°

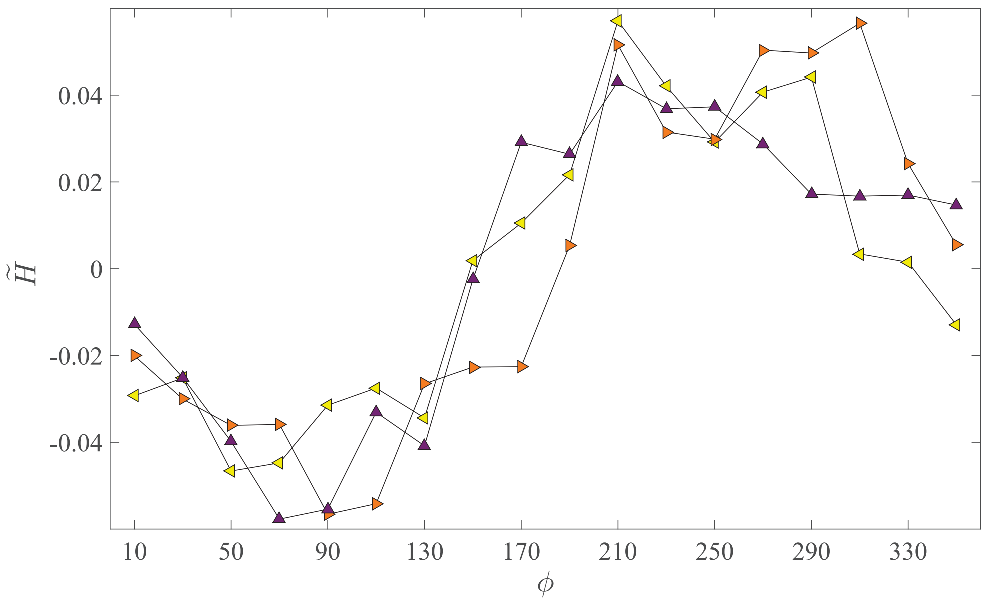

Figure 7.5: Shape factor modulation as a function of phase angle. Marker symbols are given in Table 7.1.

out of phase) with the pressure forcing and the modulation amplitude is almost identical for all cases. The time (cycle-) average shape factor is $\simeq 1.3$ for all cases.

- *Wall Shear Stress*

The oscillatory wall shear stress component plotted as a function of phase angle for the three forcing frequencies is shown in Fig. 7.6. Considering the error map provided for the wall shear stress estimation using the integral method by Mehdi *et al.* (2014) and comparing the mean velocity uncertainty of PBL and ZPGBL, the wall shear stress uncertainty of PBL is estimated to be slightly above 4%. In spite of the different modulation amplitude of the freestream velocity, all three forcing frequencies show similar modulation amplitude of the wall shear stress. The two lower frequency cases ($\omega^+ = 0.007, 0.014$) show a statistically significant "bump" in the wall shear stress in the early decelerating phase ($\phi = 110°$), which is absent in the highest frequency case (ω^+ = 0.020). Since the phase and amplitude of the

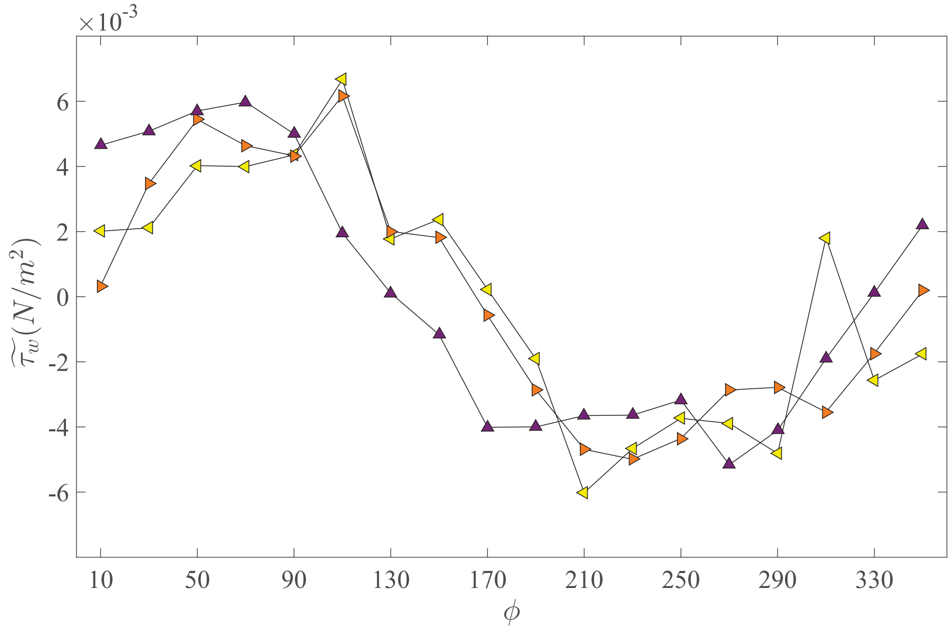

Figure 7.6: Wall shear stress modulation as a function of phase angle. Marker symbols are given in Table 7.1.

perturbation wall-shear stress are indicators of the equilibrium or non-equilibrium state of the perturbation field, they are discussed separately below.

Modulation amplitude of the oscillatory wall shear stress

Figure 7.7 compares the magnitude of the oscillatory component of the wall shear stress to the magnitude expected from Stokes boundary layer flow ($\tau_{w,s}$). Here $\tau_{w,s}$ is estimated from the oscillatory component of the freestream velocity:

$$|\tau_{w,s}| = \frac{\sqrt{2}\mu}{l_s}|U_{\infty,s}|. \tag{7.8}$$

Notwithstanding the experimental uncertainty, the modulation amplitude of the highest frequency case appears to be slightly larger than the Stokes' flow solution, while the modulation amplitude of the two lower frequency cases match with the Stokes' flow within the experimental uncertainty.

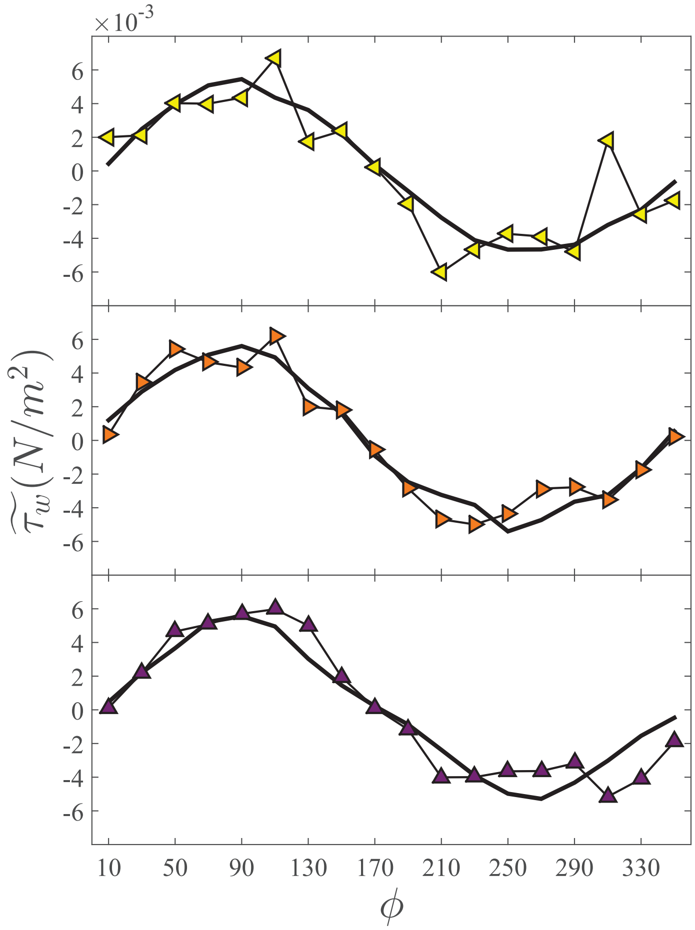

Figure 7.7: Modulation amplitude of the perturbation wall shear stress compared to Stokes' solution (black solid lines) for $\omega^+ = 0.007$ (top), $\omega^+ = 0.014$ (middle), and $\omega^+ = 0.020$ (bottom) . Marker symbols are given in Table 7.1.

Phase difference of the oscillatory wall shear stress and freestream velocity

The phase difference between the oscillatory component of the freestream velocity and the oscillatory component of the wall shear stress ($\Delta\phi = \phi_{\widetilde{\tau_w}} - \phi_{\widetilde{U_\infty}}$) is evaluated by quantifying the residuals of their normalized modulations as a function of phase angle. First, the oscillatory component of the freestream velocity is plotted as function of phase angle. Next, the oscillatory component of the wall shear stress is shifted $\Delta\phi = \pm 60°$ with $20°$ increments and the phase angle that shows the minimum residual between the two curves is selected (Fig. 7.8). Complementary visual inspection of the normalized freestream velocity and the oscillatory component of the wall shear stress as a

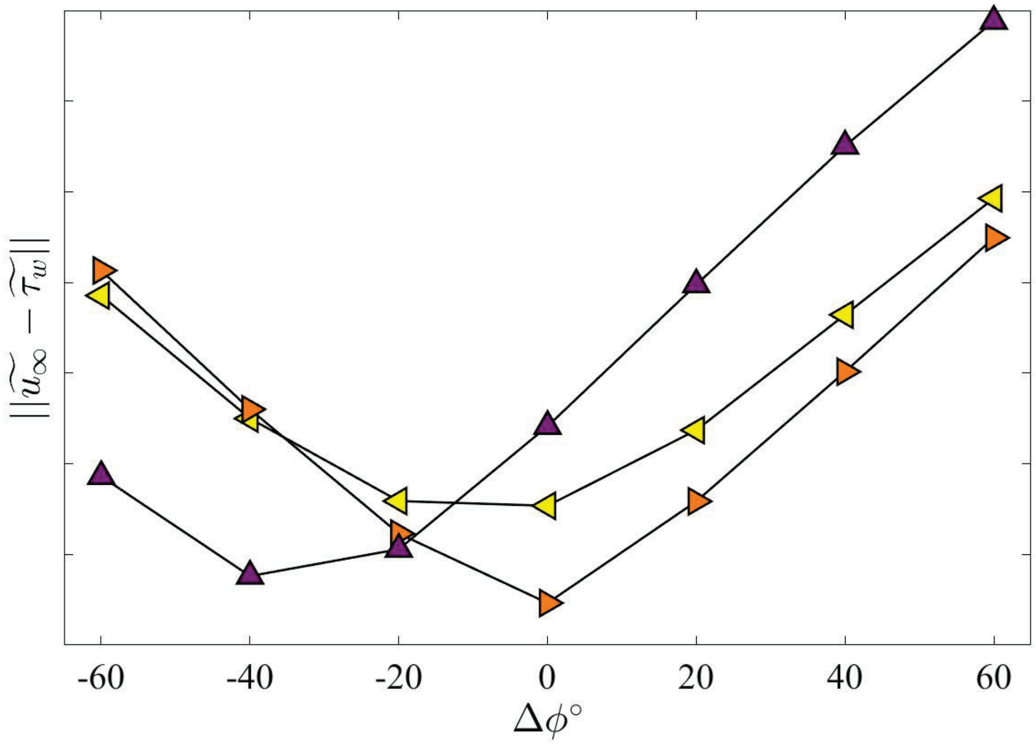

Figure 7.8: The difference between the normalized perturbation wall shear stress and the freestream velocity. $||\bullet||$ corresponds to the Euclidean norm, where $||\mathbf{a}|| = \sqrt{a_1^2 + a_2^2 + ... + a_n^2}$. Marker symbols are given in Table 7.1.

function of phase angle is used for verification (Fig. 7.9). Following this procedure, the phase lead of the oscillatory component of the wall shear stress is $\pm 10^\circ$ for the two lower forcing frequencies and $40 \pm 10^\circ$ for the highest forcing frequency. The phase lead observed at the highest frequency case matches the phase lead in Stokes' boundary layer flow, i.e., 45° within the experimental uncertainty and is in agreement with previous experimental and numerical studies performed at similar ω^+ (Brereton and Mankbadi, 1995; Scotti and Piomelli, 2001; Weng *et al.*, 2016). The fact the wall shear stress leads the freestream velocity (and hence the imposed pressure gradient) at the highest frequency case indicates non-equilibrium behaviors in PBL flow. Consequently, eddy viscosity models (EVM) will fail to predict the perturbation Reynolds stress at the highest frequency case (Weng *et al.*, 2016). Based on the measured perturbation field parameters in the present experiments, in particular the wall shear stress and the turbulence intensity, it appears that the highest

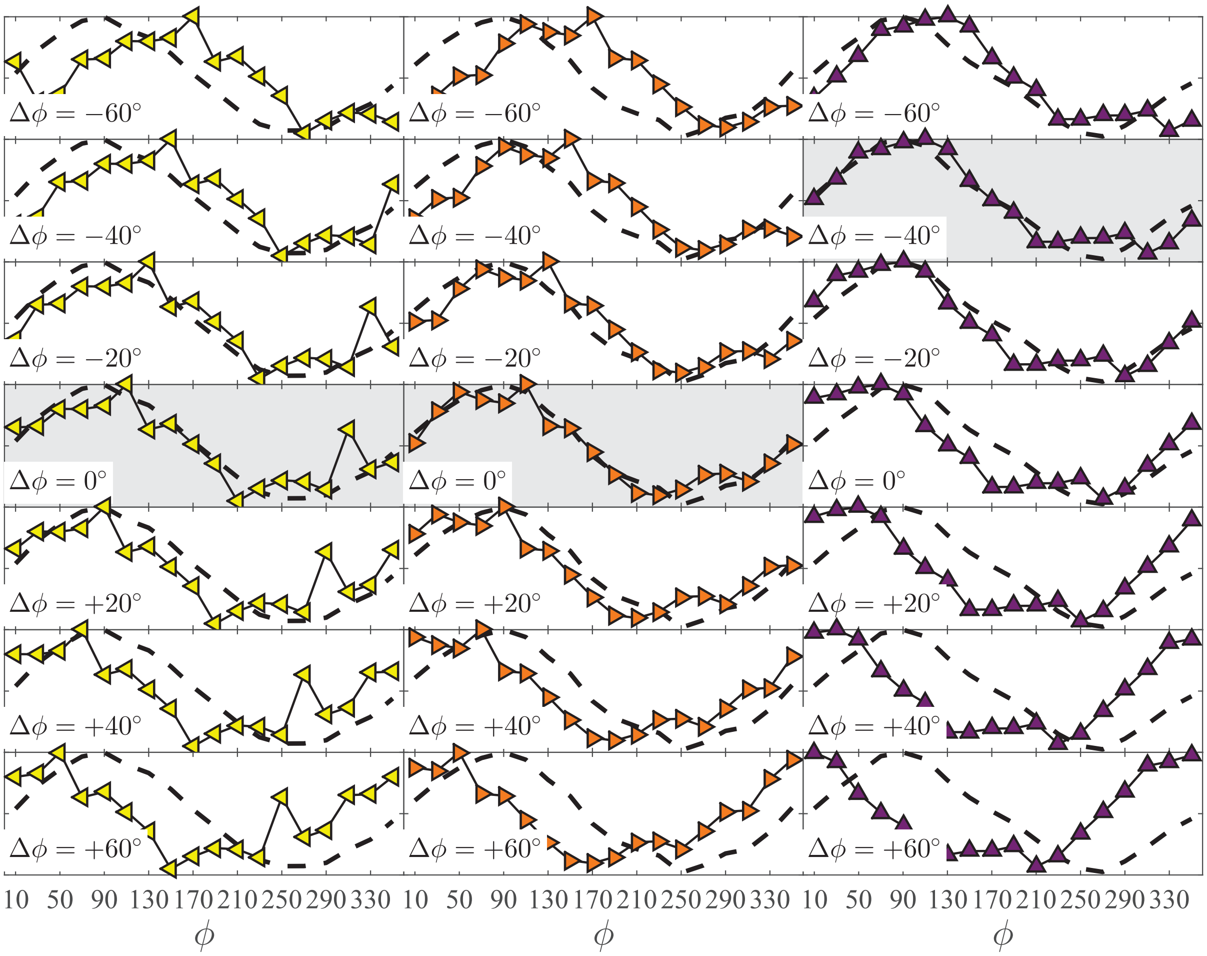

Figure 7.9: The phase difference between perturbation wall shear stress and freestream velocity for $\omega^+ = 0.007$ (left), $\omega^+ = 0.014$ (middle), and $\omega^+ = 0.020$ (right). Dashed lines correspond to the normalized freestream velocity and marker symbols are given in Table 7.1. The matching phase difference is shaded.

frequency ($\omega^+ = 0.020$) is in a different flow regime than the two lower frequencies, which is consistent with studies that find the onset of high frequency regime at $\omega^+ = 0.020$.

7.2.3 Time-averaged statistics

Wall-normal profiles in the outer coordinate

The time-averaged (averaged over discrete forcing periods) statistics of pulsatile flow is important to predict cycle-averaged transport properties (Tu and Ramaprian, 1983; Brereton *et al.*, 1990;

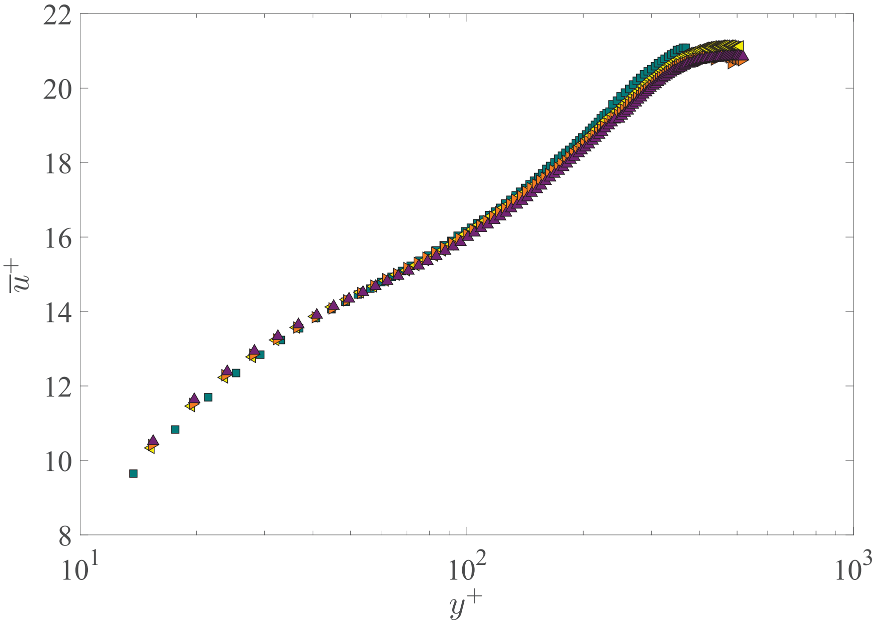

Figure 7.10: Wall-normal profiles of the mean streamwise velocity normalized by inner scales. Triangular marker symbols are provided in Table 7.1. Green squares represent the ZPG flow of approximately the same average Reynolds number.

Tardu and Binder, 1993; Tardu *et al.*, 1994; Binder *et al.*, 1995; Trip *et al.*, 2012; Weng *et al.*, 2016). In this section, the time-averaged profiles[1] of PBL flow in inner and outer coordinates are presented (triangular marker symbols). The experimental data of ZPGBL flow acquired at approximately the same Reynolds number is included for reference (square marker symbols).

- *Time-averaged Streamwise Velocity*

  The time-averaged streamwise velocity profiles as a function of inner and outer coordinates are shown in Figs. 7.10 and 7.11, respectively. The time-averaged profiles show only small differences compared to ZPGBL flow in both inner and outer coordinates. In general, the PBL flows lie, respectively, slightly above and slightly below the ZPGBL profiles in the inner and outer layers of the boundary layer, which suggest slightly higher values of the von Kármán coefficient. To investigate the existence of a logarithmic region and estimate

---

[1] The time-averaged turbulent profiles (-$\overline{u'v'}$, $\overline{v'^2}$ and $\overline{u'^2}$) are filtered using a median filter with a window size of 11.

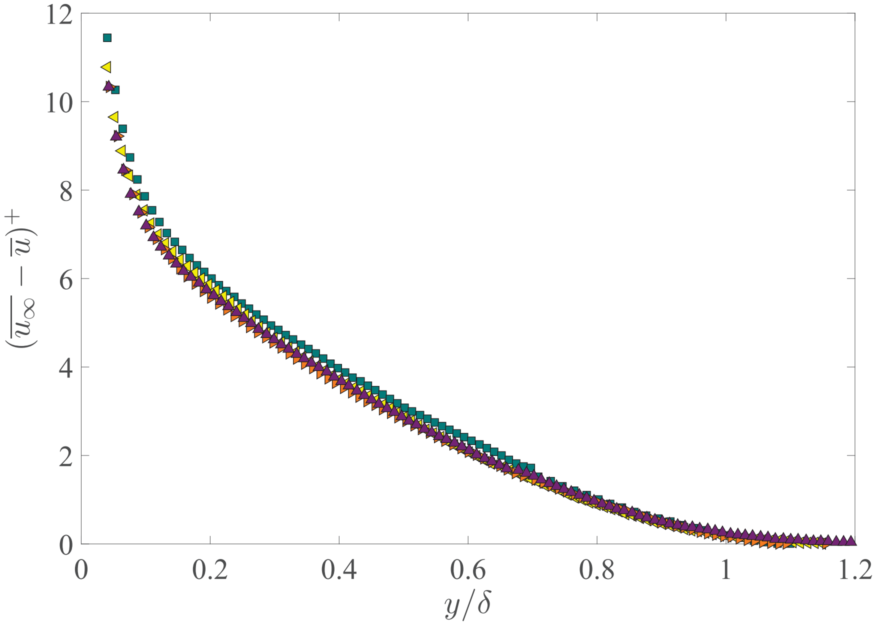

Figure 7.11: Wall-normal profiles of the mean streamwise velocity as a function of outer coordinate. Marker symbols are the same as Fig. 7.10.

the von Kármán coefficient, the indicator function $\Xi \equiv y^+ \frac{\partial U^+}{\partial y^+}$ is plotted for the PBL and ZPGBL flows. Obvious from Fig. 7.12 the time-averaged mean profiles exhibit a logarithmic behavior (i.e., a local minima) at $40 \lesssim y^+ \lesssim 70$. For ZPGBL flow, in the inertial layer, $\Xi \simeq 2.45$, which corresponds to $\kappa \equiv \frac{1}{\Xi} \simeq 0.41$. For PBL flow $\kappa = 0.45, 0.42, 0.47$ for $\omega^+ = 0.007, 0.014, 0.020$, respectively.

- *Time-averaged Streamwise Turbulence Intensity*

The time-averaged streamwise turbulence intensity profiles as a function inner, outer and mixed coordinates are shown in Figs. 7.13, 7.14 and Figs. 7.15, respectively. The highest frequency case ($\omega^+ = 0.020$) shows the smallest differences compared to the ZPGBL profile, while the lowest frequency ($\omega^+ = 0.007$) shows the largest differences. The turbulence intensity in the streamwise direction is higher than the ZPGBL in the outer layer, and it appears to asymptote to the ZPGBL in the inner layer ($y^+ < 30$). The higher streamwise turbulence intensity levels in the outer layer, which appears to be inversely proportional with

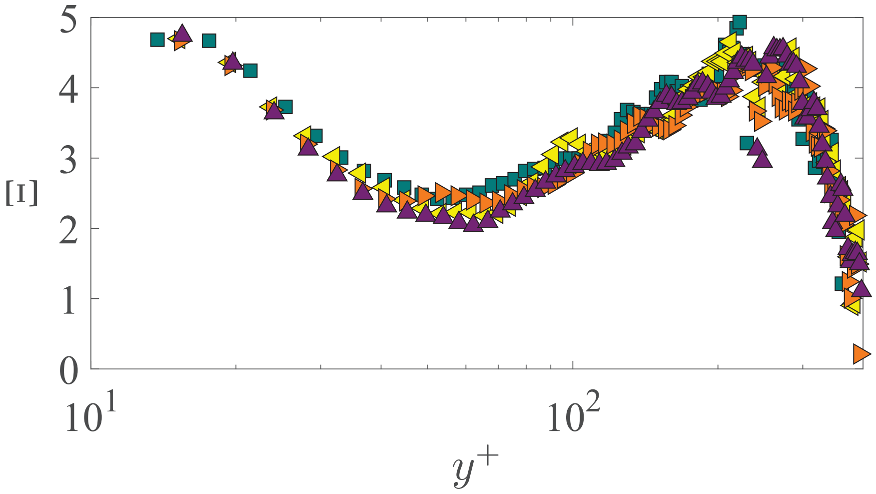

Figure 7.12: Indicator function profiles as a function of wall-normal position. Marker symbols are the same as Fig. 7.10.

flow frequency, has previously been observed by Tardu *et al.* (1994), but other studies show that the turbulent intensity profiles in the outer layer is similar to ZPGBL.

- *Time-averaged Wall-Normal Turbulence Intensity*

  The time-averaged wall-normal turbulence intensity profiles as a function of inner and outer coordinates are shown in Figs. 7.16 and 7.17, respectively. Here the highest frequency case shows the smallest difference compared to the ZPGBL profile, whereas the wall-normal turbulence intensity for the two lower frequencies are slightly higher than the ZPGBL profile.

- *Time-averaged Reynolds Shear Stress*

  The time-averaged Reynolds shear stress profiles as a function of inner and outer coordinates are shown in Figs. 7.18 and 7.19, respectively. While the lowest frequency case shows the smallest difference compared to the ZPGBL profile, the high measurement uncertainty makes it difficult to draw any definite conclusions.

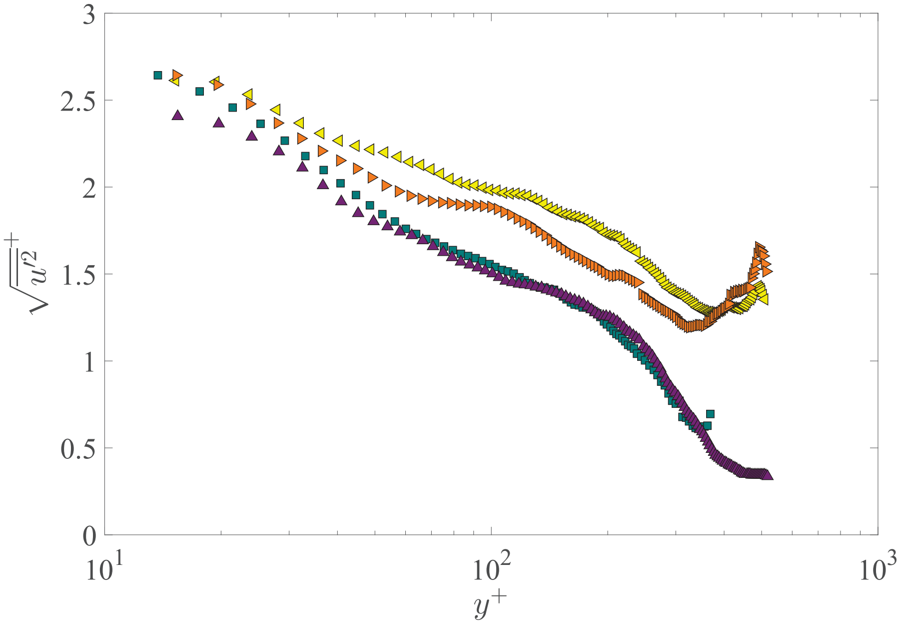

Figure 7.13: Wall-normal profiles of the streamwise RMS velocity normalized by inner scales. Marker symbols are the same as Fig. 7.10.

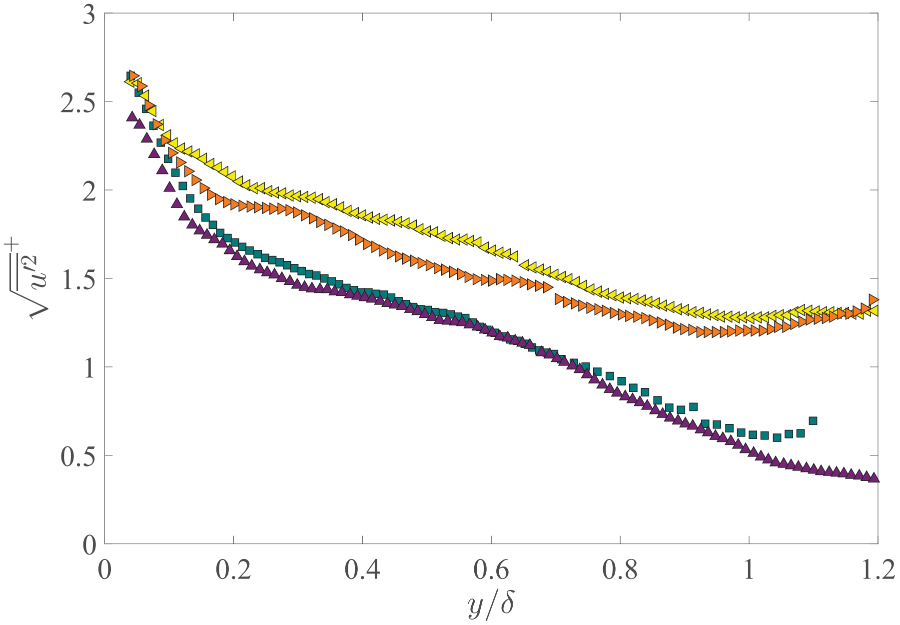

Figure 7.14: Wall-normal profiles of the streamwise RMS velocity as a function of outer coordinate. Marker symbols are the same as Fig. 7.10.

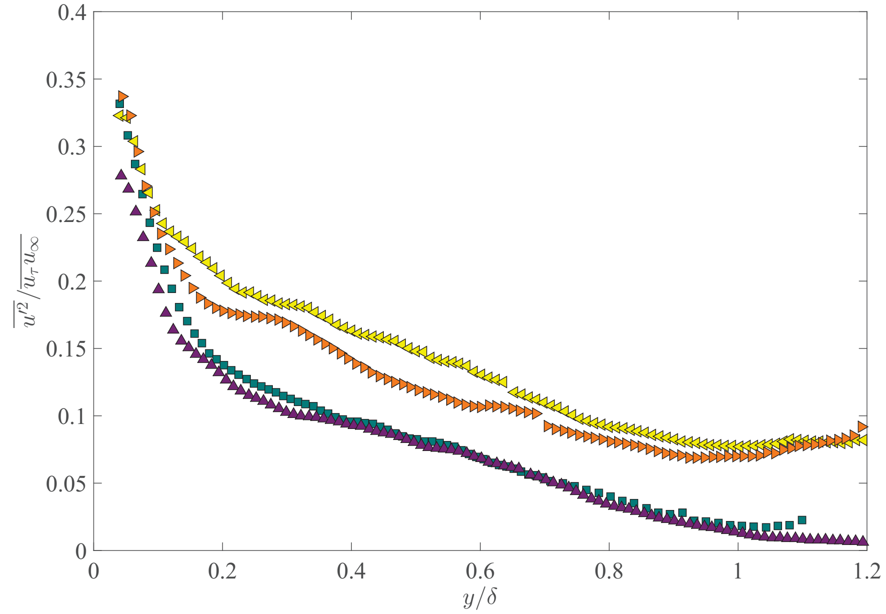

Figure 7.15: Wall-normal profiles of the streamwise RMS velocity as a function of mixed coordinate. Marker symbols are the same as Fig. 7.10.

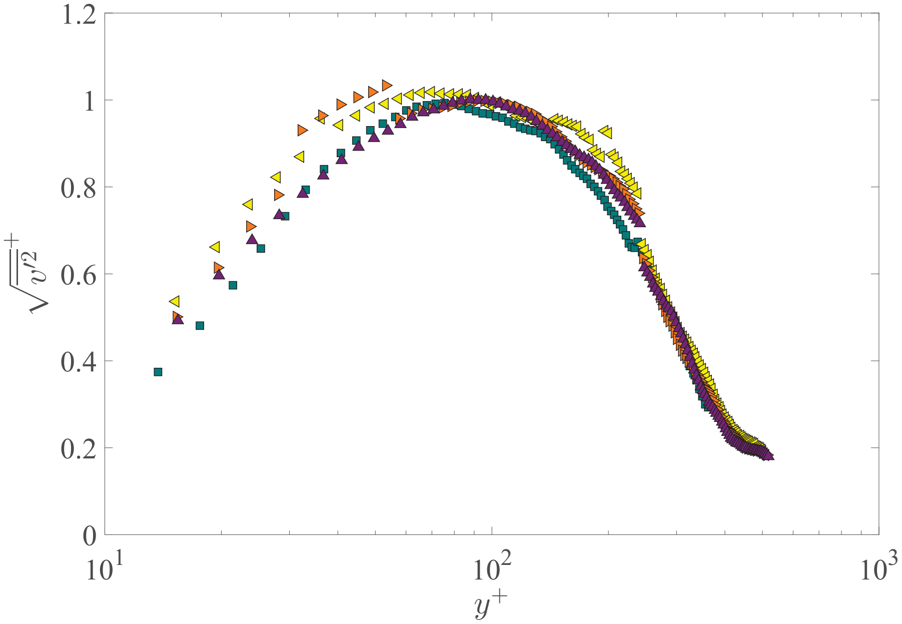

Figure 7.16: Wall-normal profiles of the wall-normal RMS velocity normalized by inner scales. Marker symbols are the same as Fig. 7.10.

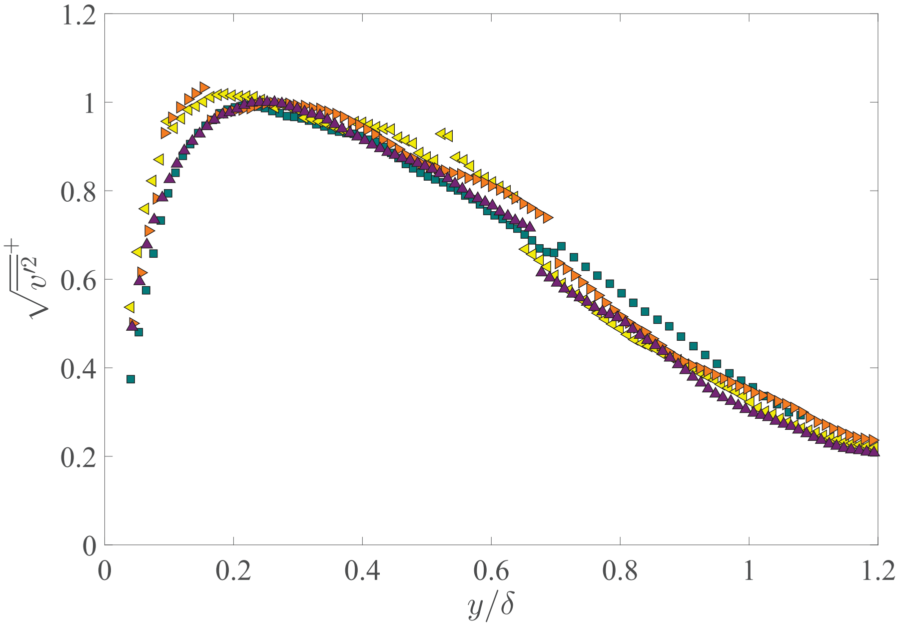

Figure 7.17: Wall-normal profiles of the wall-normal RMS velocity as a function of outer coordinate. Marker symbols are the same as Fig. 7.10.

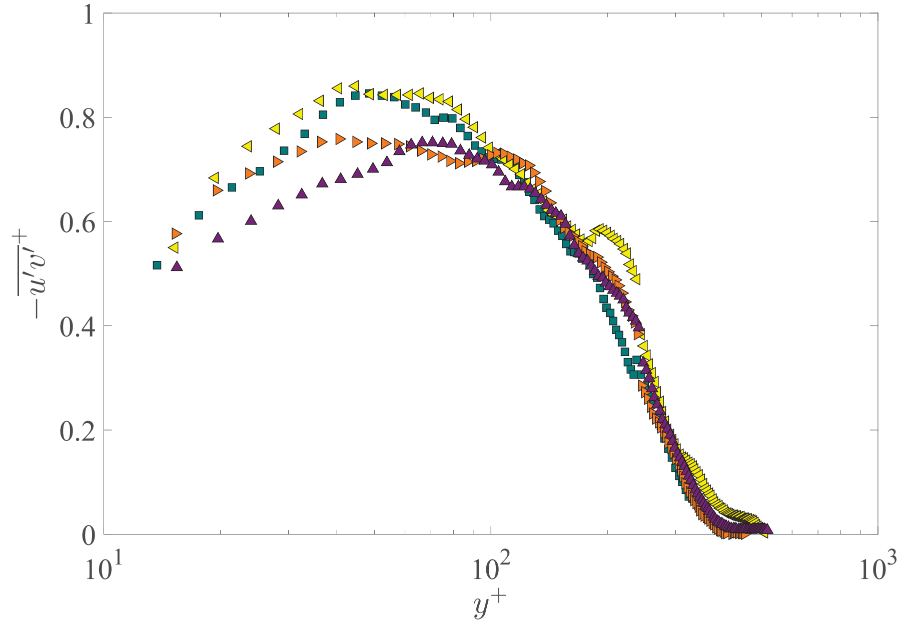

Figure 7.18: Wall-normal profiles of the Reynolds shear stress normalized by inner scales. Marker symbols are the same as Fig. 7.10.

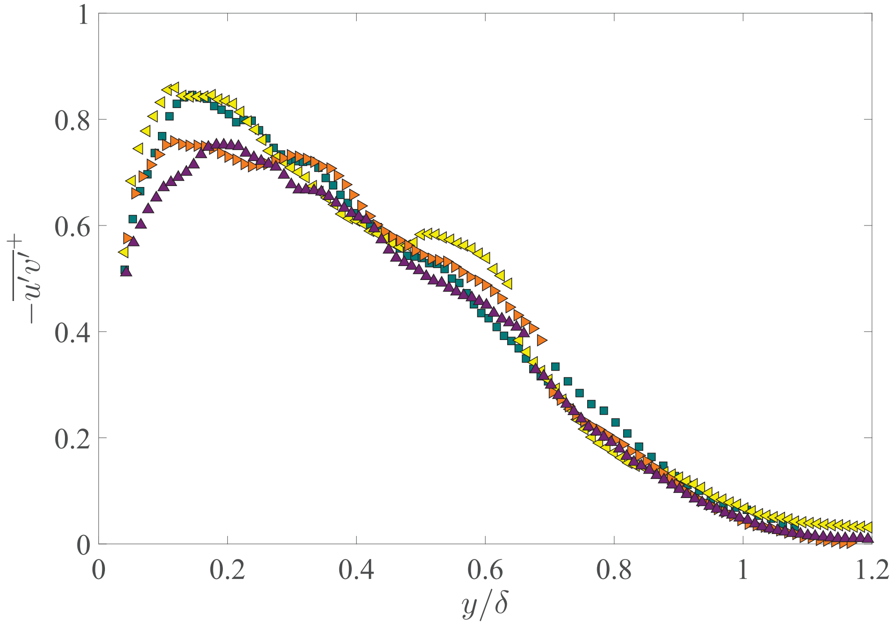

Figure 7.19: Wall-normal profiles of the Reynolds shear stress as a function of outer coordinate. Marker symbols are the same as Fig. 7.10.

7.2.4 Phase-Averaged Statistics

Wall-normal profiles normalized by inner scales

The wall-normal profiles of the phase-averaged statistics normalized by instantaneous inner scales are shown in Figs. 7.20-7.27. Results of the comparison between the phase-averaged flow statistics of PBL flow compared to ZPGBL flow are described below:

- *Phase-Averaged Streamwise Velocity*

  Wall-normal profiles of the phase-averaged streamwise velocity in PBL flow as a function of phase angle are shown in Figs 7.20 and 7.21. The fluctuations of the PBL profiles compared to the ZPGBL profile are best detected when two phases that are180° apart are compared. For example, the PBL profiles for $\omega^+ = 0.020$ are below and above ZPG profiles at $\phi = 10°$ and $\phi = 190°$, respectively. The magnitude of the fluctuations between PBL and ZPGBL are small for $y^+ \lesssim 20$. The lowest frequency case ($\omega^+ = 0.007$) exhibits the largest deviation from the ZPGBL flow at $\phi = 310°$. All cases effectively collapse on the ZPGBL flow profiles at $\phi = 230°, 330°$. Interestingly, it is at these two phases where the PBL flow experiences approximately the same favorable pressure gradient as the ZPGBL flow.

- *Phase-Averaged Reynolds Shear Stress Velocity* (Figs.7.22 & 7.23)

  The uncertainty in the Reynolds shear stress is high owing to the low number of recorded cycles ($\sim$60), which is a consequence of the limited camera RAM. Compared to ZPGBL flow, the Reynolds shear stress in PBL flow is similar in the outer region of the boundary layer. The large fluctuations in the near wall region ($y^+ \lesssim 50$) are within the experimental uncertainty.

- *Phase-Averaged Wall-Normal Velocity Fluctuations* (Figs.7.24 & 7.25)

  The shape of the profiles of the wall-normal fluctuations in PBL flow are similar to ZPGBL flow. In the outer region of the boundary layer ($y^+ \gtrsim 50$), the PBL profiles fluctuate about the ZPGBL profile. In the near-wall region ($y^+ \lesssim 50$) the large fluctuations are within experimental uncertainty.

- *Phase-Averaged Streamwise Velocity Fluctuations*

  The streamwise velocity fluctuations show large differences between the PBL and ZPGBL flows. In general the fluctuations are larger in magnitude for the PBL flow at all phases. The fluctuations are also consistently higher at the two lower frequencies ($\omega^+ = 0.007$ and 0.014). Interestingly, the PBL profiles are closest to the ZPGBL profile at $\phi = 90°$ and $\phi = 270°$, corresponding to where the flow is at maximum and minimum velocity, respectively (i.e., when the sign of the acceleration changes). The higher level of turbulence intensity in PBL flow measured in the present experiment for the current frequency range is in disagreement with previous studies (Brereton and Mankbadi, 1995; Weng *et al.*, 2016).

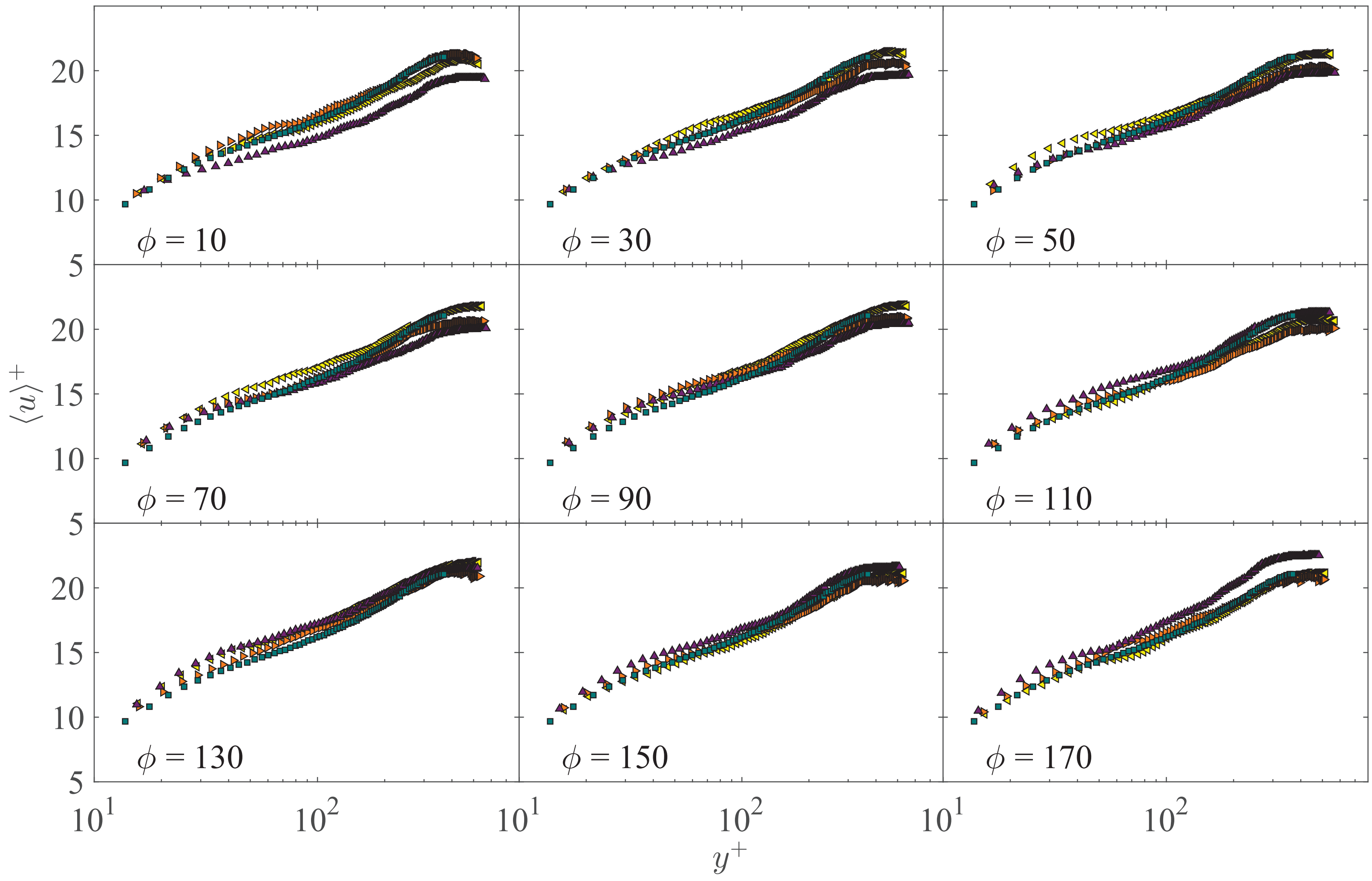

Figure 7.20: The phase-averaged streamwise velocity profiles in PBL flow. Marker symbols are the same as Fig. 7.10.

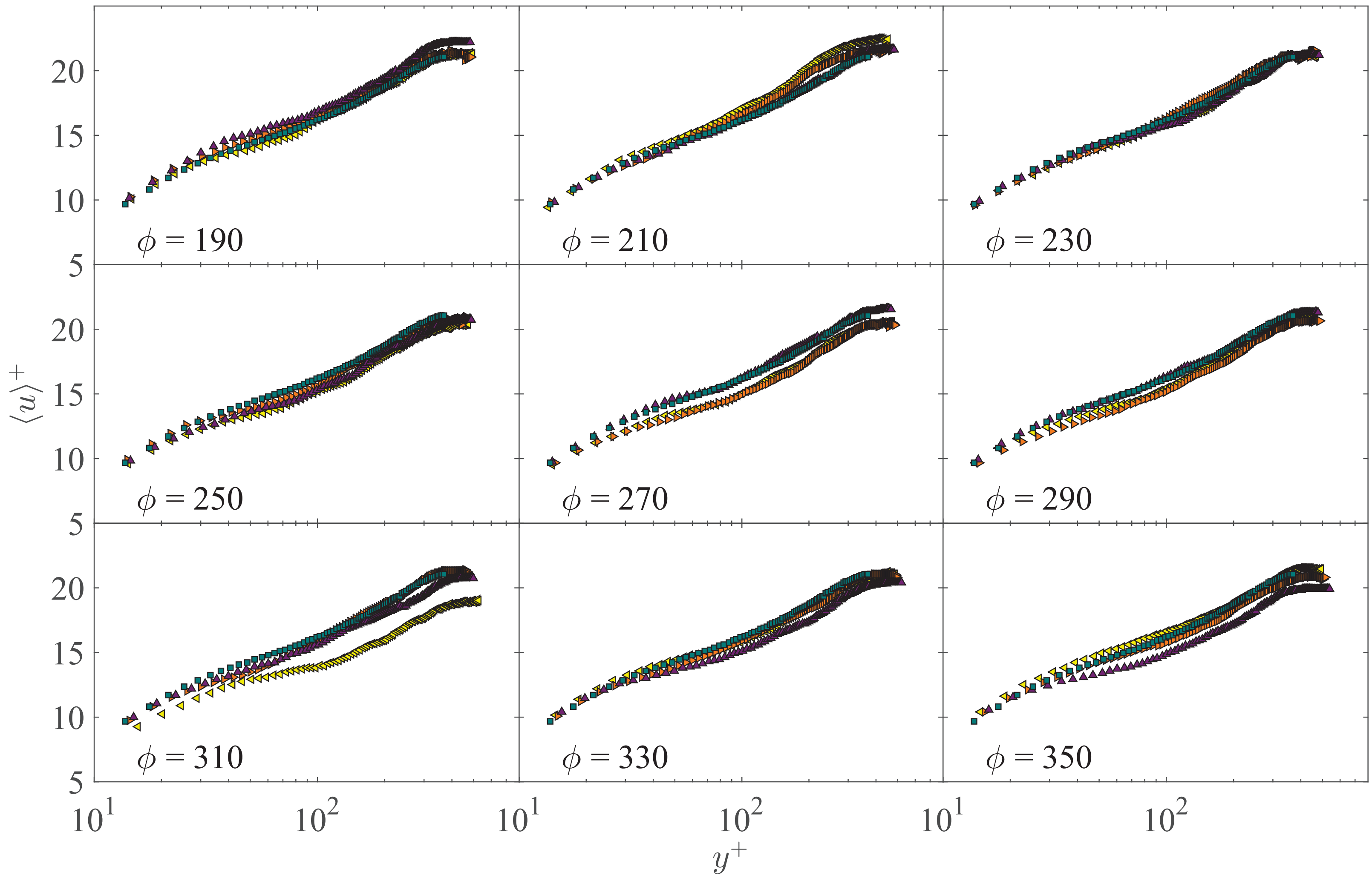

Figure 7.21: The phase-averaged streamwise velocity profiles in PBL flow. Marker symbols are the same as Fig. 7.10.

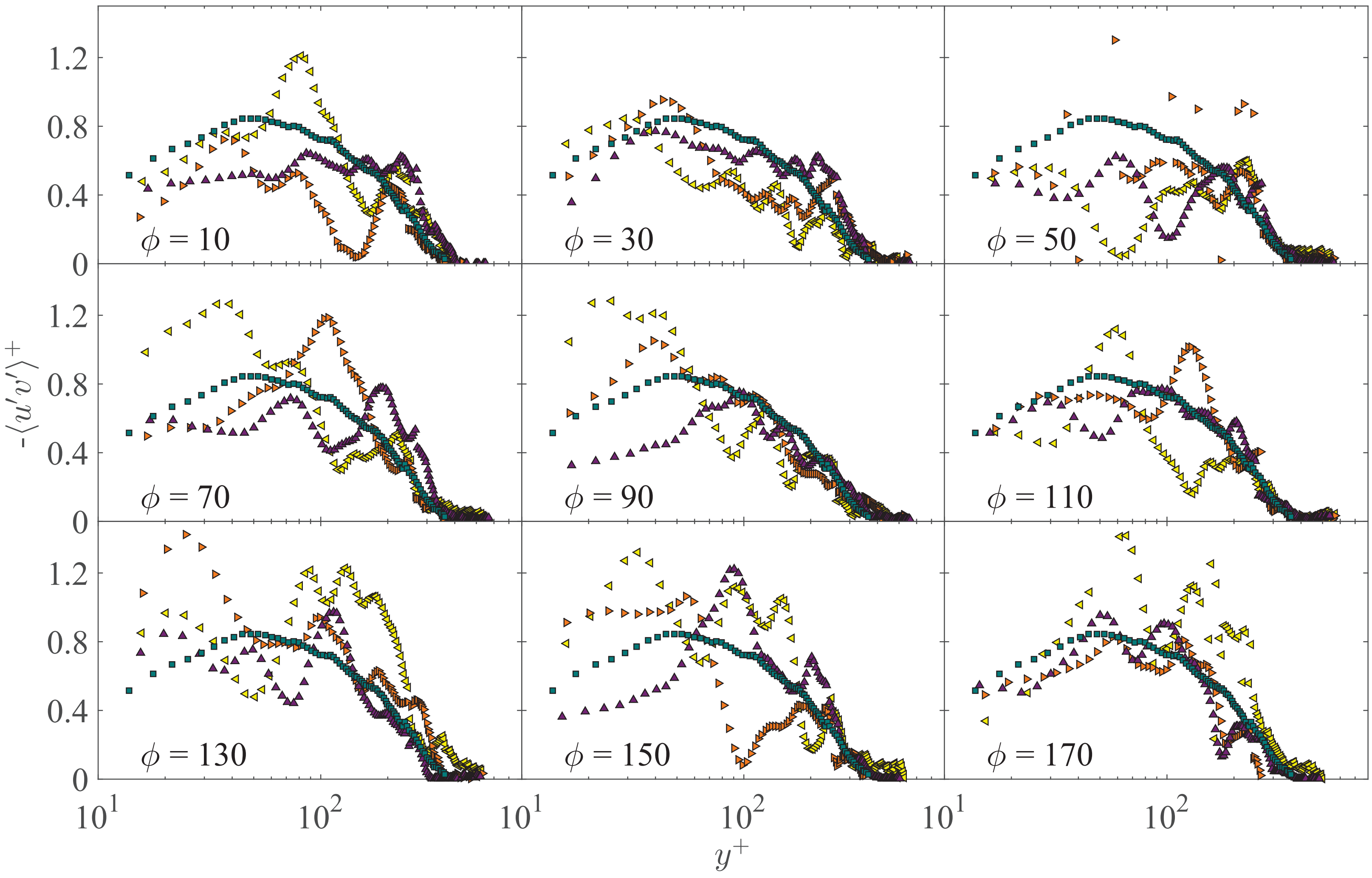

Figure 7.22: The phase-averaged Reynolds stress profiles in PBL flow. Marker symbols are the same as Fig. 7.10.

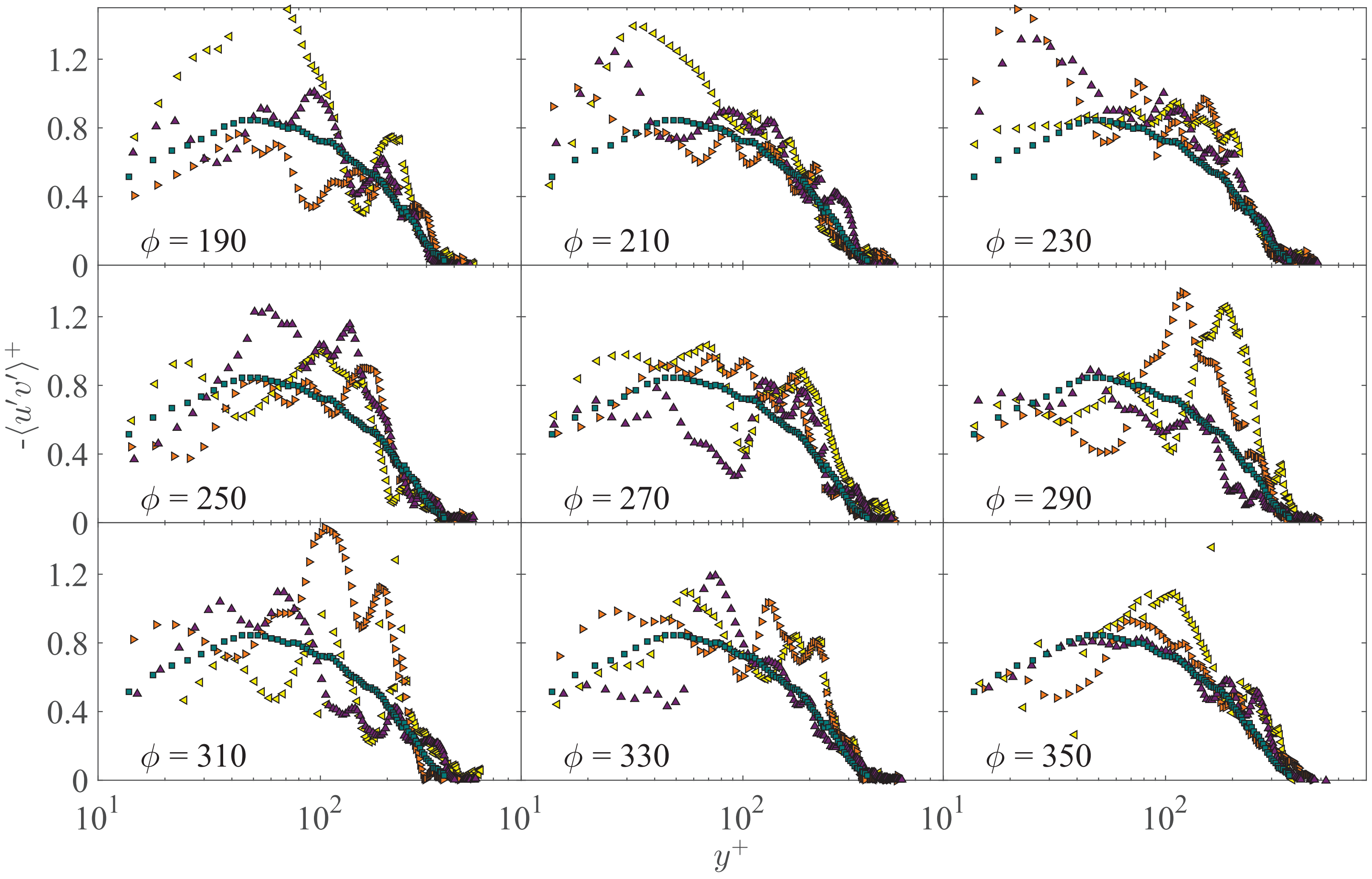

Figure 7.23: The phase-averaged Reynolds stress profiles in PBL flow. Marker symbols are the same as Fig. 7.10.

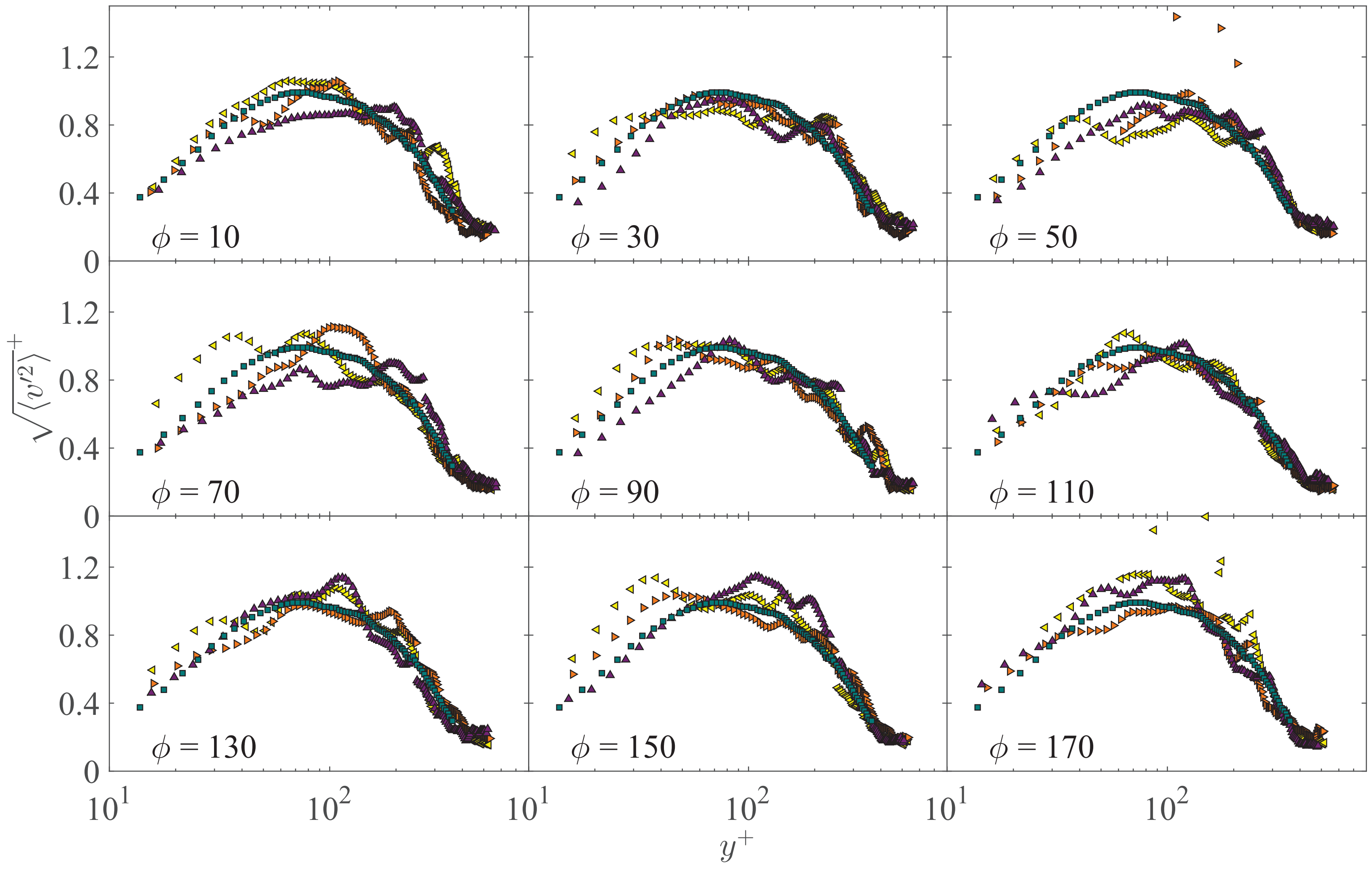

Figure 7.24: The phase-averaged wall-normal velocity RMS in PBL flow. Marker symbols are the same as Fig. 7.10.

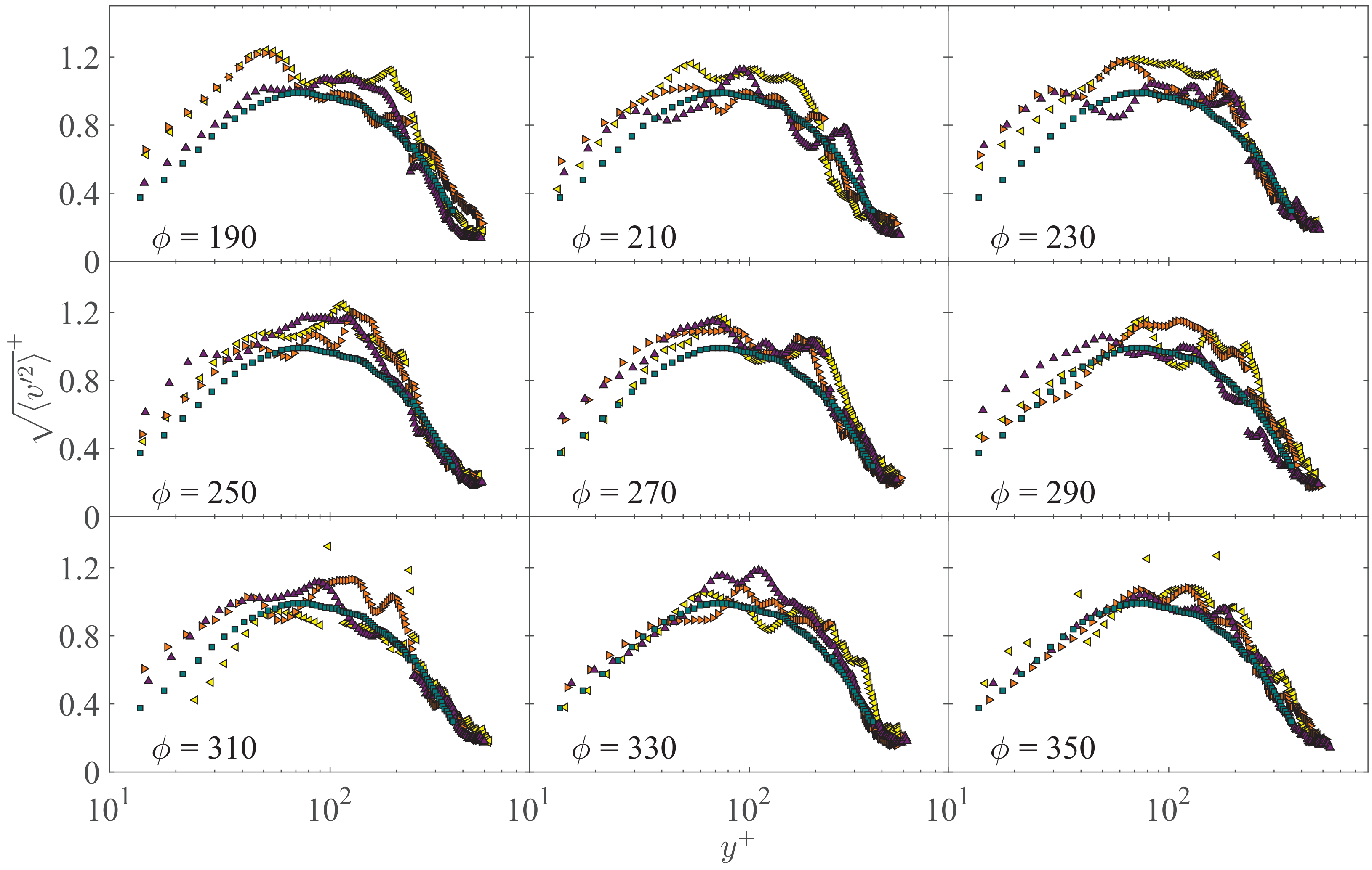

Figure 7.25: The phase-averaged wall-normal velocity RMS in PBL flow. Marker symbols are the same as Fig. 7.10.

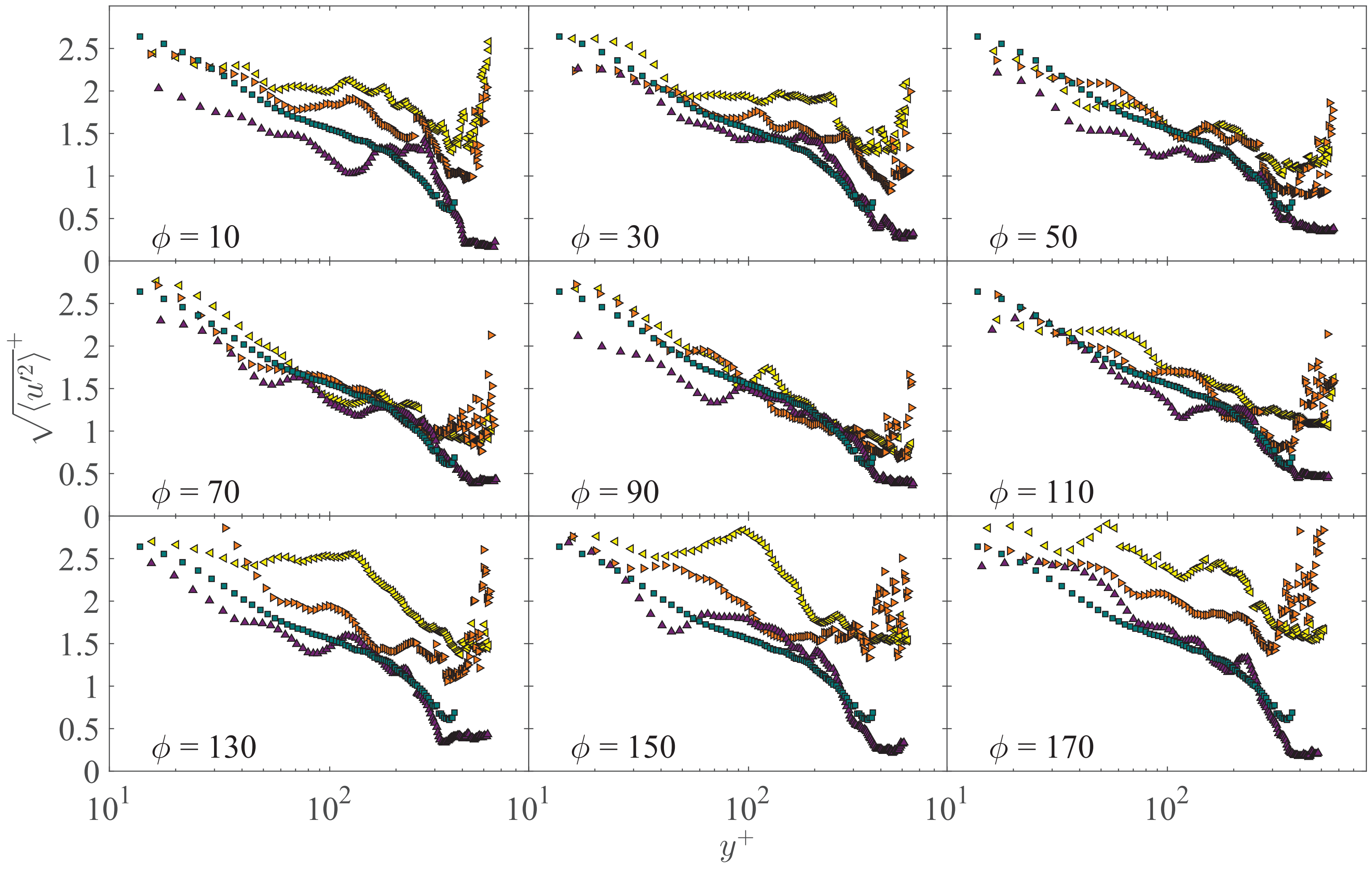

Figure 7.26: The phase-averaged streamwise velocity RMS in PBL flow. Marker symbols are the same as Fig. 7.10.

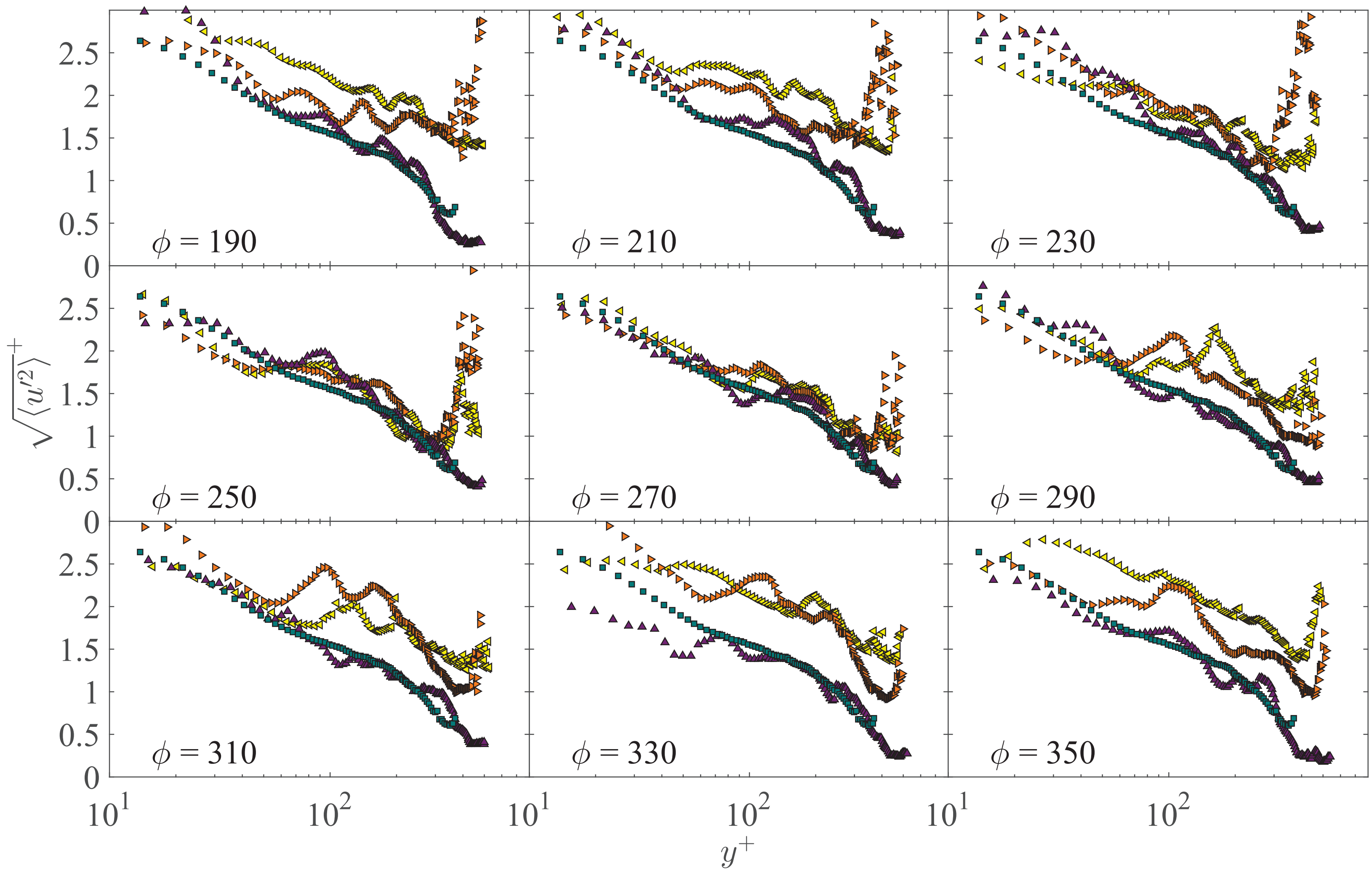

Figure 7.27: The phase-averaged streamwise velocity RMS in PBL flow. Marker symbols are the same as Fig. 7.10.

Wall-normal profiles in the outer coordinate

The wall-normal profiles of the phase-averaged statistics as a function of outer coordinate are shown in Figs. 7.28-7.37. Results of the phase-averaged wall-normal profiles of the turbulent statistics acquired in PBL flow compared to that of ZPGBL flow are provided below.

- *Phase-Averaged Streamwise Velocity* (Figs.7.28 & 7.29)

  The behavior of the wall-normal mean velocity profiles in PBL flow are different between the first-half of the cycle ($10° \leq \phi \leq 170°$) compared to the second-half of the cycle ($190° \leq \phi \leq 350°$). In the first-half, the PBL profiles are generally below the ZPGBL profiles, and the lowest frequency case ($\omega^+ = 0.007$) exhibits the least deviation from the ZPGBL profiles. In the second-half, however, the PBL profiles are slightly above the ZPGBL profiles from $190° \leq \phi \leq 250°$ and they are in close agreement with the ZPGBL profile at $270° < \phi \leq 350°$. Deviation of the mean velocity profiles from the ZPGBL flow in inner and outer layers, especially at $\phi \leq 250$ is an indicator of non-equilibrium flow behaviors in the PBL flow during the late phases of the cycle.

- *Phase-Averaged Reynolds Shear Stress Velocity* (Figs.7.30 & 7.31)

  As described earlier, the uncertainty in the Reynolds shear stress is high making it difficult to draw any conclusions regarding the effects of periodic forcing on the Reynolds stress.

- *Phase-Averaged Wall-Normal Velocity Fluctuations* (Figs.7.32 & 7.33)

  The wall-normal turbulence intensity profiles for the PBL flow are of similar shape to the ZPGBL flow. The magnitude of the fluctuations about the ZPGBL profiles is comparable between the three frequencies.

- *Phase-Averaged Streamwise Velocity Fluctuations* (Figs.7.34 & 7.35)

  The highest frequency case ($\omega^+ = 0.020$) shows the smallest differences compared to the ZPGBL profile, while the lowest frequency ($\omega^+ = 0.007$) shows the largest differences. The deviation of the turbulence intensity from the ZPGBL profiles for the two lower frequency cases is minimum from $50^\circ \leq \phi \leq 110^\circ$ and $250^\circ \leq \phi \leq 270^\circ$, where the freestream velocity is near its peak and trough, respectively.

De Graaff and Eaton (2000) introduced a mixed scaling to minimize the Reynolds number dependence of the streamwise turbulence intensity in the outer layer. In this mixed scaling, the turbulence intensity $\langle u'^2 \rangle$ is normalized by $u_\tau U_\infty$. The streamwise turbulence intensity profiles in the mixed scaling are shown in Figs. 7.36 and 7.37. While the mixed scaling appears to be more appropriate, the general observations deducted from the profiles plotted in the outer coordinate remain valid.

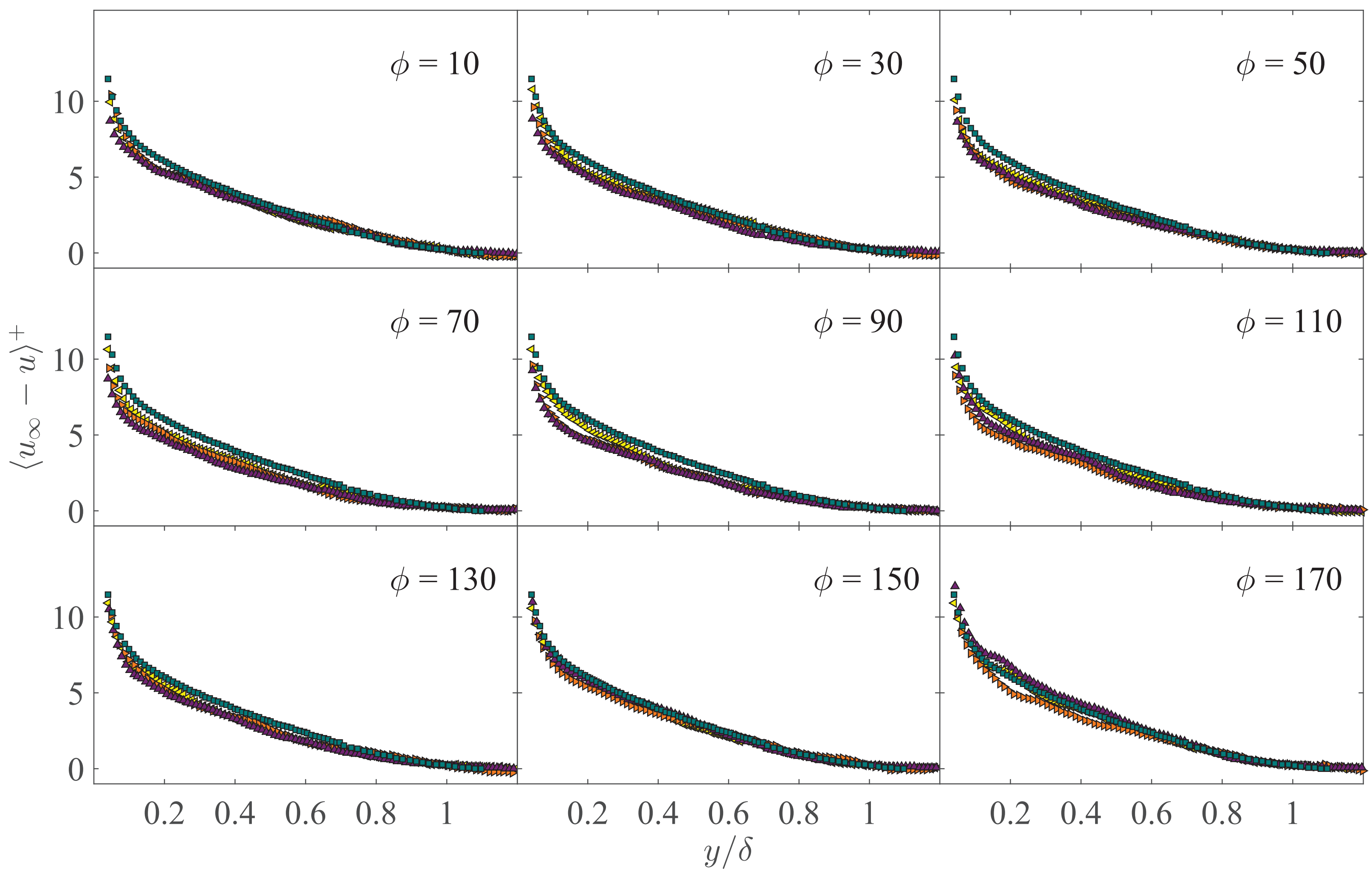

Figure 7.28: The phase-averaged streamwise velocity profiles in PBL flow. Marker symbols are the same as Fig. 7.10.

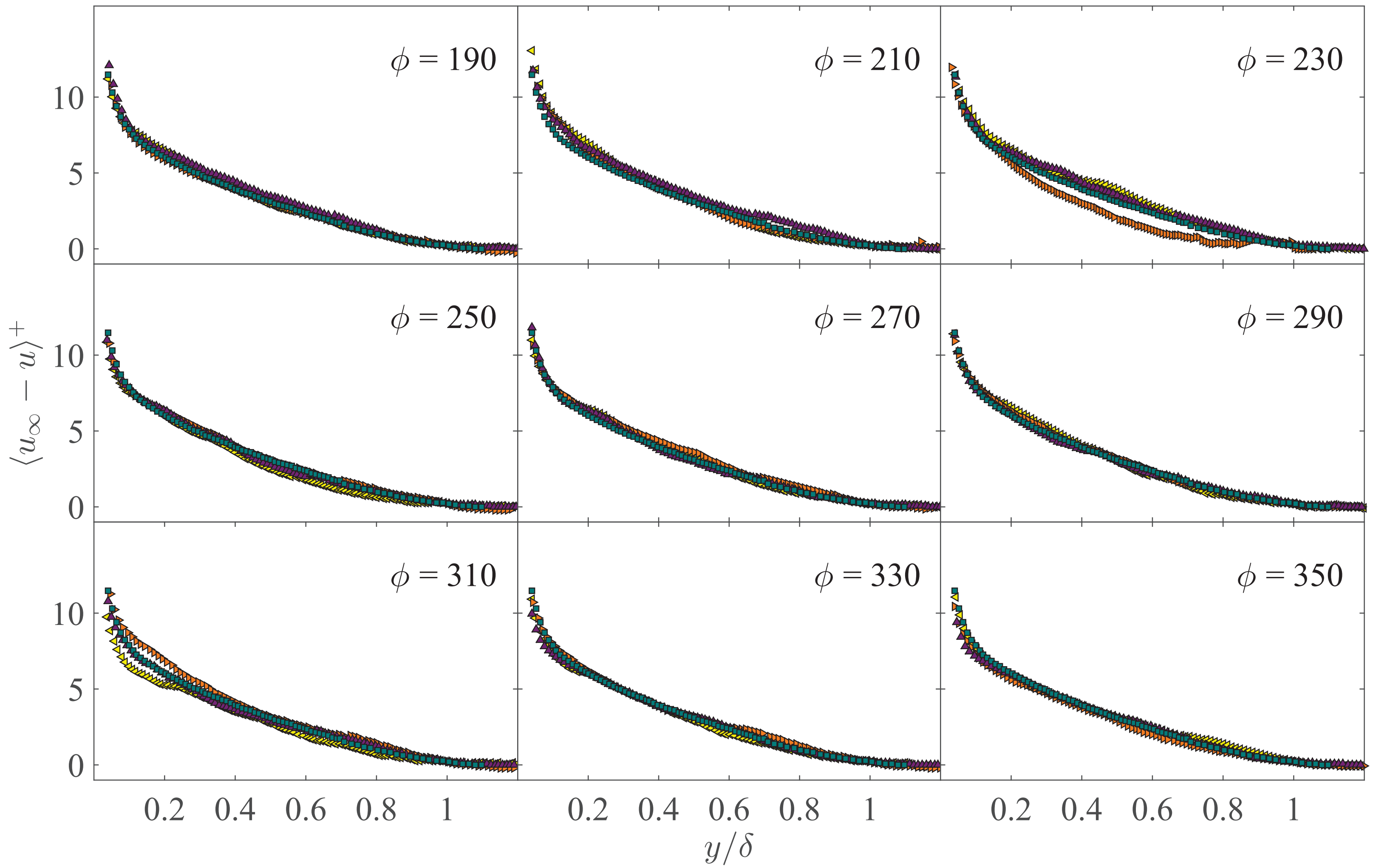

Figure 7.29: The phase-averaged streamwise velocity profiles in PBL flow. Marker symbols are the same as Fig. 7.10.

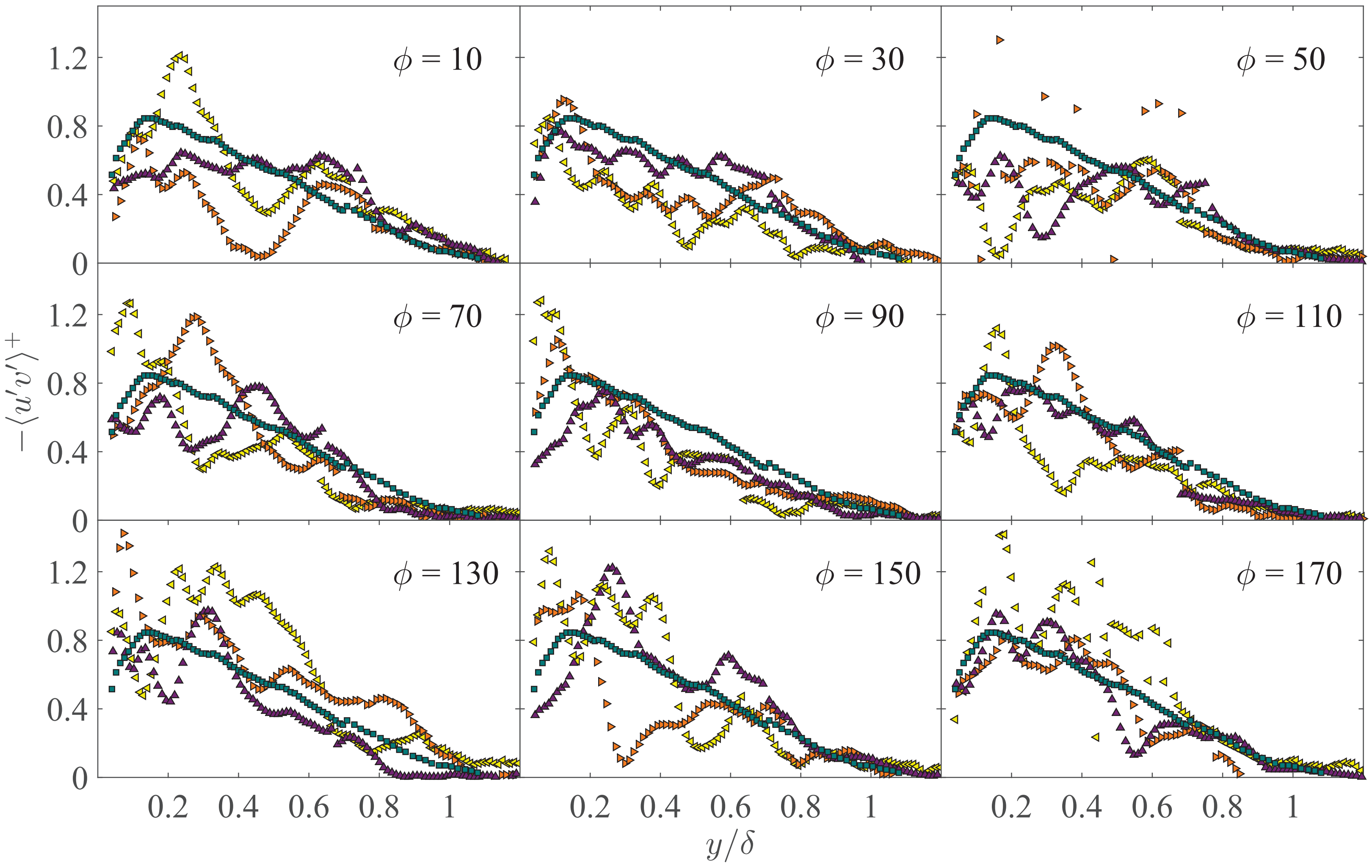

Figure 7.30: The phase-averaged Reynolds stress profiles in PBL flow. Marker symbols are the same as Fig. 7.10.

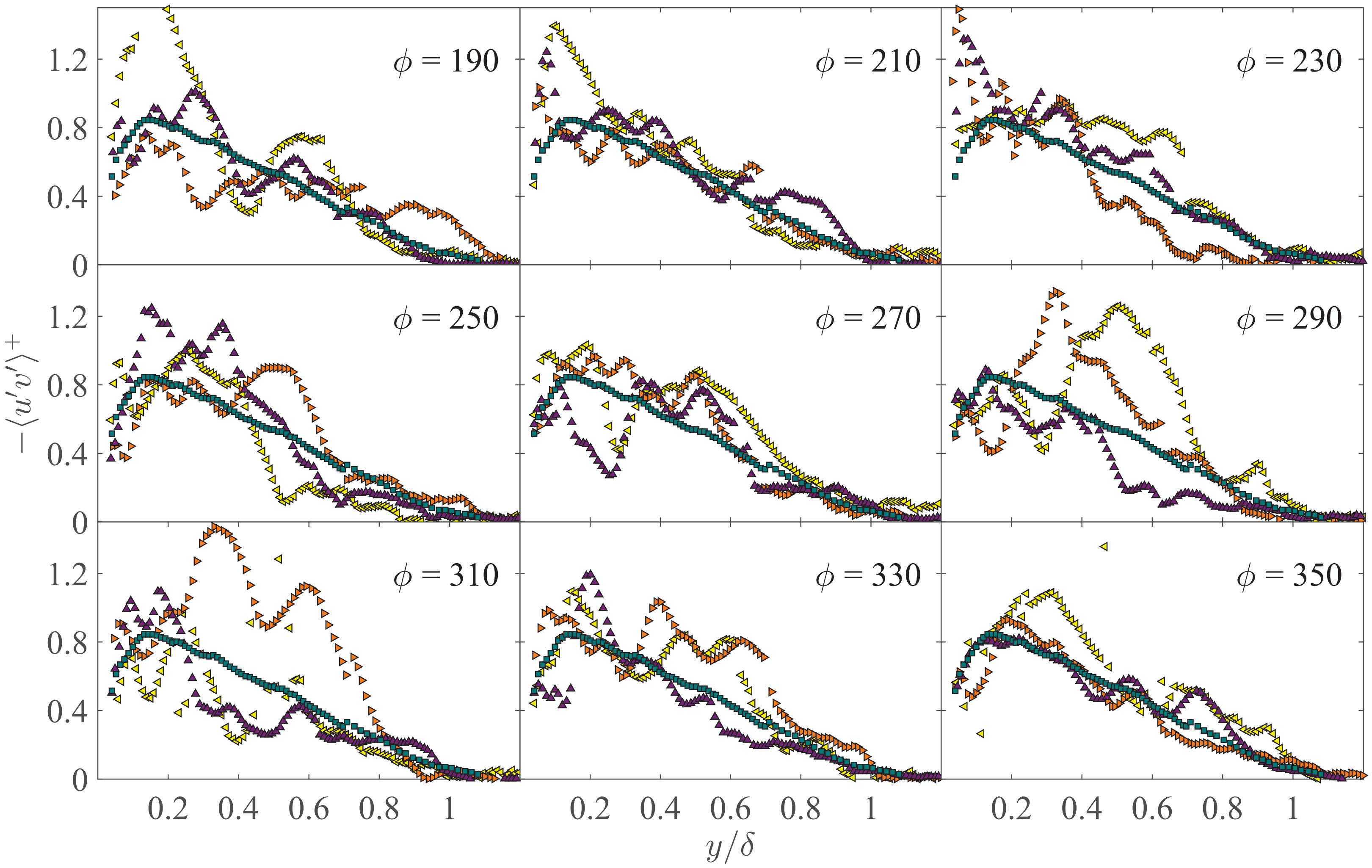

Figure 7.31: The phase-averaged Reynolds stress profiles in PBL flow. Marker symbols are the same as Fig. 7.10.

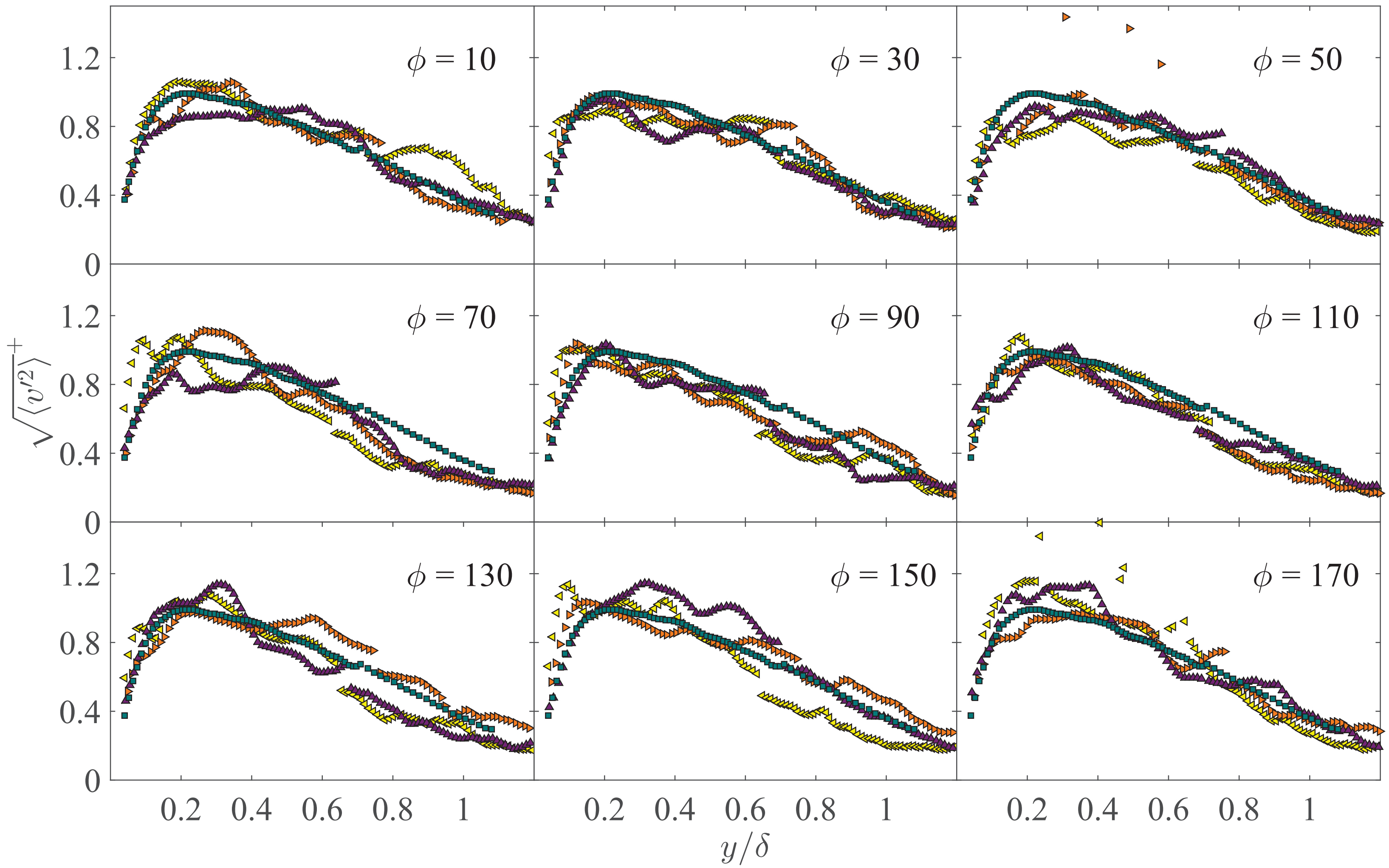

Figure 7.32: The phase-averaged wall-normal velocity RMS in PBL flow. Marker symbols are the same as Fig. 7.10.

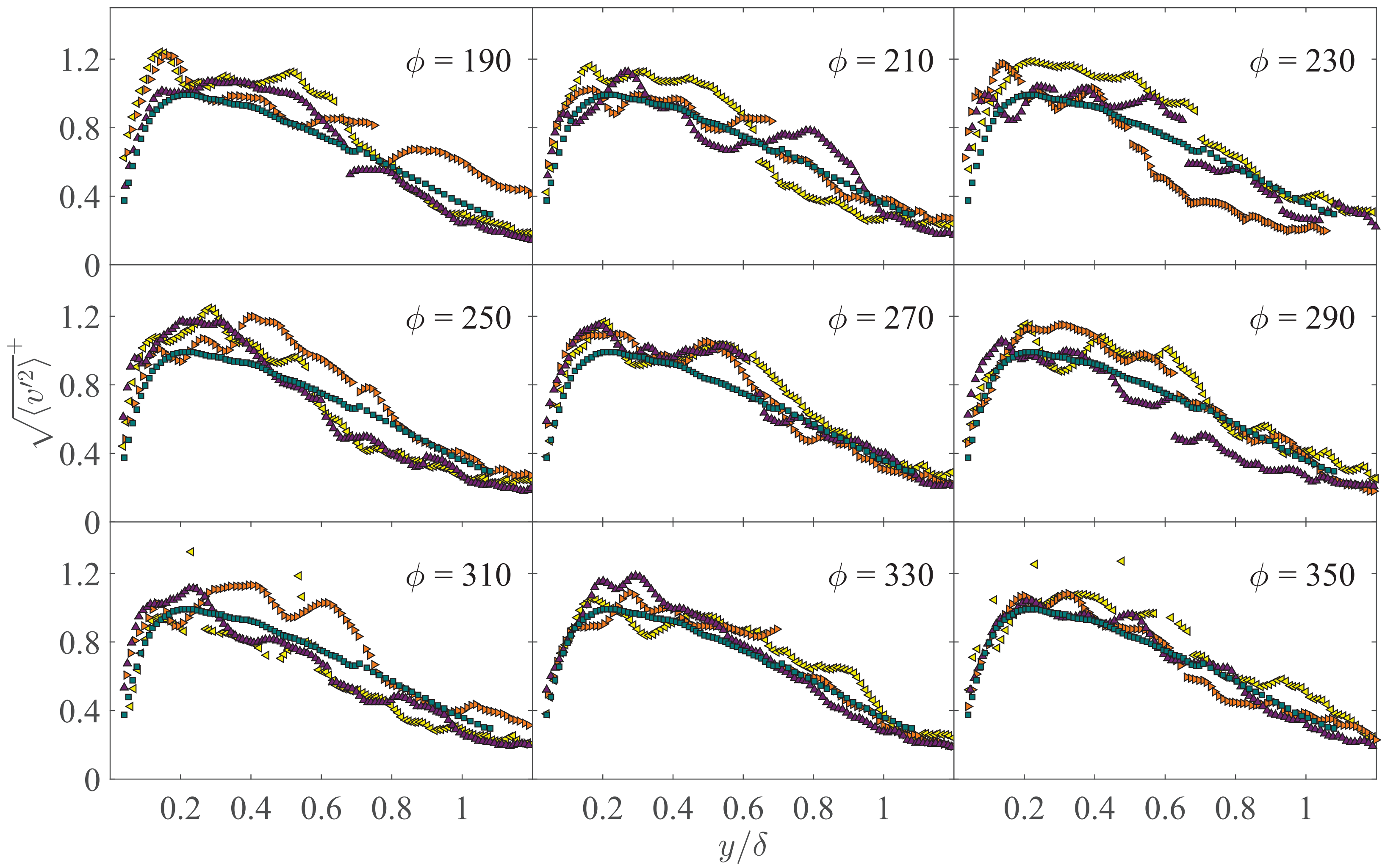

Figure 7.33: The phase-averaged wall-normal velocity RMS in PBL flow. Marker symbols are the same as Fig. 7.10.

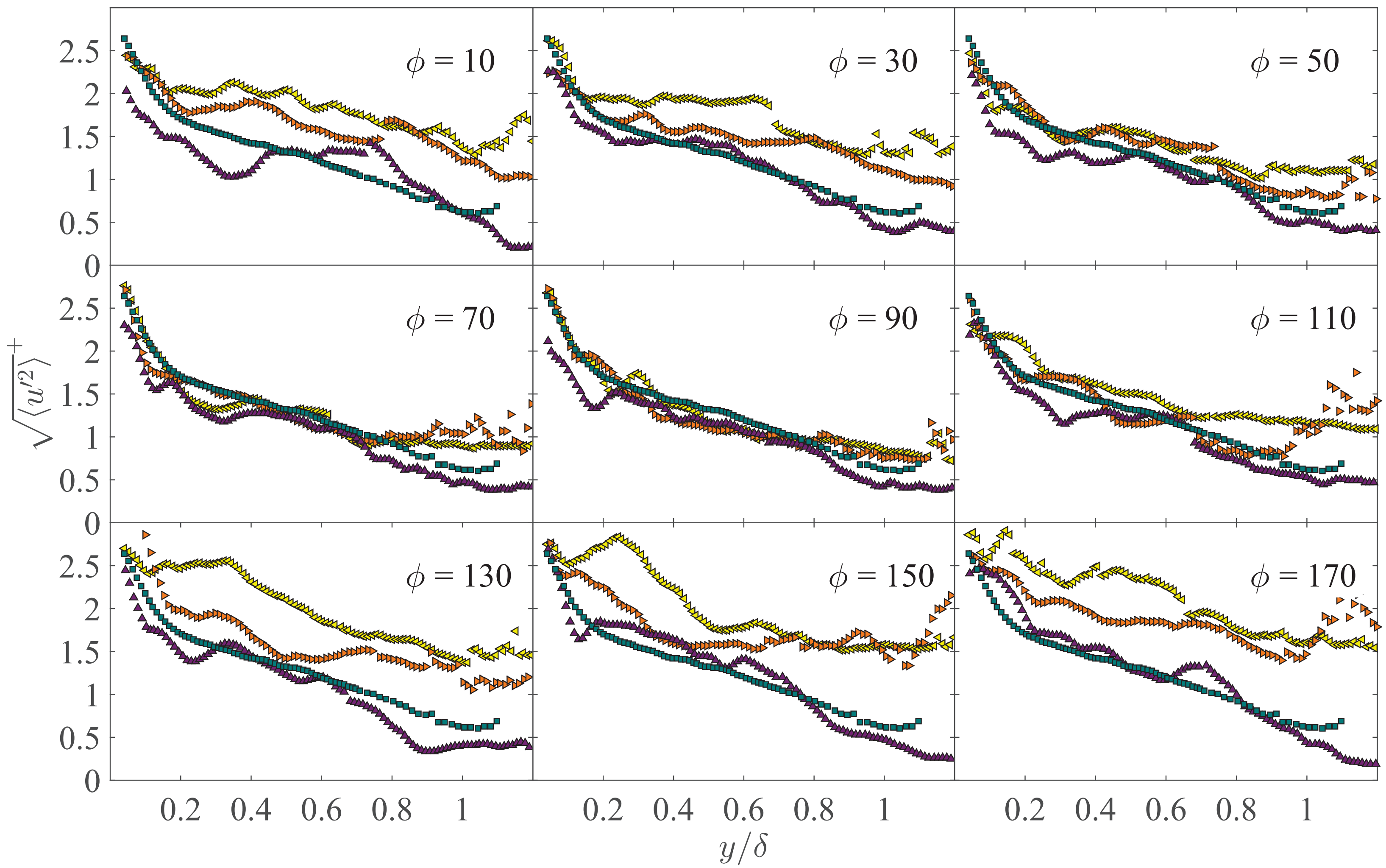

Figure 7.34: The phase-averaged streamwise velocity RMS in PBL flow. Marker symbols are the same as Fig. 7.10.

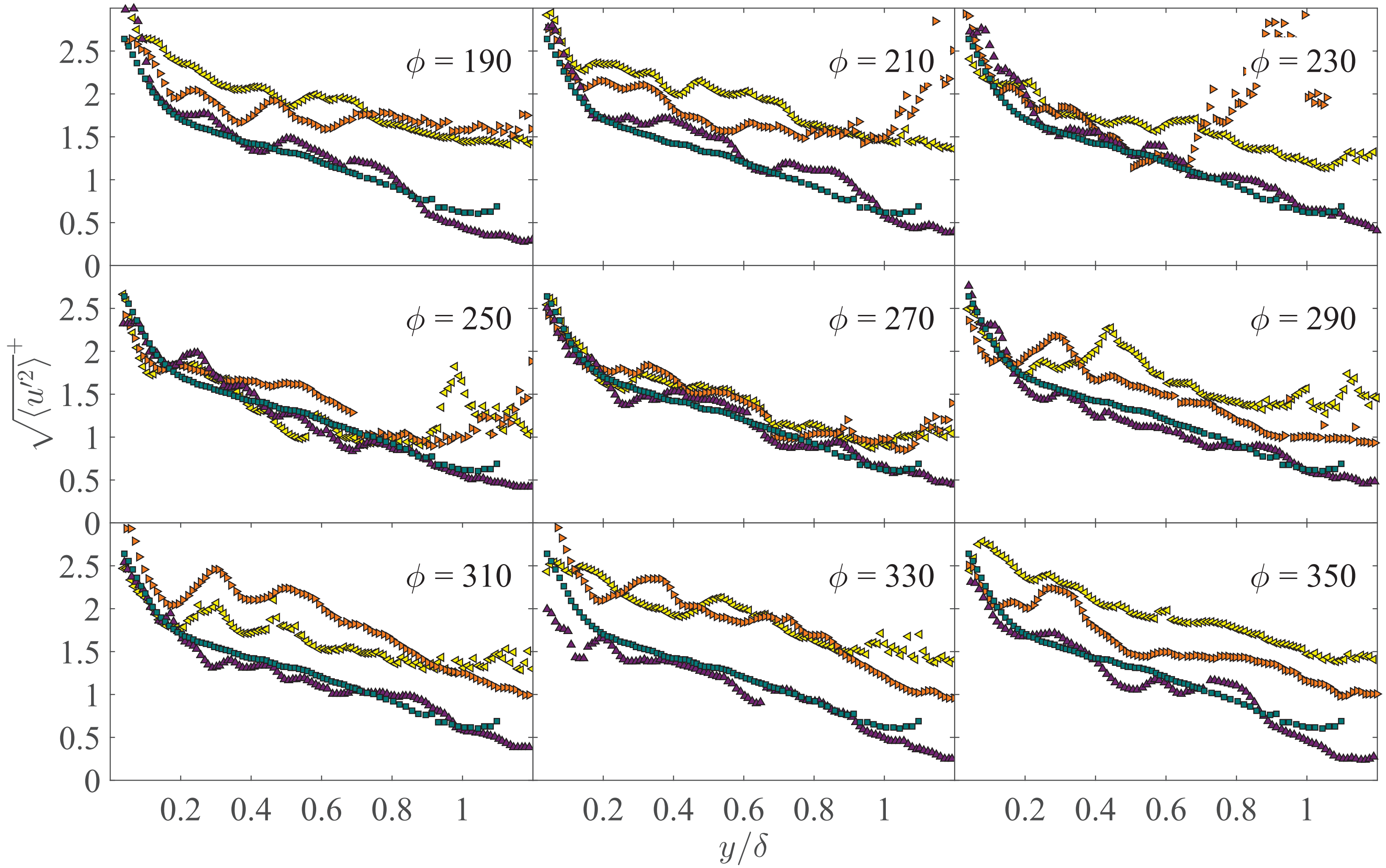

Figure 7.35: The phase-averaged streamwise velocity RMS in PBL flow. Marker symbols are the same as Fig. 7.10.

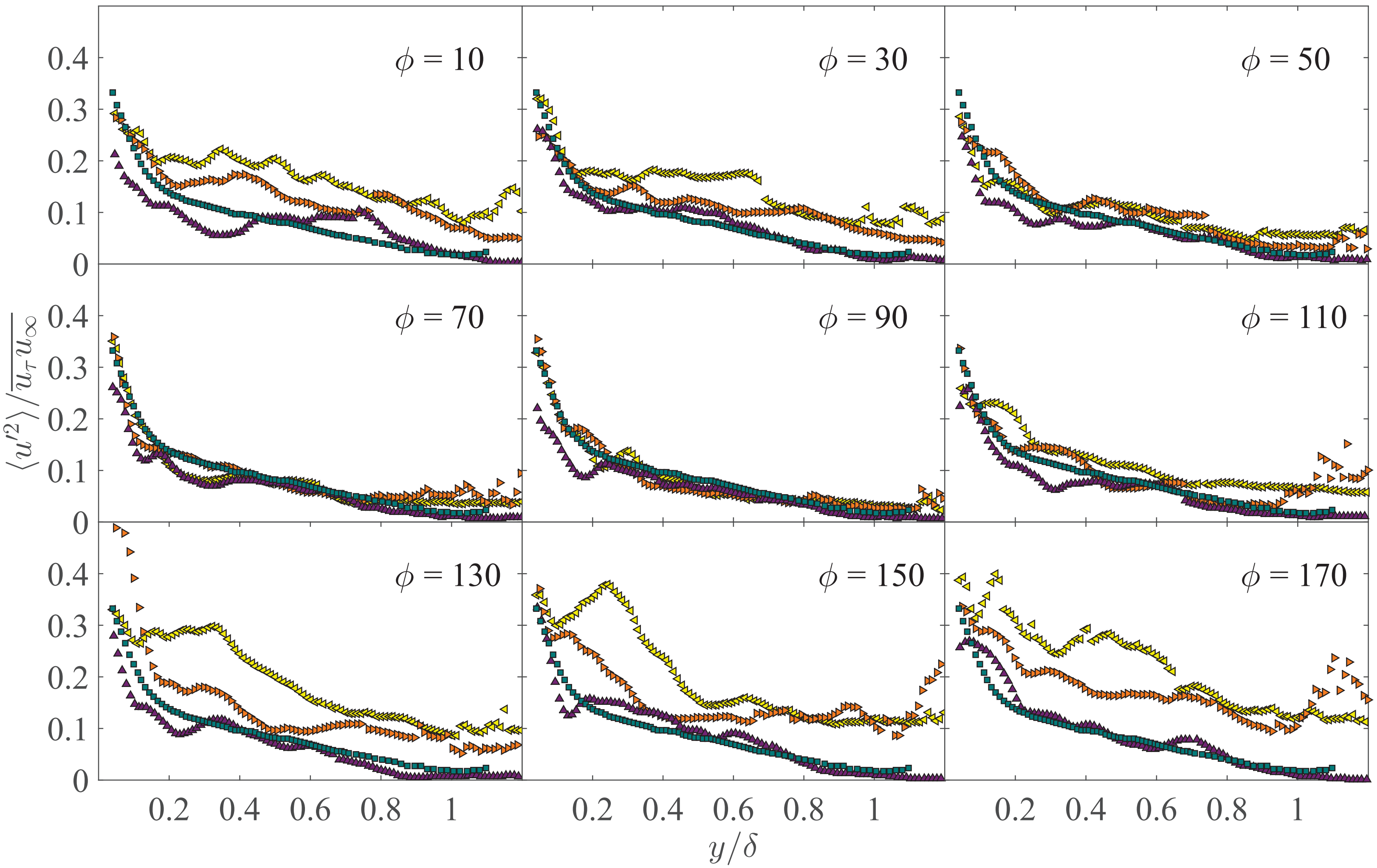

Figure 7.36: The phase-averaged streamwise velocity RMS in PBL flow. Marker symbols are the same as Fig. 7.10.

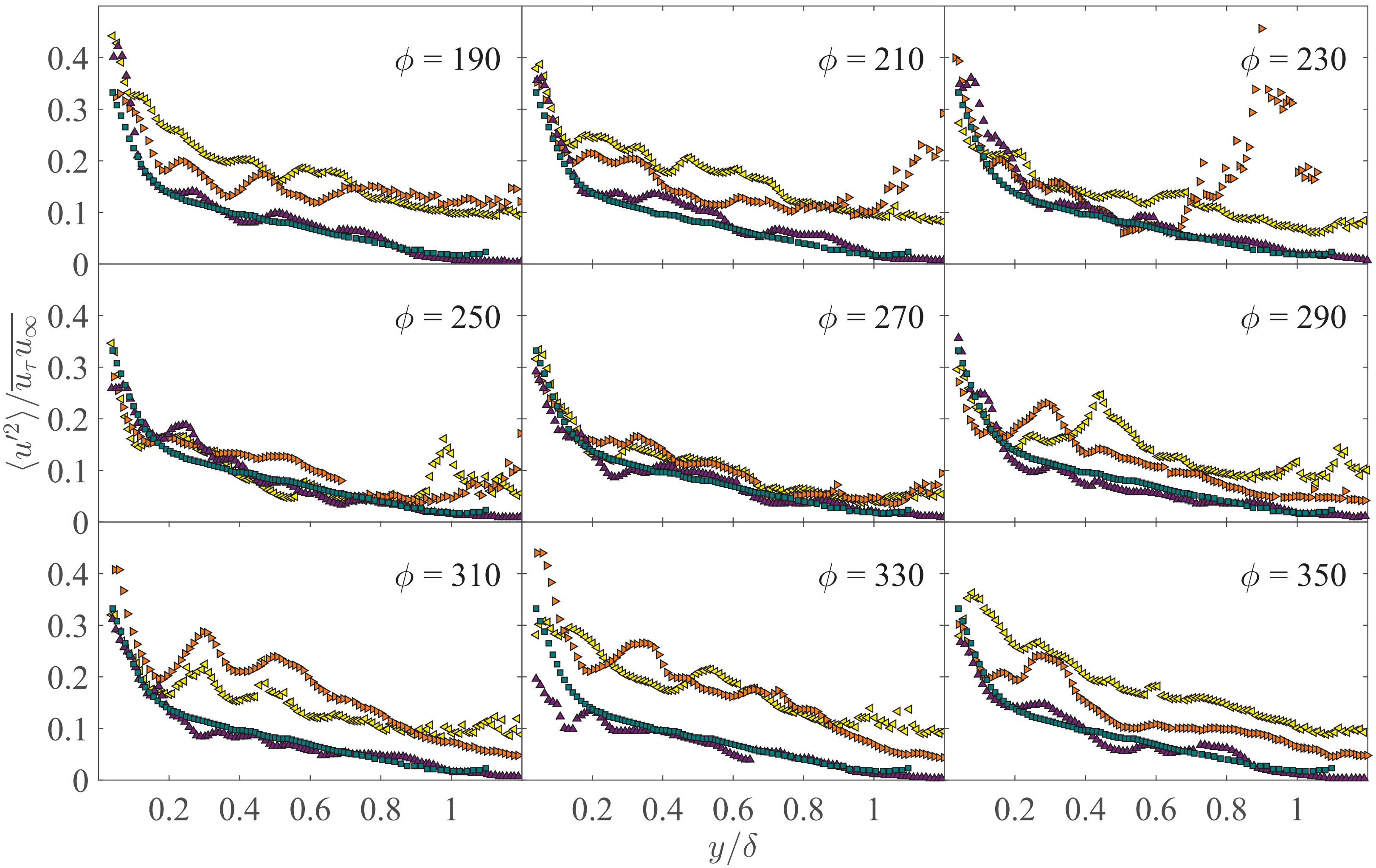

Figure 7.37: The phase-averaged streamwise velocity RMS in PBL flow. Marker symbols are the same as Fig. 7.10.

7.3 Reciprocating vs Pulsatile Wall-Bounded Flow

To summarize the study of the periodic wall-bounded flows, a brief discussion of similarities and differences between reciprocating and pulsatile flow is provided. The metrics for comparison are, however, not straightforward. In particular, in reciprocating flow, time(cycle)-averaged quantities are zero, while they are finite in pulsatile flow. Consequently, the coupling between the time(cycle)-averaged fields (both mean and turbulent quantities) and the oscillatory field is only relevant to pulsatile flow. Nevertheless, in pulsatile flow, the time(cycle)-averaged profiles (both mean and turbulent quantities) are insensitive to the amplitude and frequency of the imposed forcing. Moreover, they are not significantly different from the time-averaged profiles in steady-flow, with the exception of only the streamwise RMS velocity as observed in the present study. This suggests a weak coupling between the oscillatory field and the time(cycle)-averaged fields. Given the above, the comparison will focus on the phase-averaged fields. In reciprocating flow, the phase averaged fields (both mean and turbulent quantities) depend strongly on the frequency of the forcing. In particular, the lower forcing frequency (larger period) case transitions to fully-turbulent behaviors during a portion of the cycle while the higher forcing frequency case remains transitional throughout the entire cycle. In pulsatile flow, the phase-averaged fields show a weak dependence on the frequency of the forcing, effectively fluctuating about the time-averaged field. The highest forcing frequency shows the smallest fluctuations. The oscillatory field for the highest forcing frequency case is the most nonlinear, where the nonlinear behavior is quantified by a phase lag between the stress field and the strain field. While this may appear counterintuitive, it is not. In particular, the nonlinear behavior of the oscillatory flow is confined to the near-wall Stokes' boundary layer and does not strongly couple to the mean and turbulent fields.

Transition to turbulence in the two flow types is determined by the Stokes' Reynolds number Re_s, which is proportional to the ratio of the Reynolds number Re to the Womersley number W, i.e., $Re_c = f(W)$, where Re_c is the critical Reynolds number, and $f(\bullet)$ is a generic function. The appropriate Reynolds number for a pulsatile and reciprocating flow is based on the time-averaged and oscillating velocity, respectively. In reciprocating flow the relationship is linear and well-established, i.e., $Re_c = 700W$ (i.e., $Re_s \simeq 500$). In pulsatile flow, the relationship between Re_c and W is complicated, and several correlations have been proposed in the literature (Çarpinlioğlu and Özahi, 2012). The common agreement is the transition can be either advanced or delayed based on the Womersley number (Çarpinlioğlu and Özahi, 2012; Trip *et al.*, 2012). The reader is referred to Brereton and Mankbadi (1995); Gündogdu and Çarpinlioğlu (1999a,b); Çarpinlioğlu and Özahi (2012) for more detailed comparisons between the two flow types.

7.4 Conclusions

PIV studies were conducted in the NEAT boundary layer wind tunnel to study the transport of momentum in PBL flow. Three different forcing frequencies were investigated: $\omega^+ = 0.007, 0.014, 0.020$, falling within the *intermediate frequency* flow regime as described by Brereton and Mankbadi (1995) and illustrated in Fig. 7.1. In these experiments, the maximum velocity (hence Reynolds number) and the amplitude of the mean velocity modulation were limited by the design of the rotor-stator used to produce the periodic pressure forcing. The PIV vector fields acquired in PBL flow were analyzed by phase and time-averaging and plotted as a function of inner and outer coordinates. Bulk flow parameters and wall-normal profiles of streamwise velocity, rms velocity fluctuations, and Reynolds shear stress were compared to ZPGBL flow at the same Reynolds number.

The study results showed that the modulation amplitude of the freestream velocity is inversely proportional to the forcing frequency. The two lowest frequency cases exhibited very different flow behaviors compared to the highest frequency case. In particular, the modulation of the perturbation wall shear stress in the highest frequency case leads the freestream velocity by $40 \pm 10°$, and the amplitude of the modulation is slightly larger than that given by the Stokes' boundary layer solution. The wall shear stress modulation of the two lower frequency cases, however, is in phase with the freestream velocity and their amplitude of modulation closely matches that given by the Stokes' boundary layer solution. Moreover, the time-averaged streamwise turbulence intensity profiles in the inner, outer and mixed coordinates show that the highest frequency case ($\omega^+ = 0.020$) shows the smallest differences compared to the ZPGBL profile, while the lowest frequency ($\omega^+ = 0.007$) shows the largest differences. The higher turbulence intensity levels in the streamwise direction appears to be inversely proportional with flow frequency. The freestream turbulence intensity modulation of the two lower frequency cases is 180° out of phase with that of the highest frequency case.

The time-averaged profiles of the streamwise velocity show only small differences compared to ZPGBL flow in both inner and outer coordinates. The PBL flows lie slightly above and slightly below the ZPGBL profiles in the inner and outer layers of the boundary layer, respectively.

In general, the time-averaged profiles in a pulsatile flow are not significantly different from steady flow. While the modulation amplitudes of the current experiments remain less than 11% of the mean flow, Binder *et al.* (1985) showed the insensitivity of the oscillatory field to imposed forcing modulation for a modulation amplitude up to 80% of the mean flow. It is therefore, concluded that nonlinear coupling between the mean and oscillatory fields remain insignificant in a pulsatile flow, and the oscillatory profiles that are $\Delta\phi = 180^\circ$ are anti-symmetric.

In brief, while the time-averaged mean flow of the highest frequency case is in equilibrium, the perturbation field is not. In particular, the perturbation wall shear stress of the highest frequency case leads the freestream and the amplitude of modulation is slightly higher than the Stokes' boundary layer solution. Therefore, the EVM models are not expected to predict the perturbation field of the highest frequency case accurately. Conversely, the time-averaged mean flow of the two lower frequency cases ($\omega^+ = 0.007, 0.014$) appear to exhibit slightly different statistics, in particular with respect to the streamwise velocity fluctuations, while the perturbation field is in equilibrium. Based on these results and the value of l_s tabulated in 7.1, it is conjectured that a critical ω^+ exists below which the affect of periodic forcing will modify the time-averaged flow behaviors. Above this threshold, the perturbation field departs from equilibrium and if the frequency is large enough it will asymptote to the Stokes' boundary layer solution. Clearly, the low frequency cases of

$\omega^{+} = 0.007, 0.014$ are below this threshold, while the high frequency case is above this threshold. More work is required to verify the existence of this critical frequency.

CHAPTER 8

CONCLUSIONS AND FUTURE WORK

Collectively, the work of the dissertation has led to the development of analytical tools, and a unique experimental facility to study non-equilibrium wall bounded flows. For clarity, the concluding and future work statements are subdivided into four sections representing the four primary research fronts of this dissertation.

8.1 An Exact Integral Method To Evaluate Wall Heat Flux In Spatially Developing Two-Dimensional Wall-Bounded Flows

8.1.1 Conclusions

An integral method to evaluate the wall heat flux in turbulent wall-bounded flows based on the triple integration of the Reynolds-averaged thermal transport equation was presented. Using data from the literature, the method was shown to be fairly robust based on good agreement of the evaluated wall heat flux when compared to direct calculation of the temperature gradient at the wall using both DNS and experimental data. Complications owing to experimental limitations and measurement error in determining the wall heat flux from the proposed method were presented and mitigating strategies were described.

The need for this technique may be argued on grounds that it provides a direct measurement of the wall heat flux and is useful when profiles at multiple streamwise locations are not available or feasible, for flows with ill-defined outer boundary conditions, or when the measurement grid does not extend over the whole boundary layer thickness. Being an integral method, it is less sensitive to measurement noise than a differential method, in particular in the near-wall region of the flow. Furthermore, determination of the wall heat flux from the present method provides a means to connect transport properties at the wall to the mean flow dynamics. This is an important characteristic to better understand the underlying physics associated with the wall heat flux, in particular in non-equilibrium wall-bounded flows.

8.1.2 Future Work

The presented integral method is valid for two-dimensional incompressible flows. However, many turbulent flows in engineering applications are three-dimensional and/or compressible. Flow inside a piston engine or through a turbine are but two important examples where evaluating the wall heat flux in three dimensional, compressible flows is critically important. Suggested future work is to refine the method for three-dimensional and/or compressible flows. Other suggested future work is to explore the alternative forms of the integral method. In particular, evaluating the wall heat flux using only the mean temperature profile, and comparing the results to the differential method.

8.2 Integral Validation Technique of RANS Turbulence Models

8.2.1 Conclusions

DNS of reciprocating channel flow with heat transfer was used to evaluate the performance of two low-Reynolds-number and two high-Reynolds-number RANS turbulence models. The standard validation technique indicated that the two low-Reynolds-number models reasonably predict the transport of momentum and thermal energy in reciprocating channel flow. However, the results of the integral validation technique indicate that while the low-Reynolds-number models perform reasonably well in predicting the contributing terms to the wall shear stress, the models perform rather poorly in predicting the contributing terms to the wall heat flux. Specifically, the contributions from the turbulent heat flux are under predicted while the contribution from the gradient of the total heat flux is of opposite sign and 180° out-of-phase compared to the DNS. Importantly, the differences in the contributing terms serendipitously cancel each other yielding a reasonable prediction of the wall heat flux compared to the DNS. In addition, the integral validation technique identifies the breakdown of Reynolds analogy and deficiencies in the turbulence heat flux model as the root causes of the modeling failures. This information is critical to the improved development of turbulence models.

8.2.2 Future Work

The integral validation technique was used to evaluate the performance of "single equation" heat transfer models using an eddy-viscosity approximation, i.e., $-\overline{u_i'\theta'} = \frac{\nu_T}{Pr_T}\frac{\partial\Theta}{\partial x_i}$. Nevertheless, there are a few modified heat transfer models that purportedly outperform single equation models. For example, Abe *et al.* (1996) introduced a two-equation heat transfer model, So and Sommer (1996) introduced an explicit algebraic heat transfer model for the temperature field, and Abdol-Hamid *et al.* (2004) introduced a temperature corrected turbulence model for high temperature jet flows, among others. Using the integral validation technique, the modified models can be evaluated and their performance can be compared to the single-equation heat transfer models.

8.3 Transition to Turbulence In Reciprocating Channel Flow

8.3.1 Conclusions

The mean flow dynamics in reciprocating channel flow was studied to better understand the mechanism of transition to turbulence in periodic flows. The underlying mechanism of this transition is the emergence of an internal layer that first develops during the late phases of the accelerating portion of the cycle. The internal layer is found to be spatially coincident with a strong momentum sink/source-like behavior of the turbulent inertia. It is conjectured that the internal layer emerges from a shear layer instability that rolls-up triggering further flow instabilities that transition the flow to a fully-developed turbulent channel in subsequent phases.

8.3.2 Future Work

The identification of the potential root cause of transition to turbulence in reciprocating channel flow denotes good progress. However, further work is required to identify if the internal layer does indeed roll-up as conjectured. A suggestion for future work is to incorporate flow structure identification schemes in the transitional phases of the flow to further study differences in the turbulent structure when the flow transitions to turbulence at $Re_s = 1019$ compared to when the flow remains transitional $Re_s = 648$. The Q-R criteria scheme, and the triple decomposition of the strain rate tensor first introduced by Kolář (2007) are among several structure identification schemes that can be employed.

8.4 Experimental Facility Development and Results

8.4.1 Conclusions

The non-equilibrium and thermal (NEAT) boundary layer facility was purposefully designed and developed to study non-equilibrium thermal boundary layers. The facility can maintain various thermal boundary conditions and generate pressure gradient modulations with various frequencies and amplitudes. It was validated under equilibrium boundary layer conditions for $568 \leq Re_\theta \leq 1438$.

Particle image velocimetry (PIV) was used to study the momentum transport in pulsatile boundary layer (PBL) flow. The analysis of the PIV results show that although the phase-averaged profiles depart from the equilibrium profile, the time(cycle)-average profiles, except for the streamwise turbulent intensity $\overline{u'^2}$, are similar to steady-state, zero pressure-gradient boundary layer flow. Using $\overline{u'^2}$ as a metric for the departure of the time mean flow from equilibrium, a critical frequency $0.014 < \omega_c^+ < 0.020$ was identified, where $\omega^+ = \frac{\omega}{u_\tau^2/\nu}$, ω is the flow angular frequency, u_τ is the friction velocity and ν is the fluid viscosity. For $\omega^+ > \omega_c^+$, $\overline{u'^2}$ does not exhibit significant difference from its steady flow counterpart. For $\omega^+ < \omega_c^+$, however, $\overline{u'^2}$ has a higher value compared to the steady flow, the deviation magnitude is inversely proportional to flow frequency.

The wall shear stress modulation is investigated to study the perturbation field of the PBL flow. The perturbation wall shear stress of the two lower frequency cases is in phase with the freestream velocity and the amplitude of the modulation matches that determined from the Stokes' boundary layer solution. However, the wall shear stress of the highest frequency case leads the freestream and the amplitude of modulation is slightly larger than that determined from the Stokes' boundary layer solution. It is concluded that the perturbation field of the highest frequency case is not in equilibrium and the flow is in a different flow regime than the two lower frequency cases.

8.4.2 Future Work

The pulsatile pressure-gradient used for flow forcing in the PBL flow was produced using a rotor-stator assembly with limited capabilities. Specifically, the inherent flow blockage of the system limits the maximum flow speed in the tunnel, such that the maximum Reynolds number based on mean freestream velocity is limited to $Re_theta \lesssim 850$. In addition, the limited forcing frequency of the current setup limits the modulation of the freestream velocity in the tunnel.

Improving the design of the assembly to increase the flow rate while maintaining the pulsatile flow modulation amplitude above 5% is necessary to study PBL flow at higher frequencies and Reynolds numbers. For example, a rotating flap can replace the current rotor-stator assembly and increase the flow rate. It also can provide higher modulation amplitude for a given flow frequency.

Since PIV provides a two-dimensional, instantaneous snapshot of the turbulent velocity field, the PIV vector fields can be used to identify turbulent flow structures to study the difference in the turbulent structure between PBL and ZPG boundary layer flow. Despite the benefits of PIV, measurements over long sampling times and a high sampling frequency is not possible owing to the limited camera memory. Therefore, PIV measurements of a PBL flow for a large number of cycles (> 1000) and large number of phases per cycle (≥ 360) is very challenging. A point measurement technique such as hotwire anemometry (as long as there is no flow reversal) can provide much higher sampling frequency and longer sampling length compared to PIV, which reduces the uncertainty of the statistics.

Lastly, the thermal wall plate and feedback controllers, which are designed and manufactured as part of the dissertation, are installed and ready to use. Temperature measurements in the facility to study heat transfer in pulsatile boundary layer flow provides valuable insight of the heat transport mechanisms in non-equilibrium flows. The seeding particles introduced to the flow for PIV measurements limit the options of the experimental techniques to measure temperature. One suggestion is to use planar laser induced fluorescence (PLIF) and PIV to study the temperature and the velocity fields simultaneously. Nevertheless, since the wind tunnel is made of plastic and it is an open-circuit tunnel, finding the suitable particles for PLIF is nontrivial. The other option is to use a hotwire/coldwire combination to study the velocity and temperature fields simultaneously.

BIBLIOGRAPHY

Abdol-Hamid, K. S., S. P. Pao, S. J. Massey, and A. Elmiligui
2004. Temperature corrected turbulence model for high temperature jet flow. *Journal of Fluids Engineering*, 126(5):844–850.

Abe, K.-i., T. Kondoh, and Y. Nagano
1996. A two-equation heat transfer model reflecting second-moment closures for wall and free turbulent flows. *International journal of heat and fluid flow*, 17(3):228–237.

Adrian, R. J.
2007. Hairpin vortex organization in wall turbulencea). *Physics of Fluids (1994-present)*, 19(4):041301.

Adrian, R. J. and J. Westerweel
2011. *Particle image velocimetry*, number 30. Cambridge University Press.

Afanasyev, V., Y. P. Chudnovsky, A. Leontiev, and P. Roganov
1993. Turbulent flow friction and heat transfer characteristics for spherical cavities on a flat plate. *Experimental thermal and fluid science*, 7(1):1–8.

Afzal, N.
1982. Fully developed turbulent flow in a pipe: an intermediate layer. *Ingenieur-Archiv*, 52(6):355–377.

Aharwal, K., B. Gandhi, and J. Saini
2008. Experimental investigation on heat-transfer enhancement due to a gap in an inclined continuous rib arrangement in a rectangular duct of solar air heater. *Renewable energy*, 33(4):585–596.

Ahn, S. and J. A. Fessler
2003. Standard errors of mean, variance, and standard deviation estimators. *University of Michigan: EECS Department*.

Akhavan, R., R. Kamm, and A. Shapiro
1991a. An investigation of transition to turbulence in bounded oscillatory stokes flows part 1. experiments. *Journal of Fluid Mechanics*, 225:395–422.

Akhavan, R., R. Kamm, and A. Shapiro
1991b. An investigation of transition to turbulence in bounded oscillatory stokes flows part 2. numerical simulations. *Journal of Fluid Mechanics*, 225:423–444.

Al-Asmi, K. and I. Castro
1993. Production of oscillatory flow in wind tunnels. *Experiments in Fluids*, 15(1):33–41.

Antonia, R. and R. Luxton
1971. The response of a turbulent boundary layer to a step change in surface roughness. part 1. smooth to rough. *J. Fluid Mech*, 48(4):721–761.

Araya, G. and L. Castillo
2012. Dns of turbulent thermal boundary layers up to reθ= 2300. *International Journal of Heat and Mass Transfer*, 55(15):4003–4019.

Aubertine, C. D. and J. K. Eaton
2005. Turbulence development in a non-equilibrium turbulent boundary layer with mild adverse pressure gradient. *Journal of Fluid Mechanics*, 532:345–364.

Babuska, I. and J. T. Oden
2004. Verification and validation in computational engineering and science: basic concepts. *Computer Methods in Applied Mechanics and Engineering*, 193(36):4057–4066.

Bandyopadhyay, P. R. and A. Ahmed
1993. Turbulent boundary layers subjected to multiple curvatures and pressure gradients. *Journal of Fluid Mechanics*, 246:503–503.

Bardina, J., P. Huang, and T. Coakley
1997. Turbulence modeling validation. *AIAA paper*, 2121:1997.

Bernard, P. S. and R. A. Handler
1990. Reynolds stress and the physics of turbulent momentum transport. *Journal of fluid mechanics*, 220:99–124.

Bharadwaj, P., A. Khondge, and A. Date
2009. Heat transfer and pressure drop in a spirally grooved tube with twisted tape insert. *International Journal of Heat and Mass Transfer*, 52(7):1938–1944.

Binder, G., S. Tardu, R. Blackwelder, and J. Kueny
1985. Large amplitude periodic oscillations in the wall region of a turbulent channel flow. In *5th Symposium on Turbulent Shear Flows*, volume 1, P. 16.

Binder, G., S. Tardu, and P. Vezin
1995. Cyclic modulation of reynolds stresses and length scales in pulsed turbulent channel flow. In *Proceedings of the Royal Society of London A: Mathematical, Physical and Engineering Sciences*, volume 451, Pp. 121–139. The Royal Society.

Blackwell, B. F., W. M. Kays, and R. Moffat
1972. The turbulent boundary layer on a porous plate: an experimental study of the heat transfer behavior with adverse pressure gradients.

Blennerhassett, P. and A. P. Bassom
2006. The linear stability of high-frequency oscillatory flow in a channel. *Journal of Fluid Mechanics*, 556(1):1–25.

Blennerhassett, P. J. and A. P. Bassom
2002. The linear stability of flat stokes layers. *Journal of Fluid Mechanics*, 464:393–410.

Borman, G. and K. Nishiwaki
1987. Internal-combustion engine heat transfer. *Progress in energy and combustion science*, 13(1):1–46.

Bradshaw, P.
1996. Turbulence modeling with application to turbomachinery. *Progress in Aerospace Sciences*, 32(6):575–624.

Bradshaw, P. and G. P. Huang
1995. The law of the wall in turbulent flow. In *Proceedings of the Royal Society of London A: Mathematical, Physical and Engineering Sciences*, volume 451, Pp. 165–188. The Royal Society.

Bradshaw, P. and F. Wong
1972. The reattachment and relaxation of a turbulent shear layer. *Journal of Fluid Mechanics*, 52(01):113–135.

Brereton, G. and R. Mankbadi
1995. Review of recent advances in the study of unsteady turbulent internal flows. *Applied Mechanics Reviews*, 48(4):189–212.

Brereton, G., W. Reynolds, and R. Jayaraman
1990. Response of a turbulent boundary layer to sinusoidal free-stream unsteadiness. *Journal of fluid mechanics*, 221:131–159.

Çarpinlioğlu, M. Ö. and M. Y. Gündoğdu
2001. A critical review on pulsatile pipe flow studies directing towards future research topics. *Flow Measurement and Instrumentation*, 12(3):163–174.

Çarpinlioğlu, M. Ö. and E. Özahi
2012. An updated portrait of transition to turbulence in laminar pipe flows with periodic time dependence (a correlation study). *Flow, turbulence and combustion*, 89(4):691–711.

Castro, I. P. and E. Epik
1998. Boundary layer development after a separated region. *Journal of Fluid Mechanics*, 374:91–116.

Catalano, P. and M. Amato
2003. An evaluation of rans turbulence modelling for aerodynamic applications. *Aerospace science and Technology*, 7(7):493–509.

Childs, P., J. Greenwood, and C. Long
1999. Heat flux measurement techniques. *Proceedings of the Institution of Mechanical Engineers, Part C: Journal of Mechanical Engineering Science*, 213(7):655–677.

Clauser, F. H.
1956. The turbulent boundary layer. *Advances in applied mechanics*, 4:1–51.

Collins, J.
1963. Inception of turbulence at the bed under periodic gravity waves. *Journal of Geophysical Research*, 68(21):6007–6014.

Craciunescu, O. I. and S. T. Clegg
2001. Pulsatile blood flow effects on temperature distribution and heat transfer in rigid vessels. *Journal of biomechanical engineering*, 123(5):500–505.

Davidson, P.
2004. Turbulence: an introduction for scientists and engineers.

De Graaff, D. B. and J. K. Eaton
2000. Reynolds-number scaling of the flat-plate turbulent boundary layer. *Journal of Fluid Mechanics*, 422:319–346.

Dec, J. E. and J. O. Keller
1989. Pulse combustor tail-pipe heat-transfer dependence on frequency, amplitude, and mean flow rate. *Combustion and Flame*, 77(3):359–374.

Dengel, P. and H. Fernholz
1990. An experimental investigation of an incompressible turbulent boundary layer in the vicinity of separation. *Journal of Fluid Mechanics*, 212:615–636.

Di Liberto, M. and M. Ciofalo
2009. Numerical simulation of reciprocating turbulent flow in a plane channel. *Physics of Fluids (1994-present)*, 21(9):095106.

Di Liberto, M. and M. Ciofalo
2011. Unsteady turbulence in plane channel flow. *Computers & fluids*, 49(1):258–275.

Dubief, Y., V. E. Terrapon, C. M. White, E. S. Shaqfeh, P. Moin, and S. K. Lele
2005. New answers on the interaction between polymers and vortices in turbulent flows. *Flow, turbulence and combustion*, 74(4):311–329.

Durbin, P.
1995. Separated flow computations with the k-epsilon-v-squared model. *AIAA journal*, 33(4):659–664.

Durbin, P.
1996. On the k-3 stagnation point anomaly. *International journal of heat and fluid flow*, 17(1):89–90.

Ebadi, A., F. Mehdi, and C. M. White
2015. An exact integral method to evaluate wall heat flux in spatially developing two-dimensional wall-bounded flows. *International Journal of Heat and Mass Transfer*, 84:856–861.

Eckmann, D. M. and J. B. Grotberg
1991. Experiments on transition to turbulence in oscillatory pipe flow. *Journal of Fluid Mechanics*, 222:329–350.

Eilers, P. H.
2003. A perfect smoother. *Analytical chemistry*, 75(14):3631–3636.

Einav, S. and M. Sokolov
1993. An experimental study of pulsatile pipe flow in the transition range. *Journal of biomechanical engineering*, 115(4A):404–411.

Elsnab, J., J. Klewicki, D. Maynes, and T. Ameel
2011. Mean dynamics of transitional channel flow. *Journal of Fluid Mechanics*, 678:451–481.

Fife, P., T. Wei, J. Klewicki, and P. McMurtry
2005. Stress gradient balance layers and scale hierarchies in wall-bounded turbulent flows. *Journal of Fluid Mechanics*, 532:165–189.

Fukagata, K., K. Iwamoto, and N. Kasagi
2002. Contribution of reynolds stress distribution to the skin friction in wall-bounded flows. *Physics of Fluids (1994-present)*, 14(11):L73–L76.

Goldstein, R. and H. Cho
1995. A review of mass transfer measurements using naphthalene sublimation. *Experimental Thermal and Fluid Science*, 10(4):416–434.

Gorji, S., M. Seddighi, C. Ariyaratne, A. Vardy, T. OâĂŹDonoghue, D. Pokrajac, and S. He
2014. A comparative study of turbulence models in a transient channel flow. *Computers & Fluids*, 89:111–123.

Grossmann, S. and D. Lohse
2000. Scaling in thermal convection: a unifying theory. *Journal of Fluid Mechanics*, 407:27–56.

Gündogdu, M. and M. Ö. Çarpinlioğlu
1999a. Present state of art on pulsatile flow theory (part 1: laminar and transitional flow regimes). *JSME international journal. Series B, fluids and thermal engineering*, 42(3):384–397.

Gündogdu, M. Y. and M. Ö. Çarpinlioğlu
1999b. Present state of art on pulsatile flow theory. part 2. turbulent flow regime. *JSME International Journal Series B Fluids and Thermal Engineering*, 42(3):398–410.

Hall, P.
1978. The linear stability of flat stokes layers. In *Proceedings of the Royal Society of London A: Mathematical, Physical and Engineering Sciences*, volume 359, Pp. 151–166. The Royal Society.

Han, Z. and R. D. Reitz
1997. A temperature wall function formulation for variable-density turbulent flows with application to engine convective heat transfer modeling. *International journal of heat and mass transfer*, 40(3):613–625.

Hanjalic, K.
2005. Will rans survive les? a view of perspectives. *Journal of fluids engineering*, 127(5):831–839.

Hedley, T. B. and J. F. Keffer
1974. Turbulent/non-turbulent decisions in an intermittent flow. *Journal of Fluid Mechanics*, 64(04):625–644.

Hendricks, T. and J. Ghandhi
2012. Estimation of surface heat flux in ic engines using temperature measurements: processing code effects. *SAE International Journal of Engines*, 5(3):1268–1285.

Hosni, M., H. W. Coleman, and R. P. Taylor
1991. Measurements and calculations of rough-wall heat transfer in the turbulent boundary layer. *International Journal of Heat and Mass Transfer*, 34(4):1067–1082.

Houra, T. and Y. Nagano
2006. Effects of adverse pressure gradient on heat transfer mechanism in thermal boundary layer. *International journal of heat and fluid flow*, 27(5):967–976.

Houra, T. and Y. Nagano
2008. Spatio-temporal turbulent structures of thermal boundary layer subjected to non-equilibrium adverse pressure gradient. *International Journal of Heat and Fluid Flow*, 29(3):591–601.

Hunt, J., N. Sandham, J. Vassilicos, B. Launder, P. Monkewitz, and G. Hewitt
2001. Developments in turbulence research: a review based on the 1999 programme of the isaac newton institute, cambridge. *Journal of Fluid Mechanics*, 436:353–391.

Hussain, A. K. M. F. and W. C. Reynolds
1970. The mechanics of an organized wave in turbulent shear flow. *Journal of Fluid Mechanics*, 41(02):241–258.

Iaccarino, G. and P. Durbin
2000. Unsteady 3d rans simulations using the v2–f model. *Ann. Res. Briefs*, Pp. 236–269.

Incropera, F. and D. DeWitt
1985. Introduction to heat transfer.

Jensen, B., B. Sumer, and J. Fredsøe
1989. Turbulent oscillatory boundary layers at high reynolds numbers. *Journal of Fluid Mechanics*, 206:265–297.

Jones, W. and B. Launder
1972. The prediction of laminarization with a two-equation model of turbulence. *International journal of heat and mass transfer*, 15(2):301–314.

Jovic, S. and D. Driver
1995. Reynolds number effect on the skin friction in separated flows behind a backward-facing step. *Experiments in Fluids*, 18(6):464–467.

Jovic, S. and D. M. Driver
1994. Backward-facing step measurements at low reynolds number, re (sub h)= 5000.

Kader, B. and A. Yaglom
1991. Spectra and correlation functions of surface layer atmospheric turbulence in unstable thermal stratification. In *Turbulence and Coherent Structures*, Pp. 387–412. Springer.

Kalitzin, G., G. Medic, G. Iaccarino, and P. Durbin
. Near-wall behavior of rans turbulence models and implications for wall functions.

Kantha, L. H. and C. A. Clayson
1994. An improved mixed layer model for geophysical applications. *Journal of Geophysical Research: Oceans*, 99(C12):25235–25266.

Kato, M.
1993. The modeling of turbulent flow around stationary and vibrating square cylinders. In *Ninth Symposium on Turbulent Shear Flows, 1993*.

Kawamura, H., K. Ohsaka, H. Abe, and K. Yamamoto
1998. Dns of turbulent heat transfer in channel flow with low to medium-high prandtl number fluid. *International Journal of Heat and Fluid Flow*, 19(5):482–491.

Klewicki, J.
2013. Self-similar mean dynamics in turbulent wall flows. *Journal of Fluid Mechanics*, 718:596–621.

Klewicki, J., R. Ebner, and X. Wu
2011. Mean dynamics of transitional boundary-layer flow. *Journal of Fluid Mechanics*, 682:617–651.

Klewicki, J., P. Fife, and T. Wei
2009. On the logarithmic mean profile. *Journal of Fluid Mechanics*, 638:73–93.

Kolář, V.
2007. Vortex identification: New requirements and limitations. *International journal of heat and fluid flow*, 28(4):638–652.

Kong, H., H. Choi, and J. S. Lee
2001. Dissimilarity between the velocity and temperature fields in a perturbed turbulent thermal boundary layer. *Physics of Fluids (1994-present)*, 13(5):1466–1479.

Kurzweg, U., E. Lindgren, and B. Lothrop
1989. Onset of turbulence in oscillating flow at low womersley number. *Physics of Fluids A: Fluid Dynamics (1989-1993)*, 1(12):1972–1975.

Launder, B. and B. Sharma
1974. Application of the energy-dissipation model of turbulence to the calculation of flow near a spinning disc. *Letters in heat and mass transfer*, 1(2):131–137.

Laurence, D., J. Uribe, and S. Utyuzhnikov
2005. A robust formulation of the v2- f model. *Flow Turbul. Combust.*, 73(3-4):169–185.

Le, H., P. Moin, and J. Kim
1997. Direct numerical simulation of turbulent flow over a backward-facing step. *Journal of fluid mechanics*, 330(1):349–374.

Lee, J., S. Y. Jung, H. J. Sung, and T. A. Zaki
2013. Effect of wall heating on turbulent boundary layers with temperature-dependent viscosity.

Li, H.-Y. and W.-M. Yan
2003. Identification of wall heat flux for turbulent forced convection by inverse analysis. *International Journal of Heat and Mass Transfer*, 46(6):1041–1048.

Li, Y., E. Perlman, M. Wan, Y. Yang, C. Meneveau, R. Burns, S. Chen, A. Szalay, and G. Eyink
2008. A public turbulence database cluster and applications to study lagrangian evolution of velocity increments in turbulence. *Journal of Turbulence*, (9):N31.

Luo, J. and X. Wu
2010. On the linear instability of a finite stokes layer: instantaneous versus floquet modes. *Physics of Fluids (1994-present)*, 22(5):054106.

Mackley, M. and P. Stonestreet
1995. Heat transfer and associated energy dissipation for oscillatory flow in baffled tubes. *Chemical Engineering Science*, 50(14):2211–2224.

Mao, Z.-X. and T. J. Hanratty
1986. Studies of the wall shear stress in a turbulent pulsating pipe flow. *Journal of Fluid Mechanics*, 170:545–564.

Mehdi, F., T. G. Johansson, C. M. White, and J. W. Naughton
2014. On determining wall shear stress in spatially developing two-dimensional wall-bounded flows. *Experiments in Fluids*, 55(1):1–9.

Mehdi, F. and C. M. White
2011. Integral form of the skin friction coefficient suitable for experimental data. *Experiments in Fluids*, 50(1):43–51.

Mellor, G. L. and T. Yamada
1982. Development of a turbulence closure model for geophysical fluid problems. *Reviews of Geophysics*, 20(4):851–875.

Menter, F. and Y. Egorov
2010. The scale-adaptive simulation method for unsteady turbulent flow predictions. part 1: theory and model description. *Flow, Turbulence and Combustion*, 85(1):113–138.

Menter, F. and M. Kuntz
2004. Adaptation of eddy-viscosity turbulence models to unsteady separated flow behind vehicles. In *The aerodynamics of heavy vehicles: trucks, buses, and trains*, Pp. 339–352. Springer.

Menter, F. R.
1994. Two-equation eddy-viscosity turbulence models for engineering applications. *AIAA journal*, 32(8):1598–1605.

Miller, J. and A. Fejer
1964. Transition phenomena in oscillating boundary-layer flows. *Journal of Fluid Mechanics*, 18(03):438–448.

Mittal, R., S. Simmons, and F. Najjar
2003. Numerical study of pulsatile flow in a constricted channel. *Journal of Fluid Mechanics*, 485:337–378.

Monty, J., Z. Harun, and I. Marusic
2011. A parametric study of adverse pressure gradient turbulent boundary layers. *International Journal of Heat and Fluid Flow*, 32(3):575–585.

Moretti, P. and W. Kays
1965. Heat transfer to a turbulent boundary layer with varying free-stream velocity and varying surface temperatureâĂŤan experimental study. *International Journal of Heat and Mass Transfer*, 8(9):1187–1202.

Morkovin, M. and H. Obremski
1969. Application of a quasi-steady stability model to periodic boundary-layer flows. *AIAA Journal*, 7(7):1298–1301.

Nagib, H. M. and K. A. Chauhan
2008. Variations of von kármán coefficient in canonical flows. *Physics of Fluids*, 20(10):1518.

Narasimha, R. and S. Prasad
1994. Leading edge shape for flat plate boundary layer studies. *Experiments in Fluids*, 17(5):358–360.

Neal, S.
1975. The development of the thin-film naphthalene mass-transfer analogue technique for the direct measurement of heat-transfer coefficients. *International Journal of Heat and Mass Transfer*, 18(4):559–567.

Nerem, R., W. Seed, and N. Wood
1972. An experimental study of the velocity distribution and transition to turbulence in the aorta. *Journal of Fluid Mechanics*, 52(01):137–160.

Oberkampf, W. L. and T. G. Trucano
2002. Verification and validation in computational fluid dynamics. *Progress in Aerospace Sciences*, 38(3):209–272.

Obremski, H. and A. Fejer
1967. Transition in oscillating boundary layer flows. *J. Fluid Mech*, 29(1):93–111.

O'donoghue, T., A. G. Davies, J. S. Ribberink, *et al.*
2011. Experimental study of the turbulent boundary layer in acceleration-skewed oscillatory flow. *Journal of fluid mechanics*, 684:251–283.

Orlando, A. d. F., R. Moffat, and W. Kays
1974. Turbulent transport of heat and momentum in a boundary layer subject to deceleration, suction and variable wall temperature.

Örlü, R., J. H. Fransson, and P. H. Alfredsson
2010. On near wall measurements of wall bounded flowsâĂŤthe necessity of an accurate determination of the wall position. *Progress in Aerospace Sciences*, 46(8):353–387.

Ozdemir, C. E., T.-J. Hsu, and S. Balachandar
2014. Direct numerical simulations of transition and turbulence in smooth-walled stokes boundary layer. *Physics of Fluids (1994-present)*, 26(4):045108.

Patel, V. C., W. Rodi, and G. Scheuerer
1985. Turbulence models for near-wall and low reynolds number flows-a review. *AIAA journal*, 23(9):1308–1319.

Pehlivan, H.
2013. Experimental investigation of convection heat transfer in converging–diverging wall channels. *International Journal of Heat and Mass Transfer*, 66:128–138.

Perlman, E., R. Burns, Y. Li, and C. Meneveau
2007. Data exploration of turbulence simulations using a database cluster. In *Proceedings of the 2007 ACM/IEEE conference on Supercomputing*, P. 23. ACM.

Perry, A., J. Bell, and P. Joubert
1966. Velocity and temperature profiles in adverse pressure gradient turbulent boundary layers. *J. Fluid Mech*, 25(2):299–320.

Raffel, M., C. E. Willert, S. Wereley, and J. Kompenhans
2013. *Particle image velocimetry: a practical guide*. Springer.

Rakopoulos, C., G. Kosmadakis, and E. Pariotis
2010. Critical evaluation of current heat transfer models used in cfd in-cylinder engine simulations and establishment of a comprehensive wall-function formulation. *Applied Energy*, 87(5):1612–1630.

Ramaprian, B. and S. Tu
1983. Fully developed periodic turbulent pipe flow. part 2. the detailed structure of the flow. *Journal of Fluid Mechanics*, 137:59–81.

Ramaprian, B. and S.-W. Tu
1980. An experimental study of oscillatory pipe flow at transitional reynolds numbers. *Journal of Fluid Mechanics*, 100(03):513–544.

Reichelt, L., U. Meingast, and U. Renz
2002. Calculating transient wall heat flux from measurements of surface temperature. *International Journal of Heat and Mass Transfer*, 45(3):579–584.

Richardson, E. and E. Tyler
1929. The transverse velocity gradient near the mouths of pipes in which an alternating or continuous flow of air is established. *Proceedings of the Physical Society*, 42(1):1.

Ristorcelli, J. and J. Lumley
1992. Instabilities, transition and turbulence in the czochralski crystal melt. *Journal of crystal growth*, 116(3-4):447–460.

Roy, C. J. and F. G. Blottner
2006. Review and assessment of turbulence models for hypersonic flows. *Progress in Aerospace Sciences*, 42(7):469–530.

Samuel, A. and P. Joubert
1974. A boundary layer developing in an increasingly adverse pressure gradient. *Journal of Fluid Mechanics*, 66(03):481–505.

Sandham, N. and L. Kleiser
1992. The late stages of transition to turbulence in channel flow. *Journal of Fluid Mechanics*, 245:319–348.

Sarkar, A. and R. So
1997. A critical evaluation of near-wall two-equation models against direct numerical simulation data. *International Journal of Heat and Fluid Flow*, 18(2):197–208.

Schlichting, H. *et al.*
1979. Boundary layer theory. *McGraw-Hill*.

Schmirler, M., J. Matěcha, H. Netřebská, J. Ježek, and J. Adamec
2014. The influence of flow parameters on the transition to turbulence in pulsatile flow. In *EPJ Web of Conferences*, volume 67, P. 02107. EDP Sciences.

Sciacchitano, A. and B. Wieneke
2016. Piv uncertainty propagation. *Measurement Science and Technology*, 27(8):084006.

Scotti, A. and U. Piomelli
2001. Numerical simulation of pulsating turbulent channel flow. *Physics of Fluids (1994-present)*, 13(5):1367–1384.

Scotti, A. and U. Piomelli
2002. Turbulence models in pulsating flows. *AIAA journal*, 40(3):537–544.

Sergeev, S.
1966. Fluid oscillations in pipes at moderate reynolds numbers. *Fluid Dynamics*, 1(1):121–122.

Shea, P., Z. Berger, M. Berry, S. Gogineni, and M. Glauser
2014. Low-dimensional modeling of a mach 0.6 axisymmetric jet. *AIAA Paper*, (2014-0245).

Shima, N., T. Kawai, M. Okamoto, and R. Tsuchikura
2000. Prediction of streamline curvature effects on wall-bounded turbulent flows. *International journal of heat and fluid flow*, 21(5):614–619.

Smits, A. J., B. J. McKeon, and I. Marusic
2011. High-reynolds number wall turbulence. *Annual Review of Fluid Mechanics*, 43:353–375.

So, R. and T. Sommer
1996. An explicit algebraic heat-flux model for the temperature field. *International journal of heat and mass transfer*, 39(3):455–465.

Spalart, P. R.
2000. Strategies for turbulence modelling and simulations. *International Journal of Heat and Fluid Flow*, 21(3):252–263.

Spalart, P. R. and B. S. Baldwin
1989. Direct simulation of a turbulent oscillating boundary layer. In *Turbulent Shear Flows 6*, Pp. 417–440. Springer.

Sreenivasan, K. R. and A. Sahay
1997. The persistence of viscous effects in the overlap region, and the mean velocity in turbulent pipe and channel flows. *arXiv preprint physics/9708016*.

Stamou, A. and I. Katsiris
2006. Verification of a cfd model for indoor airflow and heat transfer. *Building and Environment*, 41(9):1171–1181.

Sterenborg, J., R. Lindeboom, C. S. Ferreira, A. van Zuijlen, and H. Bijl
2014. Assessment of piv-based unsteady load determination of an airfoil with actuated flap. *Journal of Fluids and Structures*, 45:79–95.

Stettler, J. and A. F. Hussain
1986. On transition of the pulsatile pipe flow. *journal of fluid mechanics*, 170:169–197.

Stuart, J.
1965. The production of intense shear layers by vortex stretching and convection. Technical report, DTIC Document.

Studer, G., D. Arnal, R. Houdeville, and A. Seraudie
2006. Laminar–turbulent transition in oscillating boundary layer: experimental and numerical analysis using continuous wavelet transform. *Experiments in fluids*, 41(5):685–698.

Taler, J.
1996. Theory of transient experimental techniques for surface heat transfer. *International Journal of Heat and Mass Transfer*, 39(17):3733–3748.

Taler, J. and D. Taler
2012. Measurement of heat flux and heat transfer coefficient.

Tang, H.-w., C. Cheng, C. Hong, and J.-t. Huang
2008. An improved ptv system for large-scale physical river model. *Journal of Hydrodynamics, Ser. B*, 20(6):669–678.

Tardu, F. S. and G. Binder
1993. Wall shear stress modulation in unsteady turbulent channel flow with high imposed frequencies. *Physics of Fluids A: Fluid Dynamics (1989-1993)*, 5(8):2028–2037.

Tardu, S. F., G. Binder, and R. F. Blackwelder
1994. Turbulent channel flow with large-amplitude velocity oscillations. *Journal of Fluid Mechanics*, 267:109–151.

Togun, H., S. Kazi, and A. Badarudin
2011. A review of experimental study of turbulent heat transfer in separated flow. *Australian Journal of Basic and Applied Sciences*, 5(10):489–505.

Townsend, A.
1961. Equilibrium layers and wall turbulence. *Journal of Fluid Mechanics*, 11(01):97–120.

Townsend, A.
1976. The structure of turbulent flow.

Trip, R., D. Kuik, J. Westerweel, and C. Poelma
2012. An experimental study of transitional pulsatile pipe flow. *Physics of Fluids (1994-present)*, 24(1):014103.

Tropea, C., A. L. Yarin, and J. F. Foss
2007. *Springer handbook of experimental fluid mechanics*, volume 1. Springer Science & Business Media.

Tsou, F., E. Sparrow, and R. J. Goldstein
1967. Flow and heat transfer in the boundary layer on a continuous moving surface. *International Journal of Heat and Mass Transfer*, 10(2):219–235.

Tsuji, T. and Y. Nagano
1988a. Characteristics of a turbulent natural convection boundary layer along a vertical flat plate. *International journal of heat and mass transfer*, 31(8):1723–1734.

Tsuji, T. and Y. Nagano
1988b. Turbulence measurements in a natural convection boundary layer along a vertical flat plate. *International journal of heat and mass transfer*, 31(10):2101–2111.

Tu, S. and B. Ramaprian
1983. Fully developed periodic turbulent pipe flow. part 1. main experimental results and comparison with predictions. *Journal of Fluid Mechanics*, 137:31–58.

Vardy, A. E. and J. M. Brown
2007. Approximation of turbulent wall shear stresses in highly transient pipe flows. *Journal of Hydraulic Engineering*, 133(11):1219–1228.

Varghese, S. S. and S. H. Frankel
2003. Numerical modeling of pulsatile turbulent flow in stenotic vessels. *Journal of biomechanical engineering*, 125(4):445–460.

Volino, R. and T. Simon
1997. Velocity and temperature profiles in turbulent boundary layer flows experiencing streamwise pressure gradients. *Journal of heat transfer*, 119(3):433–439.

Von Kerczek, C. and S. H. Davis
1974. Linear stability theory of oscillatory stokes layers. *Journal of Fluid Mechanics*, 62(04):753–773.

Walterscheid, R.
1981. Inertio-gravity wave induced accelerations of mean flow having an imposed periodic component: Implications for tidal observations in the meteor region. *Journal of Geophysical Research: Oceans*, 86(C10):9698–9706.

Wang, X., L. Castillo, and G. Araya
2008. Temperature scalings and profiles in forced convection turbulent boundary layers. *Journal of Heat Transfer*, 130(2):021701.

Wei, T., P. Fife, J. Klewicki, and P. McMurtry
2005a. Properties of the mean momentum balance in turbulent boundary layer, pipe and channel flows. *Journal of Fluid Mechanics*, 522:303–327.

Wei, T., P. Fife, J. Klewicki, and P. McMurtry
2005b. Scaling heat transfer in fully developed turbulent channel flow. *International journal of heat and mass transfer*, 48(25):5284–5296.

Weng, C., S. Boij, and A. Hanifi
2016. Numerical and theoretical investigation of pulsatile turbulent channel flows. *Journal of Fluid Mechanics*, 792:98–133.

Wilcox, D. C.
1988. Reassessment of the scale-determining equation for advanced turbulence models. *AIAA journal*, 26(11):1299–1310.

Wilcox, D. C. *et al.*
1998. *Turbulence modeling for CFD*, volume 2. DCW industries La Canada, CA.

Wu, X. and P. Moin
2010. Transitional and turbulent boundary layer with heat transfer. *Physics of Fluids (1994-present)*, 22(8):085105.

Yellin, E. L.
1966. Laminar-turbulent transition process in pulsatile flow. *Circulation research*, 19(4):791–804.

Zhai, Z. J., Z. Zhang, W. Zhang, and Q. Y. Chen
2007. Evaluation of various turbulence models in predicting airflow and turbulence in enclosed environments by cfd: Part 1-summary of prevalent turbulence models. *Hvac&R Research*, 13(6):853–870.

Zhang, Z., W. Zhang, Z. J. Zhai, and Q. Y. Chen
2007. Evaluation of various turbulence models in predicting airflow and turbulence in enclosed environments by cfd: Part 2-comparison with experimental data from literature. *Hvac&R Research*, 13(6):871–886.

APPENDIX A

FEEDBACK CONTROLLERS, THERMOCOUPLE AMPLIFIER AND ENCLOSURE BOX

This appendix provides detailed specifications of the enclosure box, in which the feedback controllers and the thermocouple amplifiers are installed. Each section of the setup is briefly introduced, its components are listed and instruction to repair/change/upgrade them is provided. The reader may consider this appendix as the user's manual of the feedback controller.

A.1 Feedback Controller Circuitry

Feedback controller circuitry is designed to keep the input signal (i.e., the temperature of the convective plate) at a constant level by means of a silicon controlled rectifier (SCR). The circuitry contains one NPN transistor, one SCR, a fuse, diodes, LEDs and resistors (Fig. A.1). In this circuit the transistor decouples the controlling section (i.e., the DAQ board and the computer with very low current) from the controlled section (i.e., the resistive heaters with high currents). The benefit of the isolation is two folds: 1- the high current of the controlled section would not damage the controller section, which is often very sensitive to high currents, and 2- the circuit can be controlled with very low current that is often provided by DAQ boards. The feedback controller works as follows:

The difference between the set and the convective plate temperatures is used as the input of the circuit. When the input is positive (i.e., the plate temperature is lower than the set temperature), a positive DC voltage (~ 5V) is applied to the base of the transistor. The transistor becomes active (like a forward diode) and allows the current flow from the DC power supply to the gate of the SCR. Now the SCR is in forward conducting mode and the resistive heaters are powered by AC

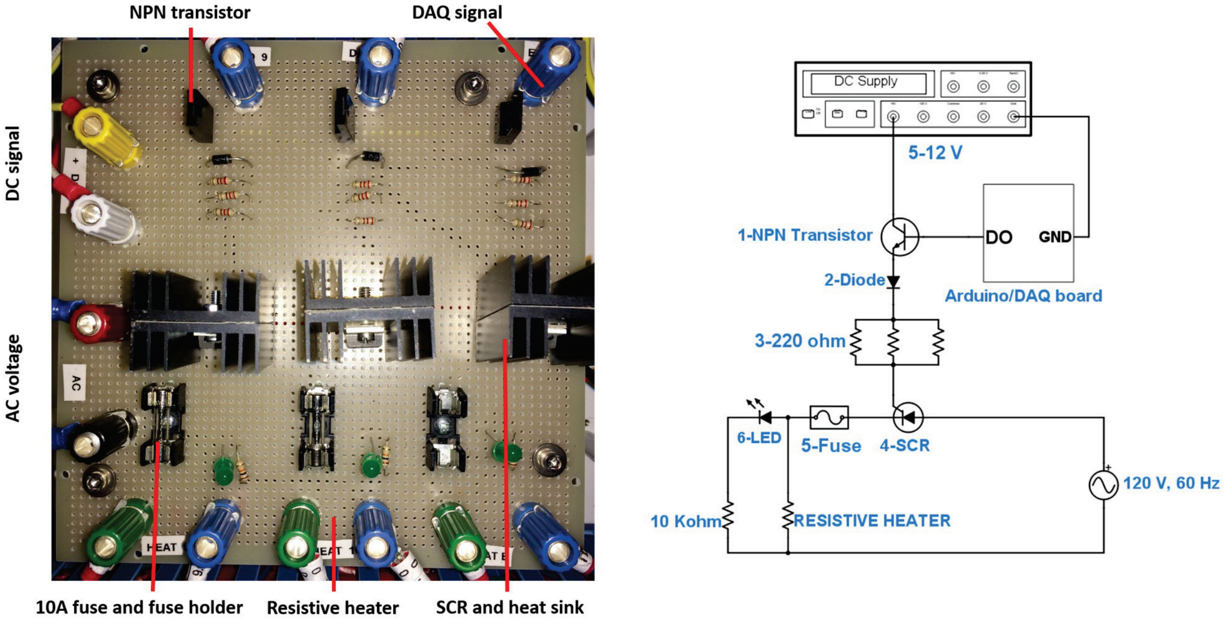

Figure A.1: Left: a photograph of the controller circuitry. Right: schematic of the feedback controller circuitry. Specifications of the numbered parts are listed in Table A.1.

voltage. When the input is negative (i.e., the plate temperature is higher than the set temperature), no positive voltage is applied to the base of the transistor and thus, the transistor is in the cutoff mode (like an open switch). As a result, the SCR gate is not charged with positive signal and the SCR switches to blocking mode (like and open switch). Hence, no current passes through the resistive heaters.

A 10A fuse is installed to protect the circuit from current overshoots. An LED is installed to help identify when the circuit is turned on or off. Specifications of the incorporated components and their suppliers are listed in Table A.1.

Reader should note that the SCR in the forward conducting mode can be assumed as a diode. Therefore, the AC current passes in half of the AC cycle and is blocked in the other half. Thus, the effective voltage applied to the heaters is half of the AC voltage input to the circuit. Limitations of the current design and suggestions to improve the performance of the controllers are provided below.

Table A.1: Specifications of the components of the feedback controller.

Number	Component	Properties	Supplier	Part number
1	NPN Transistor	230V, 1A, 2W	Digikey	2SC4793FM-ND
2	Diode	1000V, 1A	Digikey	1N4007DITR-ND
3	Resistor	220Ω, 0.25W	Digikey	CF14JT10K0TR-ND
4	SCR	400V, 10A	Digikey	S4010L-ND
4	Heat sink	TO-220	Digikey	294-1080-ND
5	Fuse	10A, 250 VAC, $5 \times 20mm^2$	Digikey	507-1235-ND
5	Fuse holder	10A, 250 VAC, Cartridge	Digikey	WK6245-ND

A.1.1 Limitations and Suggestions

The voltage is limited by the AC outlet, i.e., 120VAC. In the current setup, the supplied voltage to the resistive heaters is 60VDC. To increase the voltage one can install a resistor-capacitor in the circuit parallel to the resistive heater. This change can double the voltage and provide 120VDC to the heaters. However, the time constant of the circuit will increase as well. Therefore, one needs to be careful in choosing the values of the resistor R and the capacitor C, so the time constant $\tau = RC$ remains (much) lower than the time constant of the convective plates. Moreover, increasing the supply voltage, increases the current drawn by each circuit. The current limit of the SCRs is 10A, so one must note that the current of the two heaters that are powering the same plate, which are powered by one controller, shall not pass 10A. The maximum total current of the two heaters on the same plate with the current setup is 7.5A.

A.2 Feedback Controller Board

Feedback controller components are assembled on PCB boards. There are total of six boards (labeled as boards 1-6), each contains three circuitries. Twelve circuits (labeled as 1-12) are reserved for twelve convective plates (plates 1-12, where plate one is upstream and plate 12 is downstream of the wind tunnel), and six circuits (labeled as a-f) are saved for future use, i.e., potential upgrades. The arrangement of the circuits on the boards is explained in Table A.2. The 10A fuses of the circuits that are not in use are removed. Three AC (labeled as AC I, II and III) outlets and

Table A.2: Arrangement of the controller circuitries on PCB boards.

Board number	Active circuits	Reserved circuits
1	1	a, b
2	2, 3	c
3	4, 5	d
4	6, 7, 8	-
5	9, 10	e
6	11, 12	f

three DC plugs (labeled as DC I, II and III) are predicted for the boards. Every two boards share one AC outlet and one DC plug. A 20A fuse is installed for each AC outlet. Boards 1 and 4 share AC I and DC I ; boards 2 and 5 share AC II and DC II; and boards 3 and 6 share outlets AC III and DC III. The total current of the AC outlets with the current setup are 9A, 12A and 16, respectively. The DC current draw of of circuits are well below 1A, so one may share one power supply for all DC plugs. The grounded DC voltage between 6V to 12V is suggested for the controllers.

A.3 Thermocouple Amplifier

Analog Devices AD594 thermocouple amplifiers are incorporated to amplify the micro-voltage of the thermocouples with the sensitivity of 10 $mV/°C$. A schematic of the circuitry is shown in Fig. A.2. Every three amplifier components, which measure the spanwise temperature distribution of one convective plate, are installed on one PCB board. On each board amplifiers 1 (L), 2(C) and 3(R) are for the thermocouples mounted on the right, middle and left of the plate. Right and left are defined when one looks at the convective plate such that plate 1 is up and plate 12 is on bottom. Amplifier of plates 1-6, plates 7-9 and plates 10-12 share DC V, DC VI and DC VII. The current drawn by the amplifiers are well below 1A, so one may share one power supply for all DC plugs. The DC voltage must be between 5V to 15V. The DC voltage does not alter the sensitivity of the amplifiers, however, lower voltage induces less noise. The DC voltage of the power supply can be grounded or floating, but one must be consistent since providing floating voltage imposes a bias in

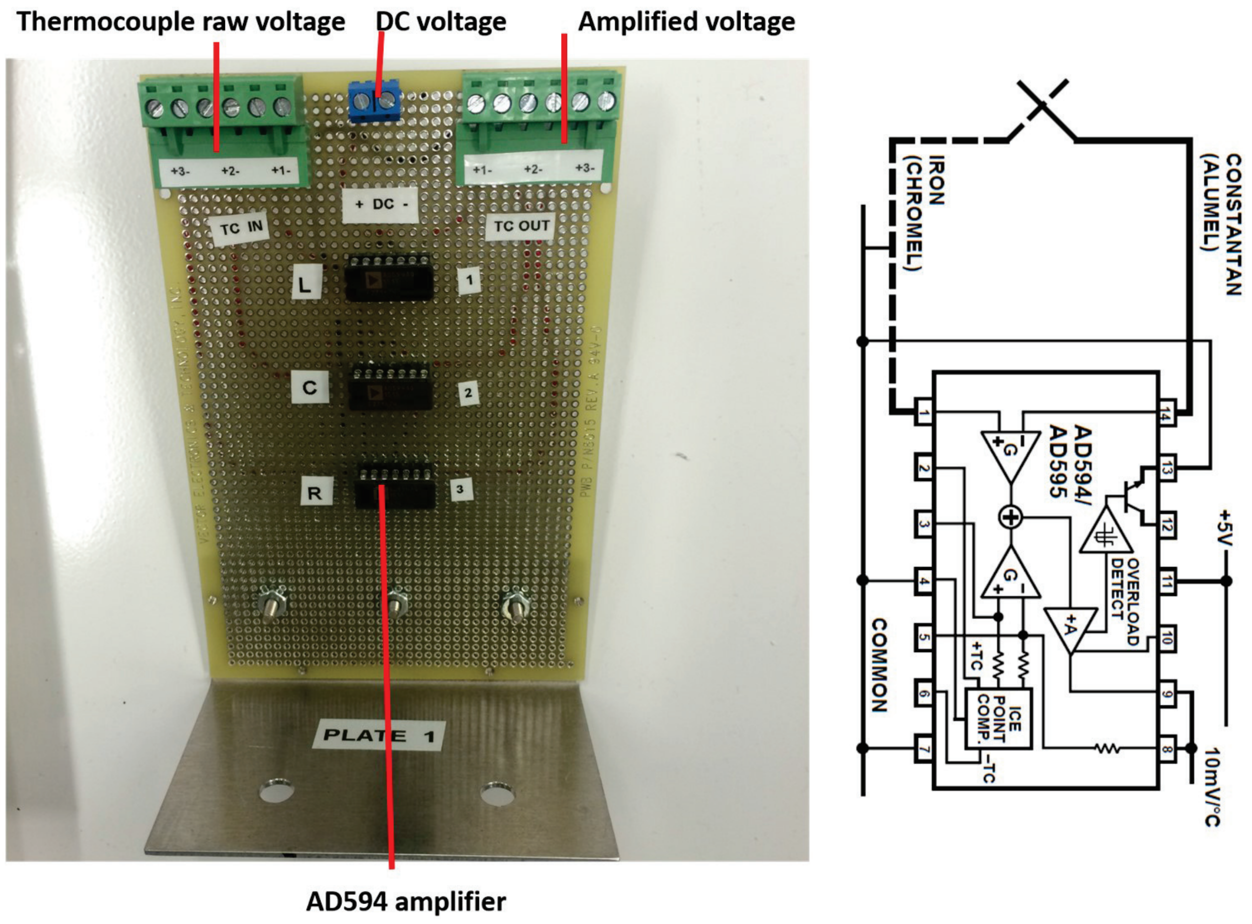

Figure A.2: Left: a photograph of the thermocouple amplifier board. Right: schematic of the the thermocouple amplifier circuitry. Diagram adopted from Analog Devices.

the voltage of the amplifiers. Therefore, a grounded 6VDC is suggested for amplifiers.

A.4 Enclosure Box

A $76.20 \times 60.96 \times 30.48 cm^3$ Hammond Manufacturing box is utilized as the enclosure box in this project. Figure A.3 shows the computer-aided design (CAD) of the box. The panel on the left-hand side (LHS) of the box is used as the interface between user and the controller boards, and the right-hand side (RHS) panel is used as the interface between user and the thermocouple amplifier boards. Six controller boards, twelve thermocouple amplifier boards and four wire ducts are installed on the mounting panel in the enclosure box. Details of the wirings between the barrier

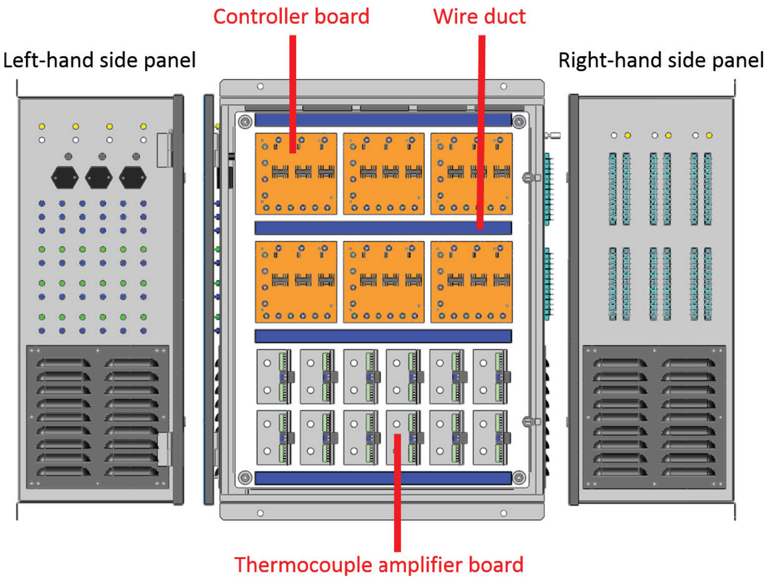

Figure A.3: Computer-aided design (CAD) of the enclosure box. Details of the electronics can be seen in Fig. A.4.

terminals and the binding posts on the side panels of the box, and the electronic boards on the mounting panel is provided in Table A.3. Five DC fans are installed on the top panel of the box to cool the SCRs. The cooling fans share DC IV and they share the power supply of the feedback controllers. A transparent window is installed on the door for visual inspections. A photograph of the mounting panel of the box is shown in Fig. A.4.

Table A.3: The arrangement, color code and the size of the hook-up wires used in the enclosure box.

From (side panel)	To (mountaing panel)	Color	Size (AWG)
DC + (LHS)	DC+ (controller)	Yellow	16
DC - (LHS)	DC- (controller)	White	16
DC + (LHS)	DC+ (Fan)	Red	22
DC - (LHS)	DC+ (Fan)	Black	22
AC hot (LHS)	AC+ (controller)	Red	14
AC neutral + (LHS)	AC - (controller)	Black	14
AC ground (LHS)	AC ground (box)	Green	14
DAQ + (LHS)	DAQ (controller)	Purple	16
Heater (LHS)	Heater (controller)	Blue	16
Heater (LHS)	Heater (controller)	Green	16
TC in + (RHS)	TC in + (amplifier)	White (TC extension)	20
TC in - (RHS)	TC in - (amplifier)	Red (TC extension)	20
TC out + (RHS)	TC out + (amplifier)	Red	22
TC out - (RHS)	TC out - (amplifier)	Black	22
DC + (RHS)	DC+ (amplifier)	Yellow	16
DC - (RHS)	DC- (amplifier)	White	16
DC + (LHS)	DC+ (controller)	Yellow	16

Table A.4: The color code of the hook-up wires that connect the resistive heaters to the enclosure box.

Plate (heater)	Wire color code
1 (1)	Red-Black
1(2)	Red-White
2(1)	Red-Green
2(2)	Red-Yellow
3(1)	Blue-Green
3(2)	Blue-Orange
4(1)	Blue-Gray
4(2)	Blue-Brown
5(1)	Blue-White
5(2)	Blue-Yellow
6(1)	Purple-Brown
6(2)	Purple-Yellow
7(1)	Purple-Orange
7(2)	Purple-Green/Yellow
8(1)	Purple-Black
8(2)	Purple-Red
9(1)	White-Yellow
9(2)	White-Black
10(1)	White-Green
10(2)	White-Blue
11(1)	Green-Blue
11(2)	Green-Yellow
12(1)	Black-Blue
12(2)	Black-Yellow

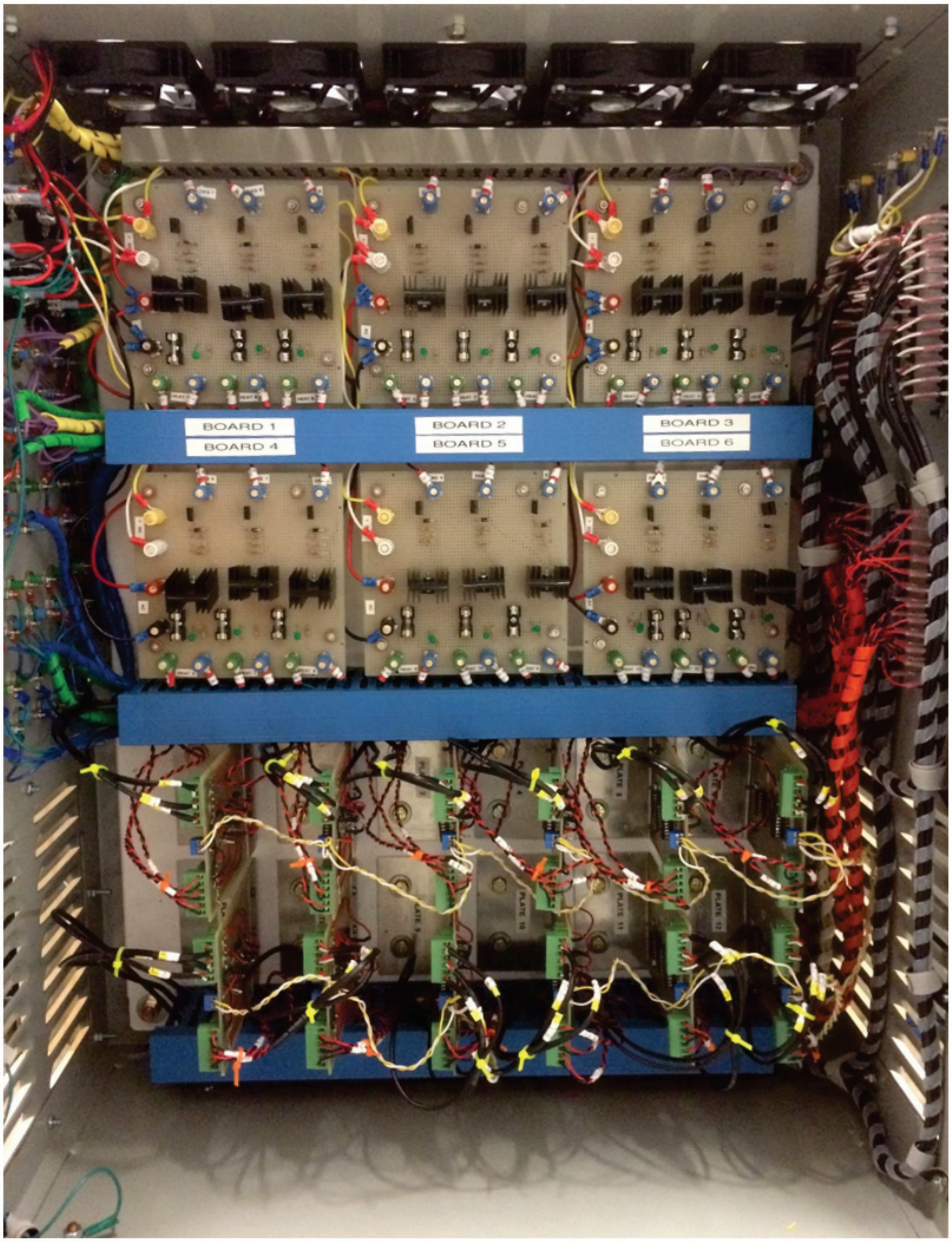

Figure A.4: Photograph of the mounting panel inside the enclosure box.

APPENDIX B

MODULATION FREQUENCY OF THE WALL SHEAR STRESS AND HEAT FLUX IN RECIPROCATING CHANNEL FLOW

A toy model is developed to relate the modulation frequency of Nu and τ_w to the forcing frequency in a reciprocating channel flow:

Near the channel centerline, viscous forces and advection can be neglected, hence, the momentum balance reduces to

$$\frac{\partial u}{\partial t} = -\frac{1}{\rho}\frac{\partial P}{\partial x}. \tag{B.1}$$

where u is mean streamwise velocity, ρ is the density, P is pressure, x is the streamwise direction and t is time. Integrating Eq. B.1 in time and replacing the pressure gradient with a cosinusoidal term, i.e., $\frac{\partial P}{\partial x} = cos(\omega t)$, results in the following

$$u(t) = C_1 sin(\omega t), \tag{B.2}$$

where C_1 can be determined by initial condition and ω is the forcing frequency.

Similarly, the thermal transport equation near the channel centerline reduces to

$$\frac{\partial \Theta}{\partial t} + u\frac{\partial \Theta}{\partial x} = 0. \tag{B.3}$$

where θ is the mean temperature. Integrating Eq. B.3 in time and assuming $\frac{\partial \Theta}{\partial x}$ modulates with the forcing frequency, results in the following

$$T(t) = C_2 cos(2\omega t), \tag{B.4}$$

where C_2 can be determined by initial condition. Equations B.2 and B.4 show that while velocity (and therefore, wall shear stress) modulate with a frequency equal to the forcing frequency, temperature (and therefore, wall heat flux) modulate with a frequency twice the forcing frequency.

APPENDIX C

EXPERIMENTAL PROCEDURE

This appendix provides a step-by-step description of the experimental procedure. The procedure is divided into eleven main operations. For each operation, a bulleted list of tasks are given.

1. **Preliminaries**

    - Close laboratory doors, turn *laser warning light* ON and place laser curtains in front of the lab doors.
    - Turn refrigerated chiller ON and wait until the laser temperature reaches $20°C$.
    - Turn the laser power supplies ON.
    - Turn fog machine ON and wait until the green *ready* indicator on the remote illuminates before pumping fog.
    - Remove camera lens caps and turn cameras ON.
    - Remove laser lens cap.

2. **Laser turn on (for alignment and camera calibration)**

    - Wear OD 0.9 @ 527nm laser alignments goggles.
    - Turn on PIV computer and launch *Davis 8.3.1*. In the toolbar click *New*, assign a *Project name* and select *PIV* as the *Type of project*.
    - Record experimental parameters such as room temperature and fan motor frequency among others to *labbook.txt*. More information will be recorded in *labbook.txt* throughout the experiment.

- Click *Recording* in the toolbar.
- Under *Device Settings-HighSpeedRecording-Laser 1*, check *Pulse T1A*, set laser mode to *off*, check both *camera 01* and *camera 02*. From the drop-down menu choose *single frame (T1A)* for both cameras.
- Under *Timing*, set *Image rate* to *0.25kHz*.
- Turn upper laser power supply to ON.
- On the laser power supply: push *Shutter* button.
- On the power supply: push *Menu* button, select *Diode Setting* and hit *Enter*.
- On the laser power supply: Turn laser enable key-switch ON.
- On the laser power supply: Push *LDD* to ON.
- On the laser power supply: Increase I_s slowly to 10A, which is the onset of lasing for laser 1, hit *Enter*.
- In *Davis* set the laser mode to *Adjust*.
- Check the laser beam and light sheet alignment.

3. **Camera scaling**

- Insert the calibration plate so that it faces camera 01 and carefully align the plate such that it's front face is grazed by the laser sheet.
- In the *Window Manager*, under *Light Source*, set laser mode to OFF.
- Under *live mode* click *Grab continuously*.
- In the live window select *F=0*, adjust camera 01 focus until the calibration plate is in focus.
- Under *Device Settings-Timing*, set *Cycle rate* to *1Hz*, *Start [Image]*, *End [Image]* and *Cycles* to 1. This setting records a single image.

- Under *Recording Sequence-Recording Sequence*, check *Store immediately after recording*.
- In the *Window Manager*, under *Recording*, set *Recording Name* to *Cam01-Calibration* and click *Recording*.
- Record camera f-# and exit *Recording*.
- In directory window, right click on *Cam01-Calibration* and click *Convert all Stream sets to native sets*.
- Repeat procedure above for camera 02.
- Remove the calibration plate from the tunnel.

4. **Calibration**

  - Click *Calibration* in the DaVis toolbar.
  - *Define experimental setup*: select *2 cameras (independent 2D+2D)*; click *Next*.
  - *Define coordinate system*: click *Next*.
  - *Select calibration plate(s) used*: select *Type 11* under *Coordinate system 1* and *Coordinate system 2*; click *Next*.
  - *Image acquisition*: click *images* and from *Cam01-Calibration* select *B00001.im7*. Under *Select frames to input from the image*, check *frame 0 (=camera1)*, check *specify camera # (overrides frame info)* and set to 1, click *OK*. Repeat for camera 02, click *Next*.
  - *Mark definition*: select *All cameras/views*, follow instruction and select 3 marks on each image (6 in total); click *Next*.
  - *Finding all marks*, click *Start search*, click *Next*.
  - *Fit mapping function*:click *Start Calibration*, click *Next*.
  - *Evaluation of corrected images*: check both calibrations under *Coordinate system 1* and *Coordinate system 2*, click *Finish*.

- In the pop-up window, select *Overwrite active project with new scales and calibration AND rescale all root image/recording dataset*, click *OK*.

5. **Move image origin**

   - Click *Calibration* in the DaVis toolbar.
   - *Define experimental setup*: select *define origin, maintain calibration*; click *Next*.
   - *Define origin / maintain calibration*: Under *Action: calibrate visible frame in working window*, select lower left corner as the placement of the origin., Click *Yes* in the pop-up window. Repeat for F=1; click *Finish*.
   - In directory window, expand *Properties* and expand *Calibration*, click *camera 01*, right click on image and select *Data properties*, select *Scales* and record scale *Factor*, click *Close*. Repeat for *camera 02*.
   - Write the calibration scales to *labbook.txt*.
   - Estimate the wall location in the image (use mouse/pixel coordinate indicator on the viewer) and record the estimated wall location to *labbook.txt*.

6. **Turn laser ON (for data acquisition)**

   - Wear OD7+ @ 527nm goggles.
   - On the upper power supply: hit *Enter* and increase the current slowly to 14A, hit *Enter*.
   - Turn on the bottom power supply, follow the same directions as described in bulleted list of operation 2.
   - Increase the current to 14A, hit *Enter*.
   - Record the laser currents to *labbook.txt*.

7. **Image settings**

   - Click *Recording* in the DaVis toolbar.

- Under *Device setting* click *camera 01: HighSpeedStar 5.1*, under *Area Of Interest*, select *Resolution* and *Origin*. The maximum frame rate for full frame (1024×1024 pixel^2) is 3.6kHz. To record at higher frame rate, the AOI must be smaller. For the current experiments, 448×1024 pixel^2 is chosen to record at 7.2kHz. The origin of the two cameras must be selected such that the two images overlap.
- If background intensity subtraction is needed, under *Timing*, set *Image rate* to a number that experiments will be performed at that frequency.
- Expand *Device setting-camera 01: HighSpeedStar 5.1*, click *Intensity Correction*.
- In the *Window Manager*, set laser mode to *On*. Shut room lights.
- Click *Take Background Image* and check *Background subtraction*. Repeat for camera 02.
- In the *Window Manager*, set laser mode to OFF..

8. **PIV measurements**

- Wear OD7+ @ 527nm goggles.
- Turn on the suction fan of the wind tunnel and set fan motor frequency to desired value.
- Turn room lights OFF.
- Under *Device Settings-HighSpeedRecording-Laser 1*, check laser(s) and select appropriate recording modes
- Under *Device Settings-Timing*, set *Cycle rate*, *Start [Image]*, *End [Image]* and *Cycles* appropriately. The settings are unique for each experimental setup. If *Double Frame (T1A+T1B)* is chosen, set *Start [Image]* and *End [Image]* to 1. If *Single Frame (T1A)* is chosen, set *Start [Image]* and *End [Image]* to 1 and 2, respectively.
- In the *Window Manager*, set laser mode to ON.
- Turn on the fog pump and wait until a sufficient fog density has filled the tunnel test-section.

- Click *Start Recording*.
- When recording is finished, set laser mode to OFF.

9. **Laser turn off**

   - Verify that laser mode is set to OFF.
   - On the top power supply: hit *Enter* and decrease I_s slowly to 0A and hit *Enter*.
   - Push *LDD* to OFF.
   - Turn laser enable key-switch to OFF.
   - Push *Shutter* to OFF..
   - Turn top power supply OFF.
   - Turn bottom power supply OFF.
   - Put laser lens cover on.

10. **Image processing**

    - Recorded images can be processed with *Davis 8.3.1*, or *Davis 8.0.6*. Author finds the latter to be more stable near the edges of image and masks. *Davis 8.3.1* image format is not compatible with *Davis 8.0.6*, To convert the format, right click on the image set and click *Convert to native set*. *Convert all Stream sets to native sets* can be selected to convert all images.
    - In the toolbar, click *Processing*. Set the desired settings in the *Operation list*. The operation settings include mask definition, interrogation area size, number of passes and overlap percentage, filtering and interpolation schemes, among others.
    - Click *Test Processing* and evaluate the vector fields qualitatively. Repeat process for a few snapshots.
    - Once the operation list is finalized, click Save icon in the *Operation list* and click *Export to file*. Choose the destination and save the operation list code.

- Click *Start Processing*.
- Once the processing is done, the vector fields can be exported as .txt files. Include a copy of *labbook.txt* in the destination folder.

11. **Tunnel clean-up**

- Facility clean-up is necessary to remove the buildup of oil from the flow facility. This must be done both periodically during an experimental run and when the experiment is finished.
- Using a damp towel wipe down and remove accumulated oil film form the thermal wall-plate, test-section wall, diffuser and the exhaust fan.
- Using a dry towel wipe down and dry the thermal wall-plate, test-section wall, diffuser and the exhaust fan.